FREE SURFACE DYNAMICS IN SHALLOW TURBULENT FLOWS

Andrew NICHOLS

Submitted for the degree of

Doctor of Philosophy

School of Engineering, Design & Technology

University of Bradford

2013

“The best image of process is perhaps that of the flowing stream, whose substance is never the same. On this stream, one may see an ever-changing pattern of vortices, ripples, waves, splashes, etc., which evidently have no independent existence as such. Rather, they are abstracted from the flowing movement, arising and vanishing in the total process of the flow”

- David Bohm

Abstract

This study aimed to understand the processes that govern free surface behaviour in depth-limited turbulent flows. Experimental data has shown that the turbulence properties at a point near the free surface relate directly to the properties of the free surface pattern. This would suggest a direct linkage between the free surface and the underlying turbulence field, but this cannot be true since the free surface pattern is strongly dynamic while the sub-surface turbulence field is relatively persistent.

An oscillatory spatial correlation function was derived which explains the de-linkage, showing that the turbulence-generated surface pattern periodically inverts as it advects downstream. A model was developed, which shows that the observed free surfaces can be considered as an ensemble of overlapping but behaviourally independent oscillons. These are shown to influence a zone of fluid beneath the surface and invert at a frequency which is a function of the root-mean-square roughness height of the free surface. The spatial frequency of free surface oscillation relates strongly to the spatial frequency of turbulent structures, suggesting that the oscillon motion may form the trigger for near-bed bursting events.

Given these relationships, it is proposed that measurement of the free surface behaviour may allow remote measurement of flow conditions. An acoustic wave probe was developed, which is able to remotely recover the key features of the water surface pattern. An array of such probes is proposed for the accurate measurement of temporal and spatial properties of turbulent free surfaces and hence the underlying bulk flow conditions.

Keywords: PIV; LIF; Free surface; Turbulence; Coherent structures; U-level; Acoustic; Ultrasonic; Scattering;

Dedication

To Erin and Imogen:

Thank you for providing foundation, motivation, and inspiration.

Acknowledgements

The author would like to express sincere gratitude to Professor Simon Tait, Professor Kirill Horoshenkov and Professor Simon Shepherd for the outstanding supervision and continuous support provided throughout this study.

Also to be thanked are the numerous technical staff who provided essential assistance and advice regarding laboratory setup, most notably Nigel Smith, Antony Daron, Ken Howell and Joanna Wood.

The various members of the Acoustics and Hydraulics groups at Bradford University deserve a special mention, along with the Acoustics Research Group at the Open University, and the Pennine Water Group at Sheffield University, with whom it was a pleasure to work.

The author would also like to express deepest appreciation to partner Nichole, and daughters Erin and Imogen for their unwavering support (and patience!) throughout the highs and lows of this study, along with parents, Roger and Mary, and sister, Tamsin, for their continued support.

Journal Publications

Nichols, A., Attenborough, K. and Taherzadeh, S., 2011. Deduction of static surface roughness from complex excess attenuation. *Journal of the Acoustical Society of America,* 129(3), pp. EL89-EL93.

Horoshenkov, K. V., Nichols, A., Tait, S. J. and Maximov, G. A., 2013. The pattern of surface waves in a shallow free surface flow. *Journal of Geophysical Research: Earth Surface*, 118(3), pp. 1864-1876.

Nichols, A., Tait, S., Horoshenkov, K. and Shepherd, S., 2013. A non-invasive airborne wave monitor. *Flow Measurement and Instrumentation,* 34, pp. 118-126.

Conference Publications

Nichols, A., Horoshenkov, K., Shepherd, S., Attenborough, K. and Tait, S., 2010. Sonic Characterisation of Water Surface Waves. In: L. Yun, W. Shiqiang, eds. 2011. *Advances in Physical Modeling and Field Investigation Technology – Proceedings of International Symposium on Hydraulic Physical Modeling and Field Investigation*. China: China WaterPower Press, pp. 40-47.

Nichols, A., Tait, S., Horoshenkov, K., Shepherd, S. and Maximov, G., 2010. An airborne monochromatic acoustic method to measure the hydraulic characteristics of shallow water flows. *Proceedings of the 160th meeting of the Acoustical Society of America & 2nd Pan-American/Iberian Meeting on Acoustics, Cancun, Mexico, 15-19 November 2010. J. Acoust. Soc. Am.*, 128, pp. 2327.

Nichols, A., Attenborough, K., Taherzadeh, S. and Shepherd, S., 2010. An airborne broadband acoustic method to measure the characteristics of a dynamically rough air-water interface. *Proceedings of the 160th meeting of the Acoustical Society of America & 2nd Pan-American/Iberian Meeting on Acoustics, Cancun, Mexico, 15-19 November 2010. J. Acoust. Soc. Am.*, 128, pp. 2327.

Nichols, A., Tait, S., Horoshenkov, K., Shepherd, S. and Maximov, G., 2011. An Airborne Acoustic Method to Monitor the Hydraulic Characteristics of Shallow Water Flows. In: *Proceedings of the 34th World Congress of the International Association for Hydro- Environment Research and Engineering: 33rd Hydrology and Water Resources Symposium and 10th Conference on Hydraulics in Water Engineering.* Barton, A.C.T.: Engineers Australia, pp. 817-824.

Nichols, A., Horoshenkov, K., Tait, S. and Maximov, G., 2011. Acoustic scattering strength of turbulence generated waves in a shallow water flow. *Proceedings of 162nd Meeting of the Acoustical Society of America, San Diego, California, 31 October - 4 November 2011. J. Acoust. Soc. Am.*, 130, pp. 2436.

Nichols, A., Horoshenkov, K., Tait, S. and Attenborough, K., 2011. An investigation into the interaction of a grazing angle broadband spherical audio signal with the dynamically rough air–water interface of shallow flows in rivers and channels. *Proceedings of 162nd Meeting of the Acoustical Society of America, San Diego, California, 31 October - 4 November 2011. J. Acoust. Soc. Am.*, 130, pp. 2513.

Nichols, A. and Shepherd, S., 2012. Visualising the variation in normality of a turbulent velocity field. In: R. Murillo, ed. 2012. *River Flow 2012, Volume 1.* Leiden: CRC Press, pp. 85-89.

Nichols, A., Tait, S., and Horoshenkov, K., 2012. Characterization of shallow flows using novel acoustic instrumentation. In: R. Murillo, ed. 2012. *River Flow 2012, Volume 2.* Leiden: CRC Press, pp. 1285-1292.

Nichols, A., Horoshenkov, K., Tait, S. and Shepherd, S., 2013. Making use of Turbulence and its Interaction with Sound: A Non-Invasive Flow Monitor. *Proceedings of the 2nd Symposium of Fluid-Structure-Sound Interaction and Control, 20-23 May 2013, Hong Kong and Macau,* pp. 162-163.

Nichols, A., Horoshenkov, K., Tait, S., Shepherd, S. and Zhang, Y., 2013. Low cost on-line non-invasive sewer flow monitoring. *7th International Conference on Sewer Processes and Networks, 27-30 August 2013, Sheffield, UK.*

Awards

SET for Britain 2012 finalist.

CIWEM new generations competition winner.

IAHR UK young person's paper competition winner.

SWIG early career researcher competition winner.

Patents

PCT/GB2012/050489, Acoustic Measurement of Dynamic Surface Characteristics.

PCT/GB2013/052182, Fluid and Sediment Conductivity Profiler.

Grants awarded

Sediment conductivity profiler, feasibility study:

Pennine Water Group Platform Grant - 3 months PDRA funding.

Establishment of field test site for sewer instrumentation:

Pennine Water Group Platform Grant - 3 months PDRA funding.

Affiliations

Member of the Chartered Institute of Water and Environmental Management.

Committee member for the Tyne and Humber Branch of the Chartered Institute of Water and Environmental Management.

Eco-committee member for Otley Street School, Skipton.

Contents

Figures

Tables

Nomenclature

a_n	Instantaneous signal amplitude	[Pa]
A_0	Amplitude of transmitted signal	[Pa]
A_r	Amplitude of received signal	[Pa]
C_p	Phase velocity of surface features	[m/s]
dh	Change in height of acoustic sensor above surface	[m]
dt	Time step	[s]
d_{U_u}	Mean event duration in streamwise velocity data	[s]
d_{U_v}	Mean event duration in vertical velocity data	[s]
D	Uniform water depth	[m]
E	Mean absolute error in elevation measurement	[mm]
E_a	Mean error relative to acoustic wavelength	[%]
E_{pp}	Mean error relative to peak-peak wave height	[%]
f	Frequency	[Hz]
f_d	Dominant surface frequency	[Hz]
f_o	Frequency of surface oscillation	[Hz]
f_r	Darcy-Weisbach friction factor	[-]
f_U	U-level event detection frequency	[Hz]
f_{shm}	Frequency according to simple harmonic motion	[Hz]
F	Function handle for minimisation	[-]
F_s	Vertical force of surface feature	[N]
g	Acceleration due to gravity	[m/s^2]
G	Mean absolute local surface gradient	[-]

h	Height of acoustic sensor above surface	[m]
h_{pp}	Mean peak-peak wave height	[m]
k	Wavenumber	[1/m]
k_m	Manning's conversion constant	[$m^{1/3}$/s]
k_s	Hydraulic roughness coefficient	[m]
k_U	U-level conditional sampling threshold	[-]
K	System stiffness	[N/m]
L	Mean/initial distance from source to receiver	[m]
L_0	Characteristic spatial period	[m]
L_b	Instantaneous distant from source to receiver	[m]
L_s	Length of turbulent structure	[m]
L_U	Length of structure determined by U-level analysis	[m]
M	Mean wave probe output during calibration	[V]
M_s	Effective mass of surface feature	[kg]
n	Manning's roughness coefficient	[-]
n_U	Number of events detected by U-level analysis	[-]
N	Number of integration points	[-]
p	Probability	[-]
p_U	U-level probability threshold	[-]
Q	Flow rate/discharge	[m^3/s]
R_h	Hydraulic radius	[m]
Re	Flow Reynolds number	[-]
Re_s	Surface-based Reynolds number	[-]
s_u	Standard deviation of streamwise velocity series	[m/s]

s_v	Standard deviation of vertical velocity series	[m/s]
$\tilde{S}$	Power spectral density	[m^2/Hz]
S_0	Bed slope	[-]
S_f	Energy slope	[-]
S_U	U-level mean distance between structures	[m]
t	Time	[s]
t_d	Time difference between two signals	[s]
T	Total measurement time	[s]
u	Instantaneous local streamwise velocity	[m/s]
u'	Instantaneous local streamwise velocity fluctuation	[m/s]
$\langle u \rangle$	Local mean streamwise velocity	[m/s]
u_{rms+}	Normalised streamwise turbulence intensity	[-]
u_N	Normalised deviate of streamwise velocity	[std]
u'_U	U-level binarized streamwise velocity series	[-]
U	Depth-local mean streamwise velocity	[m/s]
U_*	Shear velocity	[m/s]
U^+	Normalised depth-local mean streamwise velocity	[m/s]
U_b	Bulk flow velocity	[m/s]
v	Instantaneous local vertical velocity	[m/s]
v'	Instantaneous local vertical velocity fluctuation	[m/s]
$\langle v \rangle$	Local mean vertical velocity	[m/s]
v_{rms+}	Normalised vertical turbulence intensity	[-]
v_N	Normalised deviate of vertical velocity	[std]
v'_U	U-level binarized vertical velocity series	[-]

V	Depth-averaged mean streamwise velocity	[m/s]
V_a	Structure advection velocity	[m/s]
V_s	Surface flow velocity	[m/s]
w	Instantaneous local lateral velocity	[m/s]
w'	Instantaneous local lateral velocity fluctuation	[m/s]
$\langle w \rangle$	Local mean lateral velocity	[m/s]
w_{rms+}	Normalised lateral turbulence intensity	[-]
W	Correlation function	[-]
x	Temporally reconstructed spatial lag	[m]
x_s	Individual surface feature elevation	[m]
X	Design vector for optimisation routine	[-]
y	Depthwise location	[m]
y^+	Normalised depthwise location	[-]
z	Minimisation design vector	[-]
φ_s	Mean/initial phase difference	[rad]
γ	Lateral position	[m]
γ_s	Fluid surface tension	[N/m]
η	Free surface elevation	[m]
η'	Free surface elevation fluctuation	[m]
$\langle \eta \rangle$	Mean free surface elevation	[m]
η_a	Elevation measured acoustically	[m]
η_w	Elevation measured by wave probe	[m]
κ	Von Kármán constant	[-]
λ	Water surface wavelength	[m]

λ_a	Acoustic wavelength	[m]
ν	Kinematic viscosity	[m^2/s]
ν_r	Hilbert transform of received signal	[-]
ν_s	Hilbert transform of sent signal	[-]
ϖ	Angular frequency	[rad/s]
ρ	Spatial separation	[m]
ρ_f	Fluid density	[kg/m^3]
σ	Root-mean-square wave/roughness height	[m]
σ_w	Correlation radius	[m]
τ	Time lag	[s]
τ_e	Time lag at extremum correlation	[s]
Δ	Spatial separation in number of samples	[samples]
ΔL	Change in distance from source to receiver	[m]
$\Delta\varphi$	Phase difference fluctuation	[rad]
$\Delta\gamma$	Lateral spatial lag	[m]
N	Depth of influence factor	[-]

Abbreviations

B&K	Brüel & Kjær (microphone manufacturer)
CCD	Charged-coupled device (for image capture)
DAQ	Data acquisition
LDS	Laser displacement sensor
LES	Large eddy simulation
LIF	Laser induced fluorescence
Nd:YAG	Neodymium-doped yttrium aluminium garnet (laser)
NI	National Instruments (DAQ systems manufacturer)
PIV	Particle image velocimetry
PXIe	Peripheral component interconnect eXtensions for Instrumentation - express
RMS	Root-mean-square
ST	Space-time matrix
std	Standard deviation

Chapter 1 - Introduction

1.1 Background

This thesis draws from two broad research topics, turbulent shallow flows and acoustic scattering from dynamically rough boundaries, thereby addressing an under-studied area in each of these topics in order to pave the way for applications which span both areas of work.

There are many situations where an acoustic field is incident on a rough water surface (e.g. aircraft noise over sea surfaces), so an understanding of the linkage between the surface roughness characteristics and the characteristics of the scattered acoustic field is critical. This understanding should ultimately enable the prediction of the acoustic response of a given rough surface, or estimation of the surface characteristics from a given acoustic response. Although the effects of dynamically rough surfaces on acoustic fields have been extensively researched in the context of ocean waves generated by wind (Tolstoy, 1982; Qin, et al., 2008; Bass & Fuks, 1979; Dahl, 1999), there has been very little work studying the acoustic scattering by the surface of shallow flows, where the free surface pattern is generated by the turbulent nature of the flow rather than external elements such as wind-induced gravity waves. This is surprising given that shallow turbulent flows are so common in nature and in urban drainage infrastructure. Although some research studies have shown that there is a link between the acoustic field over a shallow water flow and the hydraulic properties of the flow (Cooper, et al., 2006; Horoshenkov, et al., 2004), the mechanisms or physical principles behind any relationship are yet to be investigated.

The purpose of this study is therefore to examine the processes which govern the relationship between turbulent flow properties, properties of the free surface roughness and the acoustic response of the statistically rough interface. The overall goal of this work is to develop a technique to determine the free surface behaviour and hence the bulk flow properties based on remote acoustic measurement of the free surface dynamics.

1.2 **Hypotheses**

This work focuses on a number of hypotheses. As the free surface defines the boundary between the hydraulic and acoustic processes, so it enables the two processes to be considered separately, both in relation to the free surface itself. This enables a better understanding of how these processes interact when acoustic waves are incident on the dynamically rough free surface of shallow turbulent flows.

1. The author believes that (a) free surface patterns are generated by sub-surface flow features and that (b) these features are in some way a function of the bulk flow properties and bed characteristics. In this case the surface pattern may be predicted based on the bulk flow properties, or the bulk flow properties may be estimated based on the shape and behaviour of the free surface pattern.
2. It is believed that the generated free surface pattern behaves in a predictable manner and that it measurably and predictably affects a suitable acoustic field above the surface. In this case the relationship between the free surface and the acoustic field can be considered in either direction such that free surface data can be used to predict the

acoustic response, or this acoustic response can be used to determine free surface properties.

3. The author believes that given relationships of the form described, these dependencies could be combined, allowing the free surface itself to eventually be practically inconsequential (though physically critical), simply acting as a mechanism transferring information from one phase to another. This would allow the acoustic response of a given flow to be used to determine the bulk hydraulic properties and vice versa.

1.3 **Areas covered by this work**

This work focuses on the collection and analysis of a novel and extensive set of data regarding flow properties, free surface dynamics, and acoustic response. Analysis of turbulent features will help to determine the controlling factors in the properties of turbulent structures in shallow flows and to examine the relationship between bulk flow parameters and turbulence statistics. Linking the sub-surface flow to the free surface dynamics will allow assessment of the degree to which the free surface relates to the turbulent structures beneath the surface and will help to develop an understanding of the interaction between the free surface and the flow field. Examination of acoustic data will reveal the parameters of the dynamic surface roughness which influence the scattered acoustic field. The above findings will be used to propose a non-invasive method of characterising flow properties based on the measured acoustic properties as presented schematically in Figure 1-1.

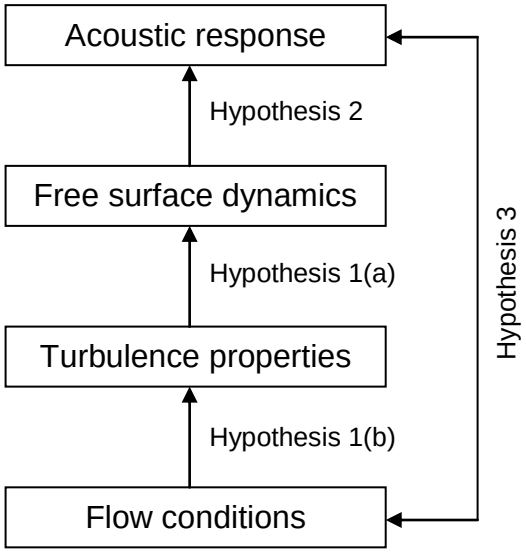

Figure 1-1: Properties to be measured, the expected dependencies, and the overall relationship sought

1.4 **Aims and objectives**

The primary aim of this research is to collect a representative set of hydraulic and acoustic data which show that the acoustic field above a turbulent flow is related to the flow conditions and that it contains unambiguous information about the flow conditions.

The free surface acts as the information exchange mechanism between the two systems, and since it provides a clear boundary, the work is accordingly divided into two related parts: (Aim 1) determine the hydraulic processes governing free surface roughness; (Aim 2) develop an understanding of the acoustic response to dynamic rough surfaces. With these aims in mind, the objectives of the study are formulated as follows:

- Establish a test facility capable of synchronously measuring the hydraulic, free surface, and acoustic properties of shallow turbulent flows.

- Use this facility to gather data for a range of flow conditions which vary in depth, discharge, bed slope, and bed type.
- Investigate and define the flow variables which influence free surface roughness, and the mechanisms by which they do so.
- Determine the meaningful characteristics of the acoustic field reflected from a dynamically rough boundary.
- Use the relationships between the flow properties and free surface roughness, and between the free surface roughness and acoustic response, to show that the acoustic field may be used to infer the flow properties non-invasively.

1.5 **Thesis structure**

In the 2nd chapter, an initial review of the previous literature and prior art spanning from the 19th century to recent years will be used to present the context of this study and to establish the void in understanding which this work is aiming to address. The development of the new experimental facilities and any potential sources of measurement error will then be discussed in chapter 3. A report of data validation will be given in chapter 4 in order to show that the measurement techniques provide sensible, repeatable and reliable information. This information will then be used in chapter 5 to investigate the generation and evolution of turbulent features within shallow flows, and the degree to which these features influence the pattern of the free surface. Results are then presented which show a mutual dependence between the free surface dynamics and the sub-surface flow field. A model is developed which provides a reliable first approximation to explain the dynamic behaviour of the free surface in response to the flow field beneath.

Knowledge of this relationship is critical for the understanding of the influence of turbulent features on a nearby acoustic field. The propagation of sound close to the air-water interface is investigated, and a simple model is developed to explain the observed response of the acoustic field to a given free surface behaviour. Combining the new knowledge of free surface behaviour with the new relationships between surface dynamics and sound propagation allows the proposal of a technique to determine the bulk flow properties from a measured acoustic field. Finally, in chapter 6, a discussion of the findings is presented, conclusions are drawn, and recommendations are made for further study and the potential to use the findings presented here as the basis for novel flow monitoring equipment.

Chapter 2 - Literature Review

This work focuses on the relationships between the hydraulic conditions of turbulent shallow flows and the properties of scattered acoustic fields nearby. There has been no work in shallow water flow regarding any direct relationship between an airborne acoustic field, characteristics of the dynamically rough surface, the flow turbulence which causes this surface roughness to appear, and the hydraulic flow properties.

The interaction of acoustic fields with hydraulic processes is not an entirely neglected subject. There has been extensive work on sound propagation underwater, with recent examples by Hegewisch & Tomsovic (2012) and Sangfelt et al. (2013). This area of research has been well explored, due in no small part to the military importance placed on underwater sound propagation and the resulting funding opportunities. Less emphasis has been given to airborne sound and its interaction with hydraulic structures (turbulence). Some studies have focussed on the analysis and modelling of acoustic fields in the presence of rough water for the prediction of noise propagation and attenuation from low flying aircraft or explosions at sea (Chapman & Harris, 1962). These surfaces however are primarily generated by wind shear, rather than by flow induced turbulence and as such may exhibit different spatiotemporal behaviours.

Acoustic models exist for the prediction of acoustic fields over statistically rough surfaces (Attenborough & Taherzadeh, 1995; Gavrilov, et al., 1992), and for estimation of static surface roughness from measured acoustic data

(Chambers & Sabatier, 2002; Nichols, et al., 2011), but not for the quantification of dynamic surface structure from measured acoustic properties.

Hydrodynamic turbulence (and in fact turbulence in general) remains one of the great unsolved problems in classical physics. Indeed, unlocking the secrets of the Navier-Stokes equations (Landau & Lifshitz, 2011) is defined as one of the seven Millennium prize problems by the Clay Mathematics Institute (Clay Mathematics Institute, 2013), earning any successful mathematician the sum of $1M. In hydraulic flows, turbulence is a critical process which can influence the bulk behaviour of the fluid. In the absence of wind the inherent flow turbulence is the only process which can be responsible for generating a rough free surface. While some studies have investigated the formation of free surface features (Savelsberg & van de Water, 2008; Tamburrino & Gulliver, 2007), the linkage and potential interdependence between the turbulence field and the free surface deformations is not fully understood. Furthermore the opportunity to gather bulk flow information from the dynamics of the free surface has not been examined.

Clearly the process linking the hydraulic and acoustic elements is the free surface itself. This free surface is generated by the turbulent flow and then influences any incident acoustic field. Whilst the roughness pattern must be generated in some way by the turbulence field beneath, it has also been remarked that the free surface exhibits a behaviour of its own (Savelsberg & van de Water, 2009). This behaviour must affect the sub-surface flow field in a similar way to wind generated waves (Cheung & Street, 1988; Oh, et al.,

2008; Sanjou, et al., 2010), but the interaction has not been quantified or explained, and its potential influence on both the acoustic and hydraulic properties on either side of the interface has not been examined.

Some work has been conducted which examines the relationship between an airborne acoustic field and the hydraulic roughness of particular flows in particular conduits (Cooper, et al., 2006; Horoshenkov, et al., 2004). Hydraulic roughness is a measure of resistance to flow generated by the physical roughness of a boundary with which the flow interacts. It is often expressed in units of length corresponding to the “equivalent diameter” of a particulate material which would generate the same level of frictional flow resistance (Barr, 1963). The original experiments which developed this concept were reported by Nikuradse (1932), and the results of this work were developed into a general form by Colebrook (1939). This technique is important in many applications since knowledge of the hydraulic roughness indicates the flow capacity and overall hydraulic performance for flow conduits, whether they be pipes, channels, or even natural rivers (Robert, 1990). While the hydraulic roughness represents a quantity related to the flow, it is often difficult to link this with some measure of the physical roughness by use of the equivalent diameter concept, particularly for natural rivers. The use of sound waves can present a non-invasive method for measuring the hydraulic roughness of channels and conduits. Horoshenkov et al. (2004) showed that the acoustic attenuation within concrete sewer pipes could be linked to the hydraulic roughness, while Cooper et al. (2006) showed for a shallow channel flow over gravel that a relationship existed between some statistical variation in the acoustic field above the dynamically

rough free surface and the measured hydraulic roughness of the flow. These studies demonstrate clear but limited evidence of a link between the properties of shallow turbulent flow and the properties of a nearby acoustic field, but they neglect any examination of the physical mechanism behind the observed relationships.

Since the free surface defines the boundary which constrains the hydraulic processes below and also defines the boundary which reflects the acoustic energy above, it seems clear that this boundary is the mechanism by which information may be exchanged between the flow and the acoustic field. In this manner the consideration of the linkage mechanism may be decomposed into three separate processes which require a deeper understanding: firstly the mechanism behind the excitation of the free surface by the sub-surface flow; secondly, the dynamic behaviour of the free surface in response to this excitation; and finally the influence of this dynamic boundary on a nearby acoustic field.

In this chapter previous studies will be summarised in order to establish the gaps in knowledge which exist and to identify the work which must be conducted in order to develop a clear set of relationships linking the acoustic response of a turbulent free surface to the dynamic nature of the interface, and the hydraulic conditions of the flow which generates it.

Focus will be applied to detailed studies of the life cycle of turbulent structures, the factors which govern their properties, and the way in which they spawn, translate, evolve, influence the free surface, and eventually dissipate. Several systematic studies have examined the effect of these

turbulent flow structures on the free surface pattern, and these will be reviewed, with particular reference to the common features of shallow free surface roughness and the relationship between the properties of the free surface and of the sub-surface velocity field.

The nature of the free surface's own behaviour in response to turbulent disturbances will be reviewed here, although (to the author's knowledge) this behaviour has not been deeply studied in the context of turbulent structures generated by a shearing flow.

The free surface is not simply a direct impression of the sub-surface vorticity or velocity field (Savelsberg & van de Water, 2009; Kumar, et al., 1998). In this manner, a free surface which exhibits independent characteristics of its own may be expected to influence the sub-surface flow field. This phenomenon has not been well studied for turbulent flow, but it has been examined in the case of wind generated free surface waves, so previous literature is reviewed in this field in order to give insight into the potential influence of surface behaviour on the sub-surface flow.

Finally, a review of the interaction between acoustic wave fields and turbulent flow surfaces will be conducted, making reference to the few existing works in this field and then examining relevant work regarding acoustic scattering from static and dynamic boundaries, and crucially the dynamic measurement of water surfaces.

2.1 **Turbulent structures in shallow flow**

2.1.1 The birth of turbulent features

Shallow flow here is defined as a flow in which the boundary roughness is similar to, or one order of magnitude less than, the flow depth, and where the depth to width ratio is below 1/5. In this type of flow, lateral velocity components are not significant (Nezu & Nakagawa, 1993). This type of flow is found in gravel-bed rivers, overland flows and in partially filled pipes in drainage systems. It is almost always turbulent. Turbulent flow is typified by areas of vortically based circulation which can be considered as an ensemble of turbulent eddies. These eddies have been shown to exist throughout the depth of the flow (Tamburrino & Gulliver, 2007; Fujita, et al., 2011; Stoesser, et al., 2008) but their conception is largely believed to be due to the interaction of the flow with the bed boundary (Shvidchenko & Pender, 2001; Grass, et al., 1991; Roussinova, et al., 2010; Cui, et al., 2003; Lawless & Robert, 2001b; Hardy, et al., 2009; Hardy, et al., 2007).

While some researchers have shown that large scale features in the flow are generated by flow separation and form drag in the lee of obstacles, significant bedforms, or dunes (Kostaschuk & Church, 1993; Müller & Gyr, 1986; Nezu & Nakagawa, 1993; McLean & Nikora, 2006), others have shown the existence of large scale turbulent flow structures in the presence of a uniform rough boundary with few or no dominant spatial features, and minimal flow separation (Roy, et al., 1999; Roy, et al., 2004; Shvidchenko & Pender, 2001) suggesting that large scale turbulent structures are general features of shearing flows. These types of flow are dominated by friction drag (grain stress).

Whilst this work focuses on the uniform roughness case, it is useful to examine the relative turbulence generating properties and generation mechanisms of both friction drag and form drag bed features. Lawless & Robert (2001a) conducted experiments into two types of bed, dominated by friction drag and form drag respectively, by using a uniform gravel and superimposing pebble clusters. They found that the mean velocity profiles and turbulence intensity profiles were significantly affected by the bed type, indicating that the bed topography is an important factor governing the generation and advection characteristics of turbulent structures. In a second paper they show that the pebble clusters exhibit vortex shedding at their crests, and that these vortices give rise to areas of fluid upwelling (Lawless & Robert, 2001b). Similar vortex shedding has been shown to arise from protruding clasts and pebble clusters in gravel bed rivers (Buffin-Bélanger, et al., 2001; Buffin-Bélanger & Roy, 1998).

Furthermore, in (Lawless & Robert, 2001a) it was shown that the uniform roughness case exhibited spatial variability in the statistical properties of the measured velocity components, and this was attributed to heterogeneity in the bed structure, indicating that the properties of the bed on a local scale can affect the local flow and turbulence properties. Conversely, Legleiter et al. (2007) showed in a real river reach that the flow stage (a proxy for relative submergence) was the dominant controlling factor in flow structure, though it was noted that roughness elements do still noticeably affect the flow turbulence. Somewhat in contradiction to this, Cooper and Tait (2008) demonstrated that the spatial organisation of time-averaged velocity features in a plane parallel to the bed were not affected by the bed at the grain scale,

and they agreed that relative submergence played a more significant role in determining the structure of the time-averaged flow velocity. The effect on turbulence properties was not shown however, so it is possible that while the mean velocity organisation was governed by relative submergence, the turbulence properties may be a function of the bed, as suggested by Hardy et al. (2007) who showed that the localized topographic gradient significantly affected the generation of flow structures.

In their later work, Hardy et al. (2009) showed that large scale turbulent flow structures were indeed generated over gravel beds, and that these structures, initiated at the boundary shear layer, grew and dissipated as they advected and moved upward through the flow depth. Since the bed surface is identified as the generation mechanism, it seems reasonable that different bed structures may give rise to different turbulence properties. Again, this somewhat contradicts the work of Cooper and Tait (2008) who show that the boundary roughness at the grain scale does not affect the space and time averaged velocity components, suggesting that the velocity fluctuations are more strongly affected by the rough boundary than the mean velocity field. This is further corroborated by Shah et al (2008) who investigated a smooth bed surface, a transitionally rough (wire mesh) surface, and a fully rough (ribbed) surface. They showed that turbulent structures were generated even in the presence of the smooth boundary, but that the turbulence intensity increased significantly as the boundary roughness was increased.

Over a similarly rough surface, Cui et al. (2003) examined the transport behaviour of generated vortices, and found that large eddies can be thrown from the bed into the outer flow. This is confirmed by Roussinova et al.

(2010) who performed quadrant analysis to examine the turbulent structures near the bed of channel flow, and found that extreme events can manifest as violent ejections which penetrate deep into the flow. These events were seen to be stronger for rougher beds than for smoother beds, indicating that the bed structure can influence the ejection behaviour. This phenomenon, usually referred to as ‘bursting’ was first observed by Kline et al. (1967) and it is generally accepted as the primary mechanism for the generation of turbulent flow features (Shvidchenko & Pender, 2001; Grass, et al., 1991; Nakagawa & Nezu, 1981). In this process, fluid is repeatedly ejected away from the wall, prompting high speed inrushes of fluid toward the wall in a sweeping motion which generates localised circulation (Roussinova, et al., 2010; Komori, et al., 1989; Kline, et al., 1967). Some authors however believe that the dependence is reversed, with large scale structures initiating the bursting process (Yalin, 1992). The true dependence between turbulent structures and boundary layer bursting events is likely to be difficult to determine, since both processes are likely to occur together (Roy, et al., 2004), unless one of these processes can be explained by an independent cause.

It has been shown that these ejection and sweep events can influence the flow field throughout the entire depth of flow for both smooth and rough beds (Grass, 1971). The mean streamwise spacing between ejection events has been found to be between 2 and 7 flow depths which is close to the observed lengths of large scale turbulent features, supporting the relationship between the two (Shvidchenko & Pender, 2001).

There appear to be two contrasting views regarding the influence of the bed structure on the flow. Some authors argue that the spatial pattern of the time-averaged velocity field is not significantly influenced by the boundary roughness at the grain scale and that this is instead governed by relative submergence or flow depth (Cooper & Tait, 2008; Legleiter, et al., 2007; Lamarre & Roy, 2005), while others suggest that the grain scale roughness of the bed is the dominant factor governing the turbulence properties (Lawless & Robert, 2001a; Lawless & Robert, 2001b; Hardy, et al., 2007; Hardy, et al., 2009; Shah, et al., 2008). Though these two viewpoints would appear to contradict one another and raise the question of whether the flow is or is not affected by the grain scale bed roughness, they are perhaps not mutually exclusive. Since the turbulence properties are described by the velocity fluctuations about the mean, and the mean velocity (by definition) does not account for these fluctuations, it is possible that the two processes are affected differently by the governing forces of bed roughness and flow stage (or water depth). Since secondary currents are generally controlled by the width to depth ratio (Nezu & Nakagawa, 1993), it seems reasonable that the organisation of secondary cells would influence the spatial organisation of the time-averaged velocity field, and that their influence may be stronger than that of the near-bed shear layer. Furthermore, since the turbulence properties are governed by fluctuations induced by localised vortex shedding from bed elements and by periodic mass ejections from the bed, it would seem reasonable that these are more significantly affected by the bed type than by the bulk movement of the flow, which perhaps behaves simply as a transport mechanism for the turbulent velocity fluctuations.

It can be concluded that the frictional forces experienced in the shear layer at the flow-bed boundary are responsible for the vortex shedding and generation of ejection events which give rise to turbulent structures. These structures are then described as being ejected into the bulk flow, where they exhibit evolution, coalescence and dissipation as they rise and advect.

2.1.2 The life cycle of turbulent features

Intuitively, the large scale eddies would not simply appear when an ejection occurs, but would sensibly grow from a small induced structure at the bed. This is suggested by Yalin (1992) where the life-cycle of a turbulent structure is described as it grows from an ejection-induced event at the bottom boundary, into a depth-scale eddy which then breaks down at the free surface into smaller eddies in an energy cascade. These depth scale features can be detected in a flow field as areas of extreme (high or low) velocity relative to the local mean (Buffin-Bélanger, et al., 2000). This is consistent with the model proposed by Falco (1977) which links these large scale flow features back to the small scale eddies generated at the bed, and the observations of Brown and Thomas (1977) who described the generation of a ‘horseshoe’ vortex which is formed in the inner boundary layer of turbulent flow, and grows into a large scale structure which extends into the outer layer near the free surface.

Similar structures have been postulated and referred to by a variety of names such as hairpin, omega, horseshoe, and cane vortices, as summarised by Adrian et al. (2000), who presented strong evidence that each of these

observed vortex shapes represented the same structure at different stages of its development. Their results suggest that these vortices are continually generated at the solid boundary, and that they grow and coalesce to form large depth-scale regions of high and low speed flow. Several studies have reported that these features constitute large-scale turbulent structures, and that they are inclined in the direction of flow, such that the parts in the outer layer are travelling ahead of the parts in the inner layer (Roy, et al., 2004; Buffin-Bélanger, et al., 2000).

2.1.3 The parameters governing the properties of turbulent features

The processes which produce turbulent features, and the subsequent behaviour of these features are still a topic of dispute and interest, however regardless of the mechanism behind the generation of turbulent structures, and regardless even of the journey taken by them, it is useful to examine the properties of the vortical structures, and the factors which appear to govern their scale and behaviour.

Adrian et al. (2000) showed that the vortex convection velocity was close to (or just below) the depth-local mean streamwise velocity, suggesting that the structures were transported by the bulk flow, giving rise to the slanted nature of the observed extreme velocity regions which were also observed by other authors (Roy, et al., 2004; Buffin-Bélanger, et al., 2000). However, they measured the convection velocities based on the instantaneous mean velocity in the vicinity of areas of high instantaneous swirling strength. While this describes the velocity of the patch of fluid containing the turbulent

structure, it assumes that the structure is carried with this patch of fluid, which is not necessarily the case. The notion of vortices being transported at the flow velocity is more convincingly supported by Roy et al. (2004) who in order to understand the nature of turbulent flow structures in gravel bed rivers, presented a detailed study regarding the properties and dynamics of large depth scale structures. An array of point velocity measurement devices was employed with readings taken at multiple locations in order to perform a space-time matrix analysis of the collected velocity data, and estimate the size and advection properties of the large scale flow structures. They also used conditional sampling to identify large scale turbulent events at multiple streamwise locations. In this manner the events could be tracked and their velocity could be calculated irrespective of the local streamwise mean flow velocity surrounding the structures. It was found that the turbulent events were indeed transported close to the bulk mean flow velocity. This was only conducted at one depthwise position, and hence the relationship cannot be relied upon throughout the depth, but it does support the results of Adrian et al. (2000).

Adrian et al. (2000) also described qualitatively that the length of vortical structures increased from the bed to the free surface, though this was not quantified. Roy et al. (2004) studied structure length in a gravel bed river and found that the size of these flow structures scales with flow depth, such that the streamwise length of the structures was observed to be 1.0 to 3.0 times the flow depth and the width was around 0.5 to 1.0 times the flow depth, in agreement with previous studies (Nezu & Nakagawa, 1993; Komori, et al., 1989). This was reported for one depthwise location, but allows the assertion

that the areas of circulation generated at the bed increase in size until they are of a similar order to the flow depth, and meanwhile they are transported along with the bulk flow at the depth-local mean streamwise velocities (Adrian, et al., 2000).

These studies show that the scale and advection of turbulent structures are strongly influenced by the flow conditions. The assertion that these structures originate in the shear layer at the bed and are caused by the bed ejection events suggests that the bed structure, through its influence on the magnitude and frequency of bed mass ejections (Roussinova, et al., 2010; Kline, et al., 1967), may also be reflected in the intensity, frequency and length scale of the turbulent structures.

2.2 **Free surface excitation, response, and influence on the flow**

The free surface of shallow turbulent flow is never perfectly smooth. In the absence of wind shear, the apparent rough surface can only be generated by the spatial pattern of velocity fluctuations and the turbulent temporal features beneath. While it seems reasonable for the near surface flow field to influence the free surface shape, this influence is unlikely to be simple. The response of the surface to a turbulent disturbance is likely to be non-trivial, and this response itself may well influence the nearby flow field, yielding a mutual dependence and coupling between the flow field and the free surface dynamics. While the mechanisms of free surface excitation and any potential bi-directional dependence have not been explicitly defined, several key studies have highlighted some appealing relationships.

2.2.1 Influence of flow properties on surface dynamics

Traditionally, the solid-fluid boundary has received considerably more attention than the fluid-air interface and the spatial information (potentially regarding the sub-surface turbulence properties) that this upper boundary may contain. There have been a limited number of studies into the true nature of water surface roughness in turbulent shallow water flow where the rough surface features may be formed by several processes, most notably by flow turbulence and wind shear. Brocchini and Peregrine (2001) identified that the dynamics of the air-water interface were poorly studied so they suggested a framework for future theoretical and experimental studies into the role of turbulence on the behaviour of the water-air free surface. It was identified that turbulence observed at the air-water interface may be generated by two processes: breaking waves, and the impact of rising coherent flow structures generated by shearing at the bed boundary. They proposed a two parameter space, which takes into account the gravity and surface tension effects. Their two parameter space suggests the use of length and velocity scales to categorise these turbulent flow structures and the roughness of the free surface interface. Their findings suggest that the turbulent velocity governs the intensity of the observed free surface behaviour, while the scale of the turbulent structures governs the shape of the free surface features for a given intensity. As the turbulence intensity increases the surface may be described as changing from flat to textured, wavy, breaking, and finally broken. Textured surfaces may appear knobbly and rippled (length scales in the order of mm) or scarified (length scales in

the order of m, such as ship wakes) as the turbulence scale increases. Wavy surfaces represent the mid-point between flat surfaces and violent, fully breaking surfaces. Breaking surfaces can be described as bubbly or breaking as the scale increases from mm to m. Broken surfaces are categorized as splashing, ballistic, and air-drag depending on the scale and velocity (from approximately cm to m, and m/s to tens of m/s). Their work focussed on breaking wave surface turbulence, but they also identified the conditions defined as textured or wavy, in which the behaviour of the free surface was caused by the upward and streamwise movement of moderately coherent flow structures. They were not able to propose definitive boundaries between the types of rough surface excitation mechanisms due to the lack of experimental data and the limited number of studies examining the free surface behaviour. They did however qualitatively define a textured or wavy region between breaking waves and quiescent flow in which gravity dominates the response to turbulence and the impact of surface tension is limited. This region corresponds with the typical properties of river and wastewater flows and it is in this region that the current work is placed.

A number of studies have focused on the formation of surface features by the sub-surface turbulence field of shallow flows, showing a clear link between dominant features of the free surface and large scale features of the turbulent flow beneath. Many believe that large-scale flow structures (Roy, et al., 2004; Nezu & Nakagawa, 1993), sometimes termed ‘macro-turbulent structures’ (Jackson, 1976; Müller & Gyr, 1986; Nezu & Nakagawa, 1993; Babakaiff & Hickin, 1996), are expressed in the free surface, often in the form of boils

(roughly circular areas of local upwelling) or dimples (similar regions of localised downwelling).

Traditional studies investigated the temporal properties of waves at a single spatial location, or the spatial properties at an instant in time. More recent studies examined more closely the spatial and temporal nature of the dynamic wave processes, the need for which was recently reiterated by Liu (2013). There have been a limited number of fundamental studies in which observations were used to determine the dependencies between turbulent structures in the flow beneath the free surface and the dynamic roughness of the free surface itself (Komori, et al., 1989; Rashidi, et al., 1992). Studies by Nimmo-Smith et al. (1999) and Kumar et al. (1998) attempted to relate systematically the measured characteristics of the flow surface to the energy dissipation mechanisms within the flow.

Perhaps the most comprehensive experimental studies of turbulence induced free surface features were conducted by synchronous measurement of the free surface and the turbulent velocity field in a horizontal plane beneath (Savelsberg & van de Water, 2008; Savelsberg & van de Water, 2009). A novel experimental setup was presented whereby the free surface gradient field was measured by a scanning laser, while the near surface velocity field was measured by a particle image velocimetry system. The goal of the study was to examine the link between the near surface turbulence and the free surface deformations. The turbulence was generated in a flow depth of 0.31 m using an active grid, a passive grid, and by vortex shedding in flow around a cylinder. The flume used in these studies had a smooth bed, and although the turbulence generation mechanisms are different to that of the shear layer

over a rough bed boundary, it is useful to examine the surface interactions with these turbulent structures. Several appealing similarities are seen between the near surface turbulence field and the surface deformations. For well-defined shedding of vortices from a vertical cylinder, the areas of high vorticity in the flow correlate well with surface dimples. However, in the case of a fully developed turbulent flow the correlation is much less convincing. Savelsberg and van de Water (2009) propose that the effect of the turbulence field on the free surface is overwhelmed by random capillary gravity waves which propagate away from turbulent disturbances. For bed-generated turbulence features however, Fujita et al (2011) showed that boils on the free surface correlated well with rising horizontally oriented structures, and these were not obscured by common gravity waves. These boils are likely to relate to the 'head' of the horseshoe type vortices summarized by Adrian et al. (2000). Tamburrino & Gulliver (2007) used a moving bed flume to find that the areas of upwelling on the free surface corresponded to areas of vorticity beneath. They postulated that the free surface pattern was a manifestation of large structures existing throughout the depth of flow.

When considering flows over sediment deposits, studies of flow turbulence have shown that the generation and evolution of vortically based large-scale flow structures can create quasi-cyclic but persistent flow patterns (Grass, et al., 1991). The presence of such structures in nature was confirmed by further studies in gravel bed rivers (Kirkbride & Ferguson, 1995; Ferguson, et al., 1996; Dinehart, 1999; Buffin-Bélanger, et al., 2000). These authors reported that once these features were formed, they advected downstream, deforming and amalgamating to produce roughly circular regions of local

upwelling on the water surface (boils). Jackson (1976) was the first author to describe a scenario in which a vertical flow structure interacts with the water surface creating secondary vortices.

Kumar et al. (1998) conducted a detailed examination of the characteristics of the free surface pattern generated by flow over a smooth flume bed. Visualisation of the air-water interface indicated the presence of persistent structures which could be characterised into three groups: upwellings, downwellings and spiralling eddies. The upwellings appeared as areas of local elevation with flow moving into the upwelling at one side and flow moving away at the opposite side. This causes the generation of circulatory motion in opposite directions at the edges of the surface boil. Kumar et al (1998) referred to these features as ‘splats’, while downwellings hence became known as ‘anti-splats’. Splats have also been described as 'surface renewal eddies' by other researchers (Komori, et al., 1989; Rashidi, et al., 1992).

Upwellings were shown by Kumar et al. (1998) to be linked to the turbulent busts originating at the channel floor (Roussinova, et al., 2010) which were seen to impinge on the water surface, propagate along with the surface for some time and then become entrained back down into the flow. This behaviour was also suggested by Komori et al. (1989), who discovered that between 76 % and 90 % of bursting events were able to reach the outer flow layer and free surface. Downward mass movements, generated after the formation of local upwellings by burst ejections, were shown by Kumar et al. (1998) to be formed at the edges of the upwelling, as a direct result of the triggered rotational motion. In the time that an upwelling would spend at the

water surface, it would generate one or more pairs of spiral eddies. These eddies would often merge if they were rotating in the same direction, and would form bonded pairs if they rotated in opposing directions, though the coupling process occurred less frequently that the merging process.

Kumar et al. (1998) also used PIV to examine the behaviour of the flow field close to the free surface. By quantifying the flow field in a vertical plane, they illustrated that the bursting fluid motions generated upwellings on the free surface, and that these upwellings then generated spiral eddies and downwellings. By examining the spatial distribution of the lateral gradient of the instantaneous vertical velocity component, and comparing this with synchronously measured upwellings and downwellings on the water surface, they showed that upwellings were characterised by positive lateral gradients in the vertical velocity, while downwellings correlated with negative gradients.

Sometimes free surface features are described as resembling standing waves which do not significantly propagate over space and time (Tinkler, 1997), with downwellings formed in the wake of upwellings. These surface features are sometimes reported to be laterally orientated rather than becoming elongated in the streamwise direction as may be expected as a result of the streamwise shearing flow. It is has been suggested that this can occur due to the water surface causing a constraint and consequently a reduction in the vertical component of turbulent kinetic energy, with this energy being redistributed in the lateral direction (Komori, et al., 1982; Brumley & Jirka, 1987). This type of feature on the free surface appeared to be persistent over time, remaining in the same area of the water surface for an extended period, with a dynamic ripple component superimposed on top.

It is reported that as relative submergence is reduced, the scale of these standing wave patterns becomes smaller so that their spatial frequency increases in both the lateral and streamwise directions. In the carefully controlled experiments presented in the present work, laterally oriented standing waves were not observed. Hence, a distinction should be made between these temporally persistent patterns and the true dynamic free surface nature caused by impinging turbulent structures, which is the subject of this thesis.

Several studies have found that the mean diameter of dynamic free surface upwellings scales with mean flow depth (Jackson, 1976; Kostaschuk & Church, 1993; Babakaiff & Hickin, 1996). Furthermore, boils have sometimes been found to exhibit reasonable spatial persistence (Nezu & Nakagawa, 1993), while travelling at approximately the surface flow velocity (Fujita, et al., 2011). In this manner the boils behave in a very similar manner to the sub-surface structures reported by Roy et al. (2004) among others, which have previously been shown to arise from mass ejections at the bottom boundary.

A similar relationship between the free surface roughness pattern and the mean flow depth was shown by Kumar et al. (1998). They examined three different uniform flow depths and discovered that as the depth was increased, the surface transformed from being a generally flat surface scattered with many small upwellings, downwellings and eddies to a condition at the highest flow depth where the surface consisted of significantly larger scale features. They also examined flows of equal depth-based Reynolds number, but with different mean flow depths. As flow depth was increased, the number of upwellings on the water surface decreased for

a given Reynolds number. Smaller depths showed increased populations of upwellings and resultant eddies. Kumar et al. (1998) attributed this observation to the number of new upwellings, which decreases with an increase in flow depth for a given Reynolds number. This seems a reasonable observation to be made since for a given Reynolds number, an increase in depth means a decrease in the mean flow velocity, which is often linked to a decreased frequency of vortex generation. An example of this is the vortex shedding from submerged spheres studied by Sakamoto and Haniu (1990), who also reported that the vortex size increased with increasing depth for a fixed Reynolds number, which indicates that the scale of vortex growth is limited by the flow depth, and depends less on the flow velocity.

The findings of Kumar et al. (1998) suggest that upwellings may be caused by the transport of fluid towards the free surface, perhaps originating from mass ejections in the bed shear layer (Roussinova, et al., 2010), and downwellings may relate to the movement of fluid away from the free surface. It was found that changes in the free surface structure with relative submergence relate to the observed changes in the spatial structure of the vertical velocity component. The number of free surface upwellings and the number of areas displaying a net upward motion of fluid appears to decrease as relative submergence increases, while their streamwise lengths increase. The same relationships were observed for the downwellings and areas of net downward fluid motion.

The studies described thus far would suggest that there is a clear relationship between the turbulent flow structures and the observed roughness features

on the water surface, with many potential linkage mechanisms being described between the flow structure and the free surface behaviour. Some authors argue that surface upwellings relate to areas of increased vorticity (Tamburrino & Gulliver, 2007) while others argue that they relate to violent bed ejections (Kumar, et al., 1998), and others suggest they are linked to laterally oriented vortices (Fujita, et al., 2011). Some describe surface downwellings as corresponding to areas of increased streamwise velocity (Savelsberg & van de Water, 2008), while others attribute them to down-rushing fluid (Kumar, et al., 1998). Some authors suggest that near-surface vortices are spatially persistent (Guo & Shen, 2010), while others argue that they contact the free surface and then return into the depths of the flow (Komori, et al., 1989) as if repelled by some elastic force. While the authors do not always agree on the linkage mechanism, the resounding theme is that in some manner the turbulent flow structures are able to influence the free surface behaviour and may create some representation of themselves in the surface roughness pattern. Differences in the observed linkages may simply be due to differences in the generation mechanism of the turbulent structures themselves, since different scales, densities, and intensities of turbulent structures may invoke different types of response from the free surface. What is clear is that the linkage is not simple, as the free surface responds by its own nature to different types of turbulent excitation. This response must be characterised for the turbulence regime of interest, in this case, turbulent structures emanating from a rough bed in shallow channel flow.

2.2.2 Response of the free surface to a disturbance

Whatever mechanism is generating surface features, the response of the free surface to such a mechanism is not fully understood. This was highlighted by Savelsberg and Van de Water (2009), who concluded that while the free surface could be imprinted with the turbulent nature of the flow beneath, it also exhibits a behavior of its own which could not be entirely characterized. Understanding the mechanism behind the apparently random nature of free surface fluctuations could unlock the potential to predict the free surface pattern for a given flow, and to use this information to inform models used in sound propagation, turbulent mixing, energy loss, and surface current studies.

While the free surface has been shown to exhibit properties related to the flow field beneath, it is not simply an imprint of the vortical structures. When the free surface is disturbed, it must respond according to its own mechanical laws. Guo and Shen (2010) described the free surface pattern as consisting of propagating waves and turbulence generated surface roughness and developed a DNS model accordingly. They established a statistically steady, isotropic turbulence field by use of a linear forcing function and examined the resulting free surface behaviour. They found that for most realistic cases, the effects of gravity dominated over the effects of surface tension. This corresponds with the larger length scales ($>10^{-2}$ m), and moderate turbulent velocities of Brocchini and Peregrine (2001), predominantly in the wavy surface pattern regime in which the present study sits. They also found that of the potential energy of the surface only 2.2 % to 12.1 % was associated with propagating waves, suggesting that the majority of the surface structure

is governed by the gravity driven response of the free surface to the turbulence induced roughness. What is not studied is the spatial and temporal evolution of the free surface roughness pattern, and the effect that this behaviour may have on the flow beneath.

As mentioned in the previous section, Savelsberg and van de Water (2009) propose that the sub-surface turbulence can affect the free surface, but that the effect of a homogeneous isotropic turbulence field on the free surface of fully developed turbulent flow is overwhelmed by random capillary gravity waves which propagate away from turbulent disturbances. This is contrary to the potential energy proportions attributed to propagating waves by Guo and Shen (2010). While the correlation analyses and subsequent Huygens model constructed by Savelsberg and van de Water (2009) appear to support their hypothesis, the spatial domain examined was very small (55mm x 55mm). This is much smaller than the length scales of typical depth scale features reported for these kinds of flows, and is indeed smaller than most of the turbulence length scales measured by Savelsberg and van de Water (2009). It is possible that at this scale capillary gravity waves dominate, but that in a wider field of view the roughness caused by depth scale structures dominates the free surface pattern as suggested by Guo and Shen (2010).

The primary uncertainty in the model of Savelsberg and van de Water (2009) is the question of what happens at the point of the initial disturbance. The concept of gravity waves being generated outward seems intuitively sensible, as any disturbance to a water surface is likely to generate secondary ripples, but since gravity waves are essentially described as a one dimensional process involving plane waves (i.e. applying to the far field for circular wave

fronts) the near field (location of disturbance) cannot be described in the same way, and indeed would result in a singularity if it were, whereby the surface gradient would be discontinuous, a physical impossibility. This issue is avoided by Savelsberg and van de Water (2009) by describing the near field region as a Gaussian disturbance, however it is not clear what happens to this Gaussian disturbance after its initial inception. The description by Guo and Shen (2010) would appear to suggest that the disturbance persists as long as the turbulent structure beneath continues to exist, just as Nezu and Nakagawa (1993) describe the surface boils to be relatively persistent. This is also suggested by the findings of Savelsberg and van de Water (2009) showing surface dimples correlating with sub-surface vortices (known to be persistent). However, although it is not qualitatively described in the text, their analytical model includes a time dependent cosine term which would cause the initial surface feature to fluctuate up and down over time. This is in contradiction to their qualitative descriptions and raises the question of whether surface dimples truly represent sub-surface vortices, or whether these vortices are forming some kind of oscillatory motion (dimples *and* boils). This would agree with other relevant models, such as classical tsunami theory (Ward, 2003) which suggests that once a water surface is struck by an object (perhaps a turbulent structure) the point of contact would oscillate up and down with its amplitude decaying over time (akin to dropping a stone into a pond). Furthermore the tsunami model in Ward (2003) suggests that when water is the object which makes contact with the surface (effectively a raindrop arriving from above, although perhaps comparable to a turbulent structure impinging from below), the fluctuation of the initial

disturbance is at least an order of magnitude greater than the generated gravity waves propagating outward. This ratio is consistent with the potential energy proportions assigned to turbulence generated features and propagating waves by Guo and Shen (2010).

Clearly much progress has been made on the free surface's innate response to turbulent disturbances. There is a compelling case for the free surface strongly representing the flow field beneath, while there is also a strong case for the presence of capillary gravity waves which lend to the dynamic appearance of the free surface. Evidently more work is required to assess the relative importance of the local turbulence field and any induced surface waves. Critically however, the key void in present understanding is the response of the free surface at the point of interaction with a strong turbulent feature. Does the free surface simply display a boil until the turbulent structure dissipates? Does the surface respond as though it were struck by an object, fluctuating up and down? Whichever is true, can the nature and controlling factors of the evolution of the surface structure over space and time be determined? These questions need to be answered since if there is a dynamic response to structure impingement then this may well contribute significantly to the apparent dynamic nature of turbulent free surfaces.

2.2.3 Influence of surface behaviour on sub-surface field

A further limitation of previous work is that while it has been shown that the free surface may be somehow influenced by the sub surface turbulence, there is no direct experimental investigation into the degree to which the flow

velocity field may be influenced by the behavior of the turbulence induced free surface roughness. It is logical that waves generated on water will cause a necessary motion of the fluid beneath, and this has been proven and characterized in the case of wind generated waves (Craig & Banner, 1994; Chukharev, et al., 2007; Xing, et al., 2012).

Cheung and Street (1988) conducted an experimental study into the turbulent outer layer associated with wind generated waves on the free surface of water. Velocities below the water surface were measured using laser-Doppler anemometry, and the measurements were analyzed to separate the effects of the mean wind-induced flow, wave related fluctuations, and wave induced turbulence. It was found that a boundary layer is generated at the free surface and the flow velocity behavior within this layer obeys a logarithmic profile due to the wind shear and resulting roughness. For low wind cases this conformed approximately to traditional boundary layer theory, but it was found that for higher wind speeds the forward motion of the free surface pattern reduced the effective roughness. Since turbulence induced water surface roughness would presumably travel at the velocity of the turbulent structures in the flow (Fujita, et al., 2011), which travel close to the mean velocity of the flow (Adrian, et al., 2000; Roy, et al., 2004), this boundary layer is likely to be weak for the case of turbulence induced free surface roughness, and it is likely to be more similar to that observed in the high wind speed cases reported by Cheung and Street (1988). They also investigated mechanically generated waves and found a coupling between the waves and the induced turbulence field. Measured values of the mean wave-induced shear stress near the free surface indicated an energy transfer from the

waves into the mean flow. In the present work the opposite is likely to be the case when a turbulent structure influences the free surface, but just like the wind generated waves reported by Cheung and Street (1988), any free surface behaviour as a response to (rather than a direct result of) the turbulent structures beneath would presumably impart their energy on the nearby flow field.

In order to investigate this energy transfer, and any potential resulting turbulent structure generation at the free surface, Oh et al. (2008) used particle image velocimetry to measure the velocity field beneath wind generated waves for three different wind speeds. They found that for small waves, a series of coherent structures are produced close to the free surface, whose direction of rotation is not fixed. These are perhaps comparable to the surface renewal eddies reported by Kumar et al. (1998). For large scale waves a single strong coherent structure is generated below the crest of a wave, and its rotation is the same as the orbital motion of the wave itself. Either large or small waves may potentially be generated by flow turbulence, but for the shallow flows investigated here it is likely that the waves would be analogous to the small scale wind generated waves in this context. In either case, Oh et al. (2008) found that the spatial and temporal evolution of the generated turbulent features were similar. Vortices travel at a velocity similar to that of the surface waves, and interact with pre-existing vortices, subsequently amalgamating and fading.

Craig and Banner (1994) examined the influence that the wave induced turbulence could have on the existing velocity field beneath the ocean waves by modeling a turbulent kinetic energy input at the free surface. They

predicted the depth of the turbulent layer, and the dissipation rate. It was found that the model was strongly dependent on the surface wave parameters such as wave amplitude and wavelength. Although the height of their surface waves was an order of magnitude greater than those examined in this work, it does suggest that any influence the free surface may have on the near-surface flow is governed by the properties of the free surface waves.

Whilst wind generated waves have been shown to generate velocity fluctuations and turbulent structures below the free surface, the influence of the unique free surface behavior in the case of turbulence generated waves has not been investigated. It can be proposed that the information or energy exchange between the flow field and the free surface is not simply unidirectional (the flow influencing the free surface). Since the free surface may exhibit a nature of its own, it seems reasonable to suggest that this behavior may affect the sub surface flow in the same way that wind generated waves do. This would also have relevance to mixing studies, hydraulic energy losses at the free surface, the behaviour of surface currents, and mass and energy transfers at the free surface.

2.3 **Remote measurement of water surfaces**

There are numerous examples of quantities which interact with an imposed boundary without affecting said boundary, for example sound waves, light waves and waves from other areas of the electromagnetic spectrum. In the context of this work, focus will be centred on the use of these interactions to

infer surface properties, since the primary goal is to relate the acoustic field to the flow conditions.

Although an acoustic approach was selected for this study, other potential non-invasive techniques were also considered. For example, laser interferometry is often used to measure surface properties in the manufacture of semiconductor devices, and these laser techniques are steadily improving in terms of their resolution and accuracy (Peggs & Yacoot, 2002). The laser interferometry technique can be very precise but it usually acts at a single spatial location and so the method generally requires moving parts. Furthermore, laser displacement sensors require the light to be broadly reflected from a point located on the surface of interest. When this method is used with a water surface a significant portion of the emitted light is transmitted through the water surface and scattered by the bubbles and other suspended matter in the flow, causing errors in the measured surface properties (Lorenz, et al., 2005).

Other optical techniques show promise in the measurement of water surfaces. Stereoscopic (and indeed triscopic and multiscopic) imaging provides the ability to capture three dimensional images of water surfaces. The technique employs a number of cameras focussed on the surface from different angles. If the relative positions of the cameras are known, then it is possible to recreate the instantaneous three dimensional surface shape from images acquired synchronously at each camera. Tsubaki and Fujita (2005) used a technique similar to Dantec's digital image correlation system (Dantec Dynamics, 2013). This system is used in other studies (Plé, et al., 2013; Bloom, et al., 2013) whereby a known pattern, for example an irregular

pattern of bichromatic noise, is projected onto the surface, which is then recorded by two cameras. Using this system it was possible to measure water surface fluctuations as small as 1mm. In reality, free surface fluctuations may be smaller than the 1 mm lower limit, depending on flow conditions. The primary drawback of this system is that the surface under investigation must be a good reflector of light with a colour contrast enabling the discrimination of the reflected light from the transmitted. In the laboratory this is easy to achieve by adding white dye to the water, but in the field this may be impractical.

The addition of dye is not necessary for scenarios where the water is effectively opaque (or close to it), and if the lighting is sufficient to illuminate free surface features, then the surface pattern itself can be used in the image correlation rather than projecting a pattern onto the surface. This has most often been realised in the measurement of ocean waves, where the depth is sufficient so that the bed cannot be seen. For example, Bechle and Wu (2011) developed a single point wave gauge based on stereoscopic imaging which measured wave height to an accuracy of 98% when compared against a standard wire wave gauge. Benetazzo et al. (2012) conducted experiments on a much larger scale, recording three dimensional images of the water surface over an area of 1100m^2.

Other interesting approaches are being developed, for example by Muste et al. (2005) who use a fan to remotely generate wind-induced gravity waves on a free surface and optically image the wave propagation in order to estimate the bulk velocity of the free surface. A further novel optical technique used thermal cameras to track the pattern of heat distribution in a natural river in

order to measure surface currents (Puleo, et al., 2012). The technique was shown to be somewhat effective, but it can only be used where a sufficiently thermally ‘textured’ surface is present, and it fails at certain times of day, or under certain lighting conditions. For many flows, mixing of water is effective enough to distribute thermal energy efficiently, such that the thermal texture could not be used in this way.

While these techniques are developing well, there is no optical solution that is robust enough for field measurements of shallow flows where the distorted bed surface visible in the images can corrupt the surface image correlation. The various optical approaches are simply not yet adaptable enough or robust enough to provide a truly universal surface measurement method which could be applied to flows which are shallow or deep, clean or otherwise.

In this respect, airborne acoustic techniques are attractive when examining water since acoustic equipment can potentially act over an area while operating from a fixed location, and (unlike for optical methods) the free surface may be considered acoustically hard. This is due to the acoustic impedance (sound speed multiplied by density) of water being three orders of magnitude greater than that of air, allowing only very weak acoustic coupling and thereby causing the coefficient of reflection to be almost equal to unity. Much work has been conducted on the interaction of acoustic fields with static rough surfaces (Boulanger, et al., 2005; Boulanger, et al., 1998; Chambers & Sabatier, 2002; Nichols, et al., 2011; Attenborough & Taherzadeh, 1995), but comparatively less work has focussed on the effect of dynamically rough boundaries such as water surfaces. Some have

addressed the prediction of sound propagation over dynamically rough water and the majority of previous works have been focused on the acoustic field in the vicinity of wind-generated ocean waves, rather than turbulence-generated waves on a flow surface. As a result, (to the author's knowledge) the inverse problem of acoustically assessing the dynamic nature of the free surface of a shallow water flow has never been studied systematically.

2.3.1 Acoustic scattering from static surfaces

Excess attenuation theory (Attenborough & Taherzadeh, 1995) provides the opportunity to deduce statistical information about static hard rough surfaces that span a large area and will function over large distances. The excess attenuation (EA) spectrum represents the ratio of the frequency dependent amplitude of the signal received from a point source over a solid boundary to that in the absence of this boundary. The magnitude of the EA spectrum presents a series of maxima and minima resulting from constructive and destructive interference between the direct and reflected acoustic signals (Attenborough & Taherzadeh, 1995). It has been shown that the presence of roughness on the surface causes a change in the shape of the excess attenuation spectra which may be interpreted as a consequence of a change in the effective impedance. The effective impedance is related to the parameters of the surface roughness which may thereby be deduced from the complex excess attenuation data (Boulanger, et al., 2005). Although semi-analytical theory has been shown to be reliable at calculating the real and imaginary parts of excess attenuation for a known source-receiver

geometry over a known roughness, the inverse problem has to be solved numerically in the majority of practical cases (Boulanger, et al., 2005).

Nichols et al. (2011) developed an inverse model of excess attenuation, which allowed the measurement of the roughness volume per unit area to within 4% error in the case of static roughness. This represents a significant advancement in the remote measurement of rough surfaces, but the relationships were only upheld so long as there was no significant interaction or multiple scattering between roughness elements. This was found to occur beyond a packing density of 32%, where the packing density represents the percentage of the surface containing scattering elements. For a water surface this technique is therefore likely to be insufficient, and indeed when tested on water surfaces by the author, the ability to measure roughness properties was not observed.

While broadband acoustic signals allow the measurement of surface properties over a large area, they only provide the average surface properties of that area, rather than temporal properties on a local scale. The technique has proven to work over ocean-like wave patterns which are largely homogeneous in nature, but for measuring turbulence properties of a flow surface this is likely to be insufficient since the properties are dependent on the local flow and boundary conditions and, therefore, a more local measurement may be required.

Furthermore, while the mean roughness properties of the surface (mean roughness height, roughness density) may be useful, a more informative data set would provide information regarding the temporal and spatial properties

of the free surface roughness pattern. Models do exist which describe the expected acoustic field over a rough surface based on this kind of spatial and temporal data, specifically a spatial correlation function. Perhaps the most relevant example is that of Dunin and Maximov (1990), who examine the reflection of plane waves from statistically rough surfaces. The spatial correlation function of the rough surface is shown to directly affect the scattered component of an incident acoustic field. Moreover, three important properties of the surface roughness are shown to independently affect three measureable properties of the diffused acoustic field. For a two dimensional Gaussian acoustic beam, the model suggests two peaks in the scattered field superimposed onto the coherent (specularly reflected) peak. This suggests that the properties of these two scattered peaks (amplitude, angular width, and angular separation) can be used to determine the roughness height, characteristic spatial period, and correlation radius of the surface respectively.

Whilst theoretically very applicable to water surfaces, these relationships suffer from the same issue as excess attenuation in that they represent the mean response of an ensemble of statistically constant surfaces. For this reason the theory has not been tested physically and the inverse problem has not been investigated in previous studies as it would not serve a purpose for a static rough surface (the type usually of interest).

The criterion that these types of acoustic model represent the mean response of an ensemble of realisations of surfaces with the same statistical roughness properties often renders them impractical. This is because a static surface represents just one realisation, and this surface may respond very

differently to the mean response of an ensemble of similar realisations. Water surface roughness however presents a unique and previously unexplored opportunity for the development and testing of these kinds of acoustic models. For a uniform homogeneous steady state flow with stable boundary conditions, the turbulence properties (distribution of structure size, mean generation frequency, distribution of advection velocity, etc.) are relatively stable over time and over space, and therefore so too are the statistical properties of the free surface roughness. And yet at any instant in time the surface pattern itself is completely unique. An ensemble of snapshots of the free surface pattern over time literally represents an ensemble of roughness realisations provided that the roughness process is ergodic. In this case, the mean acoustic properties over time represent the mean acoustic properties over an ensemble of realisations of the same statistical rough surface, and can be directly compared with the predictions of such models.

2.3.2 Acoustic scattering from dynamic surfaces

There have been a limited number of research studies focussing on the relationships between acoustic scattering and the dynamics of rough water surfaces. The majority of studies are in the context of the statistical prediction of acoustic effects and sound propagation over ocean surfaces (Tolstoy, 1982; Qin, et al., 2008), but these do not quantify the dynamic element of the surface roughness.

Acoustic techniques are well studied in the context of range finding, and for monitoring the average location of fluid interfaces. The simplest and most

commonly used technique is a basic time-of-flight (TOF) measurement, whereby an acoustic pulse is emitted, reflects back from an area of a surface, and the time between emission and reception of the reflection indicates the average distance to the boundary (based on an assumed or independently measured local sound speed). A recent example of this kind of technology is described by Lagergren (2012). Some technologies project acoustic energy toward the surface and then analyse the phase of the received signal in order to estimate an absolute value of the mean fluid surface level (Redding, 1983). Wang et al. (1991) used phase measurements to monitor fluctuations in the overall depth, but could not resolve local fluctuations in a fluid of constant depth, and so no consideration was given to the effect of the surface pattern on the output of the system. Delafon (1973) used a similar technique to monitor level changes. This work required an acoustic waveguide in the form of a tube to be placed into the fluid to direct the acoustic field to and from the surface. The use of a penetrating physical waveguide would disrupt the flow and strongly affect the fluctuating water surface pattern, so is not suitable for measuring the dynamic nature of turbulent flow surfaces. These techniques provide a measure of the mean surface position, and in a sense measure changes over time. On the other hand, they realistically quantify only broad changes in depth over a large temporal and spatial scale.

While broadband acoustic models such as excess attenuation may be modified to provide mean roughness statistics, and plane wave theories (Gavrilov, et al., 1992; Dunin & Maximov, 1990) may be inverted to provide spatiotemporal roughness parameters, the ‘holy grail’ of acoustic

measurement of flow surfaces would be to image the free surface acoustically. This would require the measurement of the spatial profile at a number of points in time (or similarly the measurement of the temporal fluctuations at an array of locations in space). This type of acoustic imaging of free surfaces has not been found in the existing literature and will be addressed in this study.

2.4 **Literature review conclusions**

This review has examined the existing literature and current theories regarding turbulent structure generation, evolution and influence on the free surface, the free surface response and mutual influence, and the current state of acoustic processes relevant to measuring rough surfaces and, in particular, dynamic surface roughness.

The general consensus among researchers in the field of turbulent flow structures is that the vortices associated with turbulent flow are generated at the solid-fluid boundary by the shear forces between the stationary bed and the moving fluid. They can be initiated by several processes, but most notably by vortex shedding from significant bedforms or, in the absence of significant bedforms, by the repetitive sweep and ejection events typical of uniform rough boundaries and even smooth boundaries. These events are characterised by violent ejections of high energy fluid up toward the free surface, accompanied by a resulting inrush of flow which forms a sweeping motion, generating angular momentum, and giving rise to turbulent eddies. Rough beds are seen to generate stronger ejections than smooth beds,

suggesting that different types of bed give rise to different ejection behaviour and hence different scales of turbulent structures. This behaviour is supported by some authors who show an increase in turbulence intensity correlating well with an increase in bed roughness, though other authors have shown that the bed roughness does not significantly affect the spatial organisation of time-averaged velocity, which was found to be more strongly related to flow depth. However, these findings are not mutually exclusive. The spatial organisation of time averaged velocity components seems to be a function of the flow depth or relative submergence, whereas the fluctuating component which governs turbulence intensity seems to be related to the bed surface generating circulation and mass ejection. As a result, the bed shear layer appears to be the governing process in turbulent structure generation.

Once generated, the turbulent structures are carried with the velocity of the mean flow, and in fact (the author would infer) at the depth-local flow velocity. The smaller structures near the bed grow until they coalesce and combine to form larger structures which continue to grow until they occupy the entire flow depth. These structures significantly affect the free surface by generating surface features typified by upwellings (boils, or splats), downwellings (dimples, or antisplats) and eddies. Upwellings may relate to areas of increased vorticity or to violent bed ejections or laterally oriented vortices. Downwellings may correspond to areas of increased streamwise velocity or to local down-rushing fluid. The way in which the sub-surface turbulent features relate to the spatial features generated on the free surface is clearly

not fully understood, and hence nor is the turbulence information that the free surface pattern may thereby contain.

The free surface itself exhibits a nature of its own. It has been suggested that this inherent behaviour is the result of capillary-gravity waves which emanate from the turbulent disturbances, though data simulated from this type of model does not fully explain the observed patterns. It is also unclear what happens at the point of contact with a coherent structure and the air-water interface. The behaviour of the free surface in response to a disturbance caused by a turbulent structure is therefore not fully understood and warrants further investigation.

Since the free surface may not be simply an expression of the sub-surface turbulence, and may contain its own inherent behavioural characteristics, some influence of this behaviour is likely to be experienced in the nearby flow field. While this has been studied in the context of wind-generated waves, the mechanism and extent of any influence has not been studied for turbulence induced free surface fluctuations.

Finally it has been shown that while acoustic theory is sufficiently advanced to allow the prediction of sound fields over various types of rough surface including ocean waves, and even to estimate the roughness of some types of static rough surface, sound propagation over shallow turbulent flow surfaces has been somewhat neglected, and the development of a technique for quantifying turbulent free surface roughness from a measured acoustic response is needed.

Each of the areas of literature studied have suggested that relationships may exist between the flow conditions and the turbulence structure, between the turbulence structure and the free surface roughness pattern, and between the free surface roughness and a measured acoustic field nearby. However, these relationships have not been explicitly proven and the mechanisms behind any relationships have not been thoroughly investigated. Once the gaps in understanding of each of these relationships have been addressed, the possibility exists to combine the various dependencies in order to establish a direct relationship between the flow conditions of shallow turbulent flows and the acoustic responses of their free surfaces, and vice versa. This development has not been found elsewhere in previous literature.

The work presented here is designed to address the observed gaps in understanding identified by this literature review. The behaviour of flow induced turbulent structures, the resultant free surface pattern, and hence the behaviour of an incident acoustic signal will be examined for a range of shallow flows over rough beds. The work is designed to:

- Investigate the sub-surface turbulence properties for different flow conditions and bed types.
- Demonstrate that the temporal and spatial properties of free surface patterns can be characterized.
- Examine the extent to which sub-surface turbulence properties are represented in the free surface pattern.
- Identify the unique nature of free surface behaviour in response to a sub-surface excitation.

- Examine the potential of this behaviour to influence the sub-surface velocity field.
- Define the interaction mechanism of an acoustic field with dynamic flow surfaces.

By accomplishing these objectives it is intended that the gaps in our knowledge about the hydraulic processes within, and free surface roughness of, turbulent shallow water flows would be addressed so that the nature of free surface roughness would be more fully understood. This work will pave the way toward a method of characterising shallow flows based on an acoustic measurement of the turbulence properties portrayed in their dynamic free surfaces roughness patterns.

Chapter 3 - Experimental facilities & flow conditions

A series of experiments was conducted in which the behaviour of the water surface changed in response to the general flow conditions of a range of steady, uniform shallow flows over a rough boundary. This chapter will describe the experimental setup, instrumentation and measurement techniques, and the range of flow conditions examined.

3.1 Flume setup

3.1.1 The Flume

The experiments were carried out in a 12.6 m long, sloping rectangular flume which is 459 mm wide (see Figure 3-1 and Figure 3-2). In Figure 3-1 the labels ‘a’ to ‘d’ and ‘g’ to ‘i’ represent components of the flume which allow control of the flow conditions, whereas sections ‘e’ and ‘f’ represent the measurement sections of the flume, where flow visualisation and free surface measurement take place respectively.

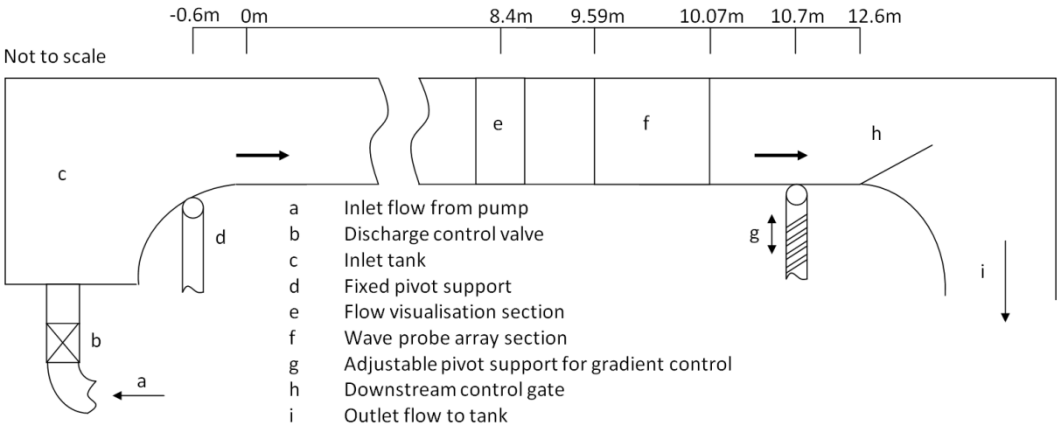

Figure 3-1: Flume overview

Figure 3-2: Photograph of the flume

3.1.2 Flow control & bulk measurement

The flume was simply supported on a pivot joint at the inlet end, and on a pivot joint attached to a screw thread at the outlet end. Adjustment of the screw thread therefore allowed the gradient of the flume to be varied. In the tests, the flume was tilted to a slope which varied from S_0 = 0.001 to 0.004 in 0.001 increments, within the range defined as “gentle gradient streams” by Rosgen (1994) who categorised natural rivers and defined gentle gradient streams as having gradients below 0.02.

A constant head pump was used to recirculate water in the flume. Control of the discharge from the pump was achieved with an adjustable valve in the flume inlet pipe. The magnitude of the discharge was determined using a u-tube manometer connected to a standard orifice plate assembly (BS5167-1, 1997). The manometer could be read to the nearest mm, meaning the flow rate was measured to an accuracy of 0.5 l/s.

The depth of the flow was controlled with an adjustable gate at the downstream end of the flume to ensure uniform flow conditions throughout as long a section as possible and, in particular, in the measurement sections of the flume (see Figure 3-1). The uniform flow depth was measured with point gauges which were accurate to the nearest 0.5 mm (between 0.6 and 1.2 % of the flow depths used). This was conducted at 4 positions, situated 4.4 m to 10.4 m from the upstream flume end in 2 m increments. At the start of each of these measurements the gauge was reset to zero datum which corresponded to the mean bed level and then it was raised until its tip was just in contact with the water surface. Since the water surface position is

hence measured relative to the channel bed, measurements of depth recorded in this manner before, after, and within the measurement sections were compared, with uniform flow being confirmed when the values agreed to within 0.5 mm, meaning that the water slope was equal to the bed slope.

Temperature was measured before and after each test using a digital thermometer accurate to ±0.5 ºC, placed 0.5 m downstream of the measurement sections so as to record a representative temperature for the water in the flume, but without influencing the flow or free surface structure in the measurement sections. The temperature measurements ensured stable thermal conditions and therefore constant viscosity and surface tension. For each flow condition the temperature changed by less than 5 % over the course of the measurement.

Free surface velocity was measured for each flow condition by timing a floating tracer as it was carried a distance of 6 m along the flume, with the visualisation section at the centre. 5 measurements were made for each flow condition and the results were then averaged. The variation in these measurements was always below 10%. It was found that 5 measurements were sufficient to achieve an average value which converged to an error of less than ±2%. The error in the measurement of mean surface velocity is hence estimated to be ±2%, although it is noted that the 10% variation mentioned could be due to both experimental error and also natural variation in the local surface velocity.

3.1.3 Bed types & bed measurement

Two bed conditions were examined during this work in order to investigate the effect of bed structure on the behaviour of the free surface of flows with similar bulk hydraulic properties. During the first phase of testing, the flume had a bed of well-mixed washed river gravel which was scraped to a uniform thickness of d_g = 50 mm (nominal) so there were no significant topographical features (see Figure 3-3 (left)). This bed type was selected to allow comparison with other field and laboratory studies of turbulent flows over gravel beds. The gravel particles had a density of ρ_g = 2600 kg/m^3 and mean grain size (by mass) of D_{50} = 4.4 mm. The grain size was approximately normally distributed, as shown in Figure 3-4.

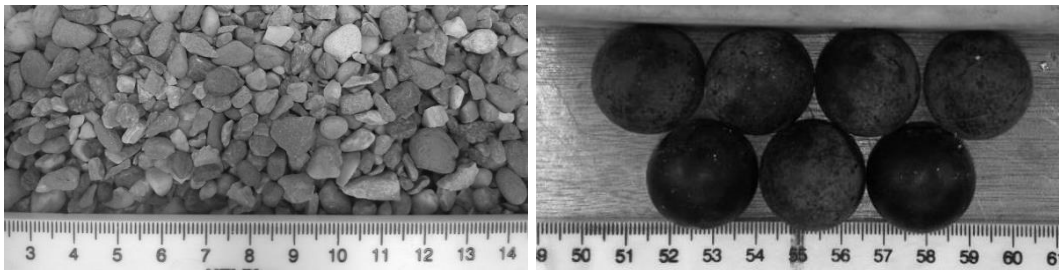

Figure 3-3: The two bed substrates used: washed river gravel with mean grain size of 4.4 mm, and 25 mm diameter polymer spheres

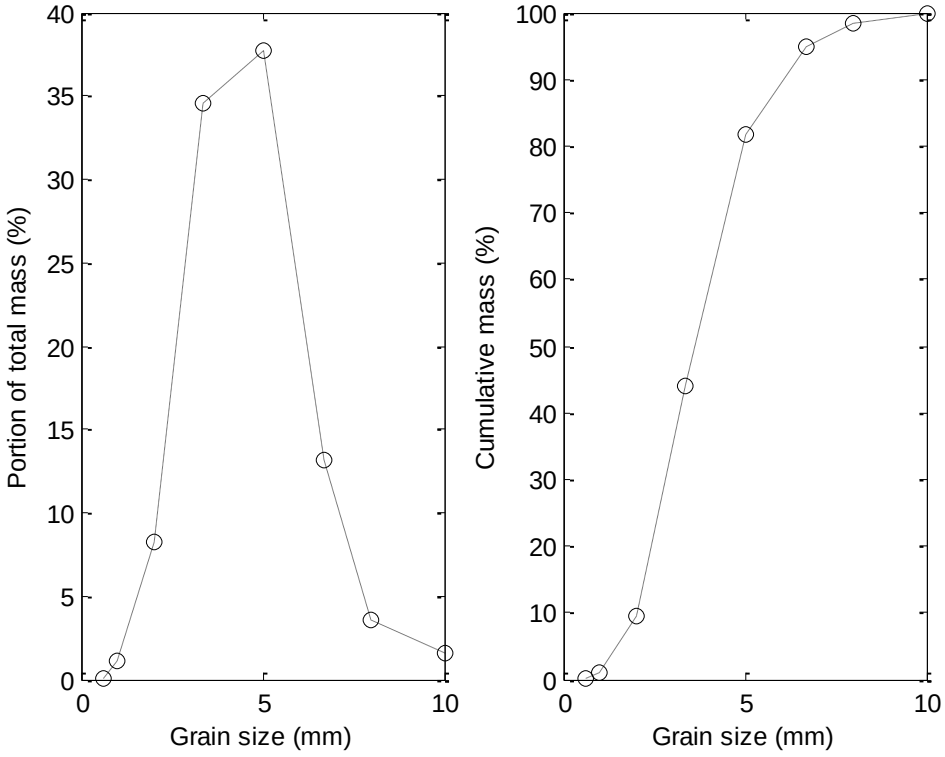

Figure 3-4: Grain size distribution by percentage of total mass

During the second phase of testing the bed was composed of a hexagonally packed arrangement of ϕ_{sph} = 25 mm diameter spheres (see Figure 3-3 (right)). This bed type was selected to give a similar flow resistance to the gravel bed, but with significantly different physical bed shape. It would also allow the data to be compared against numerical models, which often make use of well-defined geometrical shapes which can be easily repeated to simulate roughness of the sediment bed (Stoesser & Rodi, 2006). The spheres in this work were manufactured by plastic injection moulding, and had a density of ρ_s = 1400 kg/m^3. Two layers of spheres were used in order to give a bed thickness, d_{sph}, similar to that of the gravel bed, and to allow realistic interfacial flows into and out of the porous bed.

The bed surface elevation for both beds was measured at the flow visualisation section of the flume (see Figure 3-1) using a laser displacement sensor attached to a computer controlled scanning frame. The profiler was a Keyence LK-G82 laser displacement sensor (see Figure 3-5) which is stated to be accurate to within ± 0.25 μm with a spot diameter of 45 μm. Bed elevation was continuously recorded beneath the sensor at a rate of 4 Hz, while the scanning frame moved the sensor at 2 mm/s in lateral lines spaced 0.5 mm apart, giving a spatial resolution in both directions of 0.5 mm. Two 50 mm square bars were placed along the edges of the flume (see Figure 3-5) in order to indicate the beginning and end of each lateral sweep of the displacement sensor, and a Matlab routine was written to convert the elevation time vector into a spatial matrix of measured elevations.

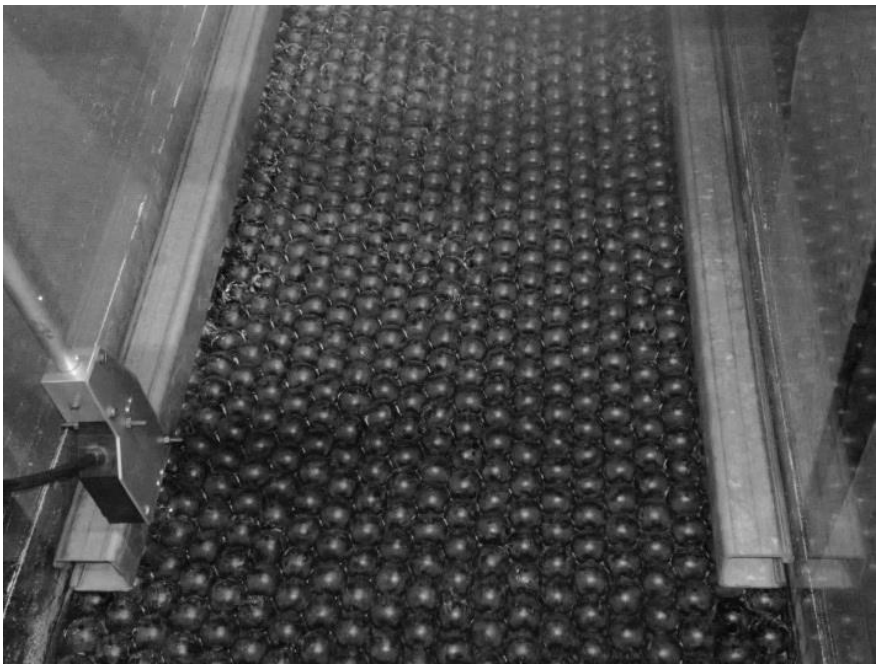

Figure 3-5: Recording bed elevation data using laser displacement sensor

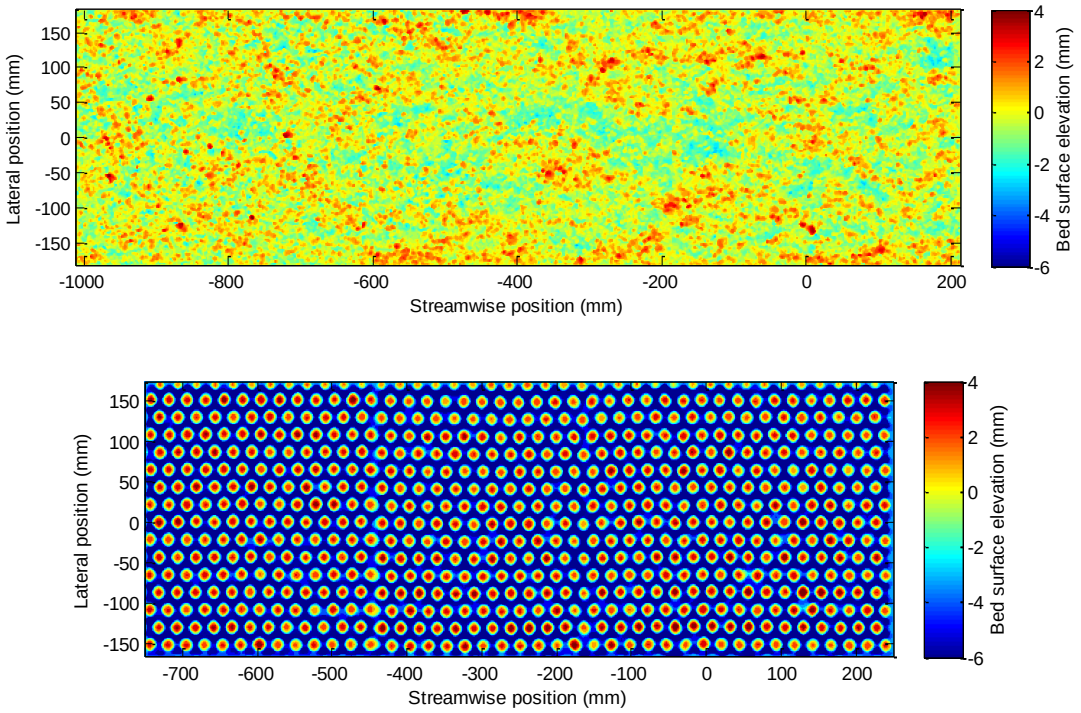

Figure 3-6: Bed elevation data for gravel and sphere beds. Lateral datum corresponds to the flume centreline. Streamwise datum is at 8.4 m from the flume inlet (corresponding with the flow visualisation datum discussed in section 3.3.3). Both bed types exhibit a maximum elevation of around 4 mm above their mean

The three dimensional bed data for the two bed types are shown in Figure 3-6. The zero elevation position is defined as the mean bed level. For the gravel bed case this is the mean of the LDS elevation data. For the sphere data it is defined as being a distance of $\varphi_{sph} / 6 = 4.17$ mm below the mean position of the top of the spheres. This is due to the mean height of a hemisphere occurring at 2/3 of the hemisphere radius. Indeed, this was the reason for selecting spheres with a diameter of 25 mm, since the maximum heights of both bed types would be located the same distance (4 mm) above their mean elevation (see Figure 3-6), and therefore it was expected that both bed types would exhibit a similar hydraulic roughness. A two-dimensional median filter was used to remove erroneous high or low readings in the LDS

data. For the gravel bed this filter was 3 x 3 in size (1.5 mm x 1.5 mm), while for the sphere bed a 5 x 5 (2.5 mm x 2.5 mm) filter was used. In both cases this window is smaller than the grain size in order to avoid smoothing or removal of real bed features.

For both bed cases, the bed elevation data were then used to calculate the second order Kolmogorov structure function of the bed topography using the method proposed by Nikora et al. (1998) and extended to 2-dimensional areas by Goring et al. (1999). This method involves comparing a fixed section of the bed elevation data with a section of the same size whose position is translated within the scanned area. By assessing the correlation between the reference area and the translated area a calculation can be made as to the correlation length of the bed topography in both streamwise and lateral directions. For this work, the reference and translated areas were 100 mm x 100 mm square. Figure 3-7 represents the bed structure correlation as the translated area is moved away from the reference area in the streamwise direction. It is apparent that above a lag of around 10 mm there is no significant spatial correlation of the bed surface elevation in either the streamwise or lateral direction. This suggests that any correlation observed on the water surface above this lag will not be a result of any feature on the bed having an individual influence on the flow surface, but that the surface pattern is an abstraction of the bed roughness as a whole. As might be expected, the highly organised pattern of the sphere bed gives rise to strong correlation between spatially separated areas of the bed. The structure function takes a similar pattern to the bed itself, with a strong characteristic spatial period of around 25 mm (the sphere diameter). Any

correlation observed in the free surface with similar period could be said to be a result of the structure of the individual bed elements. Any other period would likely be a result of the bed roughness acting as a whole.

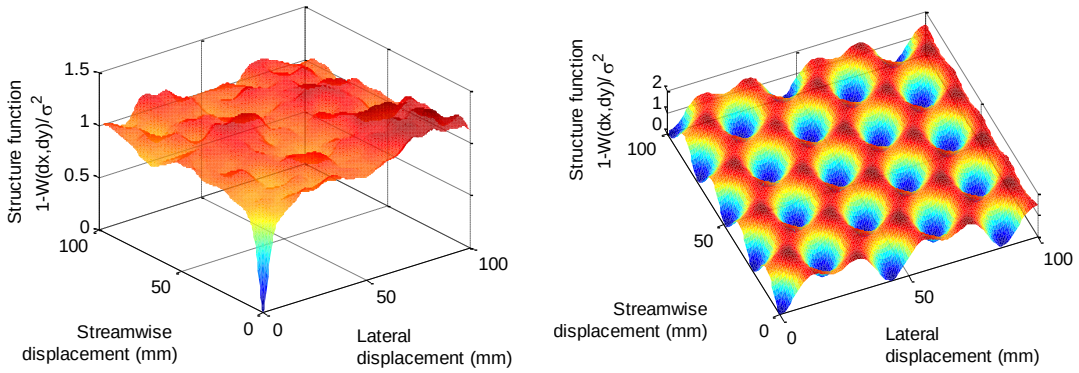

Figure 3-7: Gravel bed and sphere bed structure functions

The probability density functions of both bed types were also examined. These are given in Figure 3-8. The gravel data show a bell-shaped distribution about the mean elevation, with a maximum elevation of around 4 mm as discussed previously. The sphere bed data shows an almost bimodal distribution of elevations, with a peak near the maximum bed level of around 4 mm, and a further peak at around -2 mm. This shape is not immediately obvious. Further validation is provided by the PDF of a single scanned sphere (also shown in Figure 3-8). This confirms the general shape of the overall sphere bed PDF. It is likely that small variations in individual sphere elevation cause the local PDF of each bed element to be shifted slightly along the x-axis, such that the overall PDF is somewhat smoothed. This bi-modal density function is as a result of the two orthogonal functions governing the area of each sphere which is within each elevation bin. These two functions are the probability density of a semicircle (which increases with

elevation), and the local circumference of the sphere (which decreases with elevation). The combination of these two functions is non-trivial.

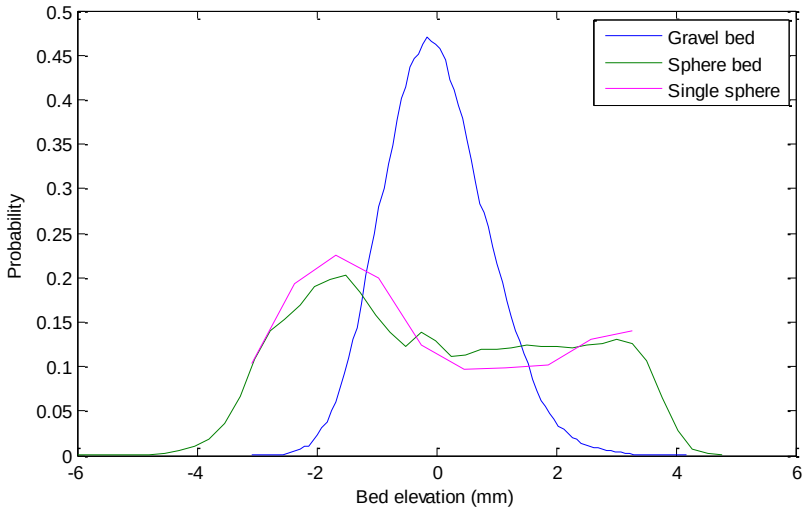

Figure 3-8: Gravel bed and sphere bed probability density functions

3.2 **Wave probes**

A non-equidistant array of seven calibrated, conductance wave probes was installed along the centreline of the flume at the wave probe test section (9.59 to 10.07 m from the flume inlet, see Figure 3-1) in order to measure the instantaneous elevation of the water surface at a number of streamwise locations.

The wave probes were arranged in order to provide a number of unique spatial separations between the various possible probe pairs. The wave monitor unit (Figure 3-10a) allows a maximum of 7 probes to be operated simultaneously. The number of unique probe pairs which can be used to calculate the spatial correlation as a function of the lag between the probes in a 7-probe array is N = 22 which includes one extra point that corresponds to a probe correlated against itself (i.e. auto correlation data for zero lag).

Arrays of this type are often referred to as sparse linear (or non-equidistant) arrays, and several algorithms exist for the optimisation of such spatial arrays, maximising the number of unique spatial separations while minimising the number of repeated (redundant) separations (Johnson & Dudgeon, 1993). In this instance it was found that the most practical arrangement was one in which the separations between adjacent probes were equal to 30, 50, 70, 90, 110, and 130 mm respectively. This yields 20 unique separations (spatial lags, ρ), and one repeated separation (ρ = 240 mm) along with the autocorrelation data. The array was oriented such that the largest separation (130 mm) was at the upstream end of the array. This configuration was chosen so that if any constructive interference were to occur between vortices shed from adjacent probes, the effect would be most likely to occur for the more downstream probes, and so if this effect were to corrupt data, the data from the more upstream probes would still be valid. The interaction between probes in the array is investigated in detail in section 4.1.

Figure 3-9 shows the position of the probe array with respect to the flume upstream end and indicates the streamwise separations between the individual probes.

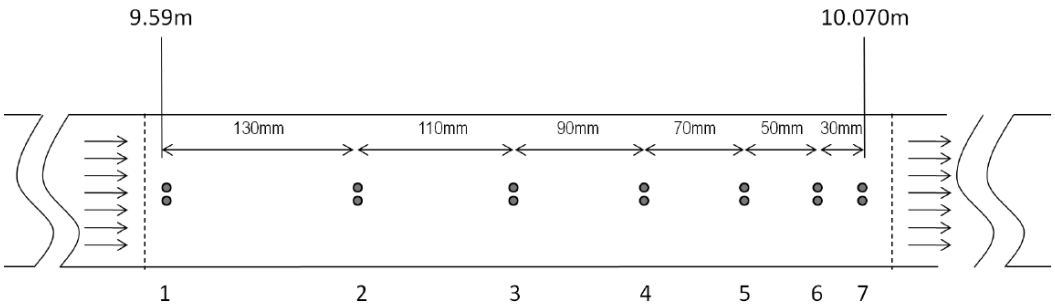

Figure 3-9: Position of conductance wave probes relative to the flume inlet

Each of the probes in the array consisted of two vertical, parallel, tinned copper wires which were separated by a 15 mm distance oriented laterally to the main flow direction. The diameter of these wires was 0.24 mm. For the gravel tests, the probe wires were attached to 2 mm thick plastic anchor plates which were held onto the base of the flume by the weight of the gravel layer. Since these anchor plates were well below the surface of the gravel layer, they did not affect the flow above the gravel bed surface. For the sphere tests, a 1 mm diameter hole was drilled for each wire through the upper layer of spheres, and the wires were fixed into these holes using adhesive. The drilled spheres were then fixed to the spheres immediately beneath which were fixed to the flume base.

The top of each probe wire was attached to a screw mechanism allowing the wires to be held under tension to keep them vertical without exceeding the elastic limit of the wire and causing permanent deformation. Once the probes were calibrated the tension was not altered.

The probes were connected to standard WM1A wave probe control modules (Figure 3-10a) provided by Churchill Controls (Churchill Controls, 2003). The control modules energised the wave probes with high frequency square wave signals (with a mean of 0 V to avoid anodising effects), and measured the conductance between the two wires. The control modules provided an analogue voltage output, to a data acquisition card (described further in section 3.6), which was capable of measuring to an accuracy of 0.3 mV. This was over a range of -10 V to +10 V, which was approximately tuned to cover

depths from 0mm to 200 mm, resulting in a theoretical measurement resolution of around 0.003 mm. On the output of each wave monitor module, a filter (Figure 3-10b) was used to eliminate aliasing of high frequency noise, since it was found that the excitation signal of the wave probes (3 to 10 kHz) can cross over to the output. The filter was a low-pass symmetrical unbalanced "T" network, with the Z_1 (transmission line impedance) component comprising two 16 kΩ (series) resistors, and the Z_2 component (shunt line impedance) being a 33 nF capacitor. This configuration results in a 3 dB roll-off at 300 Hz, without significantly affecting the phase or amplitude of signal components below around 20 Hz. With the filters in place, it was found that electrical noise was in the order of 1 mV (or 0.01 mm), and for this reason, surface fluctuation data presented in this thesis are shown in mm to two decimal places.

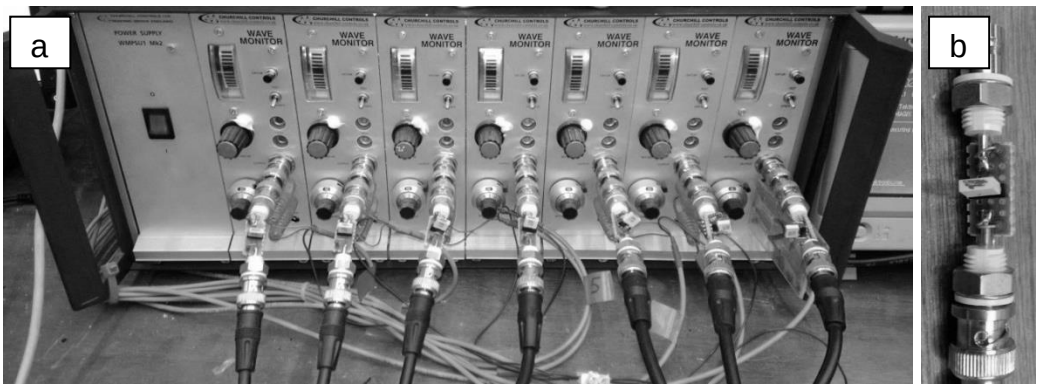

Figure 3-10: Wave monitor modules, and low-pass output filters

3.2.1 Calibration

The wave probes were regularly cleaned and calibrated to ensure the accuracy of the water surface elevation measurements for the adopted range of hydraulic conditions. The calibration procedure involved setting the flume

gradient to S_0 = 0, and inserting a blockage into each end of the flume. Water from the flume's main tank was then pumped into the flume and allowed to settle for at least 10 minutes before voltage levels were recorded for all the probes under static, still water conditions. Recordings were 60 s in duration in order to capture (and average out) several periods of any residual fluid motion which may potentially be present. In practice any such motion was always small (less than 1% of the depth). This was conducted at six different water depths that spanned the full range of flow depths considered in this work. The mean output of each wave probe, M, was plotted against the water depth, D (the circular markers in Figure 3-11). This allowed linear regression lines (the solid line in Figure 3-11) to be derived empirically to convert the instantaneous voltage recorded on a particular probe into an accurate instantaneous water depth. Calibrations, performed before and after a given flow condition was examined, showed that the calibration constants were unchanged (agreed to within 1%) over the course of the measurement. Over extended periods of time (weeks) between tests the calibration constants were seen to change by as much as 5%. The changes did not appear to correlate with any other variable such as temperature, and were likely due to several effects including the temperature, galvanic processes, and slight biological differences in the water. This is the reason for the calibration being repeated and updated regularly.

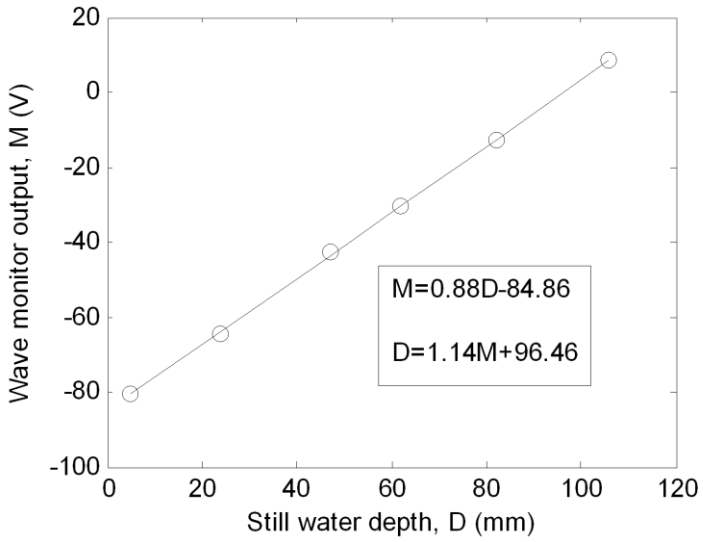

Figure 3-11: Example of wave probe calibration data along with linear regression line used to determine calibration constants

3.3 **Particle image velocimetry (PIV)**

Two-dimensional particle image velocimetry (PIV) was used to visualise, measure and quantify the time-dependent flow field beneath the surface, in a vertical plane along the centreline of the flume at the test section. The PIV system was supplied by Dantec Dynamics and uses two pulsed Nd: YAG lasers with a wavelength of 532 nm to illuminate and visualise particle motion in a plane within the flow.

3.3.1 System setup

A photograph of the PIV system is shown in Figure 3-12 while a diagram of the camera arrangement for flow visualisations is shown in Figure 3-13.

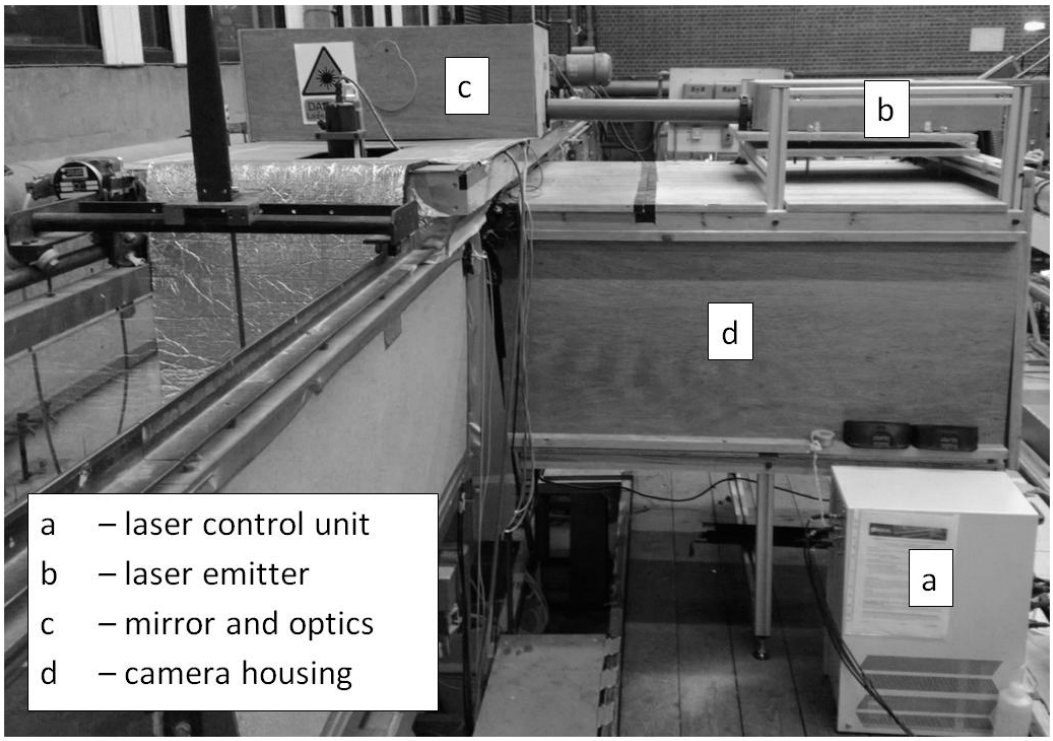

Figure 3-12: Overview photograph of PIV system setup

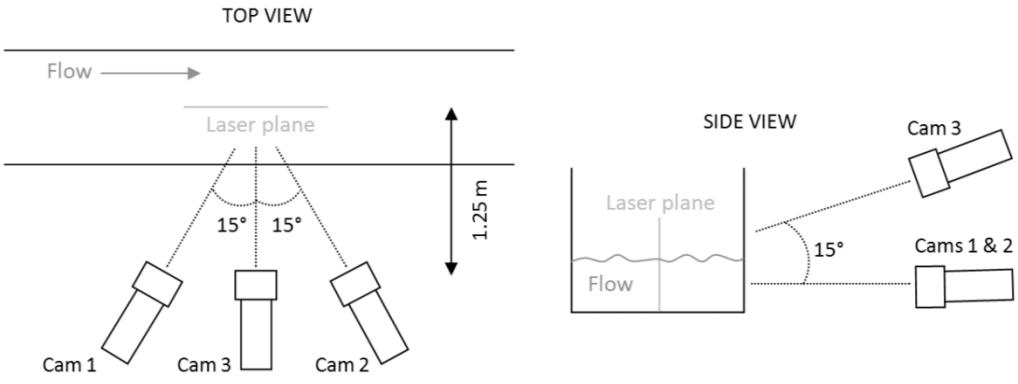

Figure 3-13: Diagram of camera arrangements for flow visualisation

The laser unit projects a beam of two concentric lasers over the top of the flume where it contacts a 45º mirror (Figure 3-14a), sending the beam vertically downwards at the centre of the flume. The beam then passes through optics designed to form and focus a light sheet. The laser sheet

illuminated a volume approximately 250 mm long in the streamwise direction and approximately 3 mm thick in the lateral direction (Figure 3-14b).

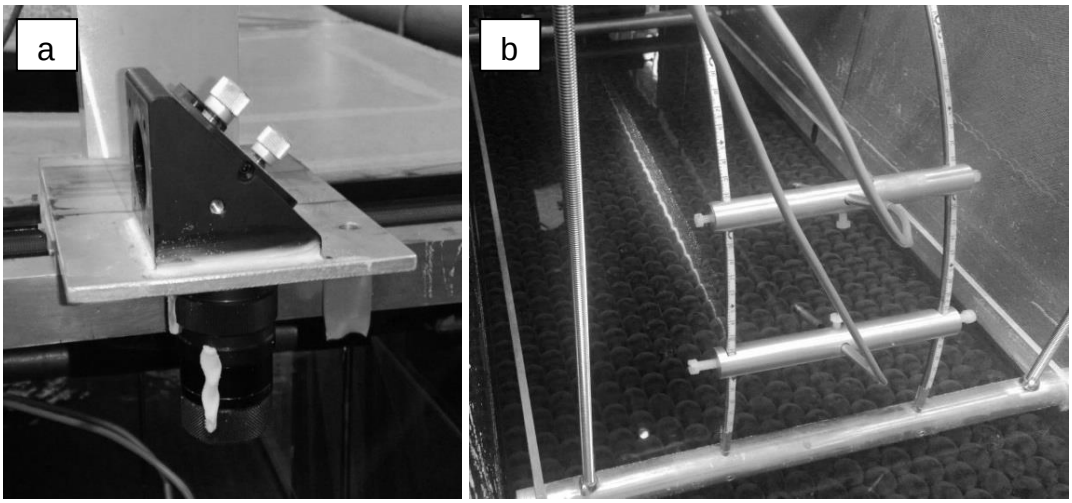

Figure 3-14: (a) PIV mirror and optics, (b) laser light sheet formed in flow

Two CCD cameras (labelled cam 1 and cam 2 in Figure 3-13), each with an image area of 1600 x 600 pixels, were focused on the laser sheet, and were synchronized with the two laser pulses. The cameras were situated a distance of 1.25 m from the light sheet, with an angle of 30° between them. The use of two cameras improves the accuracy of the vertical and streamwise velocity measurements, and also theoretically allows for transverse (through-plane) velocities to be calculated. Each camera was attached to a Scheimpflug mount, allowing the relative orientation of the CCD and the lens to be adjusted so that the full field of view was in focus even though the laser plane was not parallel to the lens. The overlapping field of view of the two cameras covered an area in the laser plane of approximately 247 mm x 89 mm. This would allow depths up to around 100mm to be

examined, while capturing data from an area between 2.5 and 6 water depths long in the streamwise direction, for the flow conditions used in this work. This length was expected to be suitable for capturing at least one large scale turbulent event given that these events are reported to be around 1 to 3 flow depths in length (Roy, et al., 2004; Nakagawa & Nezu, 1981; Liu, et al., 2001). A larger field of view would have captured a longer reach of flow, and allowed for deeper flows to be examined, however this would have reduced the spatial resolution of the measurements. By using the narrower field of view, the resolution of the images was approximately 6.5 pixels per mm in either direction, or 42 pixels per mm^2. This resolution affords two advantages. Firstly, a strong particle definition was achieved, whereby each particle in the field of view consisted of at least 5 pixels, allowing for sub-pixel interpolation of particle positions. Secondly, it allows a high spatial resolution of the resulting velocity vectors (92 x 34 for the analysis procedure used in this work, described in detail in section 4.3). This was seen as crucial for allowing the examination of turbulence properties at a number of depth-wise locations throughout each of the flow conditions examined, and critically would give at least 225 velocity vectors within each large scale turbulent structure (for the lowest flow depth examined), resulting in a clear definition of these structures.

For the PIV measurements, Plascoat Talisman 30 (a polymer powder normally used for coating metals) was introduced to the flow to act as seeding particles with a diameter of around 150 μm (Hunter, 2010) and a narrow particle size distribution (Plascoat, 2013). These particles were almost neutrally buoyant, with a specific gravity of 0.99, sufficient to maintain

suspension for several hours (Vlaskamp, 2011), and so following the flow path representatively during each measurement. The cameras were fitted with narrow band-pass filters which passed light at 532 ± 2 nm, in order to obtain light reflected from the particles only, reducing any light pollution in the images.

A pair of particle images separated by a time delay of 1 ms was captured on each camera and this was repeated at a fixed frequency. The upper limit of this frequency is controlled by the hardware limitations and image buffer resources and transfer rates. The maximum sampling frequency possible with this system was 26.9 Hz. Though a higher frequency is preferable, this was deemed sufficient since the dominant frequency components of the velocity fluctuations were seen to be below 10 Hz. Had a higher sampling rate been required, the image area could have been reduced by a factor of two or four (and hence the sample rate increased by a similar factor). This technique effectively limits the vertical scale of the field of view, so was not possible in this work since the full frame was required for capturing the flow conditions of interest. For each measurement, images were captured for a duration of 5 minutes, in order to generate a time series of image pairs on each camera (the reason for this measurement duration is explained in section 3.8). Figure 3-15 shows one of the PIV cameras with its view of the measurement plane, along with an example image of the seeding particles in a flow captured by this camera.

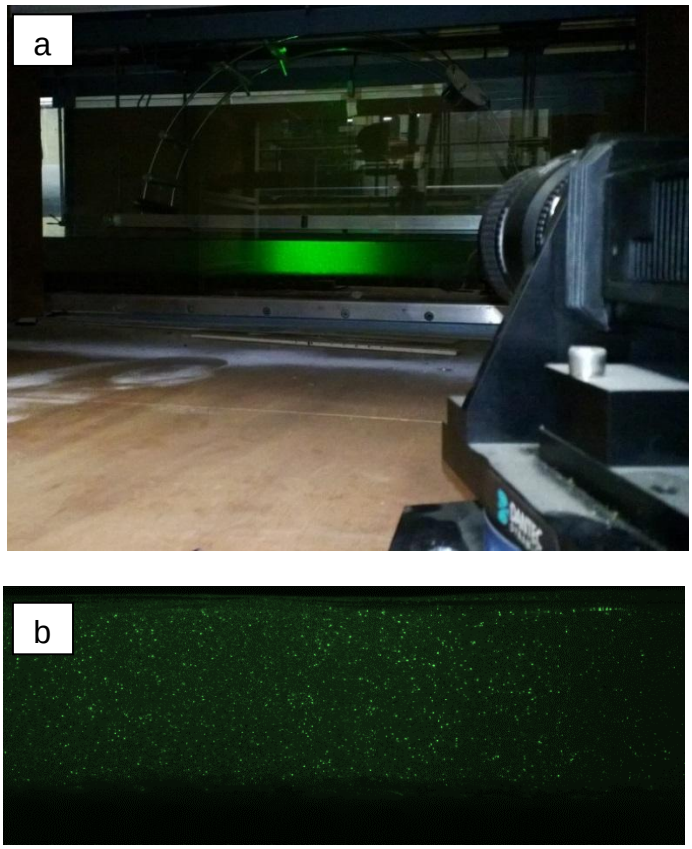

Figure 3-15: One PIV camera and its view of the seeding particles in the flow field

3.3.2 Calibration

In order for the output of the PIV analysis to be represented in real terms (velocities in m/s at spatial locations defined in mm rather than velocities in pixels/s at spatial locations defined in pixels), a calibration was performed. The calibration procedure involved the capturing of images of a calibration plate which consisted of an orthogonal grid of circular markers at known spatial positions. The 200 mm x 200 mm calibration plate is shown in Figure 3-16 along with an image captured by one of the PIV cameras. The calibration plate was positioned by use of the scanning frame on top of the flume (described in section 3.1.3). This not only allowed accurate placement and adjustment of the plate, but also meant that the horizontal axis of the

plate was always parallel with the flume bed. At the centre of the array there is a unique large marker which defines the datum position. The four markers surrounding the datum are smaller than the modal marker size, to indicate the horizontal and vertical axes. During calibration, the plate is placed in the plane of the laser, at the centre of the camera's field of view, and it is immersed in water so that any refraction effects are captured as they would be for flow conditions. For two-dimensional calibration, several images are captured on each camera, and an image-model fit is then performed using a direct linear transform to determine the calibration constants which are to be applied to the PIV data. This type of transform is suitable for applications such as this where any refractive boundary (the glass wall of the flume) is planar. For three-dimensional calibration the same process is applied but using images of the calibration target recorded at two or more locations normal to the laser plane. The out-of-plane position of the target is accounted for in the image-model fit to allow the out-of-plane velocity components to be calculated. The three-dimensional process was conducted during calibration in this work. A scanning frame was used to move the calibration target by precise distances such that images were recorded with the target at the centre of the laser plane, and at positions 2 mm either side of the plane centre. This would theoretically allow the transverse component of the calibration to apply over the full width of the laser plane.

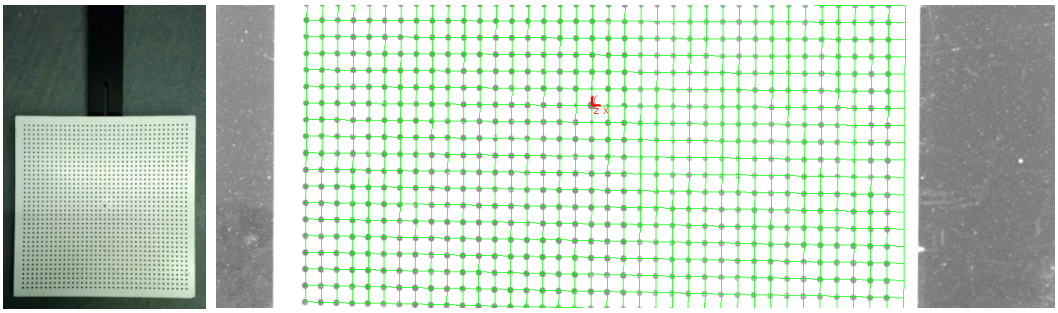

Figure 3-16: Calibration target plate used for PIV calibration, and as recorded by PIV camera superimposed with the determined linear transform matrix

3.3.3 Measuring the datum position relative to the bed

It was important to ensure that all the measurement systems operated within a common spatial frame of reference. The vertical position of the global datum is defined as the mean bed elevation, while the streamwise position is the streamwise location of the PIV datum. A procedure was therefore required to determine the streamwise position of the PIV datum relative to the bed elevation measurements of Figure 3-6, and also (since the datum of the PIV measurements is not at the vertical level of the mean bed elevation) the vertical distance between the mean bed position and the PIV datum. This distance could then be added to the vertical position of the PIV measurements in order to present each measurement relative to the bed surface. Since the calibration target was held such that it was parallel with the flume bed, only a vertical correction was required, rather than any additional rotational correction.

The following procedure was used to achieve this. The laser displacement sensor (section 3.1.3) was used to scan the bed surface in the plane of the PIV laser, in order to calculate the mean bed position relative to the LDS sensor. The sensor was then raised by a known distance so that a multi-level

target could be placed beneath it (Figure 3-17a). This target was then scanned by the LDS system so that its profile could be represented relative to the mean bed position. The PIV laser was then activated (Figure 3-17b) and images were acquired. Calibration images acquired in air were then used to dewarp the images of the multilevel target so that the profile of the target could be represented in the coordinate system of the PIV system. The difference between the position vectors of the PIV system and the LDS system could then be used to transform the PIV spatial locations into locations relative to the bed surface. Since the location of the target can be determined to within around 0.15 mm (the nearest pixel) by the PIV system, and to within 0.25 µm by the LDS system, it is thought that this technique is accurate to the nearest 0.15 mm. This is sufficient given that the length scales of the bed material, and the PIV interrogation areas, are always at least an order of magnitude greater than these spatial resolutions.

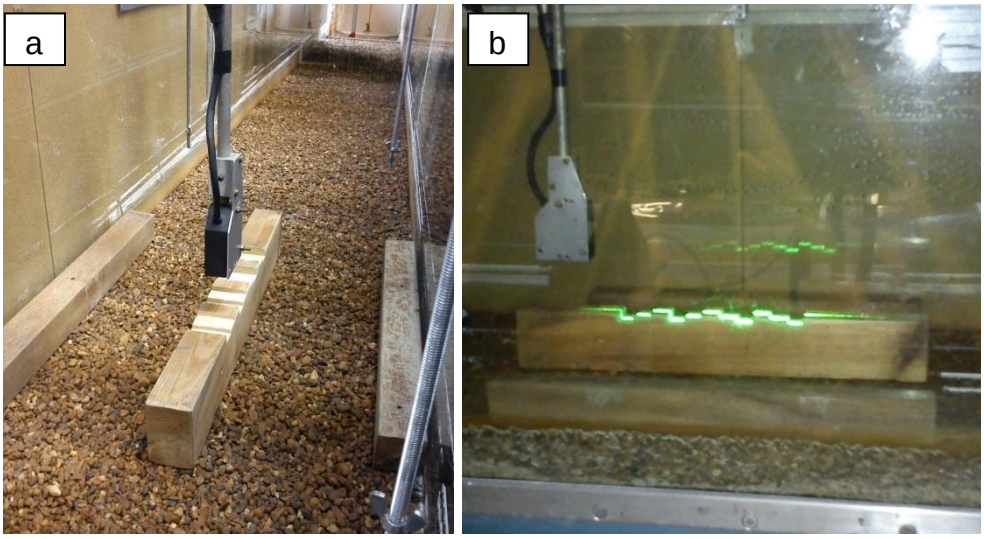

Figure 3-17: Multi-level target measured by LDS and flow visualisation cameras to determine relative position of the datum of the two systems

3.4 **Laser induced fluorescence (LIF)**

3.4.1 System setup

A laser induced fluorescence (LIF) technique was employed to measure the free surface deformation in synchronisation with the PIV measurements, and in the same plane. Hazuku et al. (2003) achieved this type of measurement using PIV images alone by observing the reflection of PIV particles in the free surface when viewed from an angle below. By matching real particles with imaginary (reflected) particles the midpoint between these pairs defined the location of the free surface throughout the image. With a similar goal, Okamoto et al. (1995) placed floating particles onto the free surface so that it could be detected in the PIV images. While these techniques were successful, it requires that the PIV cameras achieve a clear line of sight to the interface between then laser plane and the free surface. For flows where the depth is much smaller than the distance between the laser plane and the cameras, this may not be possible as surface features in front of the laser plane may obscure the surface profile of interest. Furthermore, the use of floating particles can affect the surface tension of water (Bianchini, et al., 2013), which could affect the behaviour of the free surface. For the current work, a third camera was used to image the intersection between the laser sheet and the water surface. This camera was also calibrated (in air) using the same frame of reference as the PIV data, and was installed at an elevated position, looking down towards the water surface at an angle of 15° (see Figure 3-13 and Figure 3-18a). This setup allowed for a clear line-of-sight between the surface profile and the camera, with no opportunity for higher water surface features in front of the laser plane to obstruct the view.

This camera was used to capture the position of the air-water interface at 1600 streamwise locations (one per column of pixels on the CCD) along the plane of the laser, and was synchronized with the other two cameras. In order to define the free surface clearly in the images, Rhodamine B dye was added to the flow. Rhodamine is often used to map temperature distributions (Glawdel, et al., 2009) or solute concentrations (Pearson, et al., 2010), but in this case it was used to improve contrast between the air and water phases. When illuminated with 532 nm laser light, the Rhodamine is excited, and emits light at around 595 nm. A high-pass filter lens with a cut-off wavelength of 545nm was used to discard the green (532 nm) light scattered by the particles, but allow through the red (595 nm) light emitted by the rhodamine in the water (see Figure 3-18b). This method avoids the limitations of existing techniques by requiring no maximum streamwise surface gradient and no surface seeding as were necessary in previous studies (Hazuku, et al., 2003; Philip, et al., 1996; Okamoto, et al., 1995).

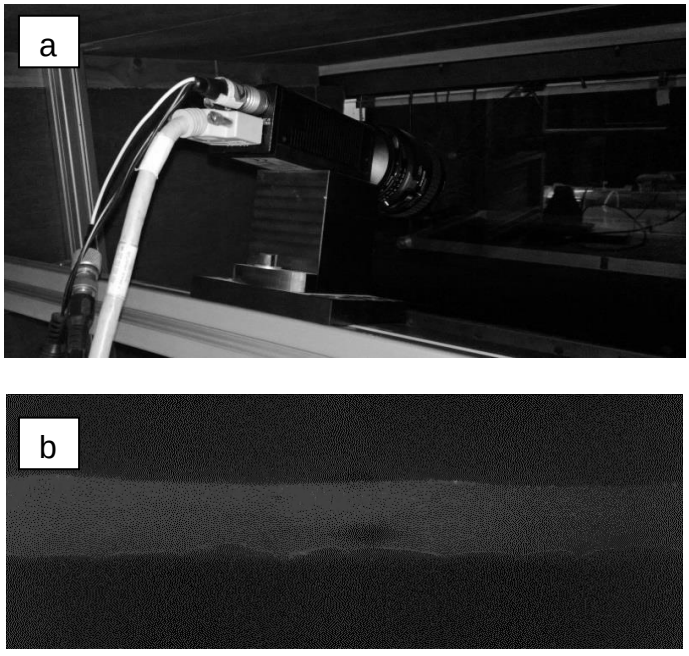

Figure 3-18: LIF surface imaging camera and an example recorded image

3.4.2 Calibration

It was important that the LIF system used the same datum and coordinate system as the PIV instrumentation (and therefore also the bed elevation measurements). For this reason, the spatial calibration of the LIF system was conducted using the same process as for the PIV system. During the PIV calibration, images of the same calibration plate were recorded on the LIF camera before water was added to the flume for the PIV image capturing. This is because the LIF camera under measurement conditions effectively operates only through the air, rather than the water. By using the same calibration grid, in exactly the same location, the resulting calibration data provided a geometric mapping to remove lens distortion and obtain surface profiles from the LIF data in the same coordinate system as that of the PIV data, so the results can be directly compared.

3.5 **Airborne acoustics**

3.5.1 Acoustic rig

The acoustic system was installed at the centre of the flume and at 8.4 m from its upstream end, effectively coinciding in position with the flow visualisation section (see Figure 3-1). A semi-circular arch-shaped acoustic rig was constructed in order to precisely control the positioning of each of the acoustic components (Figure 3-20). The arch was supported at each corner by a screw thread, allowing the height to be accurately adjusted. The base of the arch was thereby fixed at a distance of 10 mm above the mean water

surface level for all flow conditions. A 70 mm diameter ultrasonic transducer (ceramic type 043SR750) with the main resonant frequency of 43 kHz was positioned at an angle of 45° to the mean water surface position, at a distance of 0.4 m from the point of incidence. The directivity of the source is given in Figure 3-19.

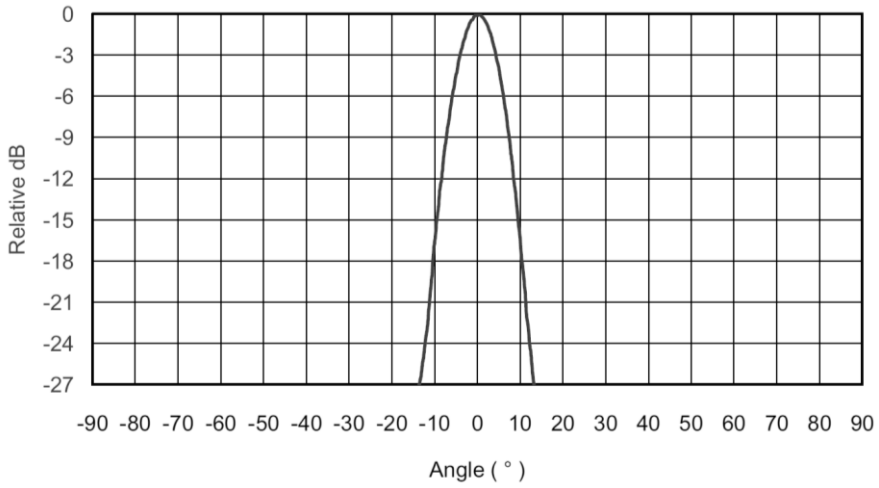

Figure 3-19: Directivity of ultrasonic source at 43 kHz

A single calibrated Brüel & Kjær (B&K) ¼" type 4930 microphone was used to receive the signals reflected by the rough water surface at the angle of specular acoustic reflection (45° from the water surface, opposite the transducer, see Figure 3-20). In this arrangement the radial distance between the microphone and the main incidence point for the sound emitted by the transducer, was also 0.4 m.

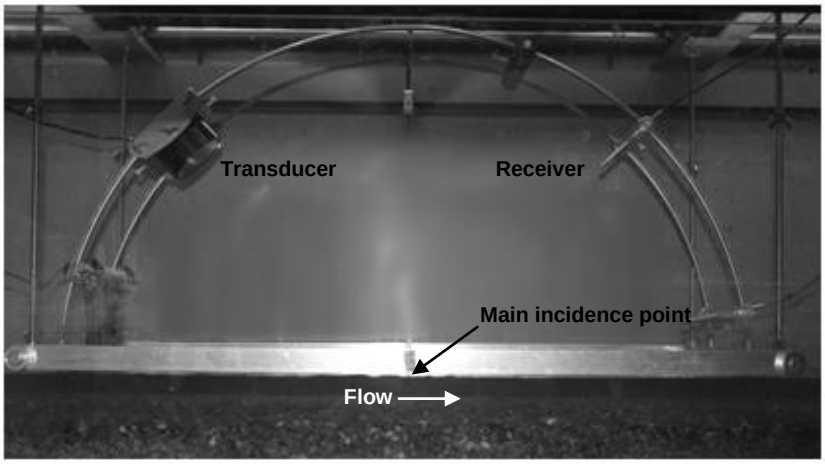

Figure 3-20: Acoustic instrumentation set up

The acoustic equipment was designed such that the PIV/LIF laser was not obstructed, and nor was the field of view of the flow visualisation cameras, allowing the acoustic, PIV, and LIF measurements to be recorded simultaneously.

The ultrasonic transducer was excited at its resonant frequency in order to produce a continuous sine wave. The signal was provided by a Tektronix AFG 3021B function generator (Tektronix, 2013), while the microphone signal was received by a B&K Nexus four-channel microphone conditioning amplifier (B&K, 2013), both shown in Figure 3-21. The output sensitivity of the Nexus amplifier was set to 100 mV/Pa, such that the output level was close to the data acquisition limit of ±10 V, without saturating, in order to make use of the maximum resolution possible. In all cases, acoustic data time series were 300 s long, as justified in section 3.8.

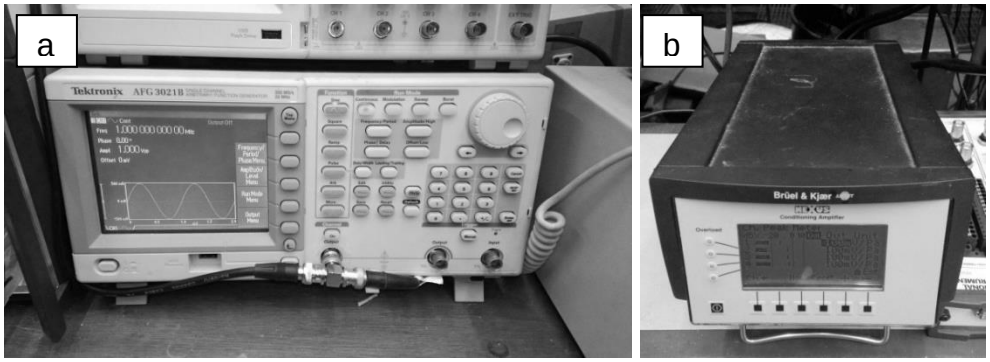

Figure 3-21: (a) Tektronix signal generator used to drive the ultrasonic transducer, and (b) B&K nexus amplifier used to receive acoustic signals

3.6 **Acquisition system**

3.6.1 Hardware

The wave monitor units provided an analogue voltage output which was proportional to the instantaneous water level on a given probe. The Nexus amplifier provided an analogue voltage output which was proportional to the instantaneous sound pressure at the microphone. Hence, a data acquisition system was selected which was capable of recording analogue voltage signals between ±10 V. A National Instruments (NI) PXIe 1062Q chassis was installed with an NI PXIe-6356 data acquisition (DAQ) card capable of simultaneous measurement on up to 8 channels at up to 1.25 MHz sampling rate. For easy connection of the devices, an NI BNC-2110 input board was used. Simple, reliable BNC cables could then be connected between the wave monitor and Nexus units and the DAQ input board.

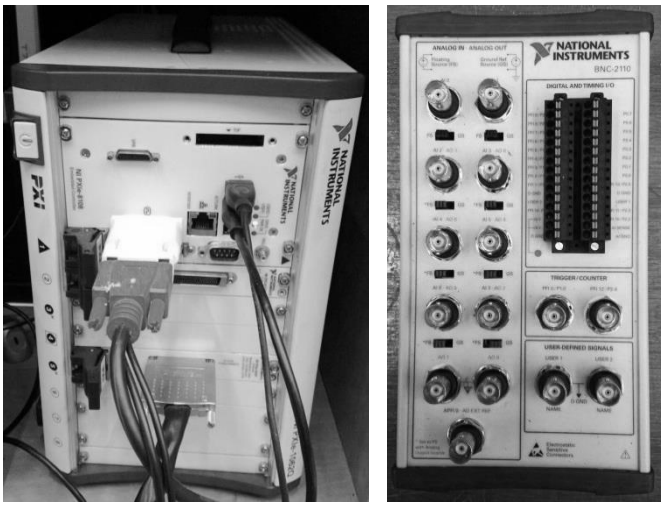

Figure 3-22: (a) The National Instruments acquisition PC, and (b) The BNC input board

3.6.2 Software

A National Instruments LabView data acquisition program was written to record the acoustic signals at 1 MHz sampling rate, and the wave probe data at 10 kHz. The data acquisition was carried out in 1 ms packets to avoid memory overflow. These packets of data were recorded synchronously on all channels, and the acquisition of each packet was triggered at a rate of 100 Hz. The resulting raw data were saved into text files, so that analysis could be performed using Matlab.

3.7 **Experimental conditions**

The hydraulic conditions studied in this work were designed to investigate the change in the water surface pattern as a function of the uniform flow depth, mean velocity, and bed topography.

Initially, the gravel bed boundary was used and a slope of S_0 = 0.004 was selected as it represents a typical bed slope found in gentle gradient streams (Rosgen, 1994). This gradient also meant that the maximum flow depth of interest (D = 0.10 m) was achievable within the discharge limitations of the flume. A range of seven flow depths from D = 0.04 m to 0.10 m was examined. This range was chosen since it represents a range of submergences typical of gravel bed rivers (Ferguson, 2007; Robert, 1990), while the upper limit (0.10 m) was chosen to avoid strong lateral components which can become significant when the depth exceeds around 1/5 of the channel width (Nezu & Nakagawa, 1993). The measurement equipment (for example the PIV field of view and spatial resolution) was therefore optimised for these seven flow conditions.

Once the system was optimised, it was used to examine flows at different gradients so that the effects of flow depth and bulk depth averaged velocity could be isolated. The majority of the adopted measurement equipment could measure flows with a wide range of depths and gradients, but the PIV/LIF system was limited in its field of view. The limiting factors regarding the feasibility of studying particular flows at particular gradients were therefore:

i) Is the bed within the PIV field of view?

ii) Is the free surface within the LIF field of view?

iii) Is the necessary flow rate achievable?

iv) Is the depth sufficient to provide good spatial resolution?

Determination of whether a given flow condition would be suitable for the PIV field of view reduced to a simple geometric calculation. For example, since

the lower edge of the PIV field of view was aligned close to the bed surface, gradients steeper than 0.004 could not be used as the bed would be out of sight. A good spatial resolution (in terms of the number of pixels or resultant velocity vectors in the vertical direction within a particular flow depth) was ensured by considering depths similar to those chosen for the 0.004 bed slope conditions.

Estimation of the discharge requirements of each possible flow condition was conducted by using the Manning formula (Arcement & Schneider, 2013):

$$n = \frac{k_m}{V} R_h^{2/3} S_f^{1/2}, \tag{3-1}$$

where n is the Gauckler-Manning coefficient which is related to bed roughness, k_m is a conversion factor with units of $m^{1/3}/s$, equal to 1 for SI units (used to ensure n is dimensionless), V is the bulk flow velocity, and S_f is the energy slope. For uniform flow, $S_f = S_0$. $R_h = Dw/(2D+w)$ is the hydraulic radius, where $w = 0.459$ mm is flume width, and D is uniform depth.

Seven flow conditions were tested with the gravel bed at the gradient of S_0 = 0.004, and a Manning's n was calculated for each of these conditions. It was estimated that the value of n was between 0.014 and 0.016, which was within the sensible range for gravel bottomed channels (Chow, 1959).

Using the mean estimate of Manning's roughness coefficient, the flow rate required for each potential flow condition was estimated by:

$$Q = \frac{Dw}{n} R_h^{2/3} S_0^{1/2}, \tag{3-2}$$

The resulting discharge estimates are shown in Table 5-1. This table also lists the regimes which could not satisfy the PIV field of view constraints. (Note: the flow condition with S_0 = 0.002 and D = 0.05 m was thought to be possible but in practice required a lower flow rate than was achievable. This is simply due to Manning's equation (Equation 3-1) being an approximation).

Table 3-1: Discharge estimates used to plan experimental program

Bed slope, S_0	0.001	0.002	0.003	0.004	0.005
Depth, D (m)	Estimated flow rate, Q (l/s)				
0.040	4.1	5.8	7.0	8.1	9.1
0.050	5.8	8.1	10.0	11.5	12.9
0.060	7.6	10.8	13.2	15.2	17.0
0.070	9.6	13.6	16.7	19.3	21.5
0.080	11.8	16.7	20.4	23.5	26.3
0.090	14.0	19.8	24.3	28.1	31.4
0.100	16.4	23.2	28.4	32.8	36.6

Flow rate unobtainable
Flow surface out of PIV area
Flume bed out of PIV area

Based on this analysis (and omitting the flow condition with S_0 = 0.002 and D = 0.05 m as mentioned above), sixteen flow conditions were selected and examined for both the gravel and sphere bed boundaries. Although the sphere bed was designed to exhibit a similar hydraulic roughness to that of the gravel bed, it was found that its roughness was higher, and so for a given depth, a lower flow rate was required to achieve the same flow velocity. For this reason, between the gravel and sphere bed tests, a new, more effective, flow control valve was installed, allowing the flow rate to be further reduced. This valve was the same kind of butterfly valve as the original but with a greater dynamic range. Since it was installed prior to the flume inlet tank, it

did not affect the flow differently to the previous valve, other than providing the opportunity for a lower flow rate.

A summary of the chosen hydraulic conditions is given in Table 3-2 and Table 3-3 for the gravel and sphere bed data respectively.

Table 3-2: Selected hydraulic conditions for gravel bed flows

Condition	Bed slope S_0, (-)	Depth, D, (mm)	Condition	Bed slope S_0, (-)	Depth, D, (mm)
1	0.004	40	9	0.003	60
2	0.004	50	10	0.003	70
3	0.004	60	11	0.003	80
4	0.004	70	12	0.003	90
5	0.004	80	13	0.002	60
6	0.004	90	14	0.002	70
7	0.004	100	15	0.002	80
8	0.003	50	16	0.001	70

Table 3-3: Selected hydraulic conditions for sphere bed flows

Condition	Bed slope S_0, (-)	Depth, D, (mm)	Condition	Bed slope S_0, (-)	Depth, D, (mm)
17	0.004	40	25	0.003	60
18	0.004	50	26	0.003	70
19	0.004	60	27	0.003	80
20	0.004	70	28	0.003	90
21	0.004	80	29	0.002	60
22	0.004	90	30	0.002	70
23	0.004	100	31	0.002	80
24	0.003	50	32	0.001	70

3.8 **Experimental procedure and bulk flow conditions**

The flow conditions were examined in the order given in Table 3-2 and Table 3-3. The measurement procedure was the same for all the flow conditions.

For each flow condition, the gradient was set, and the inlet valve and downstream gate were adjusted in order to give the desired uniform flow depth readings on the point gauges. Since the accuracy of the point gauge depth measurement was 0.5 mm, careful adjustment of the inlet valve and downstream gate could ensure that the chosen flow depths were achieved to within 0.5 mm. Once the required uniform flow was achieved, the flow was allowed to stabilise for at least 1 hour before measurements were taken.

Firstly, the following bulk conditions were recorded: uniform flow depth, D, from the point gauges, flow rate, Q, from the orifice plate and manometer, and surface velocity, V_s, from timing a floating tracer. Secondly, wave probe data was recorded from the 7-probe array for a duration of 300 s. Thirdly, combined PIV/LIF data was recorded for a duration of 300 s. Next, a 300 s long acoustic recording was made. Flow temperature was recorded at the start and end of each measurement and it was found to change by less than 5% over the measurement period of each flow condition.

The measurement duration of 300 s was selected as this is the time required for the standard deviation of the wave probe signals (RMS water surface roughness height) to comfortably settle to within ±1 %. Figure 3-23 shows the RMS water surface roughness height of wave probe time series of increasing duration as a percentage of the standard deviation of a 300 s long recording. Data is shown for all the 7 wave probes, and for three flow conditions (1, 4 and 7) representative of the full range of hydraulic conditions examined in this study. Similar settling times were observed in the RMS of the PIV velocity data recorded at different spatial locations as shown in Figure 3-24.

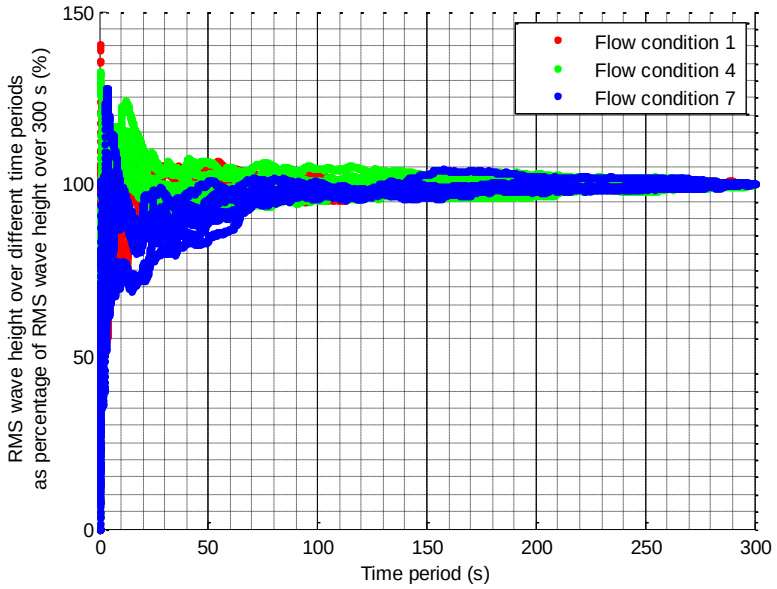

Figure 3-23: Settling time of RMS water surface roughness height for increasing recording duration

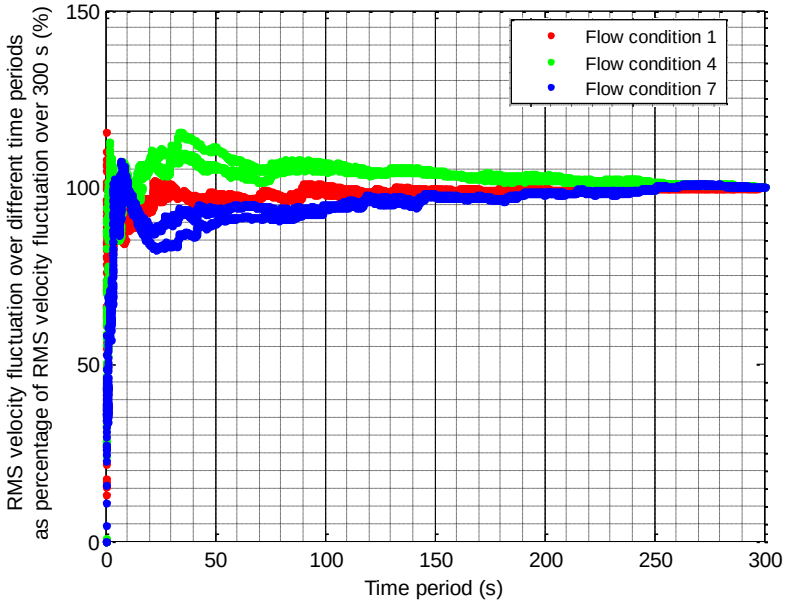

Figure 3-24: Settling time of streamwise RMS velocity fluctuation for increasing duration

The full experimental procedure was conducted for all the flow conditions. The resulting bulk flow properties are given in Table 3-4 and Table 3-5 for the gravel and sphere beds respectively.

Table 3-4: Measured hydraulic conditions for gravel bed flows

Condition	Bed slope	Depth, D, (mm)	Velocity, V, (m/s)	Re	Equivalent roughness, k_s, (mm)	Relative submergence D/k_s
1	0.004	40	0.41	17300	4.9	8.2
2	0.004	50	0.50	26500	3.8	13.3
3	0.004	60	0.55	35200	3.8	15.7
4	0.004	70	0.60	42600	3.7	19.0
5	0.004	80	0.64	54800	3.9	20.3
6	0.004	90	0.69	67200	3.6	25.3
7	0.004	100	0.74	86000	3.0	33.5
8	0.003	50	0.36	19700	8.7	5.7
9	0.003	60	0.41	25800	7.7	7.8
10	0.003	70	0.47	35500	6.3	11.2
11	0.003	80	0.52	45800	5.1	15.7
12	0.003	90	0.57	55200	4.4	20.4
13	0.002	60	0.32	19500	9.1	6.6
14	0.002	70	0.35	25900	9.1	7.7
15	0.002	80	0.40	31800	7.4	10.8
16	0.001	70	0.26	18500	7.9	8.9

Table 3-5: Measured hydraulic conditions for sphere bed flows

Condition	Bed slope	Depth, D, (mm)	Velocity, V, (m/s)	Re	Equivalent roughness, k_s, (mm)	Relative submergence D/k_s
17	0.004	40	0.28	10800	20.9	1.9
18	0.004	50	0.36	15100	15.6	3.2
19	0.004	60	0.43	24500	11.7	5.1
20	0.004	70	0.50	32700	9.2	7.6
21	0.004	80	0.57	38800	6.8	11.7
22	0.004	90	0.65	47300	4.7	19.2
23	0.004	100	0.71	59700	3.9	25.8
24	0.003	50	0.26	11000	27.3	1.8
25	0.003	60	0.35	19500	15.9	3.8
26	0.003	70	0.44	27900	8.7	8.1
27	0.003	80	0.49	32100	7.3	11.0
28	0.003	90	0.57	42400	4.7	19.3
29	0.002	60	0.22	12000	37.3	1.6
30	0.002	70	0.32	19700	14.6	4.8
31	0.002	80	0.41	30800	6.2	12.8
32	0.001	70	0.21	14300	17.8	3.9

The uniform flow depth, D, and the depth-averaged mean flow velocity, V, were varied respectively from 40 mm to 100 mm and from 0.21 m/s to 0.74 m/s. Since the depth is measured to the nearest 0.5 mm and the flow rate to the nearest 0.5 l/s, it can be shown that the calculation of depth average velocity, V, is hence accurate to the nearest 0.01 m/s.

The equivalent roughness height, k_s, for these conditions was calculated using the Colebrook-White equation modified for open channel flows (Barr, 1963). This formula was selected since it reflects the physical reality that deeper flows experience a lower resistance, and it is therefore more sensitive to the flow conditions (by definition it characterises the resistance to flow) than using a directly measured grain size, or Manning's equation which gives a more general roughness coefficient for a given physical channel. The Colebrook-White equation for open channels is presented as:

$$\frac{1}{\sqrt{f_r}} = -2.0\log_{10}\left[\frac{k_s}{14.83R_h} + \frac{2.52}{4\,\mathrm{Re}\sqrt{f_r}}\right], \qquad (3\text{-}3)$$

where

$$f_r = \frac{8gR_hS_0}{V|V|}, \qquad (3\text{-}4)$$

is the Darcy-Weisbach friction factor, S_0 is the energy slope, g is the acceleration due to gravity and Re is the depth-based Reynolds number. This number is calculated from the measurement of discharge and mean water depth, which are each accurate to 0.5 l/s and 0.5 mm, respectively. The Reynolds number is therefore presented to three significant figures as

shown in the tables. The range of flow depths was produced so that the ratio of depth to equivalent roughness height (D/k_s) varied from 1.6 to 33.5, which is within the range of relative submergence values found in gravel bed rivers without appreciable bedforms by Ferguson (2007). For brevity, the shear velocity is not shown in Table 3-4 or Table 3-5, but it is used later in the thesis for non-dimensionalising. The shear velocity can be easily calculated from the depth and bed slope data presented in Table 3-4 and Table 3-5 as:

$$U_* = \sqrt{gR_hS_0}\,, \tag{3-5}$$

3.9 **Experimental setup conclusions**

An extensive experimental setup has been carefully designed and constructed to allow the detailed measurement of multiple properties of shallow flows in the laboratory flume.

A 4.4 mm (mean) grain size gravel bed and a 25 mm diameter sphere bed have been used to generate different boundary shear layers in shallow flows, which are expected to produce different turbulence properties. The two bed types have been fully characterized by the use of a laser displacement sensor with a horizontal resolution of 0.5 mm x 0.5 mm (0.25 µm vertically).

A combined PIV/LIF system has been developed which is capable of simultaneously measuring the velocity field in a vertical and streamwise plane within the flow, and the profile of the free surface within the same

plane. The position of the datum of this system has been measured relative to the mean bed level.

An array of non-equidistantly spaced wave probes were installed just downstream of the flow visualisation (PIV and LIF) measurement section. This is to provide data to validate the LIF measurements, while allowing the behaviour of the free surface to be examined over a larger spatial range (0.48 m, as opposed to the approximately 0.2 m wide field of view of the LIF system).

Finally, an acoustic system has been devised, whereby an ultrasonic beam is directed at the free surface, and the reflected signal is received at the position of specular reflection. This setup is to validate the hypothesis that free surface fluctuations can be measured remotely by observing the behaviour of the reflected acoustic waves.

This range of complementary measurement techniques was selected in order to provide detailed insight into the properties of turbulent flow features as they propagate from the bed boundary to the free surface interacting with the air-water interface, and affecting the acoustic field incident on the dynamically rough water surface.

A range of flow conditions were selected in order to generate a range of turbulent flow fields giving rise to a range of free surface patterns. These flow conditions were chosen in order to fall within sensible ranges for bed slope and relative submergence.

A careful analysis of these flow conditions, using the unique experimental setup described in this chapter, will allow the examination of the hypotheses

presented in section 1.2, to determine the true nature of free surface patterns generated by turbulent flow, and to establish whether or not a clear link exists between the bulk hydraulic properties of shallow flows and the acoustic responses of the dynamic air-water interface.

Chapter 4 - Data pre-processing & validation

The experiments reported in chapter 3 provided a unique and extensive set of raw data which needed to be validated and pre-processed. This involved carrying out a set of standardized procedures to convert the raw data gathered into usable information about the flow surface, its acoustic scattering characteristics and the underlying flow field. In order to ensure that the data obtained after initial processing was reliable and accurate, various validation techniques were applied. The pre-processing and validation procedures for the obtained data are detailed in this chapter.

4.1 **Wave probe data**

As described in section 3.6, the analogue outputs of the wave probe control units were connected to a National Instruments X-series PXIe-6356 data acquisition card which digitized the signals simultaneously at a sampling rate of 10 kHz in 1 ms packets, with each packet triggered at a rate of 100 Hz. Each packet of wave probe data was averaged in order to reduce the effect of any residual high frequency (> 1 kHz) noise, resulting in a wave probe time series sampled at 100 Hz for each wave probe. The resultant 300 sec surface elevation data from the wave probes was detrended using a standard least mean squares technique and a 3rd order 10 Hz low-pass Butterworth filter was then applied to the data. This frequency was selected since the Churchill wave monitor includes an internal 10 Hz low-pass hardware filter,

so that any signal component above this frequency range could be considered as noise.

Figure 4-1 presents an example of the averaged power spectrum recorded on probes 1 to 7 for conditions 1, 4 and 7. Data is shown up to 20 Hz to show the roll off after 10 Hz as a response to the wave monitor's internal low-pass filter. A 20 s section of the corresponding water surface elevation time series data recorded on probe 4 is shown for each of the three flow conditions. The dominant spectral content is below 5 Hz and the amplitude of the water surface elevation spectrum above this frequency is at least an order of magnitude lower than the maximum amplitude.

A critical aspect of the wave probes' function is that they should not physically interfere with the flow, or electrically interfere with each other's signal. As the probe arrangement in Figure 3-9 shows, some of the probes on which these signals were recorded were in close streamwise proximity to each other. To minimise electrical interference, each probe was energised at a unique frequency allowing the wave monitors to distinguish the correct probe signals.

The close proximity may also give rise to the possibility of vortex shedding from an upstream probe, generating capillary waves which would influence the data obtained from the downstream probes. The frequency of the flow structures which could potentially be generated by vortex shedding was estimated using Strouhal theory for two-dimensional flow around a circular cylinder (Posdziech & Grundmann, 2007).

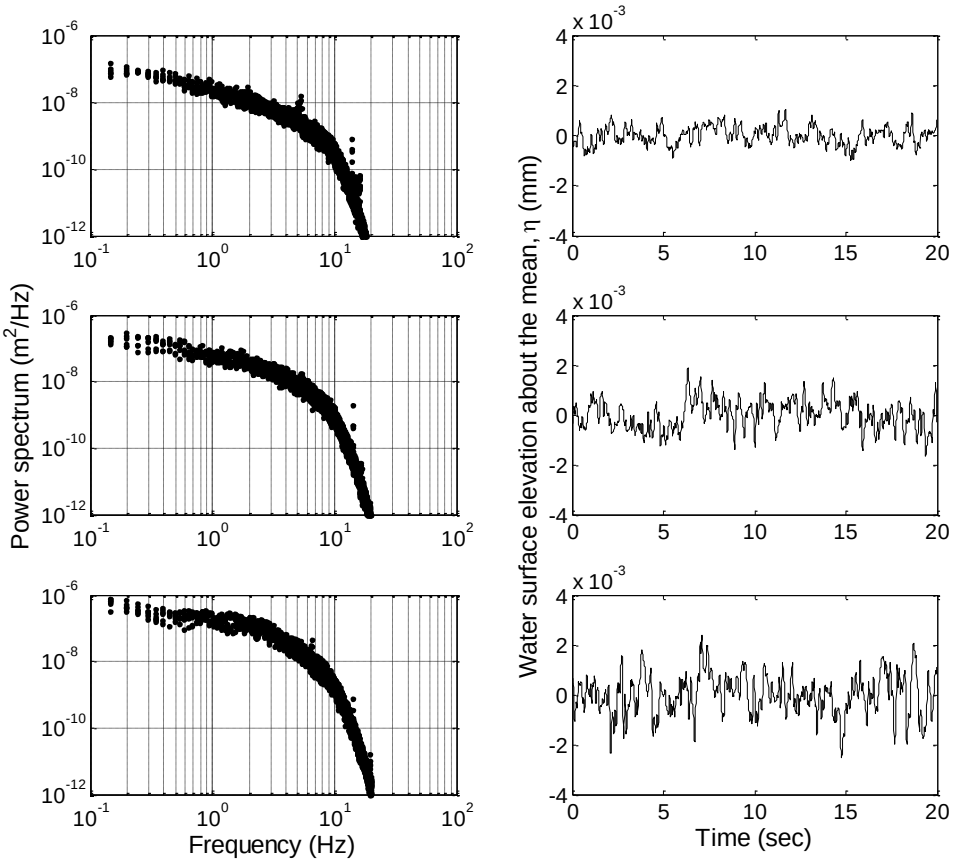

Figure 4-1: The mean power spectrum of the water surface elevation for flow conditions 1, 4 and 7 (left) and example segment of time series recorded on probe 4 (right). S_0 **=0.004;** D **=40, 70, 100 mm respectively;** V **=0.41, 0.60, 0.74 m/s respectively**

For the range of velocities given in Table 3-4 and Table 3-5, the diameter-based Reynolds numbers for vortex shedding from a 0.24 mm probe wire ranged from 80 to 170, giving respective Strouhal numbers of 0.15 to 0.19 (Posdziech & Grundmann, 2007). Vortex shedding at these Strouhal numbers and flow conditions would generate flow structures at frequencies of 200 Hz to 500 Hz, which is well outside the range of the spectral components observed in the wave probe signals. The scale of these structures would be a similar order to the diameter of the wire, at least an order of magnitude

smaller than the surface features observed. These high frequency, small scale events are unlikely to affect the low frequency larger scale surface fluctuations believed to be induced by the flow turbulence.

Furthermore, it has been empirically tested that the probe wires have a negligible impact on the statistical and spectral properties of the low frequency water surface roughness, and negligible electrical interference with one another. In a preliminary experiment, a flow similar to condition 5 was established, and individual probes were sequentially removed from the upstream end of the array so that only probe 7 remained in the array at the end. The first probe in the truncated probe array would provide a signal which had no interference from the remaining probes located downstream. The other probes in this array would provide signals which could be potentially contaminated with the vortices shed from the remaining upstream probes. The signals from the probes in the progressively truncated probe array were recorded, and the statistical and spectral characteristics of probes potentially affected by upstream vortex generation were compared against those with no upstream probes.

Figure 4-2 presents the probability density functions calculated for the wave probe signals with and without potential interference in flow condition 5. The solid lines presented in these two graphs correspond to the best fit for the Gaussian probability density function,

$$p(\eta) = \frac{1}{\sigma\sqrt{2\pi}} e^{\frac{\eta^2}{2\sigma^2}}, \qquad (4\text{-}1)$$

where η is the water surface elevation.

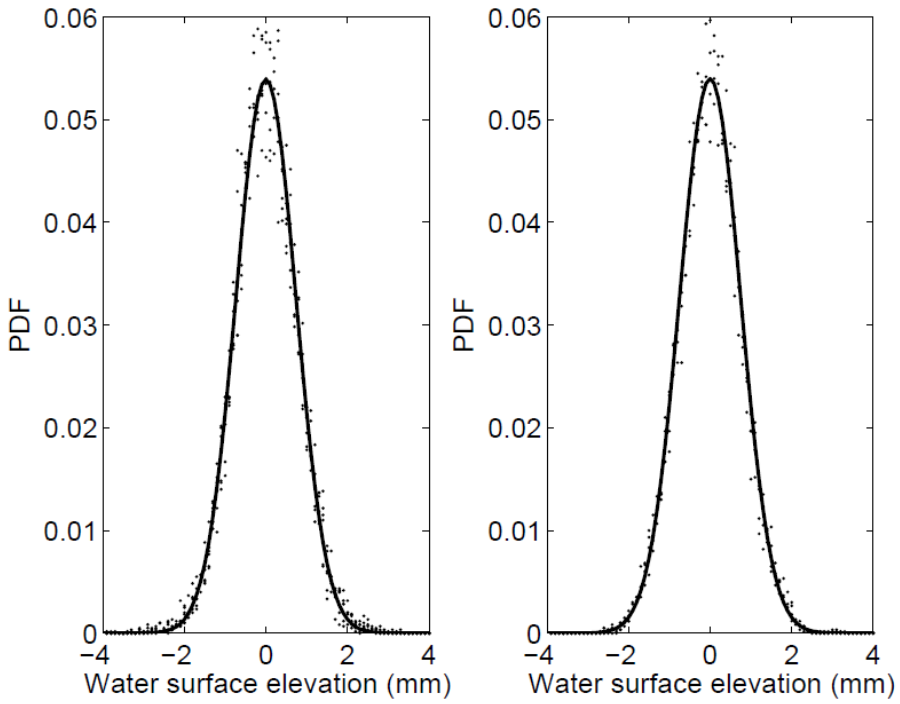

Figure 4-2: The probability density function of the water surface elevation for a flow similar to condition 5 (S_0 ≈0.004; D ≈80 mm; V ≈0.64 m/s) with potential probe interference (left) and without (right)

The values of the standard deviation (or RMS water surface elevation) which correspond here to the best fit to the PDF data with and without potential interference are: σ = 0.736 mm and σ = 0.749 mm, respectively. These results show that the presence of upstream wave probes results in little interference. The behaviour of the probability density data for the water surface elevation measured using either a truncated wave probe array or the original, 7-probe array, closely follows the Gaussian distribution, a finding that is consistent with the quasi-Gaussian statistical behaviour of the rough water flow surface reported by Nazarenko et al. (2010). The standard deviation in the fitted Gaussian distribution changes only marginally (within 2%) with the removal of upstream probe(s). The variability in the measured probability density data for the water surface elevation is relatively small,

within the measurement error, and it does not seem to change with the removal of upstream probe(s). Furthermore, any change in the PDF data related to the removal of one or more of the upstream wave probes is smaller than the degree variability between signals recorded on the individual probes.

Figure 4-3 presents the power spectral density, $\tilde{S}(f)$, calculated for the wave probe signals whose probability density functions are discussed in the previous paragraph (see also Figure 4-2). Here $\tilde{S}$ stands for the power spectral density and f stands for the frequency in Hertz. The solid lines in the graphs presented in Figure 4-3 correspond to the lines of best fit based on the power spectra below 10Hz, which were achieved using the function $\tilde{S}(f) = 1/\left(A + B\sqrt{f}\right)$ with the following values of the coefficients A and B: A = -0.0650 and B = 0.00518 for the signal spectra with potential interference from upstream probes; and A = -0.0644 and B = 0.00506 for the signal spectra without probe interference. The obtained spectral data also suggest that the effect of probe interference on the signals recorded by the probe array is small and affects the measured power spectra by less than 2%, within the level of variation observed between individual probes.

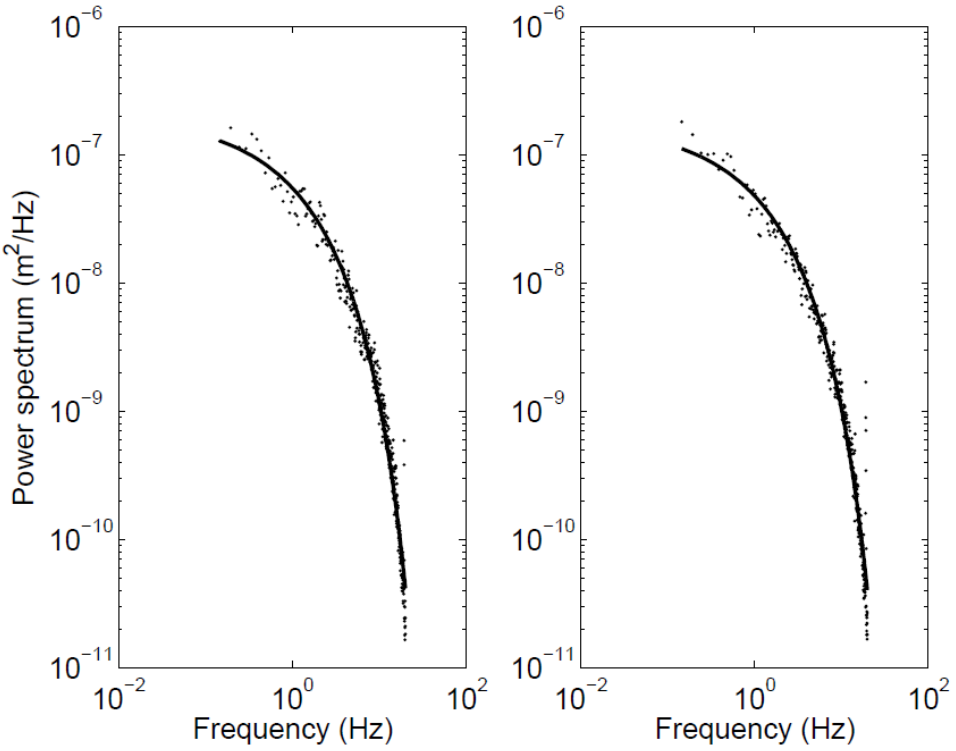

Figure 4-3: The power spectra of the water surface elevation for a flow similar to condition 5 (S_0 ≈0.004; D ≈80 mm; V ≈0.64 m/s)

Further support for the validity of wave probe data is given by the comparison with surface fluctuations measured by the LIF technique as described in section 4.2.

4.2 **LIF data**

The images from the LIF camera are used to determine the position of the free surface from each image by detecting the threshold between the illuminated flow and non-illuminated air for each column of pixels. Figure 4-4 shows the following analysis steps applied to one instantaneous image from flow condition 4: (a) raw image is loaded, (b) image pixels are binarized by setting a threshold illumination value above which a pixel is defined as

fluorescing water, and below which a pixel is defined as non-fluorescing air. The quality of the output data was sensitive to this threshold and so it was determined manually for each flow condition to ensure that the binarized images closely matched the raw images, (c) a 5 x 5 two-dimensional median filter is applied to remove spurious points of brightness within the air phase or points of darkness in the water phase. This replaces each value with the median value of the 5 x 5 grid of logical values surrounding it. Each pixel column is then analysed to determine the pixel location at which the air-water interface is located, i.e. when the logical pixel value changes from zero to unity, (d) a 30 pixel wide median filter is applied to remove small fluctuations associated with noise generated by random variation in light levels at the free surface. This operates in the same manner as the previously described median filter, but with a grid size of 31 x 1. The result is shown on the original image to illustrate the effectiveness of the technique, (e) the calibration (section 3.4.2) is used to convert from pixels into mm, giving a horizontal and vertical resolution of 0.15 mm. 10 mm of the outer edges of the profile were then discarded as they were sometimes prone to error due to receiving a lower illumination than the centre of the image.

This process was applied to each of the 8070 images acquired for each of the 32 flow conditions examined. For each condition this resulted in a time series of surface profile, allowing the examination of surface behaviour over time and space with a high spatial and temporal resolution.

The statistical and spectral properties of the LIF measured free surface fluctuations were compared against that of the wave probes. This would not only provide validation of the data acquired using both systems, but also

(since the two systems operate at different test sections of the flume) prove that the flow is statistically similar at both locations.

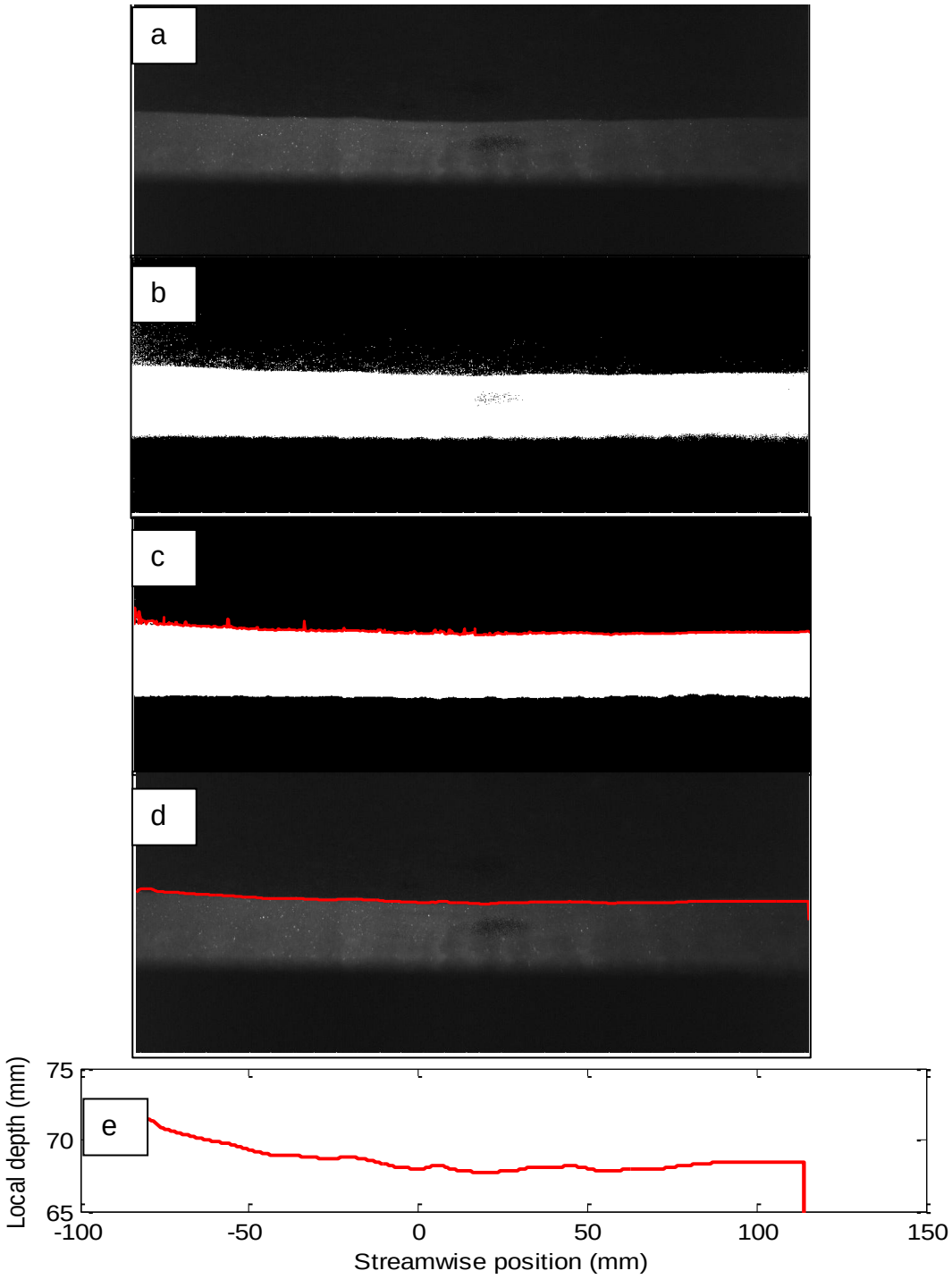

Figure 4-4: Analysis steps to determine instantaneous free surface profile from LIF images

Figure 4-5 shows the frequency spectra of the free surface fluctuations for flow conditions 1 and 6 recorded by both the wave probes and the LIF system. Data is shown up to 13.45 Hz (the Nyquist frequency of the LIF system) to illustrate the effect of the 10 Hz low-pass filter applied to the wave probe data. It can be seen that in general, below 10 Hz, the LIF and wave probe data follow the same pattern and scale in the same manner with flow condition. The LIF data however suggests higher spectral amplitudes, and this is perhaps more pronounced for the higher frequencies, particularly for the slower flow conditions.

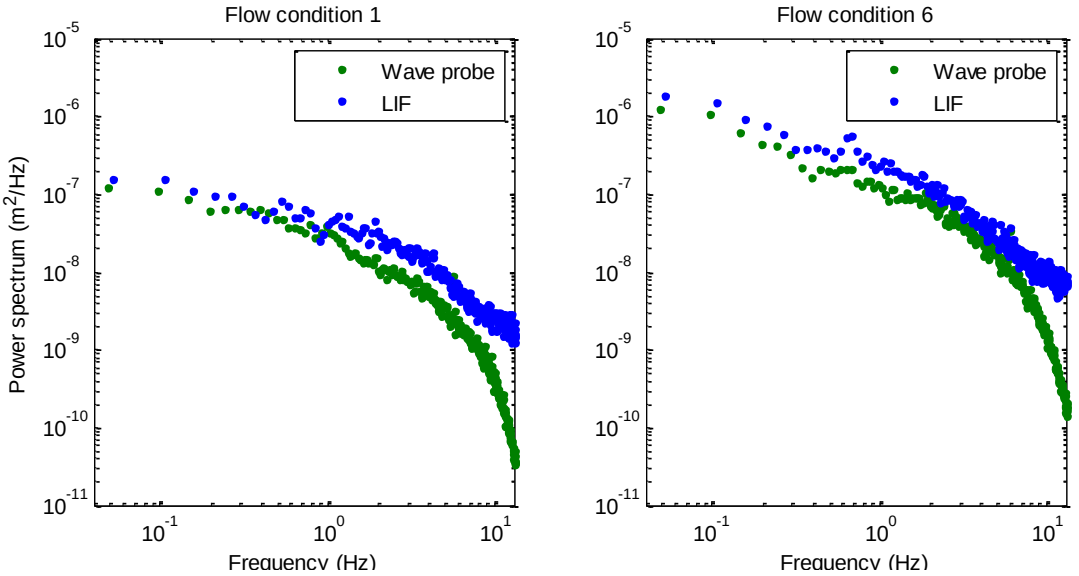

Figure 4-5: Power spectra measured by wave probe and LIF for flow conditions 1 and 6. (S_0 =0.004; D =40, 90 mm respectively; V =0.41, 0.69 m/s respectively)

The roll-off of wave probe spectra at around 10 Hz can be explained by the integral 10 Hz low-pass filter built into the wave monitor units. The generally slightly higher values of the LIF spectra can be explained by the slight

difference in the way that the two systems measure the surface location. The wave probes consist of two wires separated by a distance of 15 mm in the lateral direction. As a free surface feature (a boil for example) moves past the probe, the submergence of the probe wires changes, altering the conductance value. However, this relies on the assumption that the surface feature is two dimensional. This assumption is reasonable for features of a large spatial scale, but as the size of the surface feature decreases, its magnitude can be proportionally under-reported to a larger degree as illustrated in Figure 4-6.

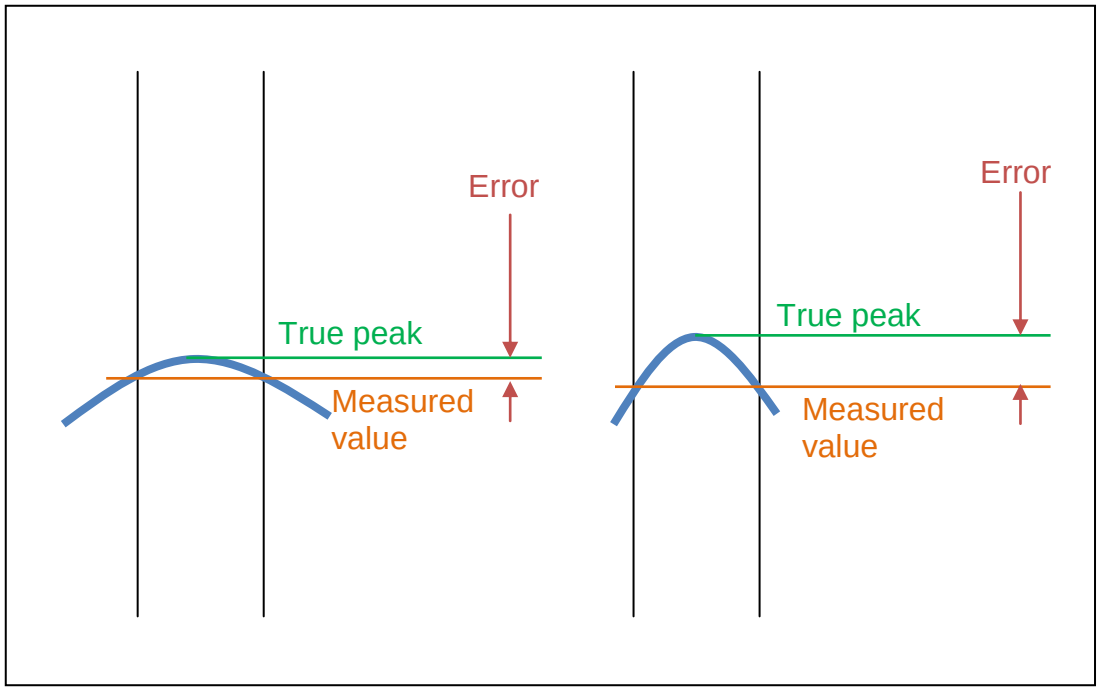

Figure 4-6: Under-reporting of amplitude of high-frequency (small-scale) surface features

Since higher frequency water surface roughness components have a smaller spatial scale in the streamwise direction (as $\lambda \approx V_s / f$), and since the lateral size scales in a similar way to the steamwise length (Roy, et al., 2004;

Komori, et al., 1989; Shvidchenko & Pender, 2001; Yalin, 1992), it is reasonable that higher frequency surface components are smaller, and hence more affected by the separation of the wave probe wires. In this manner, the wave probes act as a low pass filter, reducing the amplitude of higher frequency information. It is worth noting however that even in the LIF measurements, the higher frequencies (> 5 Hz) are at least an order of magnitude smaller than the maximum amplitude, and as such do not significantly affect the recorded time series or the subsequent analyses.

The LIF measurement obtains the maximum elevation of the free surface within a 4 mm thick light sheet. This is much closer to acting as a point measurement, effectively showing the peak elevation within the sheet, and so almost the full extent of the fluctuations are detected for all frequencies.

The probability density functions of the LIF and wave probe recorded free surface fluctuations are given in Figure 4-7 for regimes 1 and 6. The PDF curves can be seen to be very similar between the two measurement techniques. However, in agreement with the spectral analysis, the LIF method seems to be more effective in the case of the extremities of the free surface movement. This causes a slight broadening of the curve for all flow conditions and a reduction in the PDF peak, resulting in some difference in standard deviation, which is within the error shown between independent wave probes in Figure 4-2.

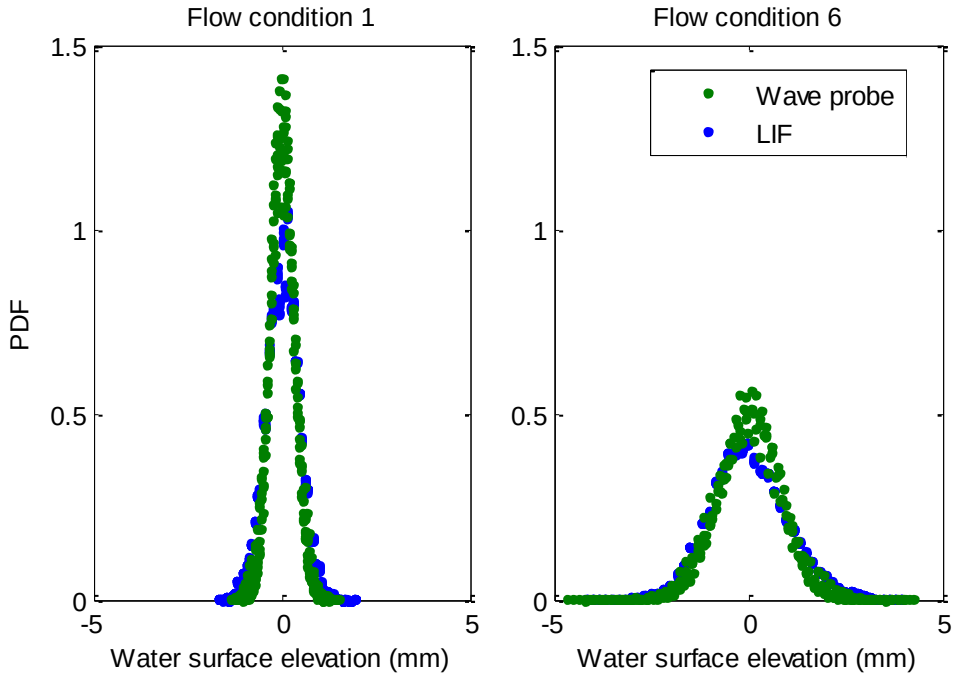

Figure 4-7: PDF measured by wave probe and LIF for flow conditions 1 and 6 (S_0 =0.004; D =40, 90 mm respectively; V =0.41, 0.69 m/s respectively)

Overall the data show strong agreement between the two independent measurement techniques, not only confirming the validity of both sets of data, but also that the free surface behaviour is largely homogeneous along the flume. Although these data suggest that the wave probes may slightly under-report the extent of free surface fluctuations, particularly at higher frequencies (> 5Hz), the difference does not affect the comparison between measurements of the same type (i.e. between two or more wave probes), and therefore does not affect the type of analysis performed in this study.

4.3 **PIV data**

Each image pair from the two PIV cameras was divided into interrogation areas of 32 x 32 pixels (with 50% overlap). This interrogation area size corresponds to a physical area of around 4.9 x 4.9 mm, with the overlap meaning the spatial resolution of the measurements is around 2.5 mm in both the streamwise and vertical directions. These settings ensured that there was sufficient particle density within each interrogation area to allow accurate estimation of local velocity, and meant that for the lowest flow depth (40 mm) there would be at least ten measurement points throughout the depth. The physical size of the interrogation area does mean that any vortical structures smaller than 4.9 mm would effectively be filtered out, but in this study the vortices of interest are the large depth-scale structures which are expected to dominate. The mean flow vector for each interrogation area was computed, resulting in a vector field of dimensions 92 x 34 vectors (247 x 89 mm). A two dimensional cross-correlation technique determined the velocity vector for each interrogation area by comparing the image captured in two frames separated by 1 ms, to determine the most likely average motion of the particles (Bastiaans, 2000), as illustrated in Figure 4-8.

Figure 4-8: Cross-correlation of particle images to obtain velocity vector (Nichols, 2008)

An example of the correlation plane for one interrogation area is shown in Figure 4-9. This shows a strong dominant peak along the streamwise axis. This was typical of most interrogation areas for all flow conditions, since the flow is predominantly in the streamwise direction, with some vertical variation. The correlation peak was determined to be valid if it was more than 20% higher than the next most significant peak (Siegel, et al., 2001; Dantec Dynamics, 2002). Interrogation areas with an invalid peak (typically < 2 % of vectors) were identified for reconstruction during the moving average validation (described later in this section).

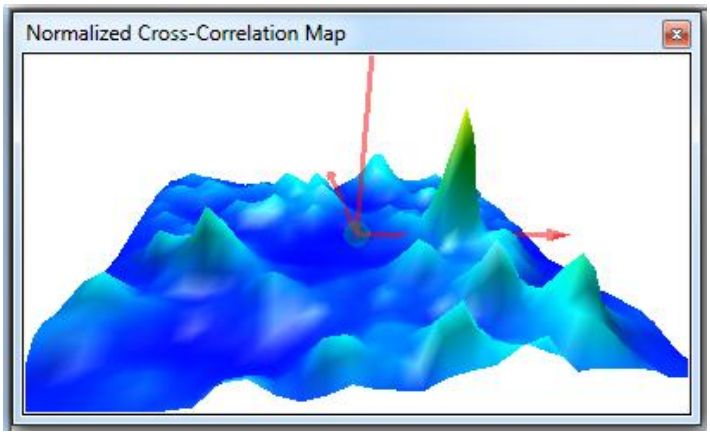

Figure 4-9: Cross-correlation plane for one interrogation area

An image mask was applied in order to avoid erroneous or ambiguous data arising from the static bed or the dynamic surface. Since the bed material and the air above the free surface were not moving, any interrogation area overlapping the upper and lower flow boundaries would give an inaccurate mean velocity value, and this error may propagate into adjacent vectors during the moving average filter (described in the following paragraph). At the

free surface the mask was required to be set at the lowest point reached by the water surface during the full 300 s measurement period. This liberal mask removed approximately 10 mm from the top of the vector field for each flow condition. Future analysis would benefit from an adaptive mask whereby the boundary would be detected and a unique mask created for each individual image. At the bed, the mask was placed just above the highest points of the static bed profile, around 4-5 mm above the mean bed level, such that the centre of the lowest interrogation area was at around 7-8 mm from the mean bed level. Since the measurement duration was 300 seconds (as selected in section 3.7), with a sampling frequency of 26.9 Hz, 8070 vector maps were constructed per flow regime.

The vector maps then underwent range validation and moving average validation in order to correct any spurious data points, with fewer than 5 % of vectors being replaced. The range validation was configured on an individual basis for each flow condition to remove only the large, physically impossible vectors. The moving average validation then swept a 3 x 3 interrogation area window over the vector field to identify vectors which were significantly different from adjacent vectors. Three sweeps were performed. Each time, any vectors which differed by more than 10 % from the mean value of the vectors surrounding it was replaced by the mean value. This also provided a vector for any interrogation areas whose vectors were removed by the correlation peak and range validation stages.

Finally, the vector maps from the two PIV cameras were combined to form the final vector field. An example section of a calculated instantaneous vector field is given in Figure 4-10. In this manner a time series of vector maps was

constructed for each of the flow conditions described in Table 3-4 and Table 3-5. This data was then exported in a numerical format to allow detailed analysis using Matlab.

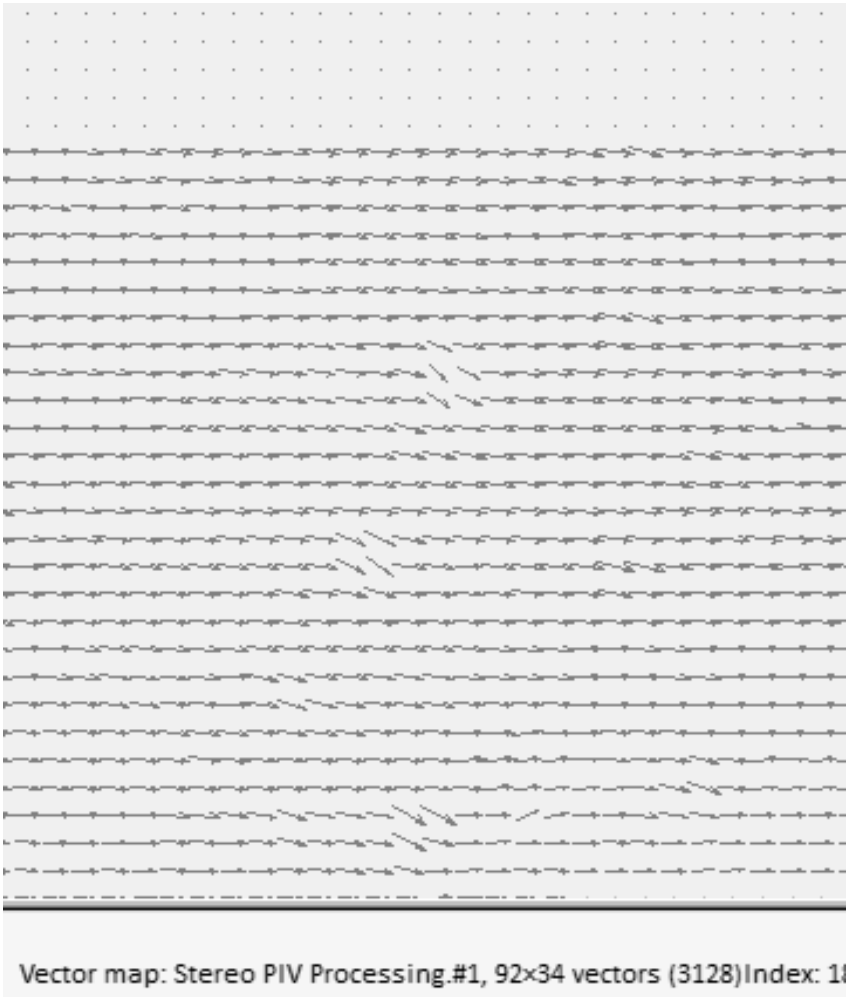

Figure 4-10: Example PIV vector field

As a first assessment of accuracy, the PIV velocity field for each flow condition was used to calculate the time and space averaged profiles of velocity and turbulence intensity (streamwise, vertical and lateral). For flow conditions 1, 4 and 7 the mean velocities are plotted in Figure 4-11 in order to visualise the shape of the profile. To quantify the error in these values, the profiles were first calculated for every vertical column of PIV interrogation

areas (i.e. every spatial location in the streamwise direction). These were then averaged to determine the double (space and time) mean. The standard deviation of the time average at each depthwise position was calculated to give an indication of variability across the measurement frame. This variability was never systematic (mean velocity increasing in upstream or downstream direction for example), but was more random, indicating that this either represents normal measurement error or the true spatial variation. These variations are small, and correspond to the error bars in Figure 4-11. That the error bars are barely visible is testament to the accuracy of the system, and the uniformity of the flow in the PIV section.

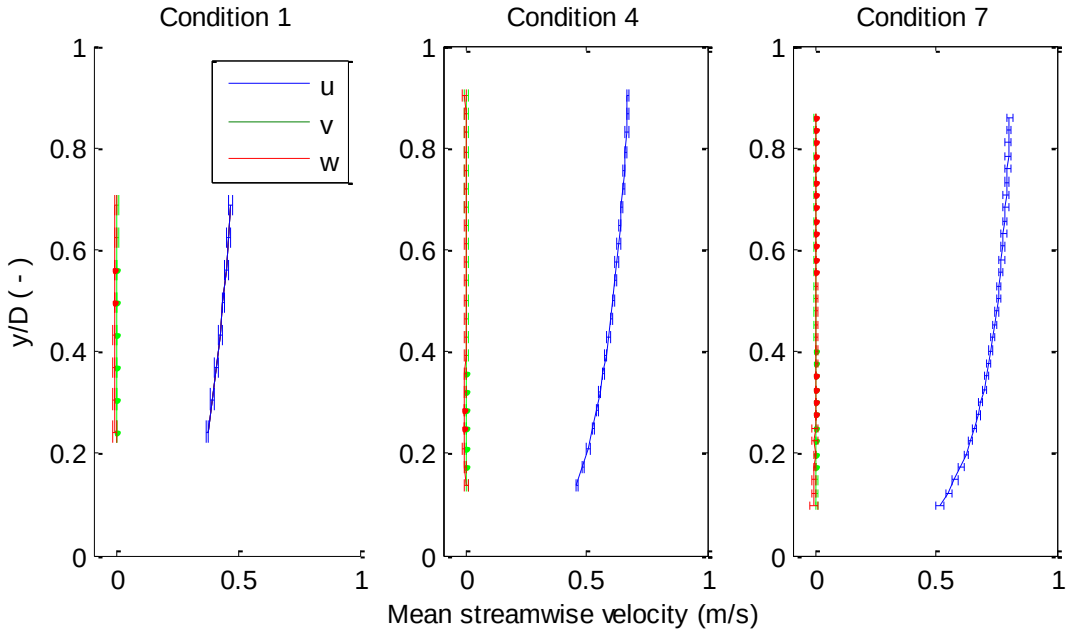

Figure 4-11: Mean velocity profiles (u, v and w) for flow conditions 1, 4 and 7. (S_0 =0.004; D =40, 70, 100 mm respectively; V =0.41, 0.60, 0.74 m/s respectively)

This figure shows the vertical and lateral mean velocities being close to zero, and the streamwise velocity increasing toward the free surface. The streamwise velocity also agrees with the mean velocity measurements of

Table 3-4. Figure 4-12 shows for flow conditions 3 and 5 the normalised mean velocity, U^+, plotted against the normalised depthwise location, y^+, (in blue with error bars defined as before) in accordance with Nezu and Nakagawa (1993), whereby:

$$U^+ = U / U_* \tag{4-2}$$

$$y^+ = yU_* / \nu \tag{4-3}$$

Also plotted (in red) are the expected profiles which match well with the measured data. The expected form is estimated from (Nezu & Nakagawa, 1993):

$$U^+ = \frac{1}{\kappa}\ln\left(\frac{y}{k_s}\right) + Ar\,, \tag{4-4}$$

where $\kappa = 0.41$ and $Ar = 8.5$. Here k_s is taken to be equal to $D_{50} = 4.4mm$.

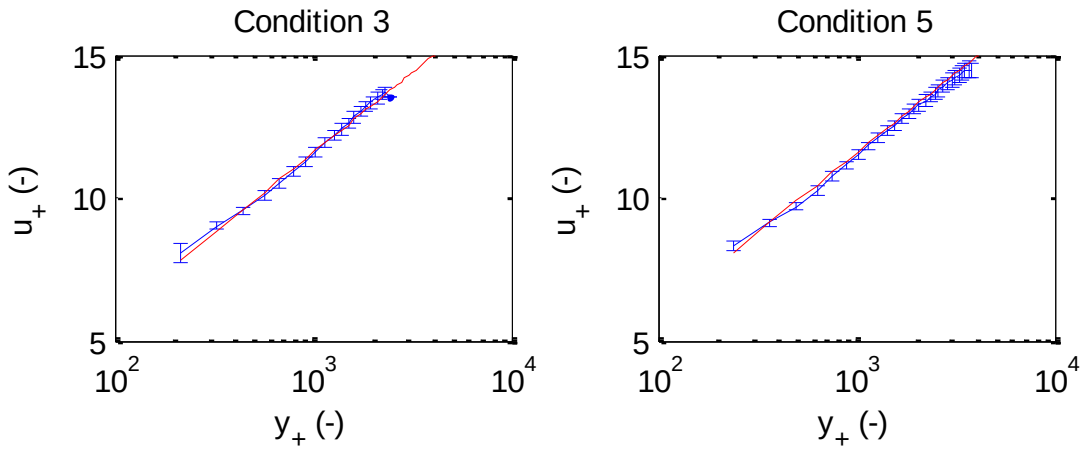

Figure 4-12: Normalised streamwise velocity profiles for flow conditions 3 and 5. (S_0 =0.004; D =60, 80 mm respectively; V =0.55, 0.64 m/s respectively)

Figure 4-13 shows the turbulence intensity profiles for the streamwise, vertical, and lateral directions for the same three flow conditions as Figure 4-11, normalised by the time and space averaged streamwise velocity profile.

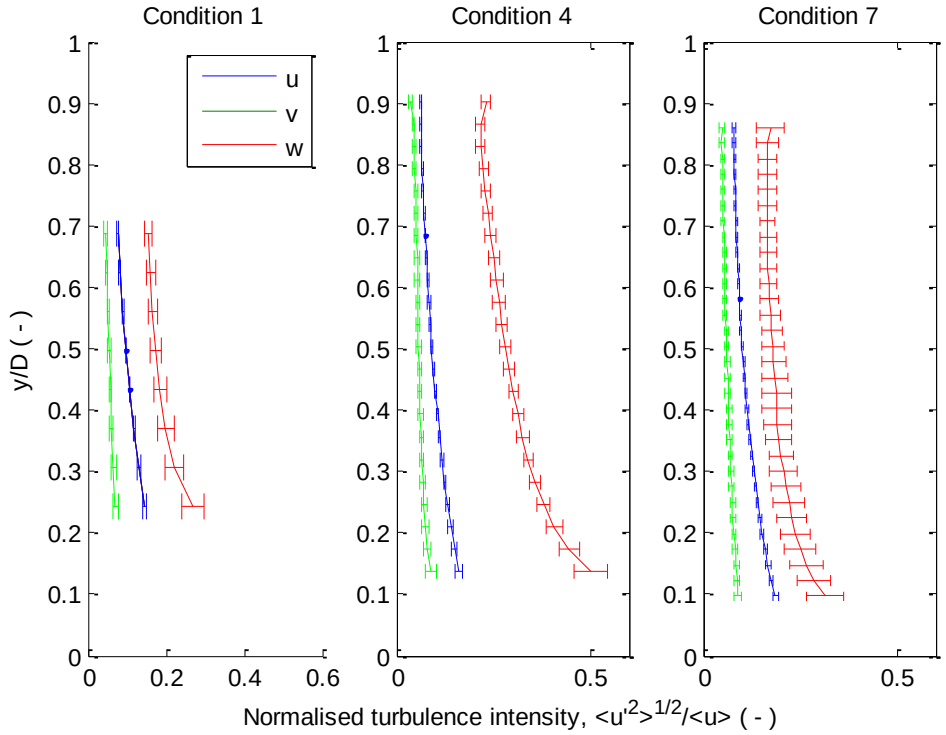

Figure 4-13: Turbulence intensity profiles for flow conditions 1, 4 and 7 (S_0 =0.004; D =40, 70, 100 mm respectively; V =0.41, 0.60, 0.74 m/s respectively). Error bars represent the spatial variability as the standard deviation of the measured profiles from each streamwise location

The profiles all take an expected form (Lawless & Robert, 2001a; Nezu & Nakagawa, 1993), with the turbulence intensity in all three orthogonal directions being strongest toward the bed where the shear caused by the steeper velocity gradient generates circulation and turbulence. The vertical turbulence intensity sensibly takes a value smaller than the streamwise turbulence intensity, but the lateral component appears very large compared

with previous observations, and shows a higher degree of variability. While the mean lateral velocity is around zero as expected, the instantaneous lateral velocity values would require further validation if they were to be relied upon. This is examined in closer detail by comparison with expected turbulence profiles defined as (Nezu & Nakagawa, 1993):

$$u_{rms+} = u'/U_* = 2.30e^{(-y/D)}, \tag{4-5}$$

$$v_{rms+} = v'/U_* = 1.27e^{(-y/D)}, \tag{4-6}$$

$$w_{rms+} = w'/U_* = 1.63e^{(-y/D)}, \tag{4-7}$$

The turbulence profiles for the three orthogonal directions are given in Figure 4-14 for flow conditions 3 and 5. The streamwise turbulence intensity (u'/U_*) shows similar values and a similar gradient to the expected form. The slightly lower values can be explained by the fact that each PIV vector represents the average over a finite area, meaning that fluctuations with a smaller spatial scale than the interrogation area are filtered out so they do not contribute to the overall measured turbulence intensity. The vertical turbulence intensity (v'/U_*) shows sensible overall magnitudes, and in general a sensible gradient. The curve does differ slightly from the expected form (though the expected curve is largely within the error bars of the measured curve), and this is perhaps due to some secondary currents in the flume which aren't accounted for in the theoretical expressions. The lateral velocity fluctuations (w'/U_*) however show very high magnitudes (around twice that predicted by Equation 4-7), and the magnitude of the error bars is also much greater than that of the streamwise or vertical turbulence intensities.

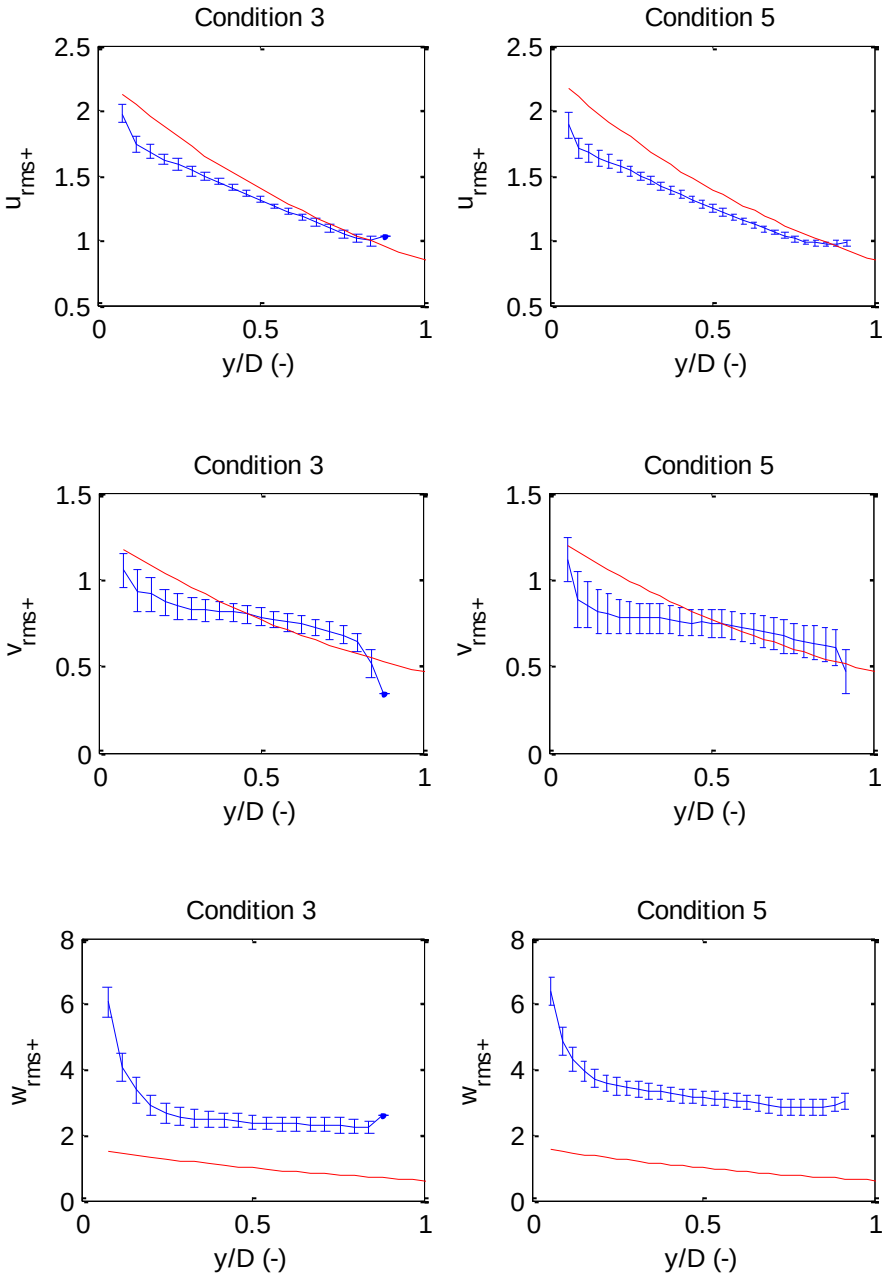

Figure 4-14: Turbulence intensity profiles for flow conditions 3 and 5 (S_0 =0.004; D =60, 80 mm respectively; V =0.55, 0.64 m/s respectively). Error bars represent the spatial variability as the standard deviation of the measured profiles from each streamwise location. Red line indicates expected form from Nezu and Nakagawa (1993)

High lateral turbulence is most likely detected due to poor accuracy in the lateral direction caused by (due to equipment limitations) the angle between

the two PIV cameras (30°) being too small. It has been suggested that in this type of experimental arrangement the ideal angular separation between cameras is 90° (Martínez-Suástegui, 2012). The angle used means that any slight velocity error in the laser plane for a given camera is increased in significance when considering the through-plane component, and also combines with the error from the other camera. This is consistent with the wider distribution in the lateral component. For this reason only the streamwise and vertical velocity components are used further in this work, since these provide sufficient information to address the thesis hypotheses.

Support for the validity of the PIV data was obtained by comparison against a large eddy simulation (LES). A model developed by Xie et al. (2013) was supplied with the LDS scan of the gravel bed (section 3.1.3), and the inlet conditions measured by the PIV system, and was allowed to run until convergence was reached. Details of the model can be found in (Xie, et al., 2013), where the model was used to estimate the flow conditions in a compound channel and it was found that the model's calculations of double averaged velocity matched experimental data to within 4%, while the turbulence intensities, and Reynolds stresses were described as being in "relatively close agreement" with experimental data, though exact errors were not quantified. The comparison between the model results and the PIV measurements of the current study are shown in Figure 4-15 and Figure 4-16 for flow conditions 1 and 7. The quantities shown are (from left to right), double averaged velocity, $\langle U \rangle / U_b$ (normalised by bulk velocity), streamwise turbulence intensity $\langle u' \rangle / U_b = std\left(U - \langle U \rangle\right) / U_b$ (normalised by bulk velocity),

vertical turbulence intensity, $\langle v' \rangle / U_b = std\left(V - \langle V \rangle\right) / U_b$ (normalised by bulk velocity), and Reynolds stress, $\langle -u'v' \rangle / U_b^2$ (normalised by bulk velocity squared). Here the bulk velocity of the LES model, $U_{b(LES)}$, was calculated as the mean velocity from the full cross-section of the flow, including flow through the upper layer of the bed (above the minimum elevation measured by LDS) and at the flume walls. Since the PIV data did not fully extend to the free surface, or into the bed material, and was only in a central plane rather than the full cross-section, the experimental bulk velocity was estimated as:

$$U_{b(PIV)} = U_{m(PIV)} \times \frac{U_{b(LES)}}{U_{m(LES)}}, \tag{4-8}$$

where $U_{m(PIV)}$ is the mean velocity calculated from the available PIV data, and $U_{m(LES)}$ is the mean velocity calculated from the LES data over the same range of the central profile for which PIV data was available. The double averaged velocity profiles are in strong agreement, within the potential 4% error of the LES model. The turbulence intensities are in strong agreement in the central area of the flow depth, and in reasonable agreement near the bed and the free surface. The Reynolds stress profiles are in reasonable agreement but with more persistent deviation. This is likely to be due to any errors becoming more pronounced for moments of this order. The errors can simply be due to the estimation of the bulk velocity for PIV measurements. It can be said that once again the model shows a similar level of agreement as it did with other experimental data (Xie, et al., 2013), suggesting that the measured PIV data are accurate to within the error margins of the model. While numerical models are usually not appropriate for validation of

experimental data, it is unlikely that both modelled and measured data would be incorrect and still in agreement.

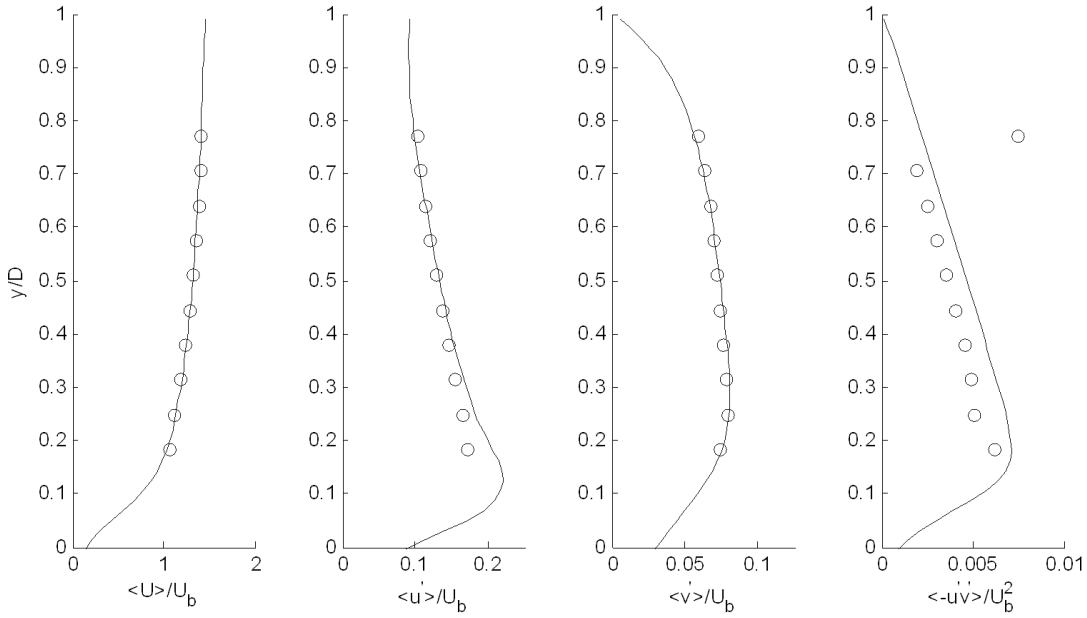

Figure 4-15: Comparison between first, second and third order moments on PIV (markers) and LES (solid lines) data for flow condition 1 (D = 40 mm, S_0 = 0.004, V = 0.41 m/s)

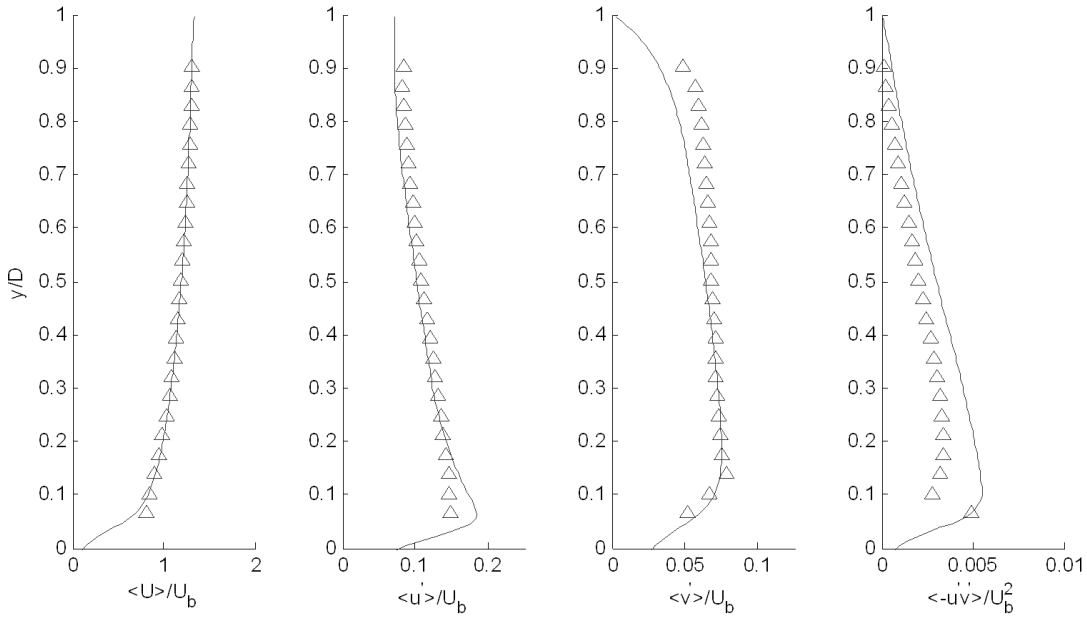

Figure 4-16: Comparison between first, second and third order moments on PIV (markers) and LES (solid lines) data for flow condition 7 (D = 100 mm, S_0 = 0.004, V = 0.74 m/s)

4.4 **Acoustic data**

The microphone was regularly calibrated using a B&K Type 4231 Sound Calibrator which determines the sensitivity to a 94 dB signal at 1 kHz. The measured sensitivity was then input into the Nexus microphone amplifier in order to adjust the voltage output accordingly. The sensitivity was found to be stable over the entire duration of this study. The microphone signal was also regularly tested at 43 kHz by recording the mean signal level at specular reflection using the acoustic setup in Figure 3-20, with the signal reflected from a still water surface. It was found that the relative sensitivity in this arrangement was also stable over the duration of the study.

Two important parameters were obtained from the acoustic data: amplitude, and phase. A mean measurement of each of these properties was calculated from each packet of data, resulting in phase and amplitude time series effectively recorded at 100 Hz (the packet triggering frequency).

The mean amplitude of the envelope of a sine wave is given by:

$$A = \sqrt{\frac{2}{N}\sum a_n^2}\,, \tag{4-9}$$

where N is the number of samples in the series, and a_n is the vector of instantaneous signal amplitude. Figure 4-17 shows one such acoustic packet, with the mean amplitude marked, along with a full time series of acoustic packets, marking the envelope of mean amplitudes taken from each packet.

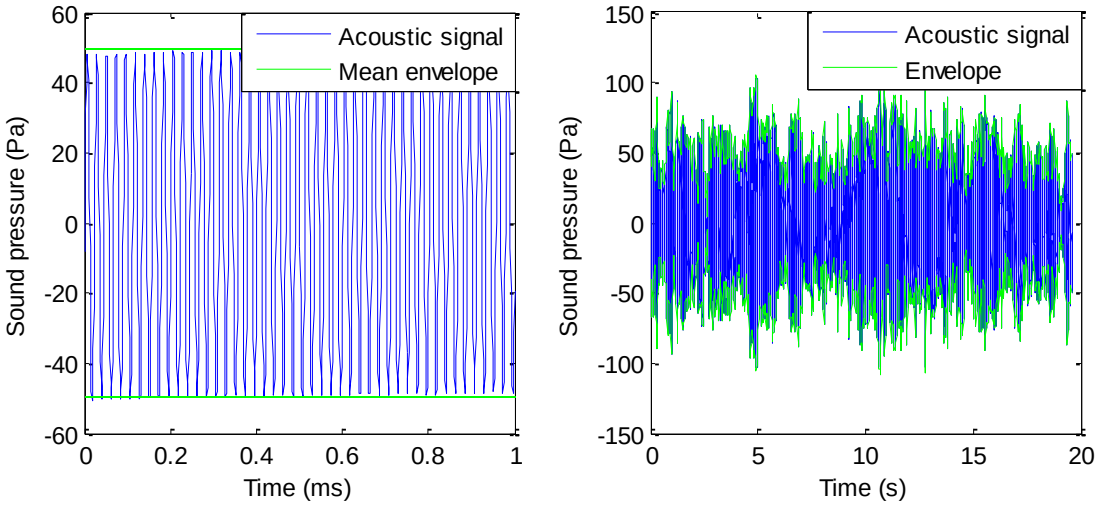

Figure 4-17: Amplitude measurement from a packet of acoustic data, and the envelope of a 20s segment of the full time series

A relatively straightforward method to determine the phase is to use a well-known relation from analytic signal theory (Hilbert transform) to determine the difference in phase between the transmitted signal and the received signal, i.e.:

$$\frac{v_r(t)}{v_s(t)} = \frac{A_r(t)}{A_0} e^{i(\varphi_s + \Delta\varphi(t))}, \tag{4-10}$$

from which

$$\varphi_s + \Delta\varphi(t) = \mathrm{Im}\left\{\log\left(\frac{v_r(t)}{v_s(t)}\right)\right\}, \tag{4-11}$$

In Equation 4-11 the time dependent term $\Delta\varphi(t)$ is of practical interest. The constant phase term, φ_s, can be determined either as the phase of the

reflected acoustic wave at time $t = 0$ or in the case of the fluctuating water level as the mean phase difference, i.e. $\varphi_s = \overline{\varphi_s + \Delta\varphi(t)}$.

Each acoustic packet was analysed according to Equation 4-10, an example of which is shown in Figure 4-18 showing (a) a section of the time series for the transmitted and received signals, and (b) the phase difference within the packet, determined by Equation 4-11. 25 % of the phase data is discarded from both the start and end of the recorded packet as it represents the edge effects of the Hilbert transform as can be seen. The central 50 % is then averaged so that the mean time-dependent phase difference is calculated for the given packet. In the example shown in Figure 4-18, the time difference observed between the two signals is $t_d \approx 6.5\mu s$. The phase difference is hence expected to be equal to $\varphi_s + \Delta\varphi = 2\pi f t_d = 1.752 rad$, and as Figure 4-18b shows, the Hilbert analysis detects this phase difference correctly. The maximum error in the phase measurement is estimated from the variation within the central 50 % of the packet, which in this case is equal to approximately ± 0.012 rad. This is typical of all the acoustic packets acquired.

The phase time series obtained from the analysis of all packets was then unwrapped in order to correct for the phase switching between $+\pi$ and $-\pi$ when the change in source-receiver path-length exceeded one acoustic wavelength ($\Delta L > \lambda \approx 7.9$ mm). This resulted in a time series of phase fluctuations.

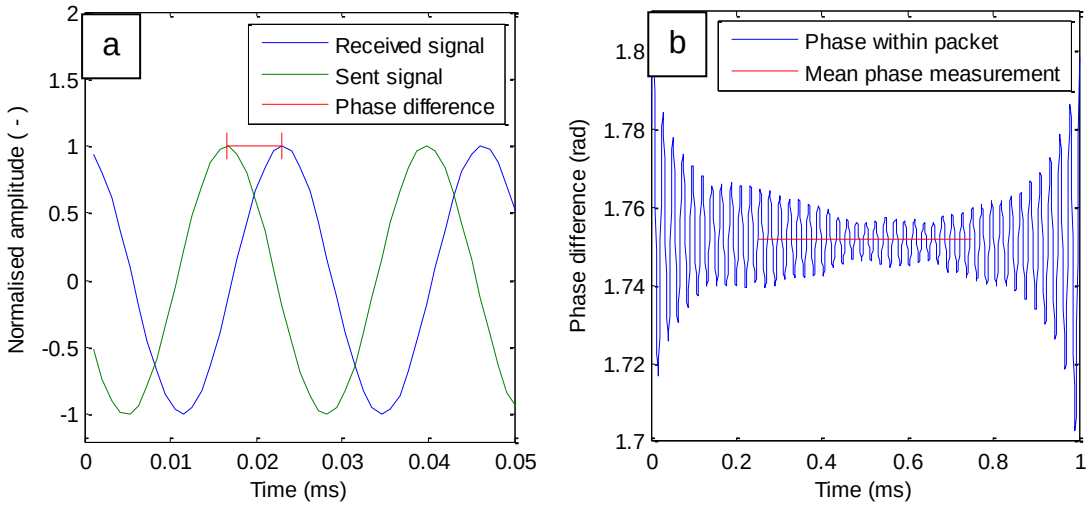

Figure 4-18: Detection of phase difference between acoustic signals

4.5 **Pre-processing and validation conclusions**

The processing, comparison and discussion shown in this chapter has developed the raw data into a form which can be used to examine the relationships between the bed topography, turbulence field, free surface pattern, and acoustic response. Statistical moments of the sub-surface velocity measured by PIV have shown good spatial homogeneity and have been validated against existing theory and an independent LES model. Free surface fluctuation data from LIF and wave probe systems have been validated against each other, and the wave probe system has been carefully calibrated and checked to ensure that there is no interaction, electrical or mechanical, between nearby probes. The acoustic components have been regularly calibrated and a reliable method was devised to obtain the time series of amplitude and phase from the receiver.

Careful analysis of these data will enable a reliable assessment of the thesis hypotheses.

Chapter 5 – Results & Discussion

In this chapter the set of laboratory data described in chapters 3 and 4 is examined to address the thesis hypotheses. The spatiotemporal behaviour of the free surface is first analysed using data from the array of wave probes, and relationships are drawn between the surface behaviour and the bulk flow properties. The reasons behind these relationships are then highlighted through an investigation of the physical linkage between the free surface and the underlying velocity field through the use of space-time matrices and U-level conditional sampling analysis of the collected velocity data. With the influence of the flow on the free surface established, the influence of the free surface on the flow is considered and quantified, and a model is derived to explain fully the dynamic nature of the free surface roughness. Finally an acoustic technique is developed for accurate measurement of the free surface fluctuations, and this data is used to propose a system to measure the bulk hydraulic conditions of the flow based on the recorded acoustic response of the free surface.

5.1 **Characterisation of the free surface features**

The free surface pattern of turbulent flows can be decomposed into three categories: standing waves, travelling waves, and turbulence induced water surface roughness. It is important to determine the dominant mechanism that occurs in shallow flows in order to prove the hypothesis that the free surface is organised and measurable.

Standing waves are temporally persistent features which do not translate in space. These are features which would be apparent if the surface profile were averaged over time. An example of temporally persistent standing waves was generated in the laboratory flume by introducing a singular bedform in the form of a small two-dimensional mound of bed material across the flume. The resulting wave pattern (Figure 5-1), generated in various flow conditions, was seen to persist a relatively long distance along the flume (around 30 water depths). Since these types of surface feature can persist so far downstream, the inlet conditions and bed surface were controlled to minimise any standing wave patterns in order to concentrate on the surface representation of, and response to, the turbulent flow. Also, since the measurement sections were always more than 30 water depths from the inlet end, any standing waves induced by the inlet were negligible at the measurement sections. Furthermore, though standing waves may be present in most real flows, these are temporally static, rather than the dynamic roughness generated by flow turbulence (and any response to it), so the static and dynamic components may be separated. In this work the dynamic surface roughness is the focus.

Figure 5-1: Standing waves induced in the flume. This was conducted temporarily to illustrate the standing wave phenomenon, and was not present during the experimental program

Gravity waves and capillary-gravity waves are travelling waves which propagate according to the restorative effects of gravity (which is usually the dominant factor) and surface tension (or capillary action, usually when water surface gradients are low so that surface tension effects are comparable to gravitational effects). These waves are the type generated by dropping a stone into a still pond (Figure 5-2). Some authors argue that in shallow flow these types of wave propagate away from surface disturbances caused by turbulent interaction with the air-water interface, and then dominate the dynamic nature of the free surface roughness (Savelsberg & van de Water, 2009).

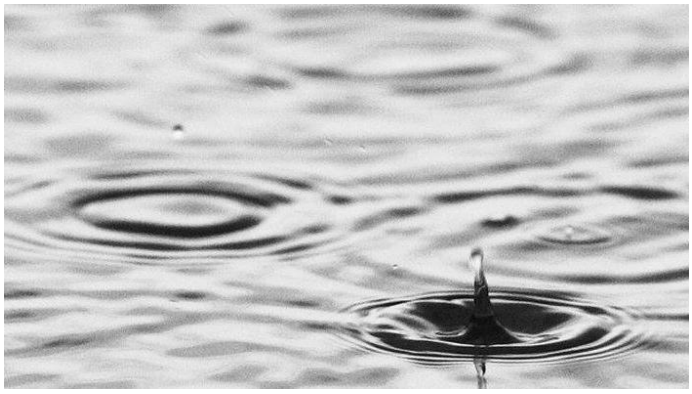

Figure 5-2: Travelling waves produced on a pond surface, propagating outward from disturbances (Frank, 2012)

Turbulence induced roughness is the component of the free surface pattern produced by nearby turbulent flow features (see Figure 5-3), as these features create persistent boils or dimples (Kumar, et al., 1998; Fujita, et al., 2011). Some authors and models suggest that these turbulent free surface

features are greater in magnitude than any resulting travelling waves (Guo & Shen, 2010; Ward, 2003).

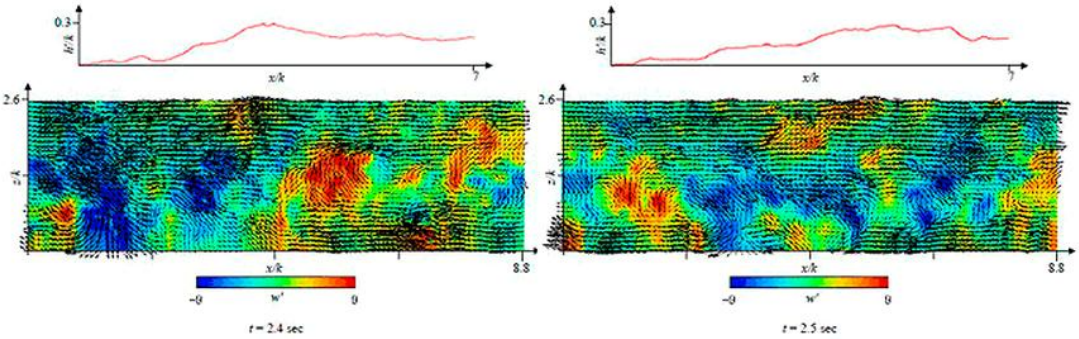

Figure 5-3: Surface roughness features shown to have some relation with the flow field beneath (Fujita, et al., 2011). x/k are aligned in the top and bottom plots. Red line indicates surface elevation, whereby high instantaneous elevation approximately correlates with high instantaneous vertical velocity below (yellow/red areas near the surface) reported by Fujita et al. (2011) to correspond to vortical structures

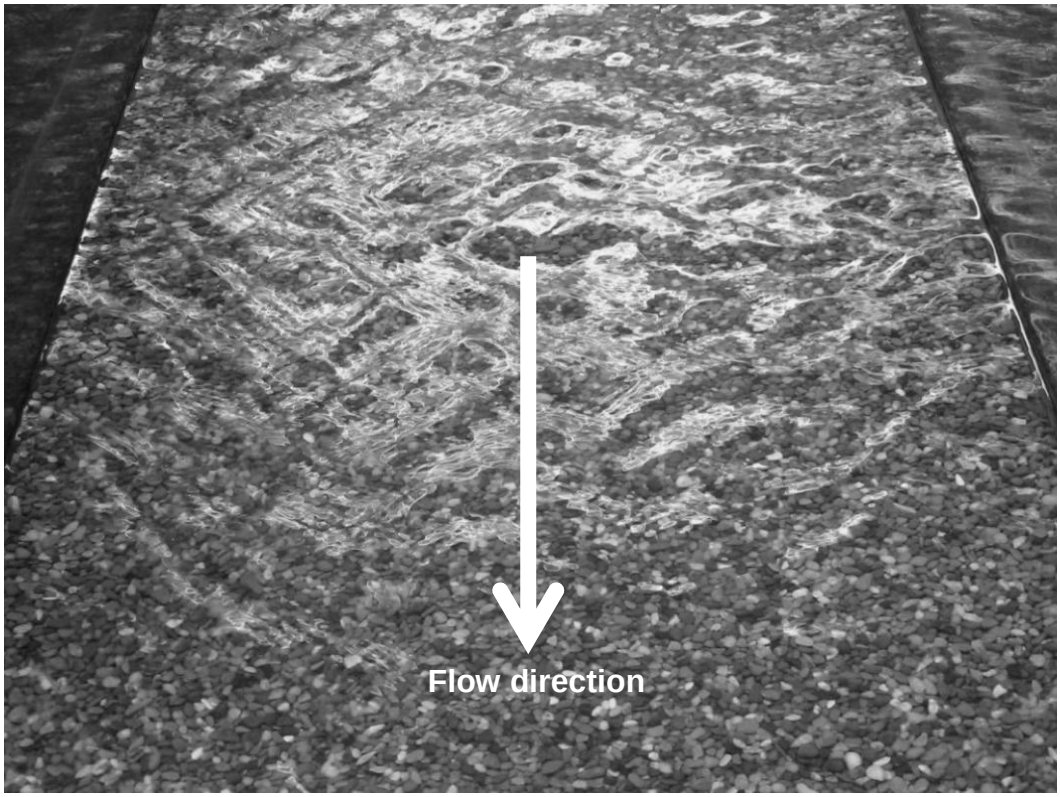

Figure 5-4: A photograph of the flow surface for flow condition 1 (D =40mm, V =0.41m/s)

Figure 5-4 presents a photograph of the water surface roughness pattern which corresponds to flow condition 1 (see Table 3-4). This image of the surface roughness pattern is representative of the hydraulic conditions studied in this work. While Savelsberg and van de Water (2009) suggest that surface roughness induced by active- or static-grid generated turbulence is dominated by propagating gravity waves, the author believes that the surface roughness patterns observed in the present study are strongly driven by turbulence generated at the bed and not significantly influenced by gravity waves. Initial visual observation of the free surface behaviour indicated no significant standing waves and no significant motion of surface features other than in the streamwise direction at approximately the surface flow velocity. This supports the findings of Guo and Shen (2010), who suggested that propagating gravity waves only account for 2.2 % to 12.1 % of the potential energy of the free surface, the rest being due to turbulence induced surface roughness. The following experimental work was carried out to justify this belief: (i) gravity waves were generated in the absence of flow for a range of depths and their dispersion characteristics were measured; (ii) gravity waves were generated in the presence of uniform, steady flow for the same range of depths and their dispersion characteristics were measured; (iii) the obtained dispersion characteristics for the gravity waves were compared against the dispersion characteristics of the observed turbulence generated water surface pattern. Gravity waves were generated in each case by impacting the free surface with a 50 mm square bar which had the same length as the flume width. This bar was applied perpendicular to the flow direction and parallel with the flow surface. In each case the bar penetrated the surface by

10 mm and then was quickly withdrawn to minimise interference with the flow and with the resultant gravity wave. These experiments were designed to illustrate that in the presence of flow, the true velocity at which a gravity wave travels in the reference frame should also include the surface flow velocity component. Therefore, the gravity waves should propagate downstream faster than the mean surface flow velocity, whereas the turbulence generated water surface roughness, which is unrelated to the gravity wave phenomenon, should propagate at a different velocity. This velocity is expected to be close to the surface velocity due to the link with underlying turbulent structures which propagate with the flow, as indicated by Roy et al. (2004) and Fujita et al. (2011).

5.1.1 Dispersion relations for gravity and turbulence generated waves

Figure 5-5 shows two graphs with the time histories of the gravity waves recorded on wave probes 4-7 in the absence (top) and presence (middle) of flow. Also shown (bottom) in the same manner is the time series data for surface waves in turbulent flow with no induced gravity wave. The vertical scale in these graphs is the probe position from the downstream end of the probe array in meters. The amplitude of the wave probe signals here is not to scale. The top signal in each of these graphs corresponds to the upstream probe (probe 4 in Figure 3-9) and the graphs illustrate how the surface features propagate downstream from probe 4 to probe 7.

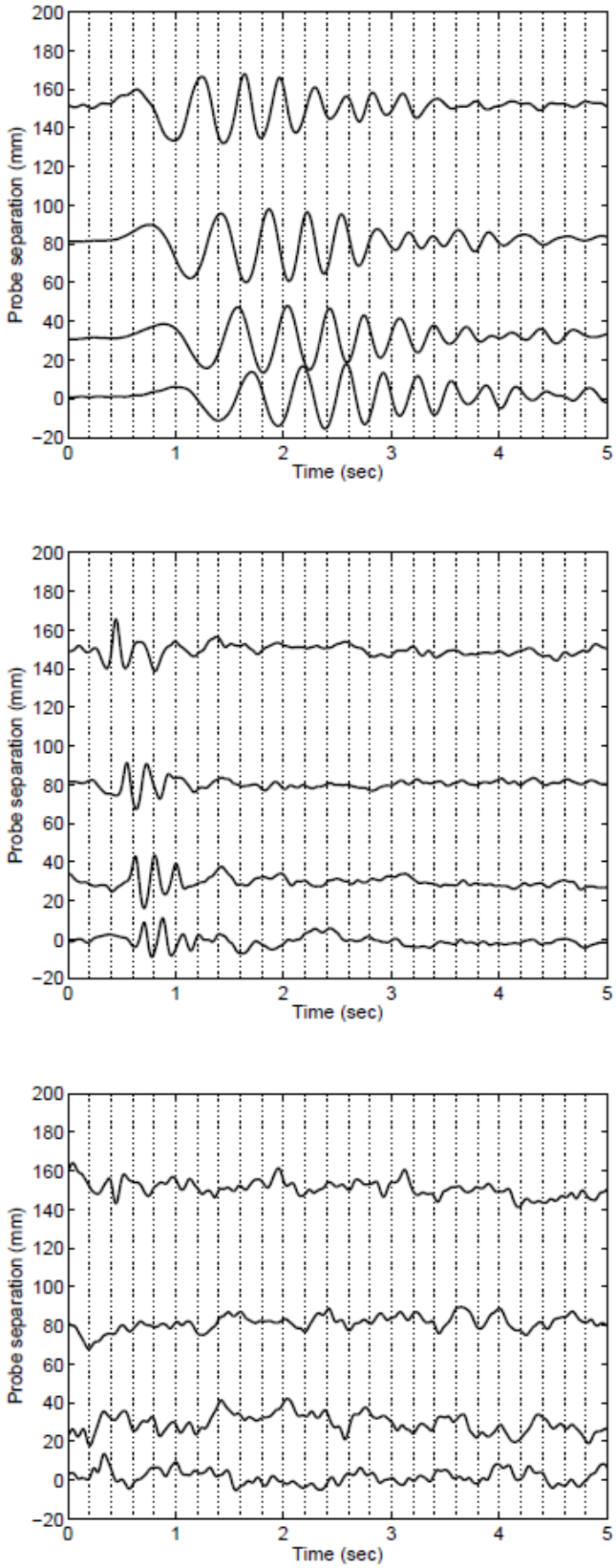

Figure 5-5: Time histories for surface water waves. Top – gravity waves in still water (D = 75 mm); middle – gravity waves in flow (D = 75 mm, V = 0.49 m/s); bottom – flow induced waves (D =75 mm, V = 0.49 m/s)

The water surface elevation data for the gravity waves recorded on the wave probe array can be used to calculate the phase velocity of these waves in order to compare it against that measured in the case of the turbulence-generated water surface roughness. The phase velocity of a wave, c_p, is defined as the ratio of the wave frequency, ω, to its wavenumber, k, i.e. $c_p = \omega / k$. In the case of water surface waves/roughness this velocity can be estimated using two different methods.

The first method can be applied when there is a good degree of coherence between two water surface elevation signals, $\eta_m(t)$ and $\eta_n(t)$, which are recorded simultaneously on two wave probes m and n separated by the distance ρ_{mn}. This can be the case when a gravity wave, which has a reasonably deterministic shape, propagates through a wave probe array. The phase velocity of this wave can be determined from the ratio of the Fourier spectra estimates for $\eta_m(t)$ and $\eta_n(t)$. Provided that the attenuation of the wave between these two points is small, the phase velocity is given by:

$$c_p(\omega) = \frac{\omega \rho_{mn}}{\arg\{\hat{\eta}_n(\omega) / \hat{\eta}_m(\omega)\}}, \qquad (5\text{-}1)$$

where $\hat{\eta}_m(\omega)$ and $\hat{\eta}_n(\omega)$ are the Fourier spectra estimates of the $\eta_m(t)$ and $\eta_n(t)$ signals, respectively.

The second method can be applied when the behaviour of the water surface elevation is more dynamic, i.e. when the pattern evolves over space and

time, as in turbulence generated surface roughness. In this case, the application of the above spectral method for phase velocity estimation can be unsuccessful because the coherence between these two signals can be too low to enable the determination of phase difference, $\arg\{\hat{\eta}_n(\omega)/\hat{\eta}_m(\omega)\}$, with a sufficient degree of accuracy. In these circumstances a bank of narrow band filters with centre frequencies, ω_j, can be adopted. The signals $\eta_m(t)$ and $\eta_n(t)$ can be passed through this filter bank so that pairs of the filtered signals $\eta_m(t,\omega_j)$ and $\eta_n(t,\omega_j)$ can be used to determine the lag $\tau_{mn}(\omega_j)$ at which the temporal cross-correlation function between these signals exhibits an extremum, $\tau_{e_{mn}}(\omega_j)$. The correlation method is described further in section 5.1.2. The phase velocity as a function of frequency can then be estimated from

$$c_p(\omega) = \rho_{mn} / \tau_{e_{mn}} . \qquad (5\text{-}2)$$

The graphs shown in Figure 5-6 present the dispersion curves for the phase velocity of the gravity waves in the presence and absence of flow and the phase velocity of the water surface roughness observed for turbulent flow over the rough gravel boundary. The flow conditions in these experiments were between those selected for conditions 4 and 5 (see Table 3-4). Here the Fourier spectrum analysis method was used to determine the phase velocity of the gravity waves from the ratio of the phase spectra measured with two wave probes separated by a known distance. Correlation analysis was applied to filtered flow data to determine the phase velocity spectrum with

which the turbulence-generated water surface roughness pattern appears to propagate.

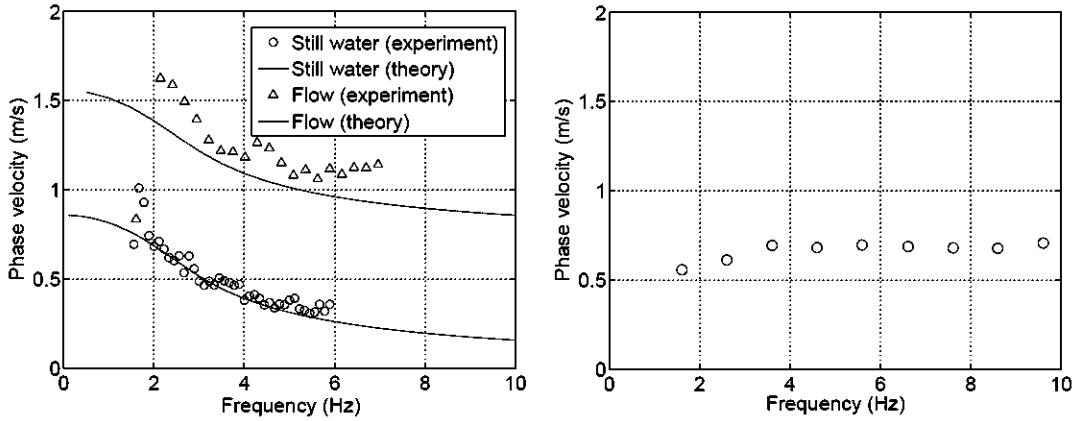

Figure 5-6: Frequency dependence of the phase velocity of (left) gravity waves in the presence and absence of flow and (right) turbulence generated water surface roughness (S_0 =0.004, D =75mm, V =0.49 m/s, V_s =0.70 m/s)

Figure 5-6 illustrates that in the absence of flow (still water) the phase velocity follows closely the theoretical curve which is obtained with the standard gravity wave theory found in Landau and Lifshitz (2011). It is clear that in the presence of flow the velocity of the gravity waves combines with surface flow velocity. The flow surface roughness patterns however propagate at a velocity close to that of the flow surface. Therefore the water surface roughness patterns observed in these shallow turbulent flows are not due to ordinary gravity waves. It can also be seen that the frequency dependence of the velocity at which the turbulence-generated flow structures propagate is markedly different to that measured in the case of the gravity waves (compare Figure 5-6 (left) against Figure 5-6 (right)). The velocity at which this pattern propagates is relatively independent of frequency, and is approximately equal to the flow surface velocity which was measured by the

averaged timing of the transport of a floating tracer over a defined length. This relationship was true for all the flow conditions examined in this study. These findings agree with the observations of Smolentsev and Miraghaie (2005) who observed that the celerity of gravity-capillary waves was different to that of water surface roughness generated by strong turbulence. These findings are also consistent with the particle image velocimetry results reported by Fujita et al. (2011) who suggested that the celerity of the roughness pattern on the free surface is close to that of the surface velocity. These observations clearly suggest a link between the advecting surface features and the underlying turbulent flow structures.

5.1.2 Spatial correlation of turbulence-generated surface roughness

It is believed that, under certain hydraulic conditions, the observed variations in the water surface elevations in a shallow water flow are controlled by the turbulent structures which emanate from the bed where the flow interacts with the sediment boundary. These structures are transported and shaped by the flow and cause the distinct flow pattern which is clearly visible on the free surface (see Figure 5-4). The pattern of the water surface is continuously changing in time and space and it is therefore convenient to study its behaviour in terms of the spatial correlation function which captures the statistical and spectral characteristics of the dynamic water-air interface. The spatial correlation function is also a convenient measure of the coherence and variance in the water surface roughness between two points which are separated in space. The time-dependent signals measured with each probe pair in each of the flow conditions listed in Table 3-4 and Table 3-5 were

cross-correlated to determine the extremum (maximum or minimum, whichever has largest magnitude) amplitude of the temporal correlation function. In this way the spatial correlation function for the water surface elevation about the uniform flow depth was reconstructed for the values of ρ that corresponded to the discrete spatial streamwise lags between pairs of individual probes in the probe array:

$$W(\rho,\Delta\gamma,\tau)=\overline{\eta(x,\gamma,t)\eta(x-\rho,\gamma-\Delta\gamma,t-\tau)}, \tag{5-3}$$

For completeness, this equation also includes a term for the correlation as a function of lateral separation, $\Delta\gamma$, though in this work the data is collected along the flume centreline (i.e. one lateral location) so this term is hence forth neglected. Table 5-1 lists the probe pairs which were used to determine the values of the spatial correlation function, and the distances corresponding to the lag between each individual probe pair, ρ_{mn}.

Table 5-1: Wave probe pairs and spatial lags used to calculate the spatial correlation

Probe pairs (mn)	77	67	56	45	57	34	23	46	12	47	35
Lag, ρ_{mn} (mm)	0	30	50	70	80	90	110	120	130	150	160
Probe pairs (mn)	24	36	13	37	25	26	14	27	15	16	17
Lag, ρ_{mn} (mm)	200	210	240	240	270	320	330	350	400	450	480

In the reported experiments the spatial correlation function was determined in two steps. Step 1 was to use data recorded on the 7-probe array to calculate the normalized temporal cross-correlation function between probes m and n which is estimated from:

$$\sigma^{-2}W_{mn}\left(\rho_{mn,0,\tau}\right)=\frac{1}{T}\int_0^T\eta_m(t)\eta_n(t-\tau)\,dt\,, \tag{5-4}$$

where $\eta_m(t)$ and $\eta_n(t)$ are the time-dependent water surface elevations recorded on probes m and n which are separated by the distance ρ_{mn}, t is the time, T = 300 sec is the measurement period and τ is the time lag. The root mean square (RMS) water surface elevations, σ, are listed in Table 5-2. The value of σ for each given flow condition was determined as the average of the standard deviations for the data recorded on each of the probes in the wave probe array. The variation in the RMS of the water surface elevations from one wave probe to another for a given flow condition was less that 10% which is supported by the probability density function data shown in Figure 4-2. A comparison with the data listed in Table 3-4 and Table 3-5 suggests that the value of σ generally increases with depth averaged flow velocity.

Table 5-2: RMS water surface roughness height measured by wave probe

Gravel bed flow conditions	RMS water surface roughness height, σ (mm)	Sphere bed flow conditions	RMS water surface roughness height, σ (mm)
1	0.34	17	0.23
2	0.40	18	0.29
3	0.45	19	0.45
4	0.57	20	0.56
5	0.74	21	0.65
6	0.86	22	0.67
7	0.97	23	0.84
8	0.36	24	0.25
9	0.43	25	0.48
10	0.50	26	0.64
11	0.58	27	0.85
12	0.67	28	1.09
13	0.23	29	0.41
14	0.36	30	0.56
15	0.43	31	0.76
16	0.11	32	0.07

The temporal, normalized cross-correlation function $W_{mn}(\tau)$ was then presented as a function of distance whereby $x = V_s \tau$, where V_s is the measured surface advection velocity.

Step 2 was to locate the extremum value (either a maximum or minimum at $\tau = \tau_e$) in the temporal cross-correlation function that would correspond to the maximum similarity (positive or negative) in the water surface roughness pattern transported by the water flow from probe m to probe n within the analysis window. The results from these two steps are illustrated in Figure 5-7 which shows the temporal cross-correlation functions between probe pairs 77 (0 mm), 76 (30 mm) and 65 (50 mm) for flow conditions 1, 4 and 7, respectively. A round marker shows the position of the extremum in the temporal correlation data. This corresponds to the instant when two signals recorded on the two probes separated in space are most closely correlated.

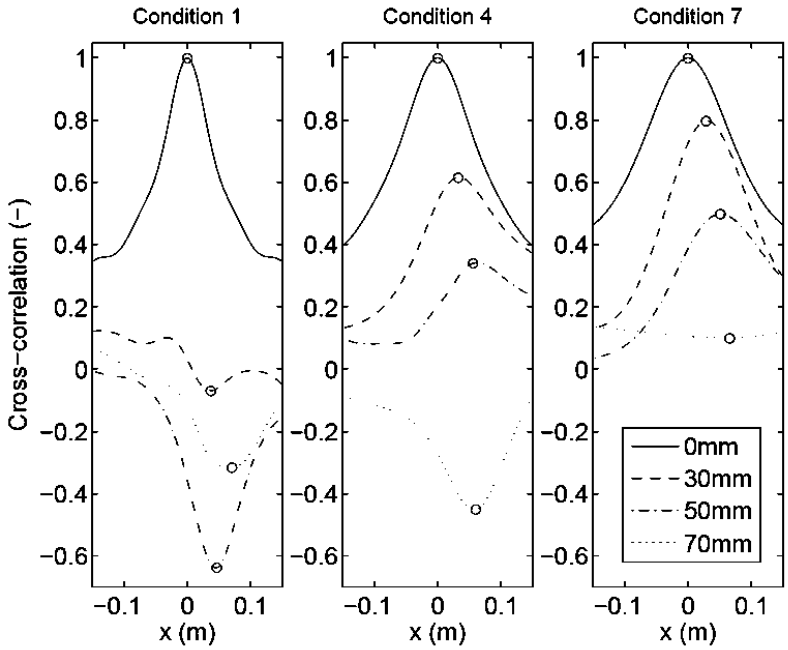

Figure 5-7: The temporal cross-correlation data for flow conditions 1, 4, and 7 (S_0 =0.004, D =40, 70, 100 mm respectively; V =0.41, 0.60, 0.74 m/s respectively)

For some flow conditions and some spatial lags, the position of this extremum was found to be close to the distance by which the two probes are separated. For others, the position of this extremum was shifted. Three sets of wave probe data were collected for each of the flow conditions in Figure 5-7 to quantify the maximum variation in the position of this extremum, which was estimated as 8 % of the expected value. Such a variability can be explained by the experimental variability, the discrete probe arrangement, and by the complex interaction of flow structures of various scales with the water surface. The observed value of the correlation lag is controlled by the timescale of the production of coherent flow structures and by the advecting flow velocity that, in turn, controls how the observed water surface roughness propagates and dissipates. Since the coherent structures transported by the flow are believed to travel at (or close to) the average depth-local flow velocity (Roy, et al., 2004), it seems reasonable that a spatial distribution of time averaged streamwise velocities over a rough boundary (Nikora, et al., 2001) will result in a distribution of the advection velocities for the coherent structures. This explains why the temporal location of the cross-correlation extrema occurs within a distribution about the temporal location for which all structures traveling at the mean surface flow velocity would occur. This level of spatial variability in the streamwise velocity relates well with the variability observed in the temporal position of the extremum value. Figure 5-7 shows that the temporal cross-correlation functions obtained for flow conditions 1 and 4 flip their sign as the spatial lag between the probes increases from 0 to 70 mm. In these two conditions the flow depth is relatively low. As a result,

the scale of the turbulent structures generated in these types of flow is believed to be relatively small, the structures themselves resembling whirls with some spatial scale, temporal period and characteristic lifetime (Hoff, et al., 2006). Because the water surface roughness, which is caused by the propagation of these structures, is quasi-periodic, the correlation function is expected to flip sign. This type of behaviour is typical for a correlation function of a quasi-periodic roughness process. The value of the spatial correlation function for this type of process will be negative when two wave probes in the probe array are separated by a distance of $\frac{1}{4}L_0 < \rho < \frac{3}{4}L_0$, where L_0 is the characteristic spatial period. Clearly, when the depth of the flow is relatively low, then the scale of the turbulent structures is relatively small and the pattern of roughness is relatively fine. For flow condition 1, the probe lags at which the data are plotted in Figure 5-7 are larger than $\frac{1}{4}L_0$, so that the correlation function flips its sign at a certain value of the lag. As the flow depth increases (see Figure 5-7 for condition 4), the scale of the turbulent structures increases proportionally and falls in the range of $50mm < \frac{1}{4}L_0 < 70mm$. In this case, the flow roughness pattern is relatively coarse and the correlation function does not flip its sign until the probe lag becomes greater than 50 mm. Finally, when the flow is sufficiently deep (condition 7), the scale of the turbulent structures is large in comparison with the probe lag, hence the function is positive and the temporal cross-correlation functions do not flip for the probe lags shown in Figure 5-7. The temporal correlation functions were obtained for all 22 wave probe pairs and

for all 32 flow conditions. The experimentally determined values of the spatial correlation function, $W(\rho_{mn},0,\tau)$, for conditions 1, 4 and 7 are presented in Figure 5-8. It can be seen that with greater spatial probe lag the correlation extrema do flip sign even for the deeper flow depths. These figures also present error bars which illustrate the variability in the temporal correlation function extrema obtained using three seperate wave probe recordings for each of these three conditions. The errors presented in these figures were estimated as the maximum difference between the results obtained from the three reproducibility experiments.

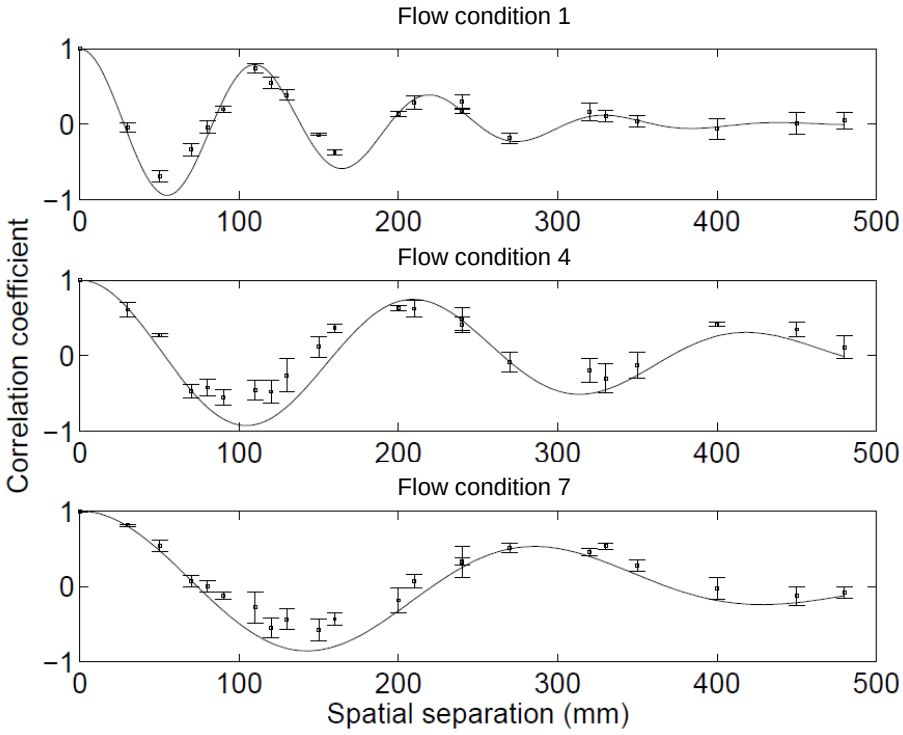

Figure 5-8: The measured and fitted spatial cross-correlation function for the water surface roughness for flow conditions 1, 4 and 7 (S_0 =0.004, D =40, 70, 100 mm respectively; V =0.41, 0.60, 0.74 m/s respectively)

These findings enable the following three conclusions: (i) the water surface roughness pattern has a clear characteristic spatial period; (ii) the amplitude

of the spatial correlation function attenuates progressively as a function of the spatial lag; (iii) the shape of the spatial correlation function can be best approximated with a simple analytical expression which is a combination of a periodic function and an exponentially decaying term, which convey information on the characteristic spatial period of the turbulence-generated water surface roughness and on the correlation radius in the water surface roughness pattern, respectively. A simple analytical expression for the spatial correlation function which combines the properties of an exponentially decaying function and a periodic process can be proposed as:

$$W(\rho) = e^{-\rho^2/\sigma_w^2} \cos(2\pi / L_0 \rho), \tag{5-5}$$

where ρ is the spatial lag. The parameters σ_w and L_0 carry a clear physical sense. The parameter σ_w relates to the spatial radius of correlation. The value of L_0 relates to the characteristic period in the water surface roughness pattern. The choice of a Gaussian correlation function (or squared exponential covariance) is not uncommon. The function is smooth, differentiable and used widely to represent a quasi-stochastic surface roughness (Paciorek, 2003; Bass & Fuks, 1979). Other functions (such as exponential covariance) were tested but did not fit the data as accurately.

It is desirable to estimate the values of σ_w and L_0 which correspond to a particular hydraulic condition. In this work the Nelder-Mead (simplex) bounded optimisation method (Nelder & Mead, 1965) was adopted to find those values of σ_w and L_0 which would provide the best fit to each

experimentally determined spatial correlation function. In this optimisation process the criterion was the minimum of the function:

$$F(X)=\sum_{j=1}^{22}\left|W(\rho_j,X)-W(\rho_j)\right|, \tag{5-6}$$

where $X=\{\sigma_w, L_0\}$ was the design vector. The values of the correlation radius and characteristic spatial period recovered from the optimisation analysis are listed in Table 5-3 for the 32 hydraulic conditions studied. Figure 5-8 illustrates the fit between the mean experimental data for $W(\rho_{mn})$ (markers) and the values of $W(\rho)$ predicted by the approximation in Equation 5-5 (continuous lines) for the values of σ_w and L_0 taken from Table 5-3 for conditions 1, 4 and 7.

Table 5-3: Correlation radius and characteristic spatial period calculated for all flow conditions

Gravel Bed Flow conditions	Correlation radius, σ_w (m)	Spatial period, L_0 (m)	Sphere Bed Flow conditions	Correlation radius, σ_w (m)	Spatial period, L_0 (m)
1	0.16	0.11	17	0.04	0.07
2	0.17	0.15	18	0.11	0.09
3	0.19	0.17	19	0.14	0.12
4	0.25	0.20	20	0.17	0.14
5	0.28	0.24	21	0.23	0.17
6	0.30	0.27	22	0.25	0.20
7	0.30	0.30	23	0.27	0.22
8	0.17	0.12	24	0.10	0.07
9	0.22	0.15	25	0.17	0.11
10	0.23	0.16	26	0.18	0.13
11	0.23	0.19	27	0.25	0.15
12	0.27	0.22	28	0.30	0.18
13	0.16	0.10	29	0.12	0.08
14	0.19	0.13	30	0.16	0.10
15	0.22	0.15	31	0.22	0.13
16	0.13	0.06	32	0.13	0.09

5.1.3 The influence of the bulk hydraulic conditions on the observed free surface roughness characteristics

It was suggested by Brocchini and Peregrine (2001) that if the water surface pattern is not associated with gravity waves then the spatial correlation pattern is related to the underlying turbulence. It is therefore useful to examine the spatial correlation parameters listed in Table 5-3 as a function of the corresponding hydraulic parameters listed in Table 3-4 and Table 3-5 for the 32 experimental flow conditions over both gravel and sphere beds. As previously suggested, for a given bed type and bed slope, the root mean square of the water surface elevation depends almost linearly with the depth averaged velocity and flow depth. This simple relationship is true for both bed types, and indicates that there is likely to be a physical connection between the bulk flow parameters and the water surface pattern. From Table 5-3 it can be seen that the values of the characteristic period and the correlation radius generally increase with depth although this pattern is less clear. Given the range of slope, velocity, depth, and bed-type combinations it is possible to determine generalised non-dimensional relationships between the water surface roughness pattern and the underlying flow. Figure 5-9 shows that the non-dimensional characteristic period demonstrates a strong, consistent non-linear relationship with the ratio of depth averaged flow velocity to shear velocity ($U_* = \sqrt{gR_hS}$). This figure indicates that the spatial characteristic length generally carries information on the shape of the vertical velocity profile and underlying bed roughness for a range of hydraulic conditions. Furthermore, both the gravel and sphere beds seem to give a similar curve. Since the shear velocity and hydraulic roughness coefficient used for non-

dimensionalising each axis are both related to the roughness of the channel bed, the relationship is shown to be independent of bed structure, at least for the two bed types examined in this work. This allows the following general expression to be proposed:

$$L_0 / k_s = 0.045 \times e^{0.54V / U_*} \tag{5-7}$$

This corresponds to the solid line in Figure 5-9, which has a strong coefficient of determination of 0.95. This expression could be a powerful alternative tool for assessing the hydraulic roughness of shallow flows, based on the measured flow velocity, depth, bed slope and free surface spatial period.

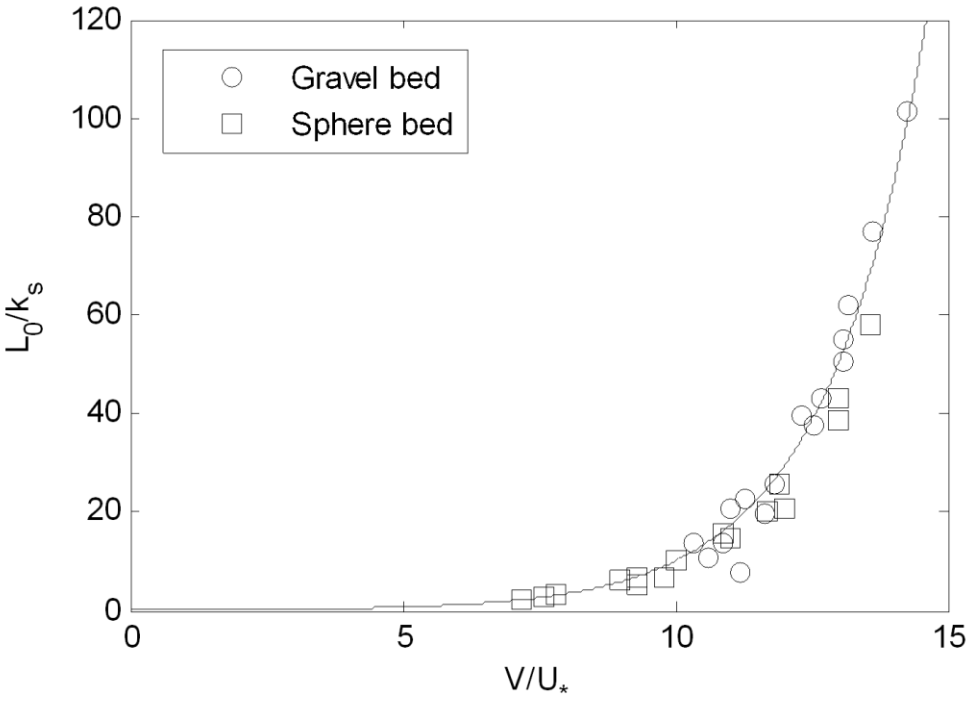

Figure 5-9: The dependence of the normalized characteristic spatial period against a non-dimensional velocity scale

Figure 5-10 shows the correlation radius, which reflects the dissipation of the surface pattern, can be non-dimensionalised with the equivalent hydraulic roughness and shown to be an approximately linear function of the Reynolds number. This carries a clear physical sense that the spatial organisation and decay of the water surface pattern is related to the dissipation of energy by the turbulent flow. The behaviour of both the gravel and sphere beds appears to follow the same trend, indicating that this relationship is independent of physical bed roughness (though obviously includes the hydraulic roughness term). This allows the following expression to be proposed:

$$\sigma_w / k_s = 1.1 \times 10^{-3} VD / \upsilon \tag{5-8}$$

This relationship is less precise than that in Equation 5-7, with a coefficient of determination of 0.85. This may be due to the less accurate estimation of σ_w which could be improved with a spatially longer array. The behaviour near the origin is unclear and deserves further investigation. Nevertheless this relationship may allow approximate estimation of hydraulic roughness in applications where only correlation radius, flow depth and velocity are known.

In order to potentially allow the assessment of hydraulic roughness using only measured free surface data, a new Reynolds number is defined as:

$$\mathrm{Re}_S = V_S L_0 / \nu \, . \tag{5-9}$$

When Figure 5-10 is re-plotted using the surface Reynolds number, a similar linear relationship is discovered (Figure 5-11), which may be expressed, with a coefficient of determination of 0.87, as:

$$\sigma_w / k_s = 4 \times 10^{-4} V_S L_0 / \upsilon \tag{5-10}$$

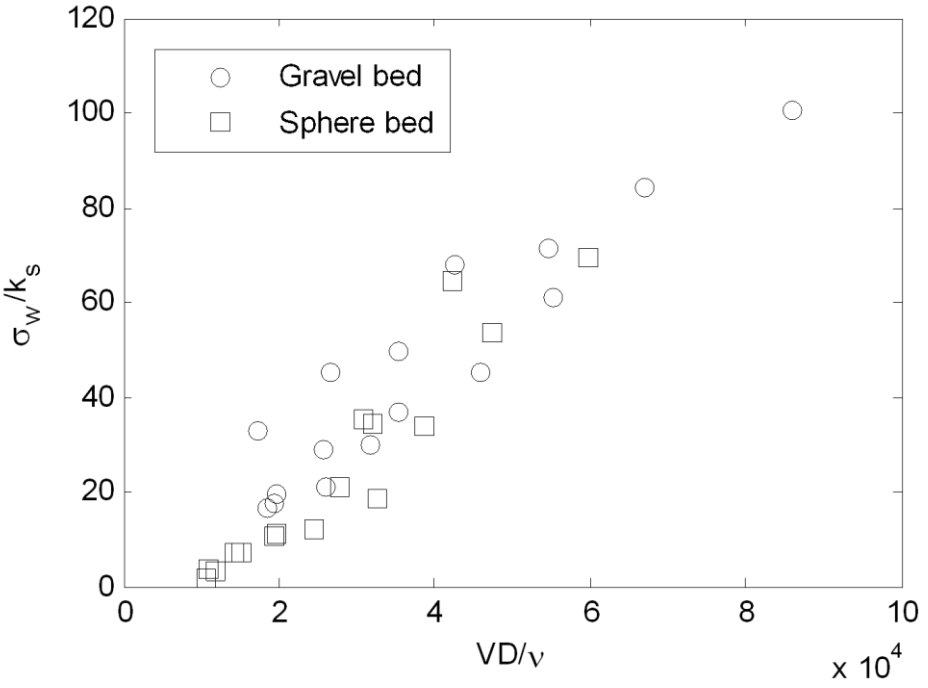

Figure 5-10: The dependence of the normalized correlation radius against flow Reynolds number

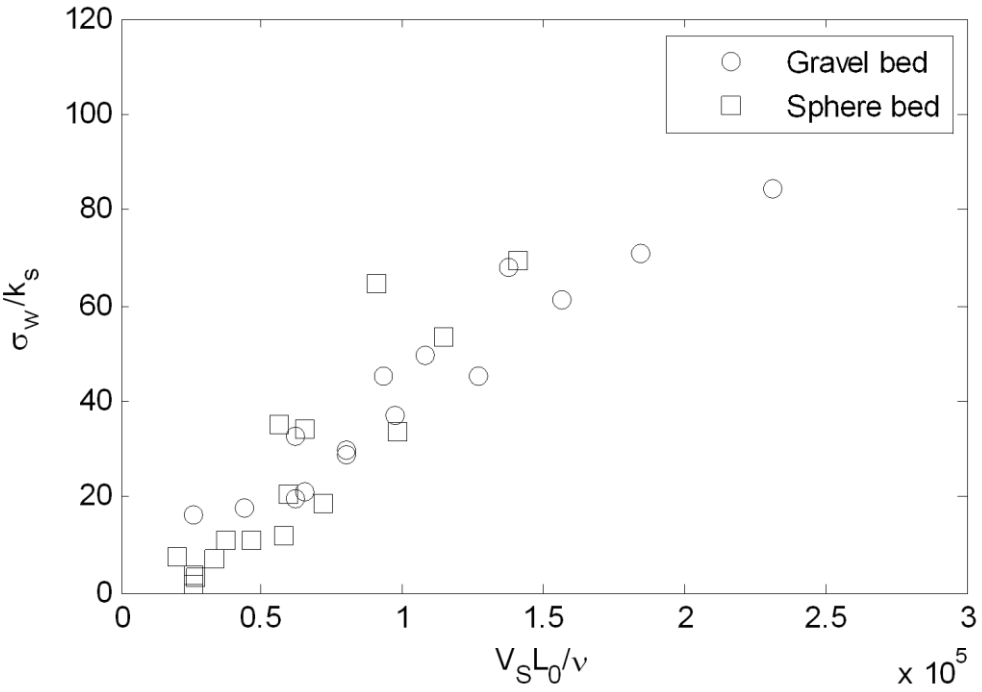

Figure 5-11: The dependence of the normalized correlation radius against free surface Reynolds number

The data collected and the analytical function used to describe the spatial correlation has been shown to provide clear evidence of a link between the surface pattern and the underlying turbulence and character of the shearing flow. By comparing the length scale of the water surface roughness with the scaling of the underlying turbulent flow features summarized by Roy et al. (2004), and by demonstrating that the celerity of the flow features is different from gravity waves, and indicating the similarity with some observations in other studies such as Smolentsev and Miraghaie (2005) and Savelsberg and Van de Water (2009), it has been shown that the water surface correlation pattern is strongly controlled by the underlying turbulent flow features. The observations in the present study do conflict to some extent with those of Savelsberg and Van de Water (2009) who conceptualized the water surface pattern as an ensemble of randomly generated capillary-gravity waves that travel in all directions but whose scale is inherited from the underlying turbulent flow. These divergent views can however fit with the concepts first proposed by Brocchini and Peregrine (2001) and the experimental observations of Smolentsev and Miraghaie (2005), which identified a wide potential range of different water surface behaviours in which the different generation mechanisms can exist but under some conditions certain processes dominate. For hydraulic conditions similar to the free surface flows encountered in gravel-bed rivers it can be proposed that it is the underlying flow turbulence that is the dominant process producing the spatial water surface pattern (i.e. negligible traveling or standing waves). Because of this dominance the detailed measurement of the temporal and spatial properties

of the water surface offers the potential to deduce the character of the underlying turbulence.

5.2 **The influence of turbulent structures on the free surface pattern**

Given the results of section 5.1, it is believed that in the absence of wind generated shear stress at the free surface, the shape of the air-water interface in shallow flow is controlled by the internal flow structures. These may be governed by any number of factors including wall roughness, flow depth and shear velocity. While section 5.1 proved that the free surface behaviour is measurable and predictable, and illustrated a link between the free surface pattern and the bulk hydraulic conditions, it did not examine the physical linkage behind these relationships. In this section, the behaviour of the free surface will be linked to the sub-surface turbulent flow features. In a similar manner to the work by Roy et al. (2004) this section will focus on the duration, frequency, length, and advecting velocity of the large scale turbulent structures. In this work however, the combined PIV and LIF measurements allow these four properties to be estimated throughout the depth of flow, and at the free surface, in order to produce vertical profiles of the turbulence properties. This will be performed for all 32 flow conditions, though the results are mainly focussed on flow conditions 1 to 7 (gravel bed), and 17 to 23 (sphere bed), since the results of these conditions are representative of all the flows examined over both bed types. First, more qualitative space-time matrices are used to visually examine the behaviour of turbulent structures, and to confirm whether the flows are suitable to undergo

a more objective analysis which would quantify the statistics of the flow surface structures.

5.2.1 Qualitative space-time matrices & frozen turbulence

The turbulent structure length can be estimated from the PIV data by observation of individual instantaneous velocity fields (a snapshot of the velocity field over the field of view of the PIV system). This process however is problematic to automate, and is only applicable when a full structure is captured in the frame of the camera. There are many instances where this is not the case, particularly for the deeper flow conditions of this study, where the scale of some structures approaches the spatial width of the cameras' field of view.

For this reason length is estimated more reliably by using Taylor's frozen turbulence hypothesis (Taylor, 1938) whereby turbulent structures are deemed to not change significantly in the measurement frame, and therefore a time series at one spatial location may be converted to a length scale by multiplying by the advection velocity (Zaman & Hussain, 1981). Nikora & Goring (2000) have shown that Taylor's hypothesis is applicable for the upper 90% of flow fields over similar rough beds.

Taylor's hypothesis can be applied to space–time (ST) velocity matrices, which allow the visualisation of the relationship between simultaneous measurements taken at different points in the flow, and depict graphically the evolution and advection of turbulent structures in space and time. This type of visualization is often used to analyse data from relatively few sensors in a

relatively sparse distribution (Buffin-Bélanger, et al., 2000; Roy, et al., 2004). The relative spatial location of each sensor or sensing position is usually presented on the vertical axis, with time on the horizontal axis. A contour or surface is then plotted whereby the elevation, shading, or colour indicates the standardized deviation of the instantaneous velocity fluctuation from the temporal mean at that measurement location. In the present study, the time series at each point is standardized by removing the mean component, and normalizing the fluctuations by the standard deviation of the velocity fluctuations at that point. This quantity is termed the normalized deviate, i.e.:

$$u_N = \frac{u'_{i,j}}{\sqrt{\left\langle u'^{2}_{i,j} \right\rangle}},\ v_N = \frac{v'_{i,j}}{\sqrt{\left\langle v'^{2}_{i,j} \right\rangle}}, \tag{5-11}$$

where i is the streamwise location, j is the vertical location, and u' and v' are the instantaneous streamwise and vertical velocity fluctuations respectively, defined by:

$$u'_{i,j} = u_{i,j} - \left\langle u_{i,j} \right\rangle,\ v'_{i,j} = v_{i,j} - \left\langle v_{i,j} \right\rangle \tag{5-12}$$

where $u_{i,j}$ and $v_{i,j}$ are the instantaneous streamwise and vertical velocity components at location (i, j) respectively. This standardization method allows structures within areas of high turbulence (usually near the bed) to be viewed on the same scale as structures with lower levels of fluctuation. Fluctuations are hence presented as normalized deviates, in multiples of the local standard deviation.

In order to establish whether Taylor's hypothesis may be sensibly applied, the streamwise velocity from the central vertical column is plotted over time in

Figure 5-12, alongside an instantaneous contour plot of streamwise velocity in the image frame, for flow conditions 1, 3, and 5 to represent a range of flow conditions. The instantaneous contour corresponds to the frame captured at the central time in the left hand plots. The time interval of these plots was estimated from the mean velocity of the flow in each case. The horizontal axis on the right hand image is reversed in order to allow direct comparison, since a structure inclined downstream (left to right) in the spatial domain would appear to be inclined in the opposite direction in the time domain. While the resolution of the temporal data effectively filters out the small scale features (causing a general blurring of the flow field), the large scale features (broad light and dark regions) are similar between the temporal and spatial data, showing that Taylor's hypothesis may be applied with confidence that the spatial scale of the large depth-scale flow structures is accurately captured in the temporal data. Further proof of the persistence and coherence of the large scale turbulent structures over space and time is given later in Figure 5-16.

Initial ST matrices are plotted using a vertical array of locations at the centre of the measurement plane. The standardized velocity fluctuations (Equation 5-11) at these locations are plotted over time on a contour plot, allowing the visualisation of the vertical shape and scale of the turbulent structures defined by the extreme velocity events (Roy, et al., 2004). The duration for which a turbulent structure is 'in view' of this column of measurements may also be estimated, and from this Taylor's hypothesis allows the estimation of the streamwise length scale based on the advection velocity.

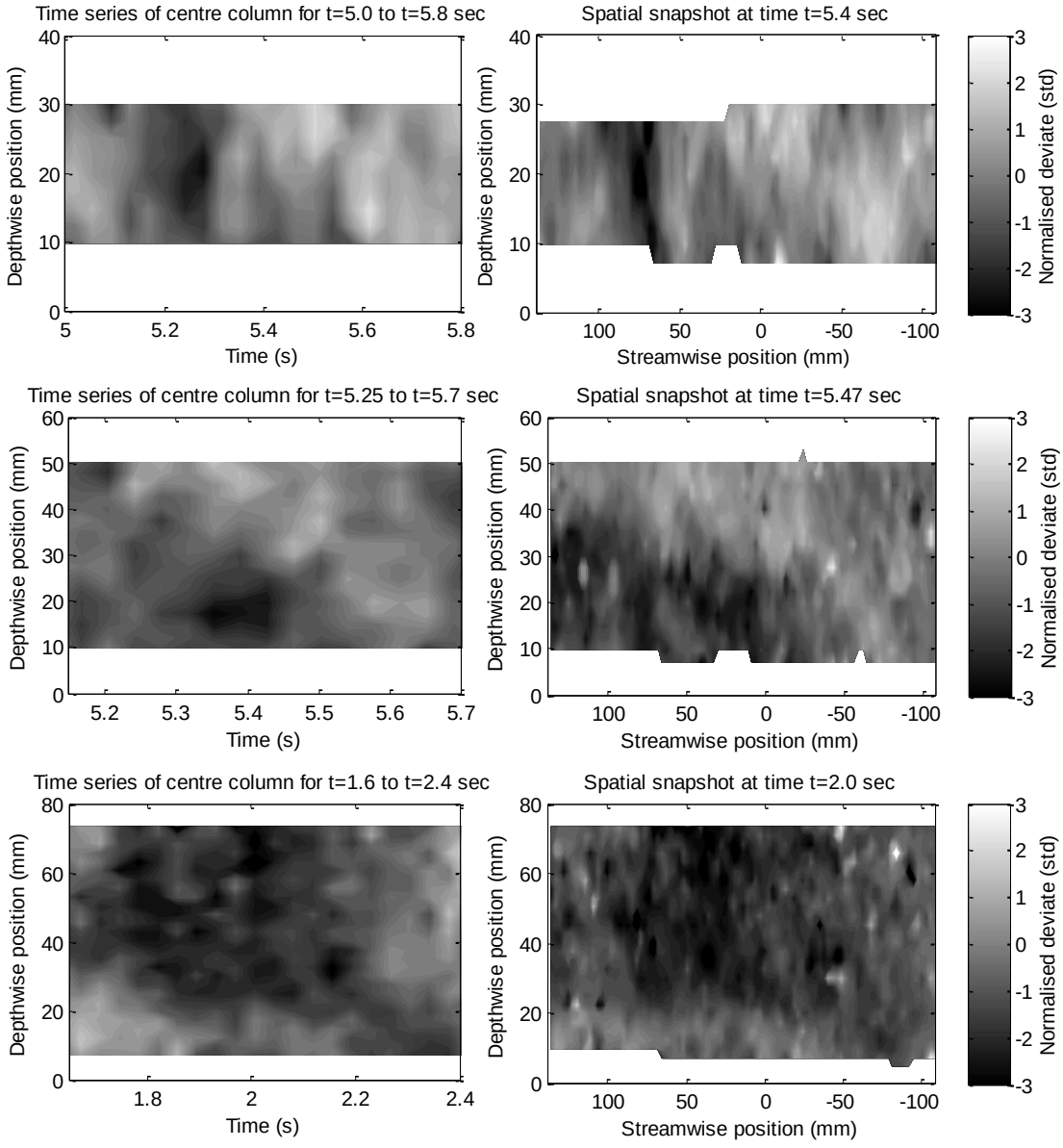

Figure 5-12: Temporal reconstruction of spatial data (left), compared to instantaneous spatial field (right), supporting Taylor's hypothesis of frozen turbulence. Flow conditions 1 (top), 3 (middle), and 5 (bottom) (S_0 =0.004, D =40, 60, 80 mm respectively; V =0.41, 0.55, 0.64 m/s respectively)

Average frequency of turbulent structure detection may also be approximated from an estimation of the mean temporal period between turbulent events, however, this is a subjective approach based on what the observer 'sees' as a coherent turbulent event. Figure 5-13 (left) shows a 30 second time series of the streamwise velocity fluctuation from flow condition 1. The well-defined

vertical striations show a clear tendency for the large scale turbulent structures to span the depth of the flow. Figure 5-13 (right) shows a closer view of a section of Figure 5-13 (left), between 0 and 2 seconds. This view confirms that structures tend to span the entire flow depth, in agreement with several previous studies (Nakagawa & Nezu, 1981; Shvidchenko & Pender, 2001; Yalin, 1992). The structures also show a tendency to be angled slightly in such a way that the upper part of the structure is ahead (downstream) of the lower part of the structure (indicated by the superimposed ellipses). This is in agreement with the findings of Roy et al. (2004) and Grass et al. (1991).

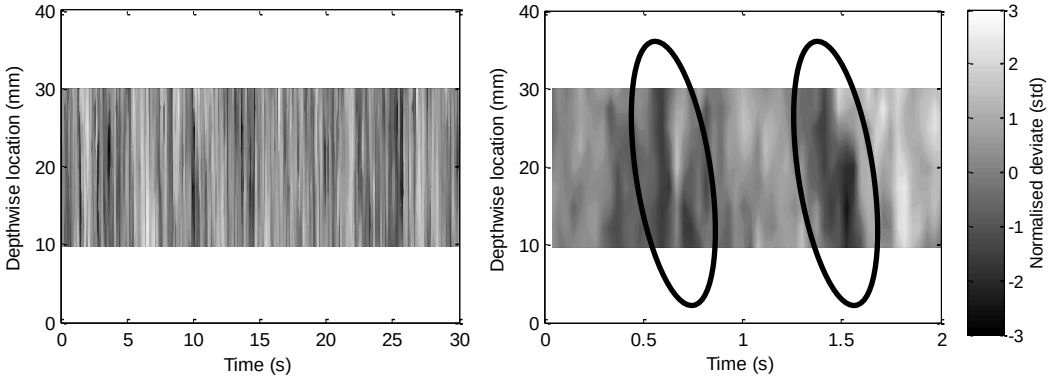

Figure 5-13: Space time matrices of normalized streamwise velocity fluctuations in a vertical column of measurement points in flow condition 1 (S_0 =0.004, D =40 mm; V =0.41 m/s) over (left) 30 s and (right) 10s

Figure 5-14 shows similar plots for the streamwise velocity fluctuations of flow condition number 7. Striations are still largely vertical, showing the same general tendency to be slanted in the direction of flow. Here flow features appear to be more disjointed with greater variation within each large-scale event, but still the broad light and dark regions appear to extend through the full depth of flow in general.

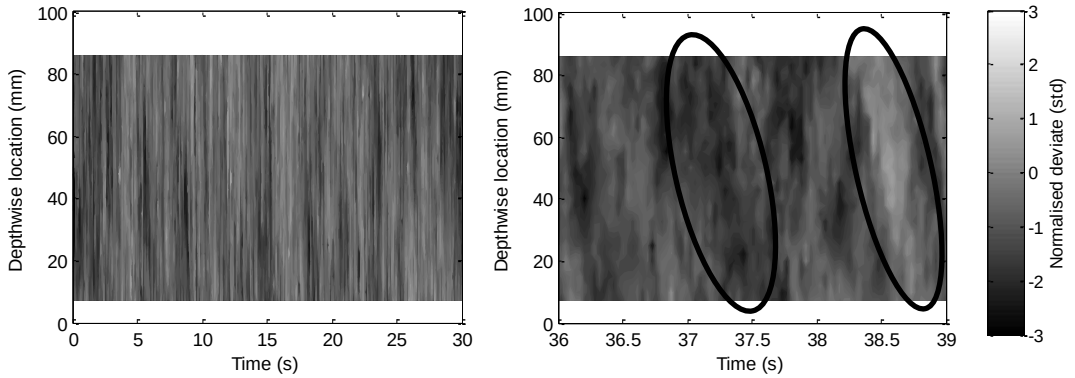

Figure 5-14: Space time matrices of normalized streamwise velocity fluctuations in a vertical column of measurement points in flow condition 7 (S_0 =0.004, D =100 mm; V =0.74 m/s) over (a) 30 s and (b) 10s

Although these plots are constructed predominantly to provide a qualitative examination of the behavior of turbulent structures, they also allow some degree of estimation of the statistical properties. Estimates are approximate however, as with subjective analysis it is difficult to define what constitutes a turbulent structure. In general, analysis 'by eye' detects events approximately 2 standard deviations from the mean, but due to the uncertainty, it is unfeasible to suggest turbulence properties to an accuracy that would allow any distinction between individual flow conditions. In general though, it can be said that for the flow conditions examined here, the structures appear at a frequency between 1 and 3 Hz and last around 0.1 to 0.3 s. With the range of flow velocities examined this suggests spatial scales of around 1 to 3 water depths, consistent with previous observations (Nakagawa & Nezu, 1981; Komori, et al., 1989; Liu, et al., 2001).

The contrast of the comparable plots generated using the vertical velocity fluctuations was not as defined as for the streamwise data, such that subjective observation proves difficult, and so these are not shown here. In

general, albeit with very poor contrast, the vertical velocity ST matrices were found to show similar patterns to those of the streamwise velocity, but with an inverted color map compared to the streamwise fluctuation data, suggesting that areas of strongly negative streamwise fluctuations coincided with positive vertical fluctuations and vice versa. This is typical of the sweep and burst nature of turbulent events measured using quadrant analysis in similar types of flow (Lu & Willmarth, 1973). Since the poor contrast made manual subjective analysis more difficult, these data would be more suited to the automated, objective analysis shown later, in section 5.2.2.

ST matrices were then plotted using measurement points distributed in the streamwise direction at a given depth. These matrices allow the visualisation of the downstream advection of the turbulence field, and any changes in the length of significant features as they propagate. Since the vertical axis is the spatial location, and the horizontal axis is time, the gradient of any persistent features represents their advection velocity. The structure duration and hence the spatial scale (by Taylor's hypothesis) may also be estimated, along with the frequency of structure detection. Due to the subjective nature of this analysis, this is conducted at a single depthwise location ($y/D \approx 0.4$) for each flow condition, as this is the depth which approximately represents the mean velocity of the flow (based on a logarithmic or parabolic velocity profile).

The resulting plots are shown in Figure 5-15 and Figure 5-16 for flow conditions 1 and 7. It can be seen that there are very clear and persistent features. This shows that the turbulent structures maintain their shape and strength as they advect over a significant spatial distance (greater than the

length of the measurement frame). This adds further credence to the applicability of Taylor's hypothesis. The clearly linear nature of the striations and the fact that the striations are largely parallel shows that the advection velocity is relatively constant over the measurement frame, and over time. The gradient of these striations indicates the advection velocity. This is clear from the two plots where Figure 5-15 (flow condition 1), has a shallower gradient than Figure 5-16 (flow condition 7), indicating a lower advection velocity (see the mean velocity values in Table 3-4). The purpose of these plots is to illustrate that at a given depth the turbulent structures have a fixed advection velocity (striation gradient) for each flow condition. This means that an automated approach can be used to track the turbulent features and obtain their mean advection velocity for each given depth in each flow condition. This will be conducted in section 5.2.2. The frequency, duration, and spatial scale may also be subjectively estimated from these figures, though as before the subjective nature makes it difficult to reliably discern meaningful differences between the individual flow conditions in this manner.

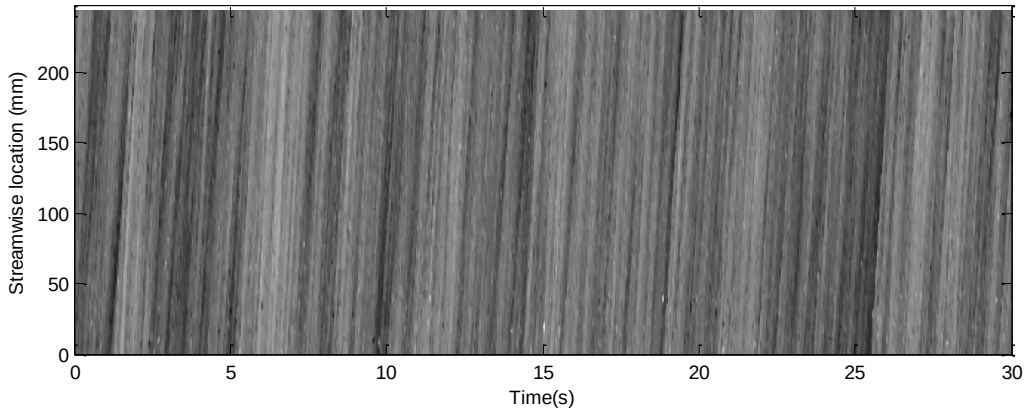

Figure 5-15: Space time matrices of normalized streamwise velocity fluctuations in a streamwise array of measurement points in flow condition 1 (S_0 =0.004, D =40 mm; V =0.41 m/s)

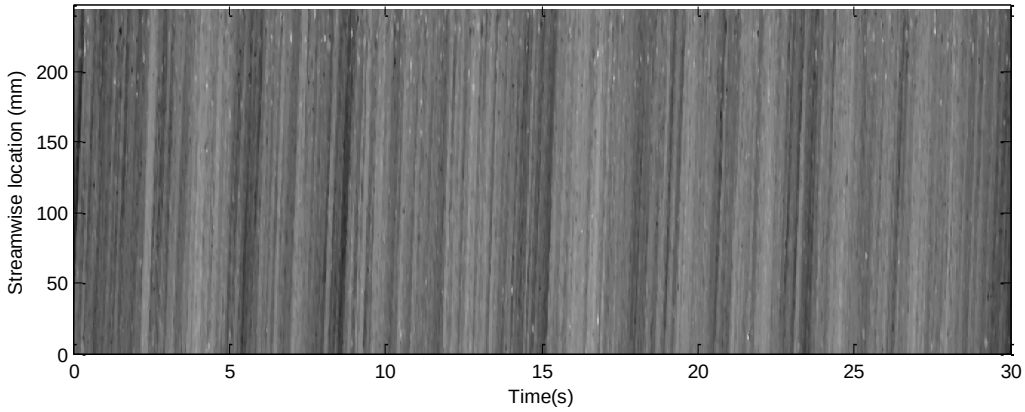

Figure 5-16: Space time matrices of normalized streamwise velocity fluctuations in a streamwise array of measurement points in flow condition 7 (S_0 =0.004, D =100 mm; V =0.74 m/s)

The purpose of the ST matrices was to visually assess the qualitative behaviour of the turbulent structures, to make some broad subjective estimates of turbulence properties to compare with previous literature, and to establish whether the data is suitable for a more objective analysis approach. Several statements can be made in conclusion:

- Large scale flow structures typically span the full depth of flow, and persist, relatively unchanged, throughout the measurement frame.
- Taylor's hypothesis applies, as shown by the temporal reconstruction of spatial data.
- Structures are inclined in the direction of the flow, such that the upper portions travel ahead of the near-bed parts.
- Structures occur at frequencies of around 1 to 3 Hz, with spatial scales in the streamwise direction of around 1 to 3 water depths.

- This visual, subjective ST matrix approach proves that the features are defined, coherent, and persistent enough to be measured using an automated approach, which will be conducted in section 5.2.2.

5.2.2 Quantitative U-level analysis

The goal of this section is to examine whether the properties of turbulent structures close to the free surface relate to the properties of measured surface features. Whilst ST matrices may be used to manually estimate the duration, length, frequency and advecting velocity of structures, this type of analysis is extremely labour intensive and is subjective in terms of defining what constitutes the beginning and end of a turbulent event. For this reason a technique was required for objectively identifying turbulent structures within the time series at each spatial location. Bogard & Tiederman (1986) described several such techniques for burst and structure detection, while Roy et al. (1996) showed that most of these techniques give similar results. For this work U-level conditional sampling was used as it has proven successful in several similar applications (Bogard & Tiederman, 1986; Krogstad, et al., 1992). This method also allows the results of this study to be directly compared to that of Roy et al. (2004).

The U-level technique identifies turbulent events as having velocity fluctuation components greater in magnitude than a given threshold, usually some fraction of the standard deviation of the time series. Luchik & Tiederman (1987) presented a modification whereby the end of an event was defined by a different threshold to the start of an event. In the modified U-

level scheme, the start of an event is detected from the streamwise velocity fluctuations, u', or vertical velocity fluctuations, v', when:

$$|u'| > k_U s_u \text{, or } |v'| > k_U s_v, \tag{5-13}$$

and the end of an event is defined by:

$$|u'| > p_U k_U s_u \text{, or } |v'| > p_U k_U s_v, \tag{5-14}$$

where k_U is a threshold value, s_u and s_v are the standard deviations of the streamwise and vertical velocity time series respectively, and p_U is a probability between 0 and 1. A probability of $p_U = 0.25$ is the most commonly used (Luchik & Tiederman, 1987; Shah & Antonia, 1989; Krogstad, et al., 1992). $k_U = 1.3$ has been shown to give sensible results in laboratory flumes (Bogard & Tiederman, 1986).

A U-level algorithm was written to transform any continuous time series vector into a discrete binary form, whereby a value of unity indicates the presence of a turbulent event and a value of zero indicates no event. This was applied to the velocity fluctuations at each spatial location over the full 300 s time series. An example is given in Figure 5-17 where the absolute values in a time series (normalized by the standard deviation according to Equation 5-11) are shown. The dotted lines show the thresholds for detecting the start and end of a turbulent event, and the black line shows the resulting binary series (multiplied by 3 simply to allow the lines to be better distinguished from one another in this figure). The binary series of the fluctuating terms u' and v' are defined as:

$$u'_U = U(u'), \text{ and } v'_U = U(v'), \tag{5-15}$$

respectively, where U represents the U-level analysis function. A simple count of the number of events present in a time series, n_U, allowed for the frequency of occurrence to be calculated as:

$$f_U = n_U / T \tag{5-16}$$

where T is the total duration of the measurement. The mean duration for which each turbulent event was detected at each point was also estimated by summing the binary time series, dividing by the number of events, n, and multiplying by the time step between samples ($dt = 1/26.9$ s). This is defined based on the streamwise and vertical binary velocity series respectively as:

$$d_{Uu} = dt\frac{\sum u'_U}{n},\ d_{Uv} = dt\frac{\sum v'_U}{n} \tag{5-17}$$

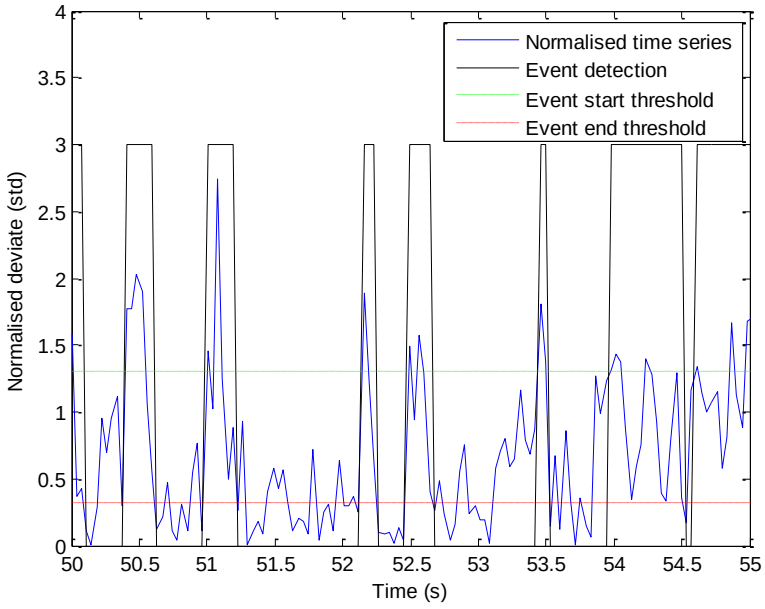

Figure 5-17: U-level turbulent event detection. Event start is detected when the time series exceeds 1.3 standard deviations, and event end is when the value drops below 25% of the start threshold. Binary detected event data (black line) have been scaled up to improve clarity

Whilst the ST matrices provided a visual approach for understanding the structure of turbulent events, and an approximation of the spatial and temporal properties, the subjective nature means that the results are not reliably comparable between different flow conditions, or between different depthwise locations of the same flow condition. U-level analysis allows an automated objective approach to characterizing the properties of the turbulent structures observed. By using the same parameters of conditional sampling for each depth of each flow condition, results can be reliably compared. Analysis time is also significantly reduced meaning the full 300 s time series at all 3128 spatial locations of each flow condition can be analysed.

The first turbulence property analysed is the advection velocity. In this work a basic cross-correlation is performed on the full time series at each depth in order to estimate the mean advection velocity:

$$V_a = \frac{1}{N}\sum_{i=1}^{N}\frac{\rho_i}{\tau_{e_i}}, \tag{5-18}$$

where N is the number of spatially distributed time series pairs examined, ρ_i is the spatial separation between measurement points, and τ_e is the temporal lag corresponding to the extremum value of the temporal cross correlation between two points, synonymous with that used for the free surface correlation data in Equation 5-2. This is performed for each possible combination of measurement locations at a given depth, and since there was

little streamwise variation (< 8 %), the resulting velocity estimates were averaged at that depth as shown in Equation 5-18.

Using the U-level results from each of the spatial locations, the turbulent events detected in the time domain were translated into a spatial form (duration converted to length scale) by the depth-local mean advection velocity, V_a to determine the mean structure length, L_U:

$$L_U = V_a d_U . \tag{5-19}$$

The mean distance between structures was also calculated as:

$$S_U = V_a / f_U . \tag{5-20}$$

It was found that for all flow conditions there was little streamwise variation (< 7 %) in the values of turbulence frequency, turbulent event scale and event duration, calculated via U-level analysis, allowing an average value of each to be calculated.

Although the primary aim of this analysis was to compare the U-level statistics measured in the free surface pattern to those measured in the velocity field immediately beneath, it was also possible to construct profiles of the turbulence properties throughout the depth of flow. Some attention will be given here to the behaviour of the turbulence properties across the flow depth, and the relationship with flow condition, while focus will be placed on the comparison of near-surface turbulence properties with the properties of the extreme events detected in the free surface roughness in section 5.2.3.

Figure 5-18 and Figure 5-19 show the advection velocity profiles calculated from the vertical and streamwise fluctuation data for gravel bed flow conditions 1, 3, 5 and 7 and sphere bed conditions 17, 19, 21, and 23 respectively, along with the mean streamwise velocity profiles. It can be seen that, in agreement with the results of Roy et al. (2004) and Adrian et al. (2000), the turbulent structures appear to travel close to the mean streamwise velocity. The data here goes further however, to confirm that the relationship is true throughout the depth of flow recorded in these tests.

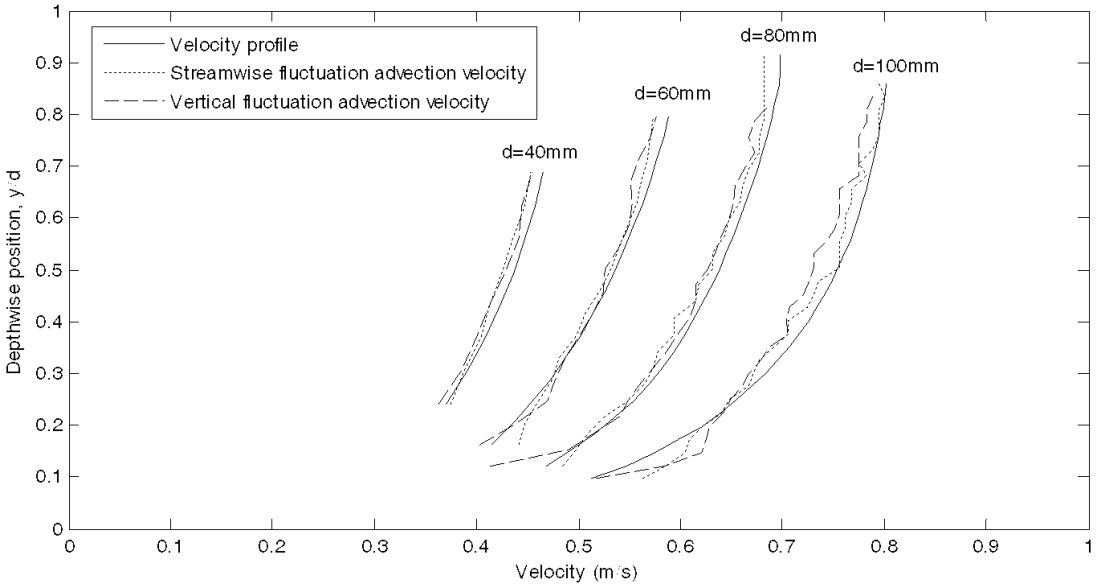

Figure 5-18: Profiles of mean velocity and turbulence advection velocity measured from streamwise and vertical velocity fluctuations for gravel bed flow conditions 1, 3, 5, and 7 (S_0 =0.004, D =40, 60, 80, 100 mm respectively; V =0.41, 0.55, 0.64, 0.74 m/s respectively)

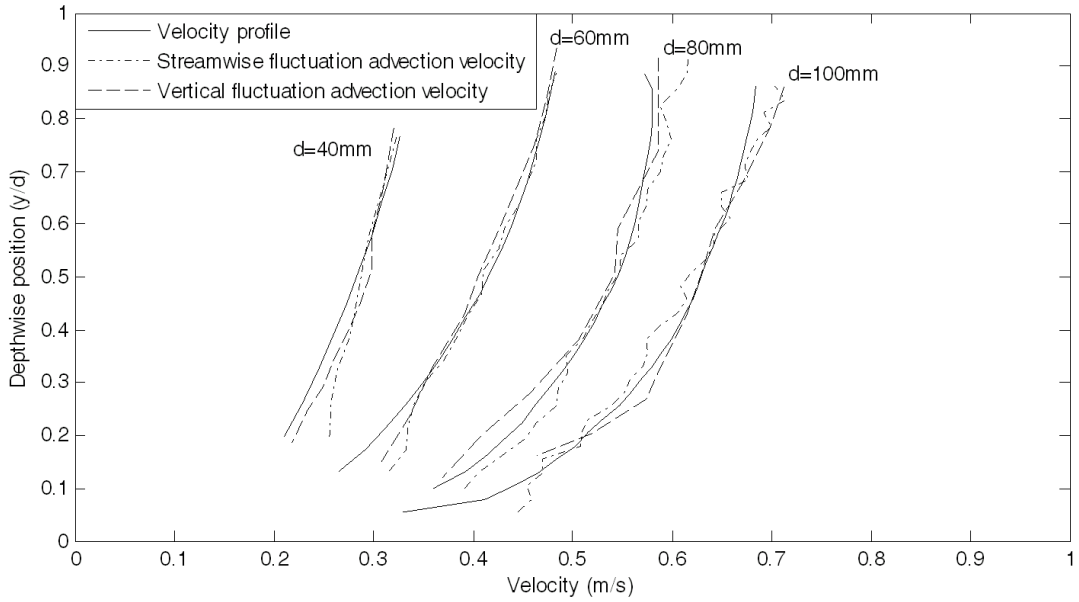

Figure 5-19: Profiles of mean velocity and turbulence advection velocity measured from streamwise and vertical velocity fluctuations for sphere bed flow conditions 17, 19, 21, and 23 (bottom. S_0 =0.004, D =40, 60, 80, 100 mm respectively; V =0.28, 0.43, 0.57, 0.71 m/s respectively)

In the following figures, data from flow conditions 1, 3, 5, and 7 will be used as the trends observed therein and the conclusions drawn are representative of all the flow conditions examined over both the gravel bed and the sphere bed. Figure 5-20 shows the frequency of turbulent structure detection (calculated according to Equation 5-16) for flow conditions 1, 3, 5, and 7 throughout the flow depth, as calculated from both the streamwise and the vertical velocity fluctuations. In general turbulent events are detected more frequently within the vertical fluctuation series, v'_U. This is likely to indicate the orientation of the structures: consider a laterally oriented depth-scale vortex - the remnant of the head of a horseshoe vortex (Brown & Thomas, 1977; Adrian, et al., 2000) - such that a period of extreme velocity (significantly higher or lower than the mean) in the streamwise direction is

preceded by a high velocity (positive or negative) in the vertical direction and followed by a substantially opposite velocity in the vertical direction.

There appears to be a general trend in both sets of data for frequency to decrease slightly as the flow depth (and velocity) increases (from flow condition 1 to condition 7). It can be seen from the streamwise data that near the bed the frequency is around 2Hz, and that this frequency decreases away from the bed, to a relative depth of around 0.25 – 0.3. This perhaps suggests that small vortices near the bed combine to form larger, less frequent structures. Above this relative depth the frequency remains largely constant, with a tendency to increase toward the surface. This may relate to a breakdown of some structures into smaller vortices when encountering the upper boundary of the flow (Yalin, 1992; Shvidchenko & Pender, 2001), surface renewal eddies (Kumar, et al., 1998), and surface generated coherent structures (Oh, et al., 2008).

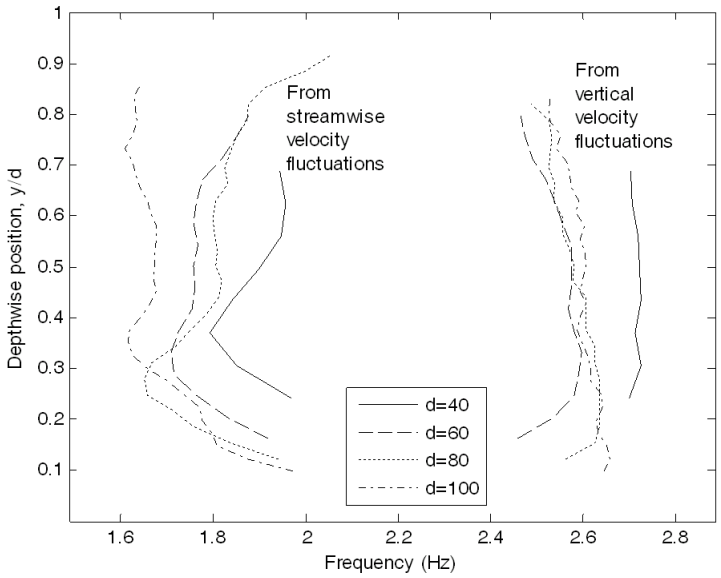

Figure 5-20: Profiles of turbulent event detection frequency measured using streamwise and vertical fluctuation data for flow conditions 1, 3, 5, and 7 (S_0 =0.004, D =40, 60, 80, 100 mm respectively; V =0.41, 0.55, 0.64, 0.74 m/s respectively)

Further understanding can be gained from comparison with the profiles of turbulent structure duration, and the structure length calculated from the duration of structure detection and the advecting velocity. Figure 5-21 shows the structure duration estimated (according to Equation 5-17) from (a) streamwise fluctuations and (b) vertical fluctuations, using the technique described earlier in this section. It can be seen that as the smaller structures coalesce near the bed, the mean duration increases, again up until a relative depth of around 0.3. Above this level the duration appears to decrease, although this is perhaps due to the increased velocity rather than any decrease in scale. This is confirmed by Figure 5-22 which shows the structure length, L_U calculated using Equation 5-19. Structures grow in size up to a relative depth of around 0.3, beyond which their size is relatively constant throughout most of the flow depth, with a slight decrease towards the flow surface, consistent with the surface interaction causing some degree of breakdown to smaller structures of higher frequency. It also appears that the streamwise fluctuations portray structures of slightly larger temporal and spatial scale. This may again be related to the orientation of the structures. In general structure duration is between 0.15 and 0.25 s, while structure length is between 1.5 to 2 water depths. This is within the range defined by Roy et al. (2004) of 1 to 3 water depths, and agrees with the estimates made from the ST matrices.

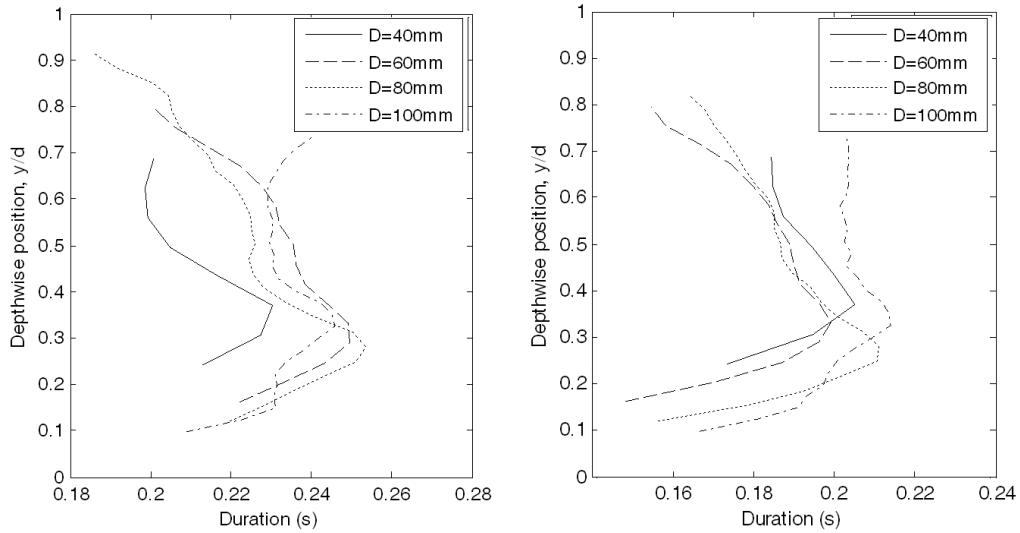

Figure 5-21: Profiles of turbulent event duration measured using (left) streamwise and (right) vertical fluctuation data for flow conditions 1, 3, 5, and 7 (S_0 =0.004, D =40, 60, 80, 100 mm respectively; V =0.41, 0.55, 0.64, 0.74 m/s respectively)

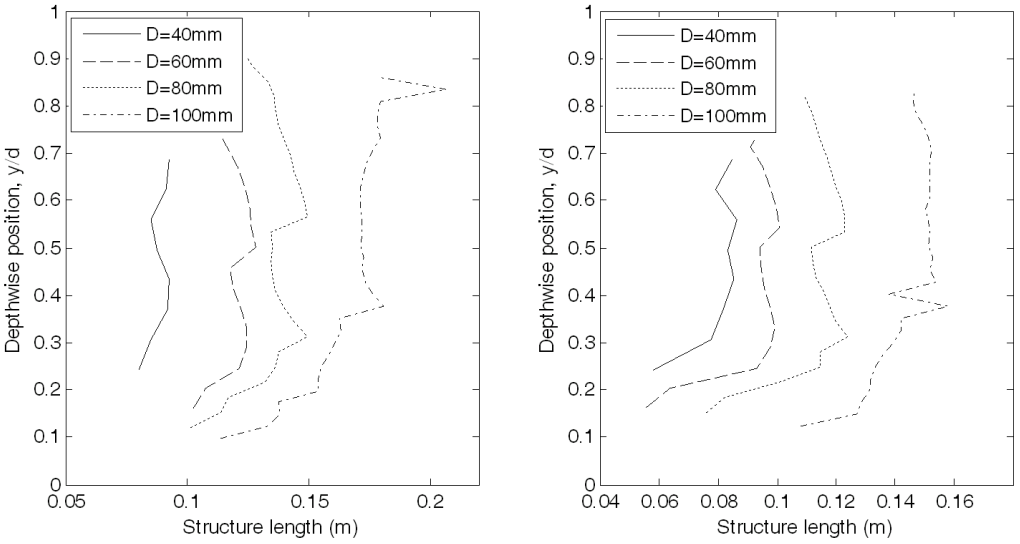

Figure 5-22: Profiles of streamwise length scales of turbulence measured using (a) streamwise and (b) vertical fluctuation data for flow conditions 1, 3, 5, and 7 (S_0 =0.004, D =40, 60, 80, 100 mm respectively; V =0.41, 0.55, 0.64, 0.74 m/s respectively)

5.2.3 Analysis of flow surface data

The primary aim of the U-level analysis was to allow comparison of the statistical nature of free surface events with that of the turbulent events

measured immediately beneath. With the turbulence properties visualised and quantified within the flow field, it was necessary to perform the same analysis on the free surface data. Streamwise ST matrices were plotted for the measured water surface elevation data, where data is standardized in the aforementioned fashion:

$$\eta_N = \frac{\eta'_i}{\sqrt{\langle \eta'^2_i \rangle}}, \tag{5-21}$$

where i is the streamwise location and η' is the instantaneous surface elevation fluctuation defined by:

$$\eta'_i = \eta_i - \langle \eta_i \rangle, \tag{5-22}$$

where η_i is the instantaneous water depth. The standardized data is then plotted on an ST matrix for visual assessment of the behaviour of the dominant features. This behaviour may then be compared to that exhibited by the velocity fluctuations measured below the free surface.

Figure 5-23 shows the space time matrices of the instantaneous water surface elevation for flow conditions 1, 3, and 6. The time and space variables are on different axes here compared to Figure 5-16 to allow easy comparison between flow conditions. Here the greyscale corresponds to instantaneous deviation from the mean water level, in units of number of standard deviations. An interesting phenomenon is observed: Rather than showing clear striations where features are persistent over space and time, these plots exhibit trains of extreme events fluctuating between high and low elevations over space and time.

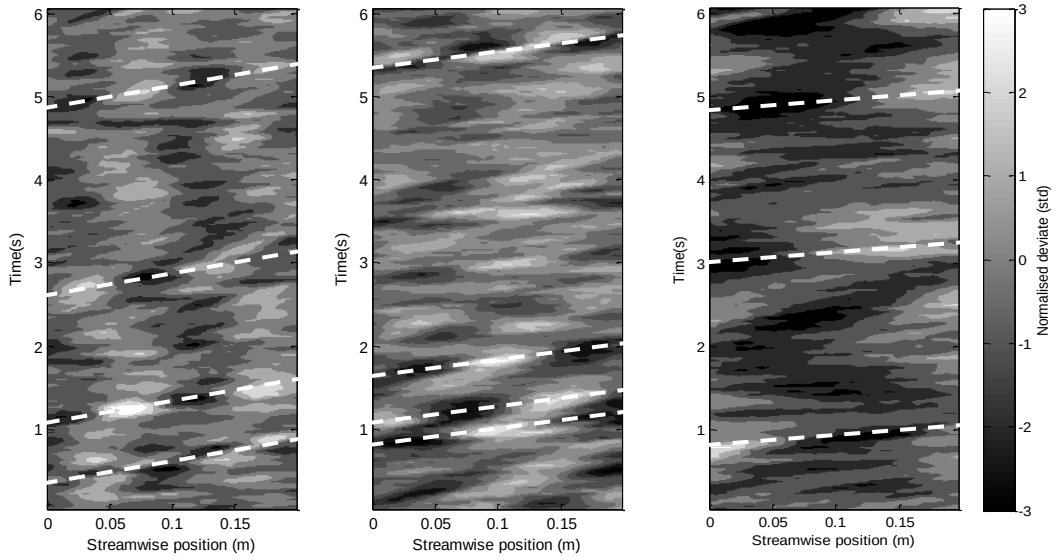

Figure 5-23: Several series of oscillatory positive and negative free surface features observed advecting over space and time for flow conditions 1, 3, and 6 (S_0 =0.004, D =40, 60, 90 mm respectively; V =0.41, 0.55, 0.69 m/s respectively)

Such an oscillatory nature was suggested by cosine term of the spatial correlation functions (Equation 5-5) of section 5.1.2. In fact the spatial periods of the oscillations shown in Figure 5-23 match well with the periods measured by wave probe (Table 5-3), as will be shown in more detail in section 5.3.1. These series of positive and negative elevations are clearly detected in the case of flow condition 1, where the spatial period of the oscillatory features allows several periods to be observed in the spatial measurement frame. For flow condition 3 the structure chains are less easy to discern, and by flow condition 6, the period is so large (almost twice the image frame) that the features can only be identified with prior knowledge of their expected form. Similar behaviour can in fact be observed in the free surface data of Fujita et al. (2011), though it was not remarked upon in their study. This behavior of the oscillation period further supports the findings of

section 5.1.2 which showed that the spatial period of free surface oscillations generally increases with flow velocity. It also confirms the findings of Savelsberg & van de Water (2008) who suggested that the free surface exhibits a dynamic response of its own. It is possible to visually assess and manually mark the trajectory of the oscillatory events over space and time (the white dashed lines in Figure 5-23), and as such the gradient indicates the approximate advection velocity. In this manner it can be seen that the advection velocity of free surface deformations increases with flow velocity, a similar behavior to the sub-surface turbulent features. It can also be estimated from observation of any vertical line on these plots that the frequency of turbulent events decreases with flow velocity, also a characteristic of the sub-surface turbulence. Also in agreement with the sub-surface data, the spatial scale of structures appears to increase with flow velocity and flow depth for a given bed slope. Figure 5-23 also suggests that some surface features may tend to form bonded pairs, a similar behavior described by Kumar et al. (1998) regarding surface renewal eddies. These trends are shown for three flow conditions in Figure 5-23, but are representative of all the flow conditions examined over both types of rough bed.

The features of the free surface do not appear to be persistent in the same way as the sub-surface features. However, although each surface feature appears to oscillate up and down, it is arguably the same feature which is travelling along in space and time. The decay of the correlation functions in Figure 5-8 would suggest that the magnitude of the oscillating surface features decays over space and time, though this is not significantly detected

in the ST matrices due to the limited field of view of the LIF system. Since the same feature can be thought of as travelling in the streamwise direction while maintaining its spatial scale (though not it's sign or vertical magnitude), Taylor's frozen turbulence hypothesis is still valid for a time series recorded at an individual spatial location and so the same U-level analysis procedure is performed here using the surface fluctuation data. Prior to the analysis, the fluctuation data was differentiated with respect to time in order to transform elevation vectors into vertical velocity vectors. Water surface events were then identified using the same U-level detection criteria ($\kappa = 0.41$, $p_U = 0.25$) as for the sub-surface field. Mean advection velocities, V_a, were measured using the same cross-correlation technique (Equation 5-18), and thereby the frequency, f_U (Equation 5-16), mean duration, d_U (Equation 5-17), and spatial scale, L_U (Equation 5-19), were estimated in the same manner. This would enable meaningful quantitative analysis and direct comparison with the sub-surface profiles.

It was found that once again the mean U-level properties were relatively homogeneous in the streamwise direction, allowing single values of frequency, duration, length and advecting velocity to be calculated for the free surface structures of each flow condition. These are given for the gravel and sphere bed flow conditions respectively in Table 5-4 and Table 5-5. As mentioned previously, the elevation data of flow conditions 7 and 23 protruded past the field of view of the LIF camera, so the free surface data for these flow conditions could not be analyzed.

Table 5-4: Surface feature properties measured in the free surface deformations using U-level conditional sampling – gravel bed flow conditions

Flow condition	Frequency f_U (Hz)	Duration d_U (s)	Length L_U (m)	Separation S_U (m)	Advection Velocity V_a (m/s)
1	2.83	0.149	0.079	0.19	0.53
2	2.80	0.148	0.086	0.21	0.58
3	2.71	0.146	0.089	0.23	0.61
4	2.63	0.145	0.097	0.25	0.67
5	2.70	0.146	0.102	0.26	0.70
6	2.58	0.144	0.112	0.30	0.78
7	-	-	-	-	-
8	2.81	0.150	0.071	0.17	0.47
9	2.75	0.147	0.075	0.19	0.51
10	2.56	0.142	0.079	0.22	0.56
11	2.69	0.143	0.087	0.23	0.61
12	2.56	0.145	0.095	0.25	0.65
13	2.83	0.149	0.067	0.16	0.45
14	2.79	0.150	0.075	0.18	0.50
15	2.76	0.149	0.082	0.20	0.55
16	2.40	0.140	0.059	0.18	0.42

Table 5-5: Surface feature properties measured in the free surface deformations using U-level conditional sampling – sphere bed flow conditions

Flow condition	Frequency f_U (Hz)	Duration d_U (s)	Length L_U (m)	Separation S_U (m)	Advection Velocity V_a (m/s)
17	2.68	0.155	0.061	0.15	0.39
18	2.77	0.149	0.066	0.16	0.44
19	2.70	0.147	0.075	0.19	0.51
20	2.66	0.146	0.079	0.20	0.54
21	2.64	0.145	0.097	0.25	0.67
22	2.60	0.144	0.101	0.27	0.70
23	-	-	-	-	-
24	2.79	0.149	0.058	0.14	0.39
25	2.75	0.151	0.070	0.17	0.47
26	2.67	0.151	0.078	0.19	0.52
27	2.69	0.151	0.082	0.20	0.54
28	2.63	0.151	0.092	0.23	0.61
29	2.69	0.150	0.057	0.14	0.38
30	2.63	0.154	0.065	0.16	0.42
31	2.63	0.154	0.072	0.18	0.47
32	2.60	0.145	0.034	0.09	0.23

These values are close to those found using the sub-surface vertical velocity fluctuations, and show the same dependence on flow condition. In order to visualize the relationships, Figure 5-24 to Figure 5-27 respectively plot the profiles of advecting velocity, frequency, duration, and structure length calculated from vertical velocity fluctuations throughout the depth for flow conditions 1 to 6, along with markers to represent the calculated free surface values. The relationships shown between free surface and sub-surface U-

level data are representative of all the flow conditions studied. The advection velocity profiles shown in Figure 5-24 clearly extend toward the free surface and the measured advection velocities at the surface show a clear dependence on the sub-surface profiles.

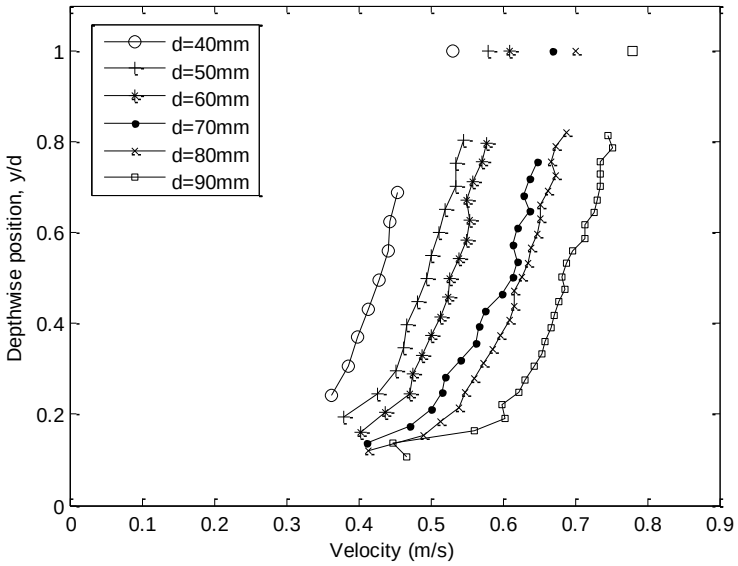

Figure 5-24: Turbulence advection velocity measured throughout the flow depth using the vertical velocity fluctuations (solid lines), and measured at the free surface using the LIF surface deformation data (individual markers)

Figure 5-25 shows the frequency profiles for the 6 flow conditions. The surface properties here do not match as clearly to the sub-surface profiles, generally being greater by around 8%. This is perhaps due to structures breaking down (Yalin, 1992), or renewal eddies being formed (Kumar, et al., 1998) in the extreme near surface layer and increasing the frequency of events. It may also be explained by the oscillatory nature of the free surface continuing to react to the fluctuations induced by a turbulent structure even after the structure itself has dissipated, hence generating additional 'phantom' structures. In general the free surface and sub-surface structure

detection frequency can be seen to reduce with flow depth (by around 10% for the flow conditions shown here).

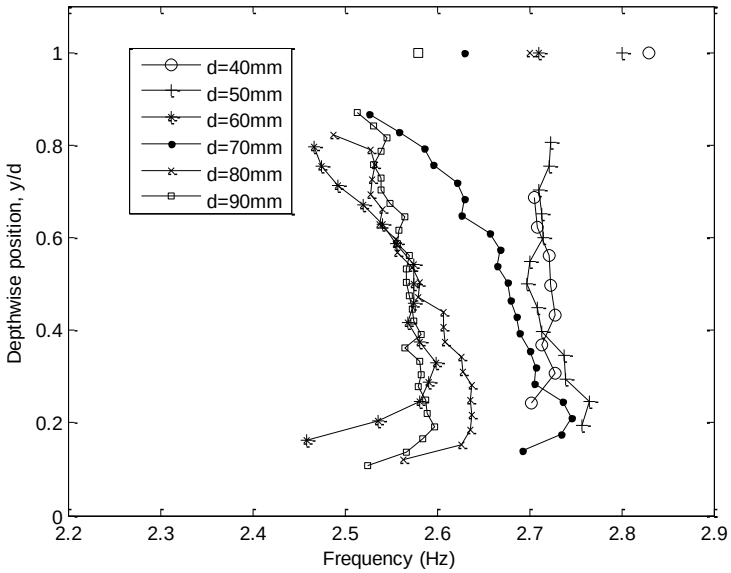

Figure 5-25: Frequency of turbulent event detection measured throughout the flow depth using the vertical velocity fluctuations (solid lines), and measured at the free surface using the LIF surface deformation data (individual markers)

Figure 5-26 shows the surface and sub-surface measurements of turbulent structure duration, the mean time for which a turbulent event is experienced at a given point. As mentioned previously, structures increase in duration up to a relative depth of around 0.25 – 0.3, beyond which the duration decreases as the velocity increases. Following this decreasing trend up to the intersection with the flow surface shows that the durations measured using the free surface fluctuation data relate well to the sub-surface profiles.

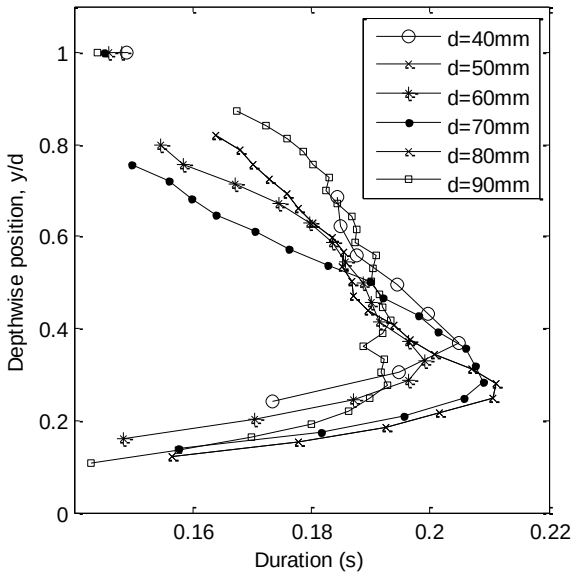

Figure 5-26: Mean duration of turbulent events measured throughout the flow depth using the vertical velocity fluctuations (solid lines), and measured at the free surface using the LIF surface deformation data (individual markers)

Finally, Figure 5-27 shows the sub-surface profiles of structure length, along with corresponding markers for structure length measured at the free surface. Once again, free surface markers show a clear dependence on the sub-surface profiles, again confirming that the surface behavior is strongly controlled by flow turbulence and not ordinary gravity waves. In this aspect ratio the tendency of structure length in deeper flows to decrease towards the surface is more pronounced. This is increasingly apparent for flow conditions 4, 5, and 6, and is perhaps due to the interaction with the free surface causing the breakdown of turbulent structures into smaller vortices (Yalin, 1992), or the generation of small-scale spiral eddies (Kumar, et al., 1998) or surface generated structures (Oh, et al., 2008).

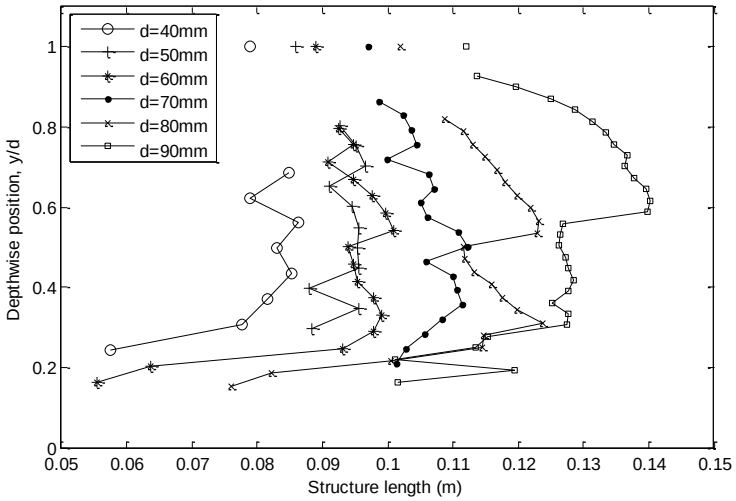

Figure 5-27: Mean streamwise length of turbulent structures measured throughout the flow depth using the vertical velocity fluctuations (solid lines), and measured at the free surface using the LIF surface deformation data (individual markers)

Clearly the temporal properties of the dynamic pattern generated at discrete points on the free surface are an expression of the turbulent flow field directly beneath. This flow field is governed by the bulk flow conditions, and can be expressed throughout the flow depth, from the rough bed to the free surface.

Since the U-level properties of the vertical velocity measured from the free surface relate to those measured in the flow, and since the same trends are observed (e.g. structure length increases with flow depth), the properties measured at the free surface may be used to investigate the relationship of the turbulence properties to the bulk hydraulic conditions. The traditional view is that the length of turbulent structures scales with flow depth, and so the length of significant features measured at the free surface is plotted against the flow depth in Figure 5-28. It can be seen that the traditional 'rule of thumb' is upheld, with structures generally increasing in size as the depth increases for a given bed type and bed slope. It is apparent however that

different bed types and bed slopes yield different relationships between structure length and flow depth. Clearly the structure length cannot be explicitly governed by the flow depth alone.

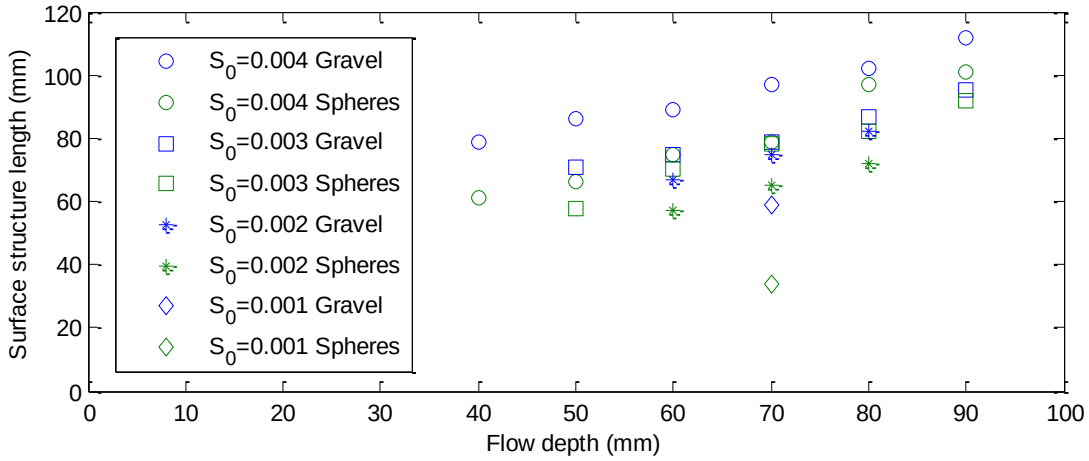

Figure 5-28: Free surface feature length (analogous to turbulent structure length) approximately scales with flow depth

In Figure 5-29 the lengths of the water surface structures are plotted against the structure advection velocity (a proxy for the depth-local mean flow velocity, in this case the surface velocity obtained by cross-correlation as described earlier). It can be seen that the data for both the gravel and sphere beds do now converge, and that the linear trend would appear to pass through the origin. This would seem to make sense since for a given depth, if the velocity is zero there will be no turbulent structures, so their length will be equal to zero. As the velocity increases, more kinetic energy is present in the flow to form larger turbulent structures, and there is a stronger shear present to stretch these structures in the streamwise direction. The relationship appears to be independent of flow depth and bed type. This is somewhat contradictory to Sakamoto and Haniu (1990) who found vortex size to scale

with depth and not velocity, but their work was based on the bulk flow velocity, rather than the free surface velocity. These results do relate with the observation of Brocchini and Peregrine (2001) that turbulent velocity governs the intensity of free surface behaviour.

Also shown in Figure 5-29 is the mean distance between large scale turbulent structures, S_U calculated from Equation 5-20 using the free surface data. It can be seen that this too is proportional to the advection velocity, and takes a value approximately 2.6 times the structure length. This again suggests that the local flow velocity is the governing factor in determining the spatial frequency and spatial scale of water surface structures (and hence, turbulent flow structures).

These relationships are possible due to the frequency of free surface event detection and duration of detection varying by less than ±5 % across all flow conditions. This has perhaps not been identified in previous literature since data is recorded at somewhat arbitrary flow depths, with each depth presumably exhibiting a different relationship between turbulent structure length and local flow velocity. It would seem however that the relationships at the free surface are general, at least for the flows studied here, and so can be expressed as:

$$L_U = 0.147V_s \,,\; S_U = 0.374V_s \tag{5-23}$$

These relationships show a coefficient of determination (R^2) of 0.99 and 0.98 respectively. The high R^2 values are due to each of the flow conditions for both the bed types exhibiting structure detection frequencies close to f_U =

2.67 Hz, and mean duration of structure detection at a given point of d_U = 0.147 s. It cannot be said whether these values are truly general, however it is possible that a given channel type (and perhaps bed type) will have values of f_U and d_U which are constant at the free surface. This would allow a powerful new understanding of the relationship between the surface flow velocity and the turbulent structure length.

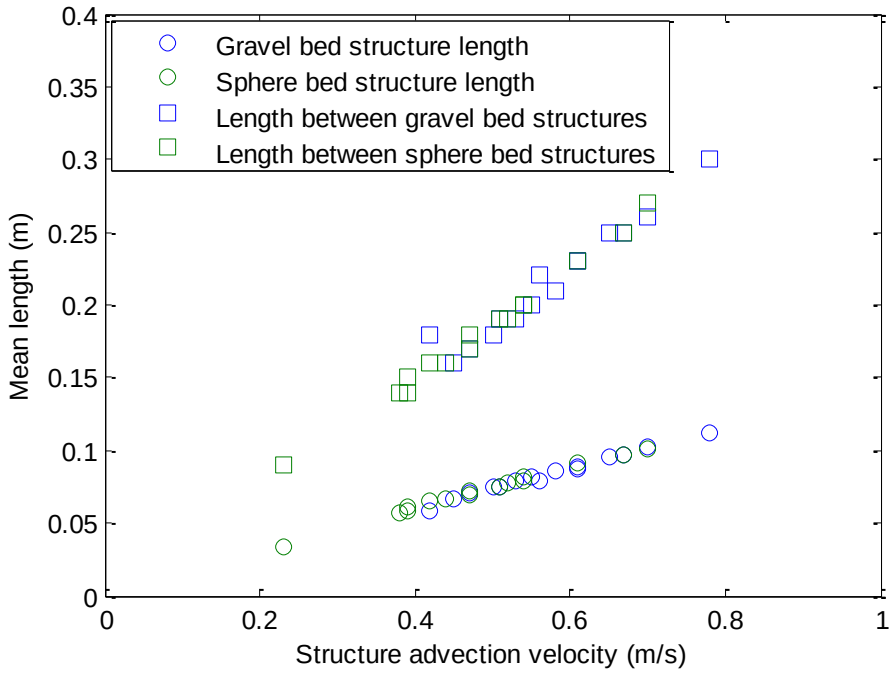

Figure 5-29: Surface structure length and spatial separation between structures is proportional to their advection velocity at the free surface

5.2.4 Turbulence throughout the flow and at the free surface - summary

In general several statements can be made about the behavior of turbulent structures throughout the depth of the flow:

- At any given depth, structures are transported at, or close to, the double-averaged mean flow velocity for that depth.

- Smaller, more frequent structures near the bed coalesce in the lower part of the flow to form larger, less frequent structures.
- These structures maintain their spatial scale up toward the flow surface.
- Close to the surface there is perhaps a tendency for structures to be broken down into smaller, more frequent events.
- The majority of the large scale turbulent structures in the flow conditions examined here span the full flow depth.
- The streamwise scale of these structures increases with flow depth, and is equal to around 1 to 3 flow depths.

The free surface is also shown to be a direct function of the sub-surface turbulence field immediately beneath. The advecting velocity, duration, and spatial length of the turbulent events observed in the free surface roughness pattern correlate reasonably well with the measured profiles throughout the flow depth. The frequency of events detected at the free surface is slightly higher (by around 8%) than the frequency of events below. This may be due to breakdown of structures very close to the surface, or may be due to the oscillatory nature of the free surface fluctuations producing ‘phantom’ events, which persist for longer than the structure which initiated them, as the restorative forces of gravity and surface tension overcompensate for the influence of a turbulent event. The key findings from the free surface data are:

- The mean structure length measured at the free surface seems to scale with the surface flow velocity, with a constant of proportionality of 0.146.
- The mean spatial distance between these structures also scales with surface velocity by a factor of 0.347.

The primary message of this section is that the U-level data obtained from the free surface velocity data correspond reasonably well with the comparable data obtained in the flow layer below, and therefore measurement of the free surface fluctuations can give an indication of the turbulent nature of the flow beneath.

5.3 **The influence of free surface pattern on sub-surface velocity field**

The previous section has shown that the large scale temporal features of the free surface are related to the large scale features of the velocity field immediately beneath. One limitation of previous work is that there has been no direct investigation into the degree to which the flow velocity field may be influenced by the behavior of the turbulence induced free surface roughness.

It is proposed that the information/energy exchange between the flow field and the free surface is not simply unidirectional. It seems reasonable that since the free surface exhibits its own oscillatory nature, this behavior must affect the sub surface flow in the same way that wind generated waves do (Craig & Banner, 1994). This would occur alongside the previously reported

influence of the flow structure on the free surface in a state of mutual dependence.

Since the free surface behavior is characterized by the spatial correlation functions of section 5.1.2, the equivalent spatial correlation of velocity data throughout the flow depth will be examined. Roy et al (2004) showed that the peak correlation between longitudinally separated sub-surface velocity measurements decreased at a constant rate with the spatial separation. However, since it has been shown that wind generated waves impose their influence on the sub-surface velocity field, it seems reasonable that the oscillatory nature of the free surface features should to some extent impose an oscillatory component on the sub-surface flow. The aim of this section is to determine whether the free surface behavior does indeed affect the sub surface flow field, and to examine the extent of any influence.

5.3.1 Spatial correlation functions throughout the flow depth and at the free surface

The spatial correlation function describes the behavior of the extremum value of the temporal cross-correlation between two time series recorded at different points in space as the separation (spatial lag) between these points is increased. For each flow condition, a spatial correlation function was calculated at several sub-surface depthwise locations using the PIV data, and at a depthwise location of $y/D=1$ (at the free surface) using the LIF time series. This allows comparison of the spatial behavior of the free surface with that of the velocity fluctuations below. In each case the raw data was simply

in the form of a number of time series recorded at different points in the streamwise direction. The spatial correlation function was calculated as:

$$W(\rho_{\Delta},0,\tau_{\Delta})=\frac{1}{N-\Delta}\sum_{i=1}^{N-\Delta}W(\rho_{i,i+\Delta},0,\tau_{i,i+\Delta}), \tag{5-24}$$

where N is the number of velocity time series in the streamwise direction, ρ is the streamwise spatial separation between two time series, Δ is the streamwise spatial separation (in samples) between two time series, and τ_{Δ} is the time lag at which the two time series show the extremum value of their temporal cross-correlation, $W_{i,i+\Delta}(\tau)=v'_{i}\otimes v'_{i+\Delta}$. Here $\otimes$ denotes a cross-correlation.

The first point on the spatial correlation function (at zero spatial lag) corresponds to a time series correlated against itself, which by definition has a correlation value of unity. The second point corresponds to a given point correlated against its adjacent neighbour. In this case all possible pairs of neighbours were analysed and were found to exhibit very little difference in the temporal cross-correlations due to the flow being uniform and steady. For this reason the extremum correlation values for all the pairs were then averaged. This process was repeated for all possible separations between the measurement points (spatial lags) resulting in an average spatial correlation function for each given depthwise location. This was performed using only the vertical velocity component of the PIV measurements, since the free surface data represents vertical motion, and was found to affect the vertical component of the sub-surface velocity field more strongly than the streamwise component.

First, plots of the spatial correlation function will be shown for discrete values of relative depth, in order to show the form of the spatial correlation function taken at different parts of the flow, and then contour plots will be used to show the continuous variation of the spatial correlation function throughout the flow depth. Figure 5-30 shows the spatial correlation function of the free surface (relative depth of unity) calculated from the LIF images for flow conditions 2, 4, and 6. Also plotted are the correlation functions obtained in section 5.1.2 by analysis of the array of conductance probes for the same flow conditions. These were calculated using the exact same cross-correlation technique, with lower spatial resolution but over a greater spatial distance. It can be seen that the functions obtained by the two different methods are in agreement, validating the LIF measurement technique. When graphically comparing free surface and sub-surface correlation functions, the LIF data will be used due to its high resolution. The surface roughness parameters (characteristic spatial period and root-mean-square water surface roughness height) used in this section are taken from Table 5-2 and Table 5-3 since the long wave probe array captured several full periods of the correlation function and so provides more accurate estimates.

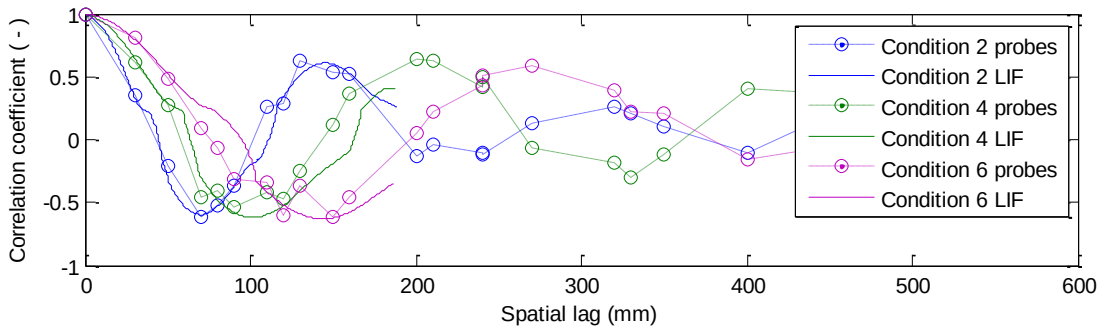

Figure 5-30: Spatial correlation function of the free surface roughness. Conditions 2, 4, and 6 (S_0 =0.004, D =50, 70, 90 mm respectively; V =0.50, 0.60, 0.69 m/s respectively)

The surface velocity was measured by determining the temporal lag at maximum (positive or negative) correlation between the surface fluctuation time series at two spatially separated points in the LIF data as described in Equation 5-18. This was conducted for a number of spatial separations and then averaged as described in section 5.2.2. This velocity matches that measured by timing a floating tracer as it passed between two points either side of the measurement area, to within three percent, and also closely matches the near surface velocity determined via PIV.

Figure 5-31 (top) shows the spatial correlation function (Equation 5-24) measured using the vertical velocity components at a depth of approximately $y/D = 0.25$ for gravel bed flow conditions 2, 4, and 6. It can be seen that a general linear decay is exhibited. This is in agreement with the findings of Roy (2004) who described a constant decrease with separation, and with (Snyder & Lumley, 1971) who showed particle velocity and turbulent energy to decay linearly with spatial separation. It would seem clear that this is the characteristic spatial behavior of turbulent structures exhibiting inception, evolution, breakdown, and coalescence deep within the flow. The fact that the linear decay begins from a correlation coefficient value of around 0.65 at zero spatial lag suggests a generally reduced correlation over the flow field, perhaps simply due to measurement error. In any case the linear trend would suggest that zero correlation is reached at around 400 mm spatial separation. This could therefore be defined as the spatial persistence length of the turbulent structures and appears to be the same for all the gravel bed flows examined here. The sphere bed data (Figure 5-31 (bottom)) shows a much sharper initial drop in correlation, to a value of around 0.3, perhaps due

to different types of turbulence field being generated by the different bed types. After this however a similar linear decay is observed, tending once again toward 400 mm spatial lag for zero correlation.

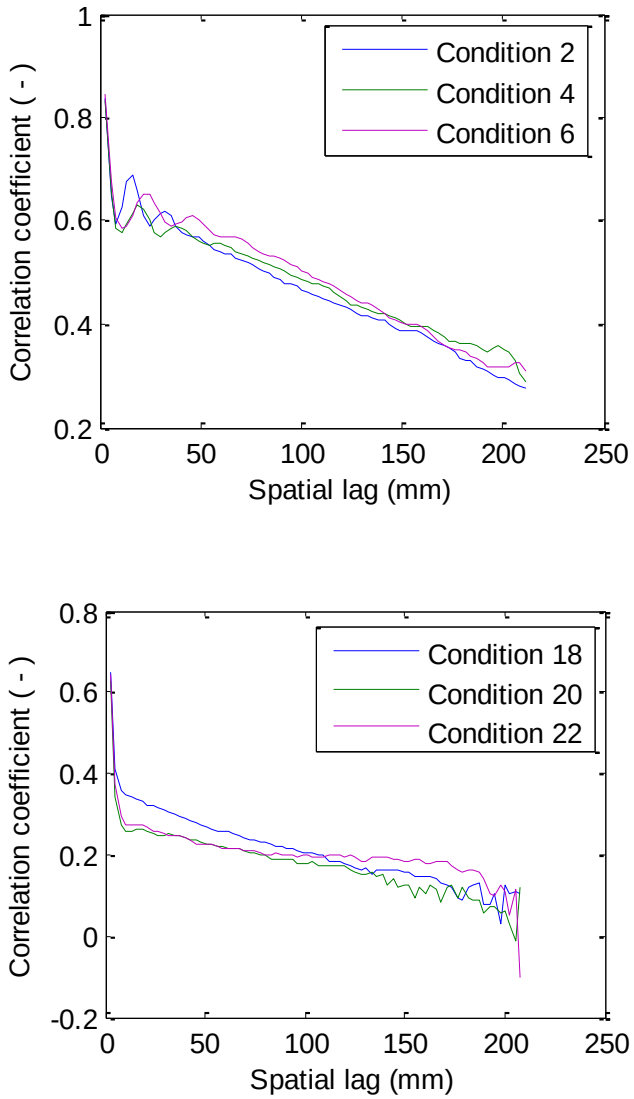

Figure 5-31: Near bed spatial correlation functions of vertical velocity fluctuation, y/D=0.25, (top) gravel bed data (S_0 =0.004, D =50, 70, 90 mm respectively; V =0.50, 0.60, 0.69 m/s respectively), (bottom) sphere data (S_0 =0.004, D =50, 70, 90 mm respectively; V =0.36, 0.50, 0.65 m/s respectively)

Close to the free surface, the spatial behavior begins to change. Figure 5-32 and Figure 5-33 show the spatial correlation function measured using the

vertical velocity components (with Equation 5-24) at a depth of approximately $y/D = 0.8$ for gravel bed flow conditions 2, 4, and 6, and for sphere bed conditions 18, 20 and 22. The correlation function now shows a clear oscillatory component, whose spatial period appears to match that of the free surface (see the dotted lines, or the data in Table 5-3), indicating that the free surface behavior is indeed being imprinted onto the sub-surface velocity field. This effect was much more pronounced in the case of the vertical velocity component data, which is understandable since the dominant movement of the free surface relative to the bulk flow is in the vertical direction. Clearly, not only does the flow field influence the free surface as previously found, but the independent oscillatory nature of the free surface also influences the sub-surface flow.

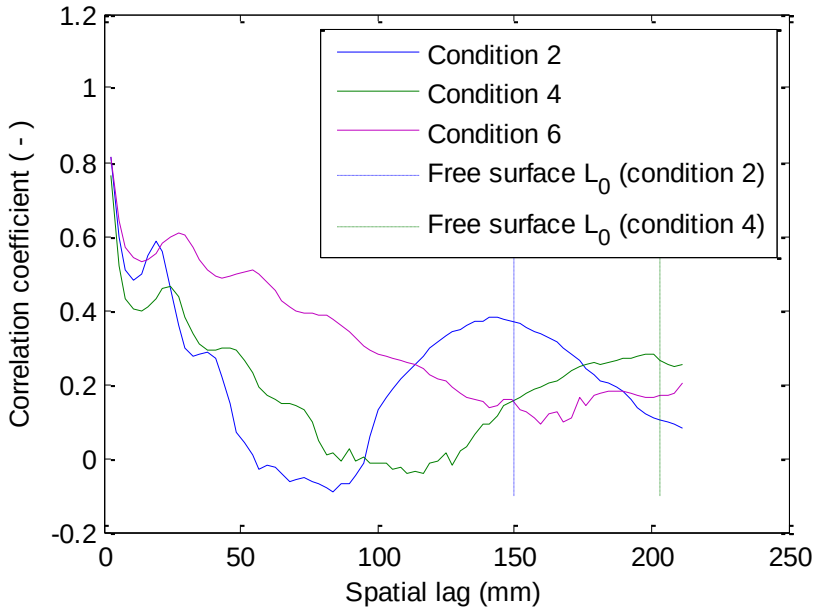

Figure 5-32: Near surface spatial correlation functions of vertical velocity fluctuation measured at y/D=0.8 for gravel bed data (S_0 =0.004, D =50, 70, 90 mm respectively; V =0.50, 0.60, 0.69 m/s respectively). Dashed lines correspond to characteristic spatial period of free surface

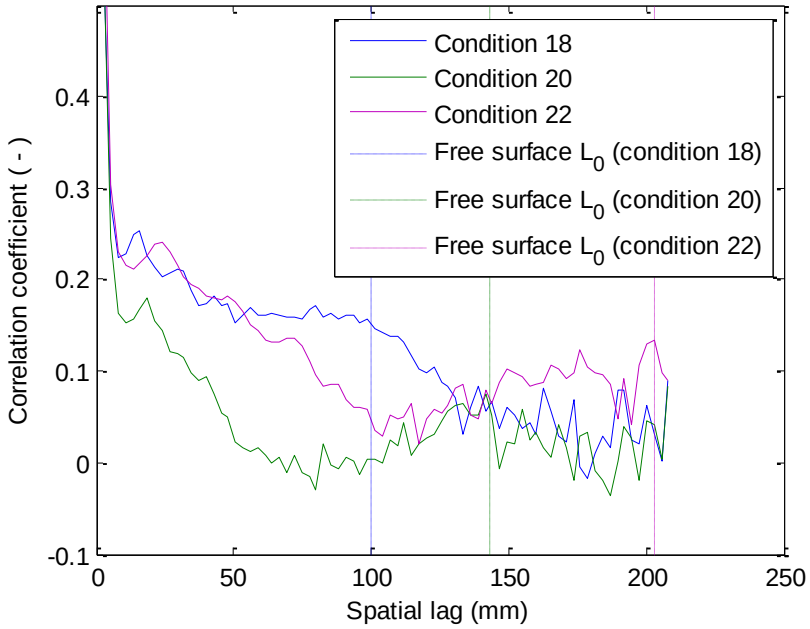

Figure 5-33: Near surface spatial correlation functions of vertical velocity fluctuation measured at y/D=0.8 for sphere data (S_0 =0.004, D =50, 70, 90 mm respectively; V =0.36, 0.50, 0.65 m/s respectively). Dashed lines correspond to characteristic spatial period of free surface

In order to assess the extent of this interdependence and to visualize the change from linear behavior to oscillatory behavior, the spatial correlation function is viewed throughout the flow depth in a continuous fashion, and at the free surface, by use of contour plots. Figure 5-34 shows the streamwise spatial correlation function measured using the vertical velocity fluctuation series (with Equation 5-24) at each location throughout the flow depth, and at the free surface, for gravel bed flow conditions 2, 4, and 6. It can be seen that in each case the spatial correlation function of the free surface dynamics influences the nearby flow field (indicated by the semi-elliptical regions of negative correlation near the free surface). There is a clear similarity between the free surface correlation function and that of the flow immediately beneath. This proves an interdependence whereby the free surface is disturbed by the

flow, but the response to this disturbance is then transferred back to the nearby flow field. Furthermore it can be seen that the effects of the free surface fluctuations are significantly experienced down to a depth of around $y/D = 0.75$ in each of these flow conditions. This was detected as the lowest depth at which zero correlation occurred, as marked by the dashed black line in Figure 5-34, and may be judged visually by the green boundary between the cyan and yellow areas. This relative depth is also proportional to the RMS water surface roughness height, σ, suggesting that the effects are experienced to a distance of around 28 roughness heights below the free surface.

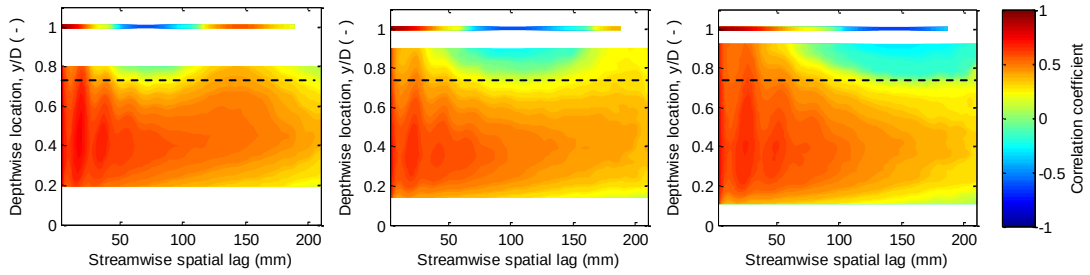

Figure 5-34: Spatial correlation function of vertical velocity fluctuation throughout flow depth and at free surface. Flow conditions 2 (left), 4 (middle), and 6 (right), (S_0 =0.004, D =50, 70, 90 mm respectively; V =0.50, 0.60, 0.69 m/s respectively). Dashed line represents the estimated depth of influence determined by the deepest location of zero correlation coefficient

In order to establish whether the fraction of the water column influenced by the free surface is a function of the depth or the water surface roughness height, the other bed slopes were examined, since these experiments were carried out at similar depths but exhibited different roughness heights. Figure 5-35 shows the spatial correlation function obtained from the vertical velocity components throughout the flow depth for four flow conditions each of D =

70mm mean flow depth, and gradients S_0 = 0.001, 0.002, 0.003, and 0.004, respectively (flow conditions 4, 10, 14, and 16). It can be seen that the area of influence is not simply a function of depth. It can be seen that the affected region generally becomes smaller as the bed slope is reduced for a fixed depth, until in flow condition 16 the free surface influence is not significantly captured in the field of view. This allows the assertion that the depth of influence appears to be proportional to the RMS roughness height, and allows the conclusion that for all gravel bed conditions examined, the influence of the free surface is experienced to a depth approximately 27 to 29 water surface roughness heights below the free surface.

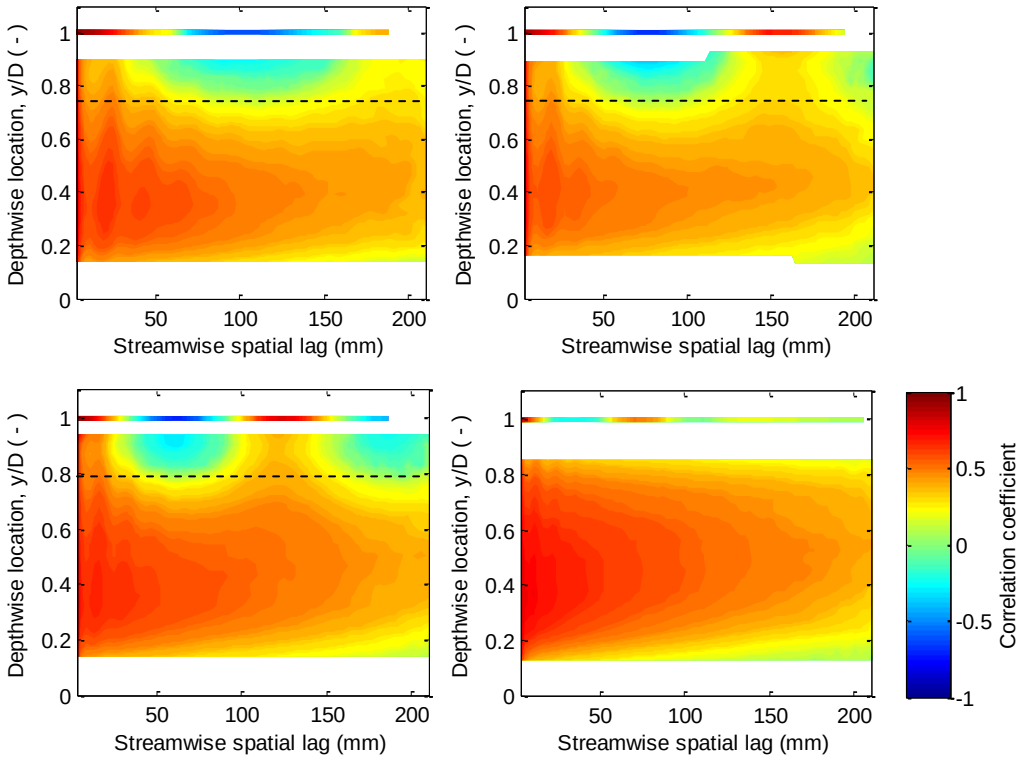

Figure 5-35: Spatial correlation function of vertical velocity fluctuation throughout flow depth and at free surface. Flow conditions 4 (tl), 10 (tr), 14 (bl), and 16 (br), (S_0 =0.004, 0.003, 0.002, 0.001 respectively; D =70 mm; V =0.60, 0.47, 0.35, 0.26 m/s respectively). Dashed line represents the estimated depth of influence determined by the deepest location of zero correlation coefficient

This dependency seems reasonable, since for a given depth, a very small surface wave would be unlikely to significantly affect the flow near the bed, whereas a very large wave with height comparable to the mean depth would be very likely to affect the near-bed flow. Therefore, it seems sensible to suggest that the depth of influence should be proportional to the roughness height. This hypothetical dependence will be tested further in the section 5.4.

In order to establish whether the depth of influence is general for all flow conditions and bed types, the same figures are plotted for the corresponding flows over the sphere bed in Figure 5-36 and Figure 5-37. It can be seen that in these flow conditions the relative depth of influence is generally much smaller than for the gravel bed conditions. Indeed the correlation across the flow field is generally weaker than for the gravel bed. This perhaps indicates a difference in the structure and behavior of the turbulence field and clearly affects the depth of influence. For all the sphere bed conditions the spatial correlation functions and the depth of influence were measured in the same way as for the gravel bed flow conditions, and it was found to be between 18 and 20 water surface roughness heights. The reason for this broad difference between the gravel and sphere bed data will be discussed in section 5.4.

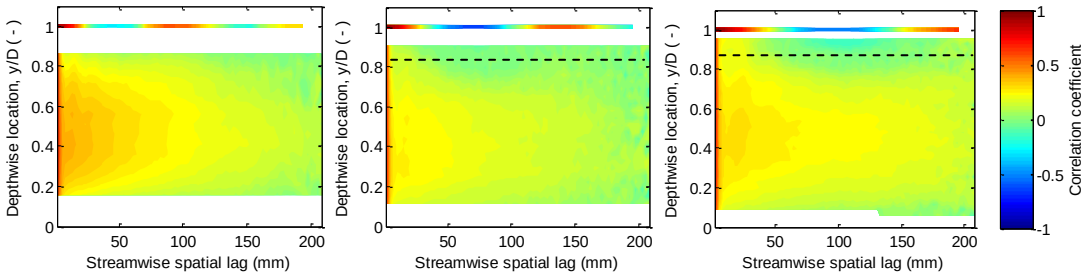

Figure 5-36: Spatial correlation function of vertical velocity fluctuation throughout flow depth and at free surface. Flow conditions 18 (left), 20 (middle), and 22 (right), (S_0 =0.004, D =50, 70, 90 mm respectively; V =0.36, 0.50, 0.65 m/s respectively). Dashed line represents the estimated depth of influence determined by the deepest location of zero correlation coefficient

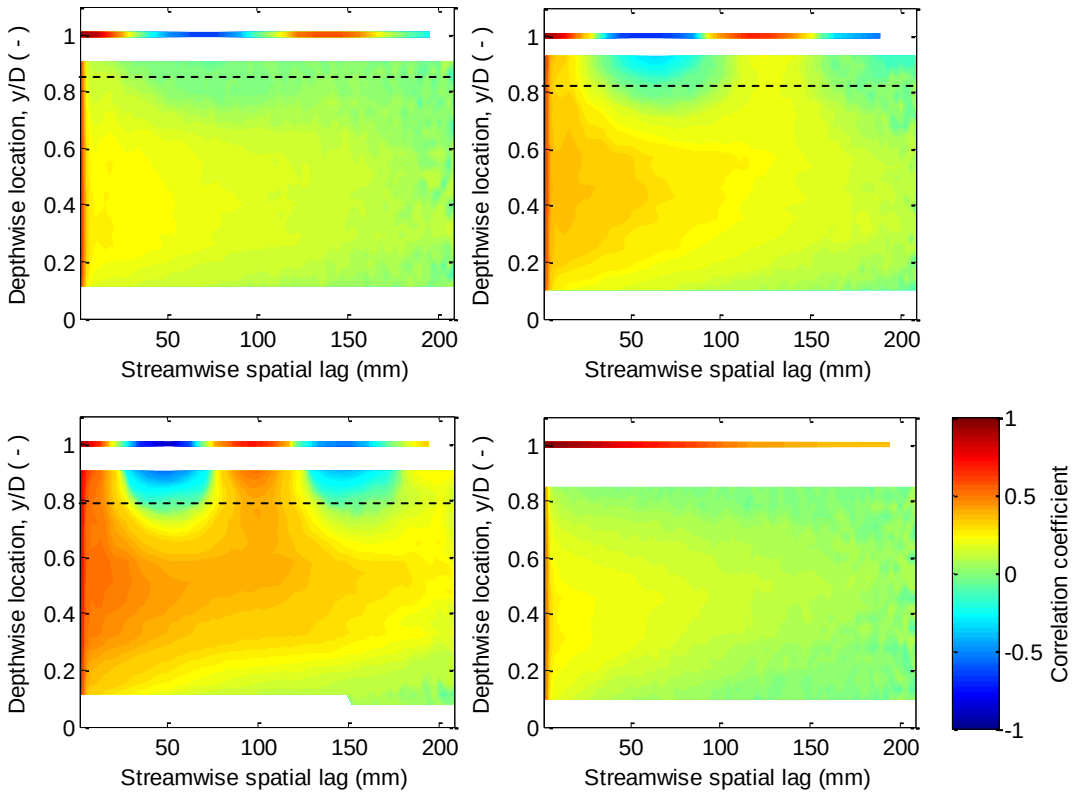

Figure 5-37: Spatial correlation function of vertical velocity fluctuation throughout flow depth and at free surface. Flow conditions 20 (tl), 26 (tr), 30 (bl), and 32 (br), (S_0 =0.004, 0.003, 0.002, 0.001 respectively; D =70 mm; V =0.50, 0.44, 0.32, 0.21 m/s respectively). Dashed line represents the estimated depth of influence determined by the deepest location of zero correlation coefficient

5.3.2 Free surface influence on near surface flow - summary

This section has shown that the near-surface velocity field of shallow turbulent flows is influenced by the behavior of the free surface, such that it exhibits an oscillatory component in the spatial correlation function, contrary to (though perhaps superimposed upon) the traditional linear decay. It has been shown that this oscillatory component reflects the influence of the inherent fluctuating nature of the free surface itself. For the gravel-bed flow conditions it has been shown that the free surface oscillations have a depth of influence equal to approximately 28 water surface roughness heights,

whereas for the sphere-bed flow conditions the depth of influence is around 19 roughness heights. The reasons behind this difference will be discussed further in section 5.4.

5.4 **A simple model for the behaviour of the free surface**

Whatever mechanism is generating surface features, the response of the free surface to such a mechanism is not well understood. This was highlighted by Savelsberg and Van de Water (2009), who concluded that while the free surface inherited some properties from the turbulent flow beneath, it also exhibited a behavior of its own which could not be fully characterised. Understanding the mechanism behind the apparent random nature of free surface fluctuations could unlock the potential to predict the free surface pattern for a given flow, and to use this information to inform models used in sound propagation, mixing, energy loss, and surface current studies. In this section the oscillatory behavior observed in the free surface fluctuations will be examined.

5.4.1 Modelling the response of the water surface to a disturbance

The correlation functions presented in Figure 5-8 are spatial correlations of temporal data in the frame of the stationary observer. These functions could equally well be represented as temporal correlations of spatial data in the frame of an observer travelling with the surface flow, by dividing the horizontal axis by the surface flow velocity. In this case it can be noted that the functions would resemble an underdamped simple harmonic motion. This

would help to explain the oscillatory nature of the free surface roughness pattern, by suggesting that the surface roughness pattern inverts periodically over time, as it advects at the surface flow velocity, giving rise to a new definition of the characteristic spatial period:

$$L_0 = V_s / f_o , \tag{5-25}$$

where V_s is the surface advection velocity, and f_o is the frequency of oscillation of the free surface pattern. This would explain the observations in Figure 5-23 which show the dominant free surface features to oscillate up and down over space and time, which can also be seen to some degree in the wave probe data of Figure 5-5. This is better understood by considering the surface roughness as an ensemble of disturbances generated by the sub-surface turbulent features as postulated by Savelsberg and Van de Water (2009), though their study focused on the resultant gravity waves rather than the behavior of the initial disturbance. It has been shown here that for passively generated turbulent free surfaces in shearing flow the oscillation of the initial disturbance is the dominant dynamic component of the free surface, with any gravity waves being negligible in amplitude in comparison. It is hypothesized that once formed, each of these initial disturbances oscillates about the mean surface level as the restorative forces of gravity and surface tension attempt to regain equilibrium. The concept of an oscillating free surface feature is new in the context of turbulence generated water surface roughness, but has been observed in other applications such as vibrating granular media (Eggers & Riecke, 1999; Rothman, 1998) and vertically vibrated pools of fluids (Shats, et al., 2012).

Umbanhowar et al. (1996) were the first to term waves of this type oscillons (oscillating solitons).

For the flows examined here, there are multiple turbulent structures formed in the flow, and hence there are expected to be multiple oscillons formed on the free surface at different points in space. These discrete oscillating features may well overlap, and since they may also appear at different times, they may well be out of phase with one another by different amounts. It was suspected that this is what gives rise to the very complex surface patterns which are observed by eye, but that perhaps this complex behavior may be explained by a number of overlapping (both in space and time) oscillons simply responding according to simple harmonic motion.

If the surface is now considered as a number of individual (albeit spatially and temporally overlapping) disturbances, the same frequency of surface inversion (and hence the same spatial correlation function, and characteristic spatial period) should be observed whether there is a single disturbance or a multitude. This will be tested by calculating the theoretical oscillation frequency of an individual surface feature, and comparing this with the measured value of oscillating frequency, f_o, determined from Equation 5-25 for all flow conditions.

First, a single free surface deformation (boil) is considered. Due to the weight of water lifted, and the component of surface tension acting downwards, a net downward force is present. Conveniently, if the system is released and the inertia causes the upward boil to become a downward dimple, the upward force is also a function of the weight of water displaced and the upward

component of the surface tension. This force sensibly increases as the mean height (or depth) of the free surface deformation increases. In this sense the system is analogous to a simple pendulum or indeed a spring and mass system, whereby the gravitational and surface tension forces act as a spring moving a mass of water up and down. The problem is thereby similar to determining the frequency at which a cork would bob up and down on a water surface, not unlike the half immersed circular cylinder described by Ursell (1949), who modeled the heave of boats, and found them to behave with a 'virtual mass' due to the influence on the nearby fluid.

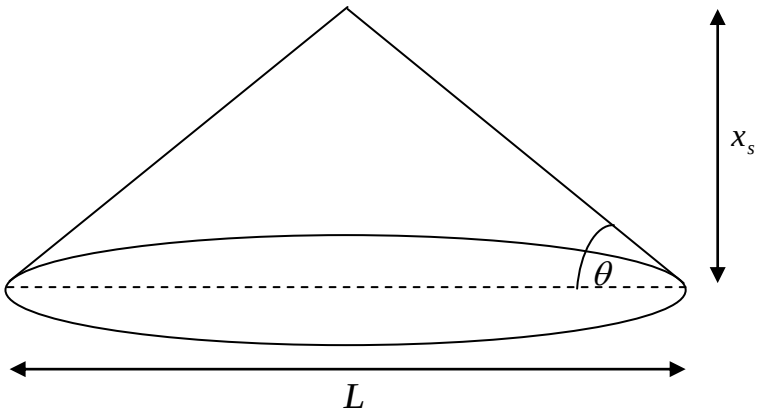

Figure 5-38: Idealized free surface deformation

Figure 5-38 considers an instantaneous surface boil as an idealized cone. Here x_s is the surface deformation height, L_s is the length of the turbulent structure generating the surface feature, and $\theta = \tan^{-1}\left(2x_s / L_s\right)$ is the idealized angle at which surface tension operates. The net downward force is given by the weight of the cone and the vertical component of surface tension around the circumference of the cone's base:

$$F_s = \pi L^2 \rho_f g x_s / 12 + \pi L_s \gamma_s \sin(\theta), \quad (5\text{-}26)$$

where ρ_f is the density of the fluid, g is the acceleration due to gravity, and γ_s is the surface tension force per meter. It can be shown that for small angles, $\sin(\theta) \approx \tan(\theta)$, allowing Equation 5-26 to be simplified to:

$$F_s = \pi L_s^{\,2} \rho_f g x_s / 12 + 2\pi x_s \gamma_s, \quad (5\text{-}27)$$

From standard spring theory, the spring stiffness $K = F_s / x_s$ is defined as the force exerted per unit of deflection. In this case the stiffness of the system can be defined as:

$$K = \pi L^2 \rho_f g / 12 + 2\pi\gamma_s, \quad (5\text{-}28)$$

The mass of the spring-mass system is now considered. Since it is known that the behaviour of the free surface is exhibited to a certain depth of influence ($\mathrm{N}\sigma$, where N is the number of water surface roughness heights, termed the depth of influence factor) below the mean surface level, the mass on which the 'spring' is acting is not simply the mass of the initial boil of water. This is synonymous with the virtual mass concept introduced by Ursell (1949). It is likely that as the amplitude of oscillation reduces, the mass of water influenced by the oscillon will also reduce, so to represent the mean behaviour of a given oscillon during its existence, the disturbance height is taken as the RMS value of water surface roughness height, σ. As a first approximation, a circular zone of influence is considered whose area decreases linearly from L_s at the free surface to zero at N roughness heights below the free surface. The volume of water in this zone of influence

is equal to that of a cylinder of diameter L_s and height $\mathrm{N}\sigma/2$. As such, the total mass of the system including the cone shaped boil is given by:

$$M_s = \frac{1}{8}\pi \mathrm{N}\rho_f L_s^2 \sigma + \frac{1}{12}\pi\rho_f L_s^2 \sigma = \frac{1.5\mathrm{N}+1}{12}\pi\rho_f L_s^2 \sigma\,, \tag{5-29}$$

It can be seen that the second term (arising from the mass of the cone) is negligible in comparison to the first term (the mass of water acted upon below). Although the mass of the cone is retained in the equation for completeness, this shows that the idealization of modeling the upward boil (or downward dimple) as a cone does not significantly affect the resulting mass.

The frequency of simple harmonic motion can be calculated by:

$$f_{shm} = \frac{1}{2\pi}\sqrt{\frac{K}{M_s}}\,, \tag{5-30}$$

and substituting in Equations 5-28 and 5-29 this gives:

$$f_{shm} = \frac{1}{2\pi}\sqrt{\frac{g}{(1.5\mathrm{N}+1)\sigma} + \frac{24\gamma_s}{(1.5\mathrm{N}+1)\rho_f L_s^2 \sigma}}\,. \tag{5-31}$$

For water at room temperature, surface tension is small ($\gamma_s \approx 0.073 N/m$), and fluid density is large ($\rho_f \approx 1000 kg/m^3$), so that the second term becomes negligible. This further shows that the simplification of modeling the disturbance as a cone does not have a significant effect on the result. Neglecting the surface tension term allows the frequency of oscillation to be expressed solely as a function of the deformation height (or RMS water surface roughness height), σ, and the depth of influence factor, N:

$$f_{shm} = \frac{1}{2\pi}\sqrt{\frac{g}{(1.5\mathrm{N}+1)\sigma}}\,. \tag{5-32}$$

Equation 5-32 was used to predict the oscillation frequency of surface features for each of the flow conditions using the RMS water surface roughness heights from Table 5-2 and $\mathrm{N}=28$, $\mathrm{N}=19$ for the gravel and sphere bed conditions respectively, as estimated in section 5.3.1. The true measured oscillation frequency was calculated from Equation 5-25. These experimental data points are given in Figure 5-39 along with theoretical curves from Equation 5-32, plotted against the RMS roughness height. The relationships carry a clear physical sense, since as the water surface roughness height tends toward zero, the mass of water being acted upon also tends toward zero, so the frequency of oscillation tends toward infinity. As the roughness height tends toward infinity, so too does the mass of affected water, meaning the frequency tends toward zero.

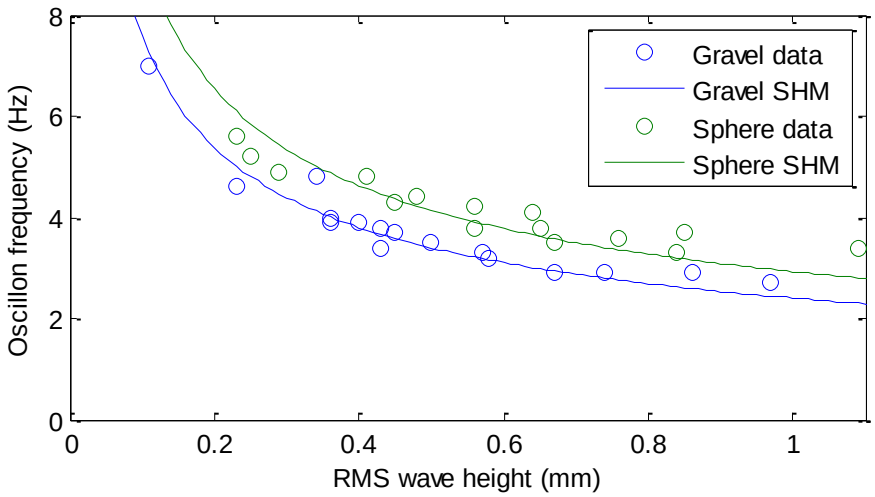

Figure 5-39: Measured (markers) and modeled (solid lines) surface oscillation frequency

While the theoretical curves match the experimental data well, the presented equation relies on the knowledge of the depth of influence of the surface behavior ($N\sigma$). In order to generate a general formula, the reason for the difference in the two depth of influence factors, N, must be established. The most likely explanation is that the two bed types establish different types of turbulence field, which may be more or less resilient to the effects of the free surface oscillation. The bed structure and porosity is expected to play some role in the oscillon behavior as the vertical pressure fluctuations may interact with the porous bed and in this process some of the kinetic energy may become lost due to the viscous friction and inertial effects within the bed pores. However the data here, and the range of bed types used (two), is not sufficient to validate these hypotheses.

Other than the bed material, the only broad difference between the gravel and sphere bed data is that due to time constraints the gravel data was collected during summer, while the sphere data was collected during winter meaning there was a broad difference of around 8 °C between the water temperature for the gravel tests and for the sphere tests. It is unclear whether the difference in temperature is significant enough to invoke such a difference in the depth of influence factor, since the effects of this temperature difference on viscosity and surface tension are small.

Further work is required to establish and isolate the effects of water temperature and bed roughness type on the depth of influence factor.

The measured data confirms the existence of turbulence generated free surface oscillons. The results support remarkably well the hypothesis that

however complex a flow surface may appear, its dynamic nature can be understood simply by each of the individual surface deformations behaving according to simple harmonic motion. The relationship is upheld irrespective of the flow conditions. The small errors seen between the measured and modelled frequencies are likely to be the combined effect of marginal errors in the surface velocity, RMS water surface roughness height, and characteristic spatial period.

The primary result of this section is that the fundamental independent nature of the free surface has been discovered and can be explained by a simple deterministic theory. This process acts alongside the appearance of new deformations and perhaps also the resulting gravity waves that were reported by Savelsberg and Van de Water (2009), (though gravity waves have not been observed on flow surfaces in this study). Together, these three processes may capture the true and complete dynamic nature of turbulence induced free surface roughness. Although in this work the presence of gravity waves was not detected, theory suggests that they must be present, and may simply be too small to be detected alongside the dominant oscillatory nature, but nevertheless should not be neglected in future work.

Further study should investigate the decay rate (correlation radius) of the spatial correlation functions. Several factors may affect the oscillon attenuation, but in the simple case this is expected to be a function of the viscous damping of surface fluctuations and the emergence rate of new turbulent structures. This is suggested by a comparison of the free surface spatial correlation radius with the spatial frequency of turbulent events at the free surface, using the free surface spatial correlation function data of Table

5-3, and the surface feature U-level data from Table 5-4. This is shown in Figure 5-40 which shows that the correlation radius tends to decreases as the spatial frequency of free surface structures increases. The reason for the variability in this relationship may be due to the difficulty in accurately estimating the correlation radius from a small number of periods of the spatial correlation function.

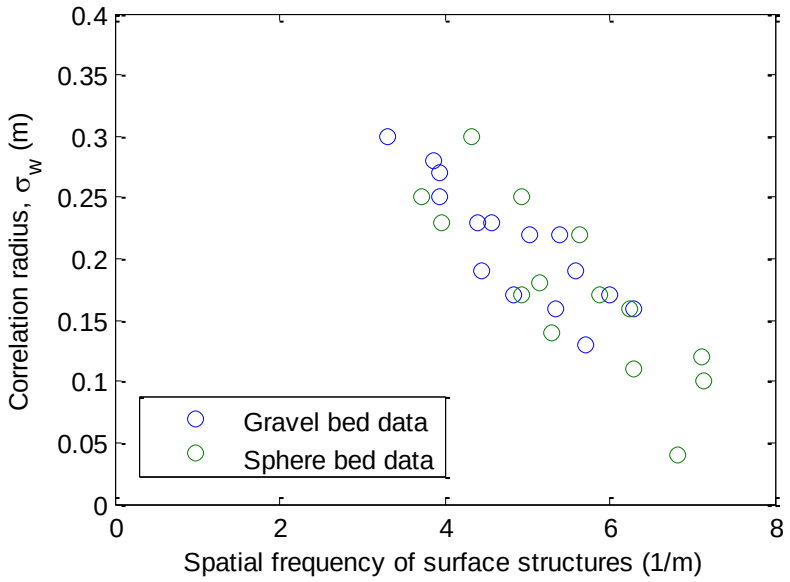

Figure 5-40: Correlation radius of free surface fluctuations generally decreases according to the spatial frequency of turbulent structures

A further relationship of note is the comparison of the spatial frequency of the free surface oscillons ($1/L_0$) and the spatial frequency of turbulent structures measured in the free surface data ($1/S_U$). It would initially seem that these properties should not necessarily show a direct general relation, since the oscillon spatial frequency depends on the bed type, while the structure spatial frequency is simply a general function of the free surface advection

velocity. However these two spatial frequencies do indeed show a general relationship (Figure 5-41) which may be expressed as:

$$\frac{1}{S_U} = 2.89 \ln\left(\frac{1}{L_0}\right) - 0.57 \tag{5-33}$$

This perhaps suggests that the bursting events which generate turbulent structures at the bed may be initiated by the vertical pressure fluctuations produced by the motion of the free surface oscillons, with the logarithmic trend arising from the interaction between turbulent structures within the logarithmic velocity profile between the bed (where structures are generated) and the surface (where they are observed). Such a trigger mechanism has not been previously proposed (presumably because free surface oscillons have not been observed in this context before). This relationship may hold the key to truly understanding why bursting events occur in shallow flows, and how this affects the resulting turbulence field and flow characteristics. This could help to resolve the ‘chicken and egg’ argument of whether turbulent bursts initiate turbulent structures or vice-versa (Roy, et al., 2004; Komori, et al., 1989; Yalin, 1992), by showing that the bursts are triggered by a different process, and not by the turbulent structures.

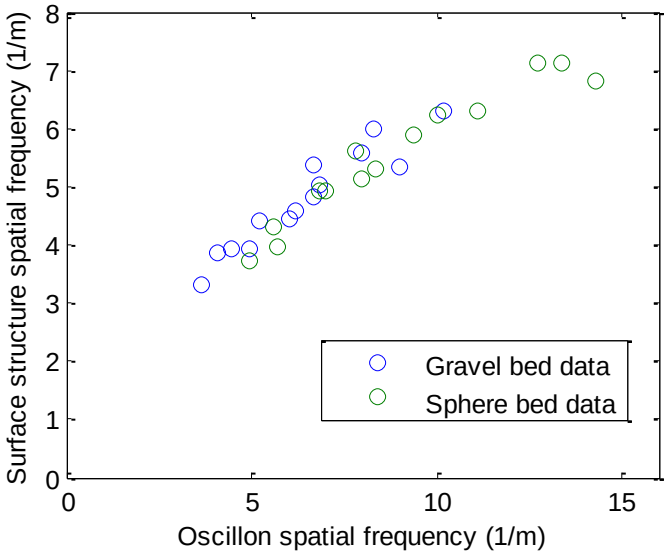

Figure 5-41: Spatial frequency of turbulent structures may be governed by the spatial frequency of the free surface oscillatory motion

5.4.2 Surface model conclusions

It has been shown that the oscillation of free surface features can be explained by simple harmonic motion, whereby the frequency of oscillation is solely a function of the RMS water surface roughness height and depth of influence factor of the free surface behaviour. This suggests that the relationship is irrespective of the longitudinal and transverse size or shape of the surface disturbances, and can be extended to other fluids so long as the effects of surface tension remain small. If surface tension becomes large, the theory should still apply but surface tension effects must be accounted for, meaning the motion also becomes a function of the surface tension and the shape and size of surface features in the horizontal plane. This model allows an understanding of the surface tension effects, critical for assessing the validity of small hydraulic river models (Peakall & Warburton, 1996). The discovered relationship allows for a radically new understanding of free

surface roughness whereby the complex surface pattern can be described as a number of temporally and spatially distributed and overlapping oscillons, induced by turbulent structures generated by the flow, and each responding according to simple harmonic motion. It is also of note that existing oscillon theory describes the attraction and pairing of opposite signed oscillons into stable dipoles. While this is not conclusively observed in this study, some of the features in Figure 5-23 appear to be grouped in this way, warranting further investigation.

5.5 **Flow surface and sub-surface behavior and interaction - summary**

It can be concluded from these analyses that the apparently complex dynamic nature of flow surfaces can be decomposed into three unambiguous processes: (1) new structures impinge on the free surface and form local deformations, (2) these deformations behave as oscillons according to simple harmonic motion, (3) These oscillons may generate gravity waves which propagate radially (this would seem sensible though the evidence in this study suggests the influence of these waves to be negligible in this context).

This section has shown that the free surface behavior and the bulk flow properties are inherently linked. The key relationships discovered are summarized in Table 5-6.

Table 5-6: Summary of discovered surface/sub-surface relationships

Equation number	Equation	Explanation
5-7	$L_0 / k_s = 0.045 \times e^{0.54V/U_*}$	The characteristic spatial period of the free surface carries information about the bed roughness and the velocity profile.
5-8	$\sigma_w / k_s = 1.1 \times 10^{-3} VD / \upsilon$	The correlation radius of the free surface roughness to the bed roughness and the flow Reynolds number.
5-10	$\sigma_w / k_s = 4 \times 10^{-4} V_S L_0 / \upsilon$	The correlation radius of the free surface roughness to the bed roughness and the free surface based Reynolds number, allowing hydraulic roughness to be defined in terms of surface properties alone.
5-23	$L_U = 0.147 V_s$	The length of turbulent structures apparent in the free surface pattern is proportional to surface velocity. This is general for all flow conditions and bed types studied.
5-23	$S_U = 0.374 V_s$	The distance between turbulent structures apparent in the free surface pattern is proportional to surface velocity. This is general for all flow conditions and bed types studied.
5-32	$f_{shm} = \frac{1}{2\pi}\sqrt{\frac{g}{(1.5\mathrm{N}+1)\sigma}}$	The frequency of oscillation of free surface features (oscillons) is governed by the RMS surface roughness height and the depth of influence of the surface behavior.
5-33	$\frac{1}{S_U} = 2.89 \ln\left(\frac{1}{L_0}\right) - 0.57$	The spatial frequency of the free surface oscillons is strongly related to the spatial frequency of turbulent structures observed in the free surface pattern, suggesting structure generation at the bed may be controlled by surface oscillon behaviour.

This knowledge may allow for measurement of bulk flow conditions based on the free surface fluctuation data, but for many applications the conductive wave probes are too invasive, and the PIV system is not practical. A robust, non-invasive technique is required for the measurement of free surface behavior if the relationships discovered in this section are to be of any practical use.

5.6 **Acoustic measurement of the dynamic boundary**

The previous results sections have shown that measurement of the temporal properties of free surface fluctuations can facilitate conditional analysis of the turbulence properties beneath the surface, and that these properties are directly related to the flow conditions, while spatially distributed measurements allow the calculation of flow surface velocity and the spatial correlation function, which also relates to the flow conditions. This section will focus on the development of acoustic theory to allow the remote measurement of free surface fluctuations, and (by reversal) the prediction of the effect of a dynamic surface roughness on a nearby acoustic field.

This work is based on the use of a continuous monochromatic ultrasonic wave as it enables direct analysis of the time series, rather than statistical analysis of discrete measurements as suggested by Cooper et al (2006). The ultrasonic transducer adopted in this work provides a directional acoustic signal which facilitates the minimisation of unwanted multiple reflections.

5.6.1 Acoustic theory

Consider an incident acoustic plane wave radiated by the source (see Figure 5-42),

$$v_s(t) = A_0(t).e^{i\omega_s t}, \tag{5-34}$$

and reflected from a flat, acoustically hard surface which oscillates vertically. The reflected acoustic wave,

$$v_r(t) = A_r(t).e^{i\omega_s t + i\varphi_s + i\Delta\varphi}, \tag{5-35}$$

which is received at a microphone some distance away has a difference in phase, $\varphi_s + \Delta\varphi$, when compared to the transmitted signal due to the time taken for the acoustic wave to travel from source to receiver. Here ω_s is the signal frequency, A_0 is the amplitude of the incident sound wave, A_r is the amplitude of the reflected wave, t is the time, φ_s is the mean (or initial) phase difference, $\Delta\varphi$ is the fluctuating phase term generated by the surface movement, and $i = \sqrt{-1}$. When the reflecting boundary is stationary the phase difference is constant and time independent. If the surface moves vertically, then the phase difference and the amplitude of the reflected wave can be altered due to the change in path-length as shown in Figure 5-42.

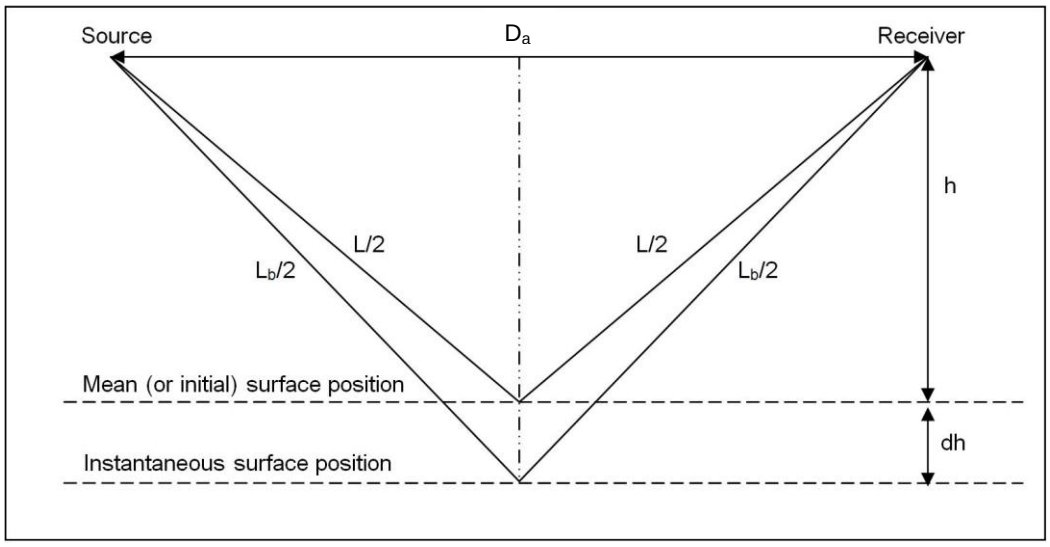

Figure 5-42: Change in effective path-length caused by surface movement

Here the source and receiver are both a distance h above the mean position of the water surface, separated by a distance D_a. The change in phase

difference, $\Delta\varphi$, caused by the surface moving down by a distance of $\Delta h(t)$ is given by:

$$\Delta\varphi(t) = -2\pi\Delta L(t)/\lambda\,, \tag{5-36}$$

Here λ is the acoustic wavelength and $\Delta L(t)$ is the time dependent change in path-length given by:

$$\Delta L = L_b - L\,, \tag{5-37}$$

where L and L_b are the original and new path-lengths respectively, given by:

$$L = 2\sqrt{\left(\frac{D_a}{2}\right)^2 + h^2}\,, \quad L_b = 2\sqrt{\left(\frac{D_a}{2}\right)^2 + \left(h+\Delta h\right)^2} \tag{5-38}$$

In Equations 5-37 and 5-38 time dependence is omitted for brevity. Reversing the process, the change in surface position, Δh, can be calculated directly from the recorded variation in phase difference:

$$\Delta h = \sqrt{\left(\frac{L_b}{2}\right)^2 - \left(\frac{D_a}{2}\right)^2} - h\,, \tag{5-39}$$

where

$$L_b = \Delta L + L\,, \text{ and } \Delta L = -\Delta\varphi\lambda/2\pi \tag{5-40}$$

Again, time dependence is omitted for brevity. The phase time series used here is that calculated from Equation 4-11 in section 4.4.

The spatial accuracy of this technique is limited by the assumption of a ‘flat’ surface and the ‘footprint’ of the acoustic signal, i.e. the ensonified area of the surface which contributes to the sound field at the receiver point. This

may be estimated by Fresnel theory (Nocke, 2000), which enables the definition of a zone on the reflecting surface for which the distance from source to receiver, via any point in that zone, does not exceed the distance of the specular reflection by more than a predetermined value $F\lambda_a$. This value of the path length difference is usually expressed in multiples of the acoustic wavelength, λ_a. For acoustically hard surfaces, such as water, two adjacent Fresnel zones defined by $F = n/2$ with $n = 1,2,3...$ will cancel as their contributions to the total field are out of phase. This has been proven experimentally by Spandöck (1934) for acoustic waves. Furthermore, as the amplitude excited by following Fresnel zones decreases, the first (half) zone makes the most important contribution to the total field, e.g. $F = 1/2$. Assuming that all areas of this dominant Fresnel zone contribute equally to the received signal, this would mean the technique would be suitable for measuring water surface waves/roughness with a spatial period greater than the Fresnel Zone diameter. This forms the first criterion (criterion 1). In reality, transducers have directivity patterns which generate greater energy levels in the specular direction. Therefore the effective Fresnel zone is generally smaller than that predicted by the Fresnel theory and depends on the transducer directivity.

5.6.2 Experiments

It has been shown above that fluctuations in water surface position may theoretically be quantified by measurement of the variation in the phase difference between a sent and received signal reflected from a dynamic air-

water interface. To demonstrate this, the flume (with the gravel bed) was first set to a horizontal gradient and simple gravity waves with large spatial scale were generated in still water. Then the flume was tilted to a gradient of 0.004 and a range of steady uniform flows were established in order to generate surface fluctuations of varying scale and spectral composition. For these tests, the ultrasonic transducer was positioned at an angle of 45° to the mean water surface position, and a single microphone was placed in the path of the specular reflection as described in section 3.5 and shown in Figure 3-20.

To quantify the performance of the acoustic based instrumentation the water surface elevation at the point of specular reflection was recorded using a calibrated Churchill twin-wire conductive wave probe (the same equipment as used in section 5.1).

Each acoustic packet was analysed according to Equation 4-11 so that the mean time-dependent phase difference was calculated for each packet. The phase time series obtained from this analysis was then unwrapped in order to correct for the phase switching between $+\pi$ and $-\pi$ when the change in surface elevation exceeded one acoustic wavelength ($\Delta L > \lambda_a = 7.9$ mm at 43 kHz in air). The process described by Equation 5-39 and Equation 5-40 was then used to convert phase difference values into surface elevation measurements so that the water surface elevation fluctuation could be presented as a function of time.

A 3rd order 10 Hz low-pass Butterworth filter (the same type applied to the wave probes) was applied to the surface elevation data from the acoustically

derived measurements. The wave probe data was then used to validate the results of the acoustically based measurements.

5.6.3 Gravity waves

In the first stage of testing, the flume was set at a gradient of zero with its upstream and downstream ends sealed, and still water was introduced. The water surface was then excited with simple pseudo-sinusoidal surface gravity waves generated by manually oscillating a plate at one end of the flume, hinged at the bed as shown in Figure 5-43. Waves were generated at four different depths: 85 mm, 119 mm, 158 mm and 181 mm. At each depth the excitation plate was manually operated at three approximate frequencies of 0.5 Hz, 1 Hz, and 2 Hz. For each frequency at each depth, the angular range of motion of the excitation plate was manually controlled to approximately ±5°, ±10°, and ±20° from vertical. This resulted in thirty-six individual wave conditions, each with different wave properties (frequency, wavelength, wave height, phase speed).

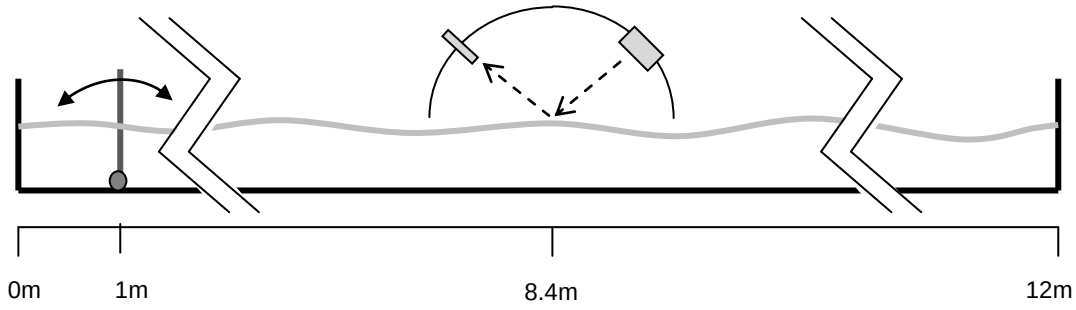

Figure 5-43: Simple surface wave excitation

For each of the thirty-six wave conditions, surface elevation data was recorded synchronously by the wave probe and the acoustic device. A time window was applied so as to eliminate any waves reflected from the end of the flume. The wave probe data was used to quantify the mean depth, D, and the root-mean-square (RMS) wave height, σ. The dominant frequency component, f_d, was also calculated by taking a weighted average of the frequency spectrum, whereby the frequency components were weighted by their Fourier coefficient. Using the measured depth and frequency, a least squares minimisation routine determined the phase speed, C_p, by finding the optimum value to minimize variable z in Equation 5-41, which is based on linear wave theory for gravity wave propagation (Airy, 1841; Landau & Lifshitz, 2011).

$$z = C_p - \sqrt{\frac{gC_p}{2\pi f}\tanh\left(\frac{2\pi f_d D}{C_p}\right)} \tag{5-41}$$

Once the dominant frequency and phase speed were known, it was possible to calculate the dominant wavelength, $\lambda = C_p / f_d$. These data are given in Table 5-7.

Table 5-7: Gravity wave conditions (wave probe data)

Wave condition	Average depth D (m)	RMS wave height σ (mm)	Fluctuation frequency f_d (Hz)	Phase speed C_p (m/s)	Wavelength λ (m)
1	0.085	0.02	1.5	0.79	0.51
2	0.085	0.02	2.0	0.71	0.36
3	0.085	0.03	1.4	0.81	0.56
4	0.086	0.04	1.0	0.86	0.85
5	0.085	0.05	1.2	0.84	0.71
6	0.085	0.08	1.1	0.85	0.78
7	0.085	0.11	0.8	0.88	1.07
8	0.085	0.15	1.1	0.85	0.77
9	0.085	0.21	0.7	0.89	1.22
10	0.119	0.36	2.2	0.69	0.31
11	0.119	0.47	1.1	0.99	0.94
12	0.119	0.56	1.4	0.91	0.65
13	0.119	0.98	0.7	1.00	1.34
14	0.119	1.04	1.2	0.96	0.82
15	0.119	1.23	0.9	1.00	1.13
16	0.119	1.68	2.0	0.75	0.38
17	0.119	1.88	1.6	0.86	0.54
18	0.119	2.06	0.9	1.00	1.08
19	0.158	1.02	2.1	0.75	0.37
20	0.158	2.04	1.0	1.00	1.00
21	0.158	3.60	0.7	1.00	1.36
22	0.158	4.06	0.9	1.00	1.09
23	0.158	4.58	2.0	0.77	0.38
24	0.158	4.83	1.9	0.79	0.41
25	0.158	6.20	1.5	0.94	0.61
26	0.158	8.05	1.4	0.99	0.71
27	0.158	9.78	1.3	1.00	0.77
28	0.181	1.35	1.7	0.88	0.51
29	0.181	1.70	1.0	1.00	0.98
30	0.181	2.27	1.0	1.00	1.05
31	0.181	5.04	2.0	0.76	0.37
32	0.181	5.60	1.8	0.83	0.45
33	0.181	5.94	0.8	1.00	1.32
34	0.181	7.60	1.3	1.00	0.79
35	0.181	8.03	1.4	1.00	0.73
36	0.181	8.61	1.5	0.97	0.64

These simply excited gravity waves were approximately sinusoidal in nature. In all wave conditions the wavelength is greater than the diameter of the first Fresnel zone which, in the experimental setup used in this work, equates to approximately 0.11 m. This satisfies the criterion derived in section 5.6.1, suggesting that the acoustic theory should apply. The time series of wave probe and acoustic data from wave conditions 7, 17, and 32 are shown in Figure 5-44. Recordings were started when the first strong wave reached the measurement location, and were cropped to 6 seconds to avoid including any reflections from the flume end. Zero on the vertical axis represents the mean surface position. Note the change in scale on the vertical axis.

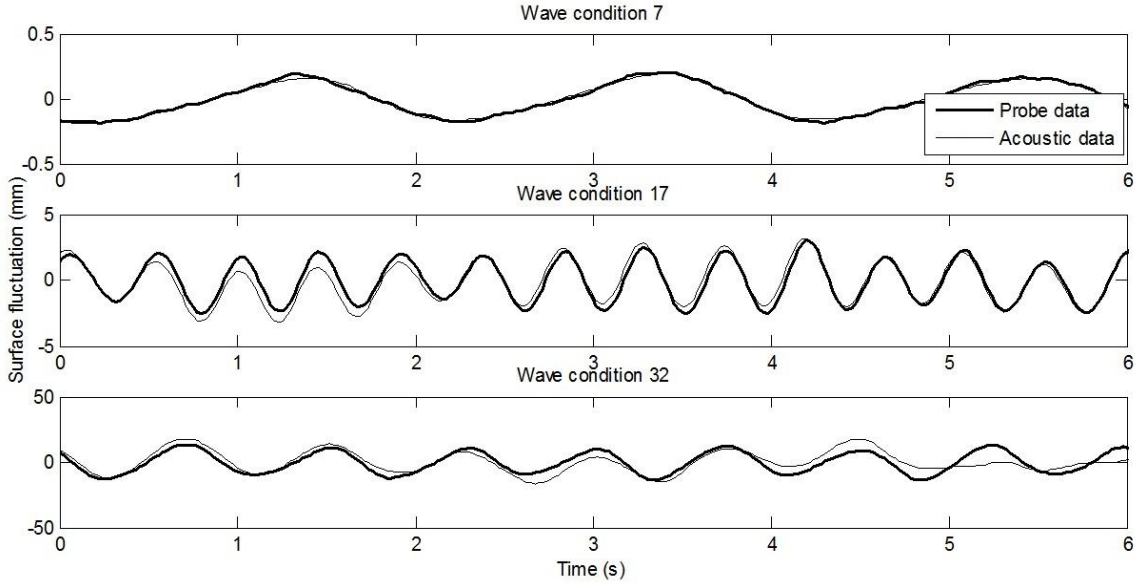

Figure 5-44: Comparison of acoustic and wave probe data for gravity wave time series for wave conditions 7, 17 and 32, with wave properties respectively: λ =1.07, 0.54, 0.45 m; σ =0.11, 1.88, 5.60 mm; C_p =0.88, 0.86, 0.83 m/s; f =0.8, 1.6, 1.8 Hz

It can be seen that the variation in acoustic phase generally tracks the fluctuations in local water surface elevation. The system is effectively acting as an acoustic wave probe. This relationship is strong for wave condition 7,

even though the fluctuations themselves are very small ($\sigma = 0.11$ mm). For wave condition 17 some deviation between probe and acoustic data is observed in some areas of the time series. For wave condition 32 there are departures of a larger magnitude, and toward the end of the series there is sustained deviation. There are two initial explanations for this progressive error. First, the Fresnel zone approximation would suggest that as the wavelength of gravity waves is decreased, errors become more likely, as closer adjacent wave features begin to affect the reflection of sound from the dominant Fresnel zone. Secondly, as is apparent from the vertical axes in Figure 5-44, an increased wave height may cause an increase in the error. In order to investigate this, the measurement error was calculated for each wave condition. By comparing the wave probe data against the acoustically estimated surface elevation data it was possible to determine the mean absolute error, $E = \langle | \eta_a - \eta_w | \rangle$ where η_a is the acoustically measured fluctuation time series, and η_w is that measured by wave probe. Since the accuracy is governed by the resolution of the phase measurement, which itself is governed by the wavelength of the acoustic signal, in order to examine the accuracy of the method the absolute error value may also be expressed as a percentage of the acoustic wavelength ($\lambda_a = 7.9$ mm), $E_a = E / \lambda_a \times 100\%$. The relative error, $E_{pp} = E / h_{pp} \times 100\%$, expresses the absolute error as a percentage of the peak to peak wave height, since this gives a more practical measure of how closely the wave data is captured by the acoustical system. These data are given in Table 5-8, along with the RMS wave height, σ, peak to peak (p-p) wave height, h_{pp}, and dominant wavelength, λ.

Table 5-8: Gravity wave measurement accuracy

Wave condition	RMS wave height σ (mm)	p-p wave height h_{pp} (mm)	Wavelength λ (m)	Mean absolute error E (mm)	Mean error as % of acoustic wavelength E_a (%)	Mean error as % of p-p wave height E_{pp} (%)
1	0.02	0.10	0.51	0.01	0.11	8.25
2	0.02	0.10	0.36	0.01	0.12	8.60
3	0.03	0.13	0.56	0.01	0.13	7.25
4	0.04	0.19	0.85	0.01	0.11	4.47
5	0.05	0.22	0.71	0.01	0.13	4.27
6	0.08	0.56	0.78	0.01	0.14	1.82
7	0.11	0.45	1.07	0.01	0.14	2.34
8	0.15	0.59	0.77	0.01	0.17	2.22
9	0.21	0.76	1.22	0.01	0.15	1.54
10	0.36	2.00	0.31	0.04	0.59	2.23
11	0.47	2.03	0.94	0.02	0.32	1.21
12	0.56	2.58	0.65	0.05	0.60	1.75
13	0.98	4.18	1.34	0.02	0.33	0.59
14	1.04	4.24	0.82	0.07	0.95	1.70
15	1.23	5.27	1.13	0.05	0.61	0.88
16	1.68	6.61	0.38	0.19	2.51	2.88
17	1.88	9.05	0.54	0.22	2.88	2.41
18	2.06	7.56	1.08	0.06	0.79	0.79
19	1.02	7.39	0.37	0.18	2.38	2.44
20	2.04	7.85	1.00	0.05	0.70	0.67
21	3.60	13.58	1.36	0.35	4.64	2.58
22	4.06	15.88	1.09	0.12	1.54	0.73
23	4.58	20.34	0.38	2.38	31.52	11.71
24	4.83	26.63	0.41	2.71	35.84	10.17
25	6.20	26.58	0.61	3.15	41.67	11.84
26	8.05	33.98	0.71	5.01	66.34	14.75
27	9.78	44.29	0.77	5.73	75.90	12.95
28	1.35	8.96	0.51	0.11	1.39	1.17
29	1.70	8.63	0.98	0.07	0.93	0.81
30	2.27	11.22	1.05	0.10	1.27	0.85
31	5.04	27.10	0.37	3.39	44.92	12.52
32	5.60	29.63	0.45	3.10	41.01	10.46
33	5.94	25.03	1.32	0.35	4.69	1.42
34	7.60	39.45	0.79	3.98	52.67	10.09
35	8.03	41.28	0.73	5.45	72.14	13.21
36	8.61	39.58	0.64	5.37	71.03	13.56

Examining the theory that reduced wavelength or increased wave height may prompt an increase in error, the mean absolute error values are plotted against wavelength and RMS wave height in Figure 5-45. It can be seen that the data falls into two groups, one with low error (mean absolute error <5%) and one with high error (mean absolute error >30%). Although there is a general pattern among the high error data whereby decreased wavelengths and increased wave heights appear to cause increased error, this dependence cannot be relied upon because several of the low error data points have small wavelengths, and several have large wave heights.

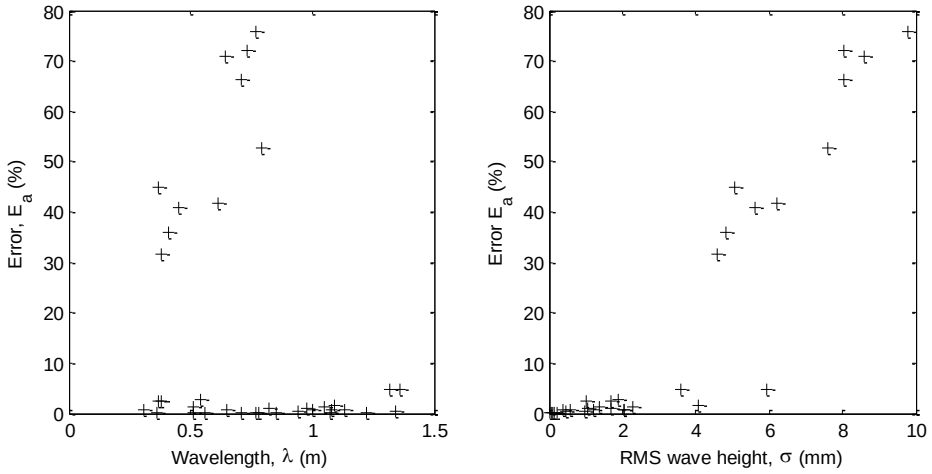

Figure 5-45: Mean absolute measurement error vs. wavelength and wave height

It was noted that the wavelength and wave height may be affecting the validity of the measurement technique when their influence is examined in combination. It was found that the ratio of wave height to wavelength is strongly correlated with the measurement error. Figure 5-46 shows the mean error (as percentage of acoustic wavelength, $E_a = E / \lambda_a \times 100\%$) as a function of the ratio of RMS wave height to wavelength.

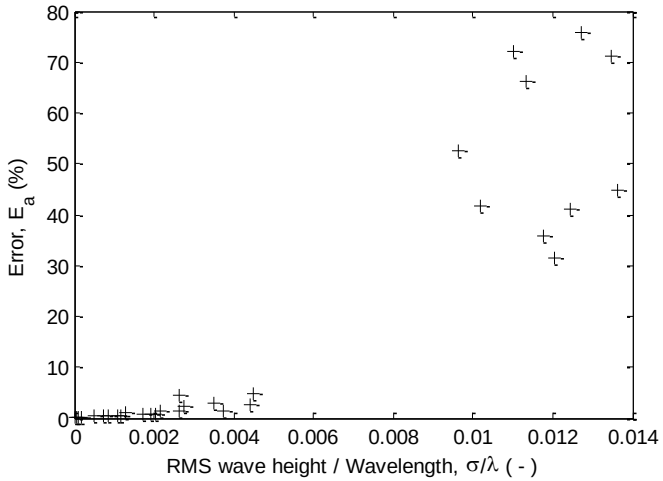

Figure 5-46: Mean absolute error vs. wave height / wavelength

Figure 5-46 can be used to define a threshold beyond which the error becomes significant. In order to expect that the mean error in the water elevation measurement is below 5% this threshold can be set as $\sigma / \lambda = 0.005$. Below this threshold the errors may be dominated mainly by the accuracy in the phase measurements and by the size of the Fresnel zone. This ratio of wave height to wave length can be thought of as a measure of the local surface gradient. Indeed, by using the recorded time series of surface elevation, η, and the calculated values of C_p, the mean absolute local gradient, G, of a time series of N samples can be calculated for each wave condition as:

$$G = \frac{1}{N} \frac{\sum_{i=1}^{N} \left| \frac{d\eta}{dt} \right|}{C_p} \tag{5-42}$$

This is plotted against the ratio of RMS wave height to wavelength in Figure 5-47.

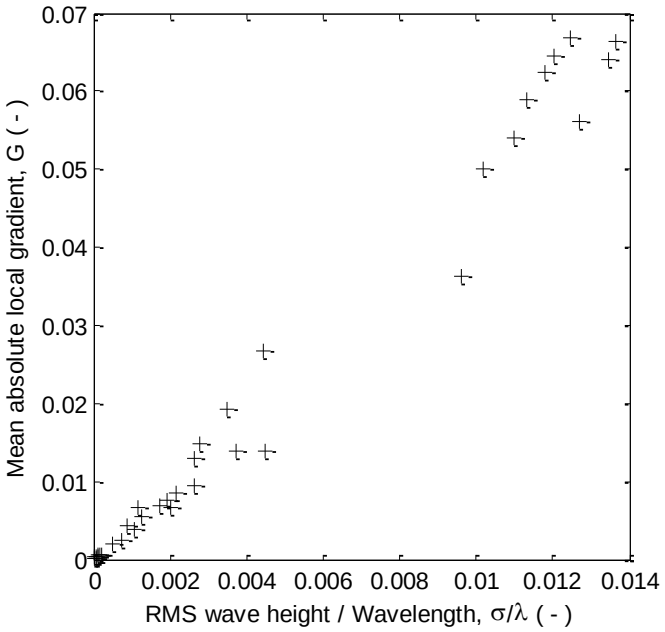

Figure 5-47: local gradient vs. wave height / wavelength

It can be seen that the relationship is close to linear. In this case the threshold mean absolute surface gradient beyond which the technique would likely fail is $G = 0.025$. The $\sigma / \lambda = 0.005$, or $G = 0.025$ threshold forms the next criterion (criterion 2). In some cases, where the water surface pattern has a broad spatial spectrum, it may be difficult to estimate the dominant wavelength and wave height. In these instances measurements of the local surface gradients may be more practical as they can be estimated from photographs.

These results show that for a given application, the expected error of this measurement technique may be predicted by visual estimation of the dominant wavelength and wave height or, for more complex surface patterns, an assessment of the local surface gradients. As the errors have been non-dimensionalised with the acoustic wavelength and expressed in terms of the

local surface gradient, the result is general, and provided a situation meets the wave gradient threshold the same level of accuracy can be expected.

The *relative* error, $E_{pp} = E / h_{pp} \times 100\%$, is the *absolute* error, $E = \langle | \eta_a - \eta_w | \rangle$, expressed as a percentage of the peak to peak wave height, h_{pp}. It gives an indication of how closely the acoustic phase variation matches the measured wave pattern, and is a more practical description of the accuracy of the system as it is presented in relation to the scale of waves being measured. For the wave conditions which satisfy the $\sigma / \lambda = 0.005$ criterion, this relative error, E_{pp}, is plotted against h_{pp} in Figure 5-48, along with the absolute error as a percentage of the acoustic wavelength.

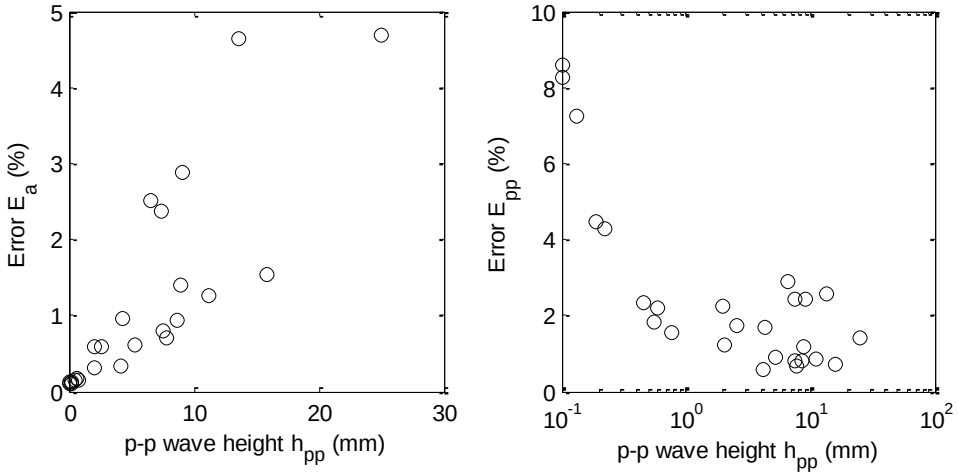

Figure 5-48: Error relative to acoustic wavelength, E_a, and relative to p-p wave height, E_{pp}, plotted against the p-p wave height, h_{pp}

In the plot of relative error, E_{pp}, the horizontal axis is logarithmic in order to emphasise the behaviour in the case of small wave height conditions. Although the *absolute* error for these wave conditions generally increases with wave height, the error *relative* to the wave height is significantly higher

for waves of low amplitude. In these experiments, for the wave conditions which satisfy the gradient criterion, the relative error becomes larger (>3%) when the peak to peak wave height, h_{pp} is below 0.3 mm or 4% of the acoustic wavelength. This provides an additional criterion whereby waves of very small wave height (less than 4% of the acoustic wavelength) may result in high relative errors (criterion 3). This also suggests that the wavelength of the acoustic system can be optimised to provide higher accuracy for a given range of water wave amplitudes.

5.6.4 Turbulence generated water surface roughness

With the accuracy of the system quantified, it was then tested on more realistic free surface roughness patterns. For this purpose eight steady, uniform water flows were created over the flat gravel bed in the flume. These flows resulted in complex turbulence-generated water surface patterns, which were measured using the same wave probe and acoustic setup as described in section 5.6.2. The gradient of the flume was set to 0.004 and a range of steady flow conditions were examined. The mean flow depth and RMS water surface roughness height were calculated from the wave probe data. Peak to peak water surface roughness height was calculated based on the two-sigma rule as $h_{pp} = 4 \times \sigma$ since this captures 95% of the data, and therefore represents the mean peak to peak amplitude, while neglecting any uncharacteristically high instantaneous water surface roughness heights. This works well for a normally distributed roughness population, and was selected since the height distribution of the water surface roughness

observed in these experiments has been shown to be close to normal in section 4.1. For this type of flow the surface features are turbulence induced, rather than gravity waves, and thereby propagate at close to the velocity of the flow as shown in section 5.2.2, so local surface gradients were calculated using the flow velocity and the wave probe time series. These data are presented in Table 5-9.

Table 5-9: Hydraulic flow conditions

Flow condition	Depth D (mm)	Mean velocity V (m/s)	RMS roughness height σ (mm)	p-p roughness height h_{pp} (mm)	Mean absolute local gradient G (-)
b1	32	0.34	0.28	1.12	0.004
b2	38	0.37	0.28	1.12	0.005
b3	58	0.51	0.41	1.64	0.006
b4	64	0.56	0.44	1.76	0.007
b5	75	0.61	0.61	2.44	0.006
b6	89	0.66	0.75	3.00	0.007
b7	107	0.76	0.89	3.56	0.005
b8	119	0.83	1.11	4.44	0.005

For these flow conditions the surface pattern is more complex than for gravity wave conditions, containing a broader range of frequency components. This was investigated by calculating the frequency spectra (Figure 5-49).

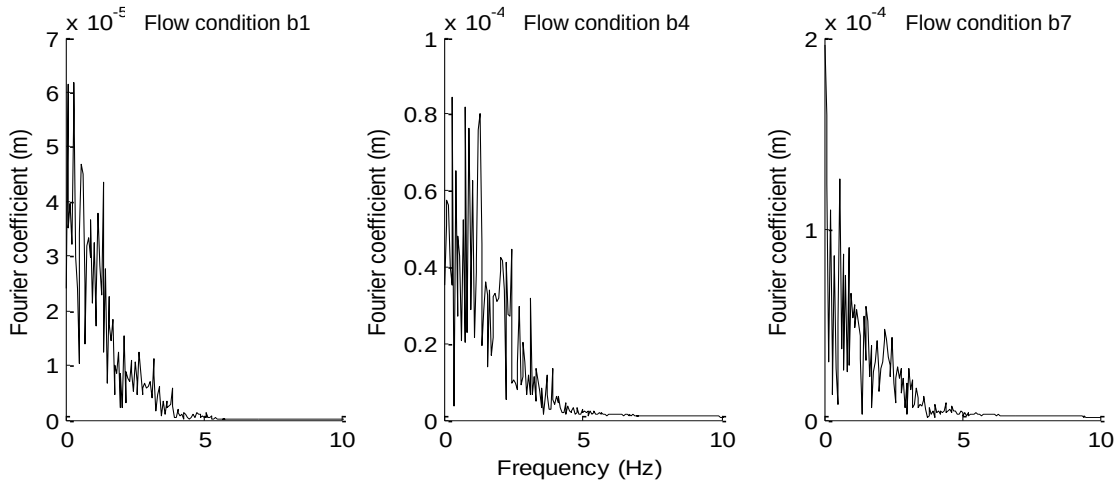

Figure 5-49: Frequency spectra of turbulence generated water surface roughness conditions b1, b4 and b7, with flow properties respectively: S_0 =0.004; D =32, 64, 107 mm; V =0.33, 0.46, 0.67 m/s; σ =0.28, 0.44, 0.63 mm

The spectral content of all the conditions is similar, though they differ in magnitude. It can be seen that the dominant spectral components fall below around 3 Hz, but the spectrum extends further in frequency, up to around 5 Hz. Even at the lowest velocity (condition b1, 0.34 m/s), the dominant components (<3 Hz) would provide a wavelength of 0.11m, just satisfying criterion 1 ($\lambda > 0.11\text{m}$). Although the components between 3 Hz and 5 Hz are small, they may be significant enough to violate the first criterion, particularly for conditions b1 - b3. Table 5-9 also shows that the mean local surface gradient, G, does not exceed the predetermined limit of 0.025 (criterion 2) and that the water surface roughness heights are all greater than 4% of the acoustic wavelength (criterion 3). This would suggest that the mean absolute error should not exceed 5% of the acoustic wavelength, and the mean relative error should not exceed 3% of the peak to peak water surface

roughness height, h_{pp}. The resulting time series from conditions b1, b4 and b7 (see Table 5-9) are shown in Figure 5-50. It can be seen from Figure 5-50 that the *absolute* magnitudes of the errors are similar in each case. The mean absolute errors, E, are calculated in Table 5-10, and are also presented as percentages of the acoustic wavelength, E_a, and as percentages of the peak to peak water surface roughness height, E_{pp}.

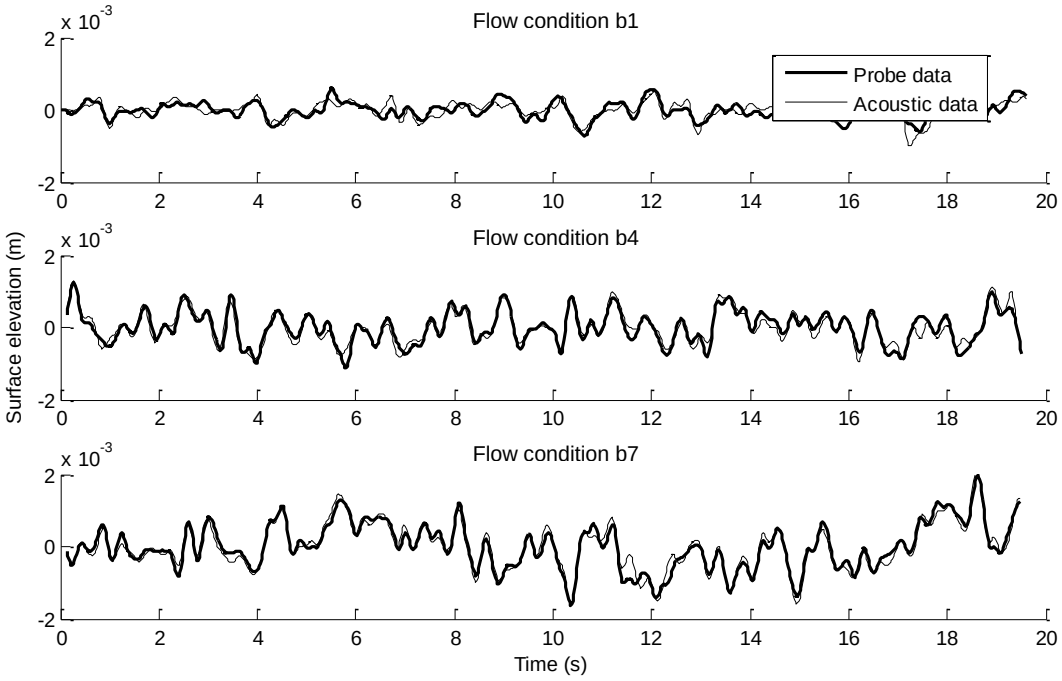

Figure 5-50: Acoustic probe accuracy for turbulent flow surface, conditions b1, b4 and b7, with flow properties respectively: S_0 =0.004; D =32, 64, 107 mm; V =0.33, 0.46, 0.67 m/s; σ =0.28, 0.44, 0.63 mm

The *absolute* error does not appear to be a function of the local gradient, perhaps because the gradients are so far below the limits defined in section 5.6.3. Errors here are most likely due to incoherent acoustic scattering as some of the surface wavelengths violate the Fresnel zone limit of the first

criterion, and also due to any small errors in the phase measurement (described in section 4.4).

Table 5-10: Error in turbulent free surface measurement

Flow condition	RMS roughness height σ (mm)	p-p roughness height h_{pp} (mm)	Mean absolute error E (mm)	Mean error as % of acoustic wavelength E_a (%)	Mean error as % of p-p roughness height E_{pp} (%)
b1	0.28	1.12	0.15	1.9	13
b2	0.28	1.12	0.18	2.3	16
b3	0.41	1.64	0.16	2.0	10
b4	0.44	1.76	0.13	1.6	7
b5	0.60	2.44	0.11	1.4	5
b6	0.59	3.00	0.19	2.4	6
b7	0.63	3.56	0.12	1.5	3
b8	0.51	4.44	0.16	2.0	4

In flow conditions with smaller water surface roughness heights these *absolute* errors cause greater *relative* deviation between the wave probe and acoustic data (as can be seen from condition b1 in Figure 5-50). For conditions which strongly violate criterion 1 (conditions b1-b3), the error relative to the water surface roughness height is above 10%, but for the other conditions the relative error is less than 10%. This is approximately twice the relative error measured for gravity waves, and is most likely due to the more complex nature of the turbulence generated water surface roughness (i.e. small wavelength components causing some amount of interference of the acoustic signal). This could be improved further by optimising the acoustic wavelength if small water surface roughness heights are to be measured, and adjusting the geometry of the acoustic equipment in order to minimise the first Fresnel zone.

5.6.5 Acoustic free surface measurement – summary

It has been shown that for several free surface wave/roughness conditions, analysis of the temporal variation of the phase difference between a sent ultrasonic signal and the ultrasonic signal reflected from the dynamically rough surface facilitates direct non-invasive measurement of the surface elevation over time at a “small” point on the surface. Effectively, this system behaves as an acoustic wave probe. This system can be used to measure surface fluctuations acoustically and also to predict the acoustic response of surfaces with a known dynamic component.

The performance of the constructed acoustic wave probe is demonstrated by comparison with data from a standard conductance based wave probe. A theoretical minimum characteristic wavelength in the surface roughness pattern which can be accurately resolved with the acoustic probe is determined based on established theory of Fresnel zone ensonification (criterion 1), whereby any smaller wavelengths would result in multiple surface features being within the first (half) Fresnel zone of acoustic reflection and would result in multiple points from which interfering signals can reach the receiver and obscure the signal from the specular point of reflection. The dominant wavelengths examined in this study have been greater than this limit. Using artificially generated gravity waves it was determined that the magnitude of the local surface gradient could significantly affect the validity of the acoustic approach. This may be through a combination of effects. Firstly, a significant local gradient at the point of specular reflection would cause a proportion of the acoustic energy in the

incident sound wave to be reflected in a direction other than that of the receiver, yielding lower signal levels from the point of interest. Secondly, the finite directivity of the transducer suggests that there will be a coherent scattering component in the signal reflected by the rough surface which will reach the receiver via paths other than the specular reflection. Thirdly, high gradients in the surface roughness may give rise to multiple scattering effects, whereby an acoustic path may make contact with two or more points on the flow surface before reaching the receiver, obscuring any useful phase information. Using this information a surface gradient limit is defined beyond which the technique is liable to give erroneous readings. This limit is defined as $G = 0.025$, or for simple gravity waves this can be defined by the ratio of RMS wave height to dominant wavelength $\sigma / \lambda = 0.005$ (criterion 2). This may perhaps be improved by adjusting the incidence angle. The accuracy of the system was also examined in relation to the scale of water waves under investigation, and it was found that the relative error in the instantaneous water level increased significantly if the RMS wave height was below 4% of the acoustic wavelength (criterion 3).

Using these established criteria, the errors in measuring the surface level fluctuations associated with the turbulence generated water surface roughness were examined. It was found that the dominant surface roughness components for all the flow conditions satisfied the three established criteria, although some weak high frequency features produce short wavelength components which violate criterion 1. The mean absolute errors were below 0.15 mm or 2% of the acoustic wavelength, and mean relative errors were generally below 10% of the representative (peak to peak) water surface

roughness height. Errors were in general greater than those for gravity waves. This is attributable to the small spectral components which violate the first criterion affecting the accuracy of the acoustic data.

It is believed that these errors may be reduced further by selecting an excitation frequency to ensure that the acoustic wavelength is suitable for the expected water surface roughness heights (according to criterion 3), and by setting the component geometry such that the operative Fresnel zone is smaller than the dominant wavelengths (according to criterion 1). The directivity of the source is also critical in order to reduce the effective Fresnel zone, and to avoid multiple scattering and unwanted reflections that may occur if a more omnidirectional source were used. This being said, one disadvantage of using an ultrasonic signal is that the atmospheric absorption can be high, limiting the operational range. This could be overcome by increasing the emitted sound power, or for applications requiring a much larger range, sources of lower frequency could be investigated.

It should also be noted that while the acoustic wave probe accuracy is validated against that of the conductive wave probe, the accuracy of the conductive wave probe is not perfect when the scale of the roughness pattern becomes small, due of the finite separation between wires (as discussed in section 4.2). This may mean that the accuracy of the acoustic probe is superior to that of the conductive probe for these kinds of regimes, so the errors shown are worst case scenarios.

While the microphone used was a suitable receiver for the laboratory experiments, a matched transducer may provide a more robust receiver for

field use, or indeed a low cost water resistant microphone could be used. Further embodiments could see the source and receiver operating very closely to reduce the length of the Fresnel zone, or indeed being combined into one transceiver.

In addition to the functional benefits of a non-invasive acoustic wave monitor, the type of system presented here would also provide a low cost alternative to traditional wave sensing technologies, with a full system (transducer, receiver, controller) costing an order of magnitude less than the equipment currently available for conductive wave sensing.

This technique provides a unique, low-cost non-contact method for quantifying fluid surface fluctuations. Such a device would enable robust and efficient monitoring of surface properties in a number of applications, and may even be used to monitor the hydraulic properties of shallow flows. While an acoustic approach is sensible for local measurements, the technique is also suitable for alternative excitation signals, such as microwaves, or radio frequency signals. These techniques may be more robust to changes in atmospheric conditions, and may be operated over a greater distance.

5.7 **Acoustic measurement of flow conditions**

Sections 5.2, 5.3, 5.4, and 5.5 have shown that the free surface behaviour (both temporally and spatially) is strongly dependent of the bulk flow conditions and turbulence field. It has been shown that an array of conductance-type wave probes is capable of accurately capturing this temporal and spatial behaviour. It is proposed that this type of free surface

information may allow for rapid determination of flow conditions, but the invasive conductance probes are impractical for many applications. The acoustic wave probe developed in section 5.6 has been shown to allow highly accurate non-invasive measurement of free surface fluctuations. It is proposed that a linear array of such acoustic wave probes would facilitate spatial free surface measurements comparable to that of the conductance probe array. Such a device may consist of an array of source-receiver pairs, or may make use of a single source and multiple receivers in order to obtain the necessary multiple surface fluctuation measurements. This type of acoustic system would present a new non-invasive, low-cost flow monitoring device for environments and applications where traditional invasive methods are too impractical and too expensive.

Chapter 6 – Thesis conclusions

The aim of this work was to establish the relationship between the bulk hydraulic properties of shallow flows, their resulting free surface roughness patterns, and the effect that this dynamic roughness has on an incident acoustic field. To address these issues, data was gathered regarding flow conditions, velocity fields, free surface profile, and acoustic reflection from the free surface for a range of bed slopes, bed types, and relative submergences. Here the results of each analysis will be summarized and conclusions drawn, and initial hypotheses will be addressed in the context of the acquired results.

6.1 **Summary of findings**

Data from a series of laboratory tests has shown that by measurement with a device consisting of an ultrasonic source-receiver pair, the local fluctuations of a small point on the free surface can be recorded. This type of data allows the root-mean-square (rms) water surface roughness height and temporal properties of free surface features to be calculated. A spatial correlation function may be estimated from similar measurements at an array of streamwise locations. These remotely measured properties allow the estimation of the bulk hydraulic properties based on the derived expressions summarised in Table 5-6 in section 5.5.

The reason that these relationships exist may be explained by the processes that control the free surface. The free surface is a physical barrier which

almost completely reflects the acoustic signal, and constrains the flow, but has been shown to allow the transfer of information from the liquid phase to the acoustic field via the dynamic fluctuations. In the absence of wind shear, the water surface pattern apparent on the free surface of steady uniform shallow flows can only be initiated by the underlying turbulence field, and similarly, any spatial and/or temporal variation in the nearby acoustic field (in comparison to the response of a flat surface) can only be generated by the temporally and spatially dynamic free surface roughness.

In this study the phase of a reflected acoustic signal is used to study the influence of the dynamic surface roughness on the surrounding acoustic field. It has been shown for several free surface wave/roughness conditions that analysis of the temporal variation of the phase difference between a sent and received ultrasonic signal reflected from the dynamically rough surface facilitates direct non-invasive measurement of the surface elevation over time at a “small” point on the surface (Nichols, et al., 2013). Effectively this technique behaves as an acoustic wave probe, and the data is therefore suitable for use in measuring the wave/roughness height and free surface fluctuations at a given spatial location. The performance of the constructed acoustic wave probe has been demonstrated by comparison with data from a standard conductance based wave probe. The accuracy of the acoustic system has been described in the context of three criteria which enable the use of such a system. These are: (1) The spatial wavelength of free surface waves of interest must be greater than the first (half) Fresnel zone of acoustic reflection in order to minimise multiple scattering and/or shadowing effects; (2) The instantaneous local gradient of the free surface pattern must not

exceed $G = 0.025$, which may also be defined by the ratio of RMS wave height to dominant water surface wavelength $\sigma / \lambda = 0.005$. This avoids the dominant acoustic lobe being directed away from the receiver, and minimises the opportunity for the acoustic signal to make contact with multiple points on the surface before reaching the receiver; (3) The RMS wave height must be above 4% of the acoustic wavelength in order to minimise the relative error of the wave measurements. Under these conditions the mean error of the system is within 5% (and usually within 1%) of the acoustic wavelength, and is generally within 10% of the wave amplitude for turbulence generated waves, and 3% of the amplitude for gravity waves. The absolute errors are independent of wave height, so for larger wave heights, the relative error can be considerably lower. For the turbulent depth-limited flows examined here, the dominant surface waves fall well within the criteria. This acoustic system may be further improved by selecting an excitation frequency to ensure that the acoustic wavelength is suitable for the expected water wave/roughness heights, and by setting the component geometry such that the operative Fresnel zone is smaller than the dominant water surface wavelengths.

It has been shown that the temporal and spatial properties of the free surface (whether measured acoustically or otherwise) are strongly related to the bulk hydraulic flow conditions. The behaviour of the air-water interface and it's linkage with the underlying flow field have not been explained before in this level of detail for the case of turbulent shallow flow. Previous literature would suggest that the free surface is excited by the coherent turbulent structures beneath, but that these disturbances generate gravity waves which overwhelm the information carried by the turbulent structures themselves

(though these studies were primarily concerned with turbulence generated by an upstream grid rather than solely by the bottom boundary). In this study it has been shown that the free surface pattern generated by the shearing flow induced turbulent structures does not significantly exhibit gravity waves, since the free surface features were observed to advect downstream at a velocity close to the surface flow velocity. In this case the free surface pattern was thought to be linked directly to the turbulence field beneath and to therefore be primarily turbulence driven.

This was apparent from the data collected using a combined particle image velocimetry and laser induced fluorescence system which was capable of the simultaneous measurement of the free surface profile and the sub-surface velocity field. U-level conditional sampling analysis (Bogard & Tiederman, 1986; Luchik & Tiederman, 1987) was applied to each depthwise layer of sub-surface velocity data, and to the free surface data. U-level analysis identifies a turbulent structure by a period of extreme velocity (beyond a threshold value). This method allowed the estimation of the mean duration for which a structure was present at each point in the flow, along with the frequency of structure detection at each point. A streamwise advection velocity was determined by finding the temporal lag which provided the peak cross-correlation of two time series separated in the streamwise direction by a known spatial lag. This velocity (through application of Taylor's frozen turbulence hypothesis) allowed the temporal properties to be converted into a spatial scale, yielding the mean structure length, and mean distance between structures. It was found that these properties were homogeneous in the streamwise direction for all depthwise planes in all flow conditions

(supporting the applicability of Taylor's hypothesis), allowing them to be averaged at each depthwise location and thereby provide a vertical profile. The advection velocity of turbulent structures was shown to be close to the depth-local mean velocity of the flow. It has previously been shown that structures generally travel at the bulk flow velocity (Roy, et al., 2004) and/or the surface flow velocity (Fujita, et al., 2011), but (to the author's knowledge) the structure advection velocity profile has not been quantified in this way before. The majority of the large scale turbulent structures spanned the full flow depth and had a streamwise scale of around 1 to 3 flow depths, consistent with previous studies (Roy, et al., 2004; Yalin, 1992; Shvidchenko & Pender, 2001; Komori, et al., 1989). The structure length and structure detection frequency also allowed the assertion that smaller vortices formed in the shear layer at the bed had a tendency to coalesce into larger structures in the main flow, and that these structures generally maintained their size up toward the free surface, perhaps breaking down close to the surface into more frequent smaller structures. Crucially it was shown that the free surface properties measured via applying this same method to the free surface fluctuation data corresponded to the turbulence properties measured in the flow layer immediately beneath. This allows the turbulence properties of the flow to be estimated from measurement of the temporal properties of the free surface. It is also of note that when using free surface data, the mean streamwise length of turbulent structures, whilst generally scaling with depth as noted by previous studies (Yalin, 1992; Shvidchenko & Pender, 2001; Roy, et al., 2004), appeared to be linearly proportional to the surface flow velocity, as did the mean streamwise separation between structures.

That the turbulence properties measured in the temporal free surface data appear to correspond with those of the near surface velocity data, would suggest that the free surface deformations are a literal representation of the turbulent structures immediately beneath. However, this would result in a relatively static free surface pattern, advecting downstream and changing slowly as the governing turbulent structures gradually evolve and dissipate to be replaced by new features (Nezu & Nakagawa, 1993; Guo & Shen, 2010). In most practical flows this is shown to not be the case (Savelsberg & van de Water, 2009; Fujita, et al., 2011). The water surface is clearly dynamic, changing shape with every temporal 'snapshot' from (in the present study) the LIF system. The spatial evolution of the free surface pattern (and the sub-surface velocity field) was investigated by means of defining a spatial correlation function for each depthwise position, and at the free surface. The spatial correlation function defines the extremum (positive or negative) similarity between two time series separated in space as a function of the spatial separation (lag). In agreement with previous work, the correlation between spatially separated points decreases linearly with spatial lag in the main flow (Snyder & Lumley, 1971; Roy, et al., 2004). However, near the surface this linear decay is superimposed with an oscillatory component. This component is shown to arise from the independent behaviour of the free surface itself, which displays a strong decaying oscillatory nature in its spatial correlation function (Horoshenkov, et al., 2013). This oscillatory component is shown to imprint onto the sub-surface spatial correlation function to a depth which is controlled by the RMS wave height, and the depth of influence factor. What governs the value of the depth of influence factor has not been

established but it was shown to be similar for flows with the same bed type. The oscillatory nature indicates that the recorded time series inverts periodically over space, which in turn suggests that the individual free surface features invert periodically over space and time. Indeed through the presentation of space-time matrices it is shown that while the sub-surface turbulent features are relatively persistent and unchanged as they advect downstream, the free surface features fluctuate between being an upward boil and a downward dimple. This is what gives rise to the more complex dynamic surface which is seen by the eye (Bohm, 1980).

The oscillatory nature of the free surface spatial correlation function was examined in more detail by a non-equidistant array of conductance-based wave probes. Using this probe array, the spatial correlation function could be captured over several periods, and was found to be closely approximated with a simple analytical expression $W(\rho)=e^{-\rho^2/\sigma_w^2}\cos(2\pi/L_0\rho)$, where σ_w is the spatial correlation radius, L_0 is the characteristic spatial period, and ρ the spatial separation. The parameters σ_w and L_0 can define objectively the surface wave pattern which develops in this type of flow. The values of these parameters have been found to vary systematically with bulk hydraulic parameters and so were considered to carry a carry clear physical sense. The value of L_0 describes the characteristic period in the wave pattern observed on the flow surface and carries information regarding the bed roughness and velocity profile, while and the value of σ_w relates to the rate with which the coherent turbulent structures dissipate in the flow. These

findings quantify a clear physical linkage between the spatial correlation pattern of the water surface and the prevailing flow conditions.

It was proposed that this complex oscillatory surface behaviour may be explained by considering the dynamic surface as a number of overlapping (both spatially and temporally) free surface disturbances. In this case each disturbance could act independently, while the integration of disturbances would provide the full dynamic nature of the free surface. It was shown that the theoretical frequency at which an individual free surface feature would oscillate up and down can be modelled as an under-damped simple harmonic motion acting on a mass of water controlled by the depth of influence of the free surface. This theoretical frequency closely matches the measured frequency for all the flow conditions examined. The decay of the spatial correlation function is shown to be related to the spatial separation between turbulent events; if more new structures are formed as the spatial lag increases, then the time series extremum correlation decreases more rapidly. Solitary waves acting in an oscillatory manner are termed oscillons (Umbanhowar, et al., 1996). The discovery of oscillons in turbulent open channel flows is new, and allows for a radical new understanding of free surface roughness whereby the complex pattern seen by the eye can be simply described as a number of temporally and spatially distributed and overlapping oscillons each responding according to simple harmonic motion.

It can be concluded that the apparently complex dynamic nature of flow surfaces can be decomposed into three unambiguous processes: (1) new structures impinge on the free surface and form local deformations; (2) these deformations behave as oscillons according to simple harmonic motion; (3)

these oscillons generate much weaker (Ward, 2003) gravity waves which propagate radially (Savelsberg & van de Water, 2009) (these were not observed to be significant in this study but theoretically must exist and so are included here for completeness).

6.2 **Thesis hypotheses revisited**

Here the thesis hypotheses will be re-examined with respect to the outcomes of the study.

"1. The author believes that (a) free surface patterns are generated by sub-surface flow features and that (b) these features are in some way a function of the bulk flow properties. In this case the surface pattern may be predicted based on the bulk flow properties, or the bulk flow properties may be estimated based on the shape and behaviour of the free surface pattern."

This hypothesis has been shown to be predominantly correct. The temporal free surface behaviour is shown to be directly governed by the sub-surface velocity field. This dependence is what gives rise to the presented relationships which show the linkage between the bulk hydraulic conditions and the free surface roughness pattern. Furthermore it has been shown that the linkage between the free surface and the bulk flow is bi-directional, such that oscillatory free surface fluctuations, initiated by the sub-surface turbulent structures, impart their spatial behaviour onto the sub-surface velocity field.

“2. It is believed that the generated free surface pattern behaves in a predictable manner and that it measurably and predictably affects a suitable acoustic field above the surface. In this case the relationship between the free surface and the acoustic field can be considered in either direction such that free surface data can be used to predict acoustic response, or acoustic response can be used to determine free surface properties.”

It has been shown that the free surface behaviour is governed by an ensemble of surface disturbances, generated by sub-surface turbulence and oscillating according to simple harmonic motion. This behaviour may be captured at a small spatial location by analysis of the phase shift of a reflected acoustic signal.

“3. The author believes that given relationships of the form described, these dependencies could be combined, allowing the free surface itself to eventually be neglected, simply acting as a mechanism transferring information from one phase to another. This would allow the acoustic response of a given flow to be used to determine the bulk hydraulic properties and vice versa.”

The equations governing the response of the acoustic field to the free surface have been shown to give direct measurement of free surface fluctuation at a

point. An array of similar measurements allows the measurement of the spatial characteristics of the free surface. This information may allow the assessment of flow conditions based on the discovered relationships with the free surface behaviour. It is proposed that an acoustic device can accurately acquire the spatiotemporal surface fluctuation data required to make such an assessment possible. The intermediate step of calculating the free surface properties would be inconsequential in the eventual estimation of the flow properties. Such a system would therefore provide a remote unambiguous measurement of flow conditions.

6.3 **Applications and commercial considerations**

The presented acoustic technique has the potential to provide a unique, low-cost non-contact method for quantifying fluid surface fluctuations. Such a device would enable robust and efficient monitoring of surface properties in a number of applications and, through the relationships discovered in this work, may also be used to monitor the hydraulic properties of shallow flows. The new method is based on the observation of the pattern in the water surface waves from which the nature and scale of the hydraulic processes in an open channel flow can then be inferred. This allows measurements of hydraulic conditions in such shallow turbulent flows, when the insertion of conventional flow measurement instrumentation may not be possible due to practical constraints.

Commercial products have previously been developed which use acoustic signals to estimate the depth-averaged velocity of flow within a channel or

partially filled pipe using a backscattered acoustic Doppler technique (IETG, 2013). These devices were developed based on an empirical approach, with no true understanding of why the Doppler shift of the received acoustic signal should correspond to the velocity of the flow. It is surmised that the signal responds to the movement of the rough pattern on the free surface, that this travels close to the surface velocity of the flow, and that this is reliably related to the bulk velocity, but these assumptions are not verified. A similar radar based device (HachFlow, 2013) claims to measure the mean flow velocity directly from the air-water interface, since the Doppler shift generated is an amalgamation of the effect of a large area on the surface which is assumed to exhibit a horizontal velocity distribution similar to the vertical velocity profile within the flow. Once again this is an assumption and is not verified. In fact it is known that some Doppler based devices have a high margin of error, suggesting that the measured Doppler shift may be a measure of some other process(es) rather than simply the flow velocity, so perhaps the assumptions are not always valid. A further inherent disadvantage with these types of device is that the majority of the emitted signal is scattered forwards, away from the sensor. This means that in order to achieve a strong signal to noise ratio (SNR) in the backscattered portion, the emitted signal is required to be of relatively high energy. There are also concerns regarding the directivity of the acoustic signal, since any signal content reflected in a vertical manner will exhibit a much stronger signal level and as such the Doppler shift generated by the vertically moving surface below may obscure the Doppler shift of interest. While these devices show that there is some loose relationship between the acoustic signal and the flow velocity, the linkage governing the

relationship is not understood and cannot be relied upon. The acoustic system developed as part of this thesis does not suffer from these inherent disadvantages.

The patented acoustic flow monitor has clear market potential. In addition to the functional benefits of a non-invasive flow monitor, the type of acoustic system presented here would also provide a low cost alternative to traditional wave sensing technologies, with a full system (transducer, receiver, controller) costing an order of magnitude less than the equipment currently available for conductive wave sensing. The system presented provides a significant advantage over traditional electrical based techniques by requiring no calibration, avoiding temperature and salinity effects and, crucially, not requiring direct contact with the flow, avoiding potential clogging and minimising maintenance requirements. The technique is favourable over non-invasive optical methods for single point measurements as again a calibration is not required, and the flow surface does not need to be coloured or seeded.

The overall system paves the way for a new generation of non-invasive, low-cost flow monitoring equipment for environments and applications where traditional methods would be too difficult, costly or impractical to employ. The intelligent interpretation of the temporal data and spatial correlation function may allow such a device to quantify hydraulic properties not currently measurable with existing technology.

6.4 **Recommendations for further work**

Whilst addressing the thesis hypotheses and developing the knowledge of turbulent free surface behaviour and acoustic response, this work has also identified the need for further study into a number of areas.

The observation of the oscillon phenomenon in the context of turbulent shallow flow surfaces is new and needs further investigation. The primary unresolved issue is the depth of influence factor of the free surface deformations. For all the gravel bed cases the depth of influence was equal to approximately 28 RMS water surface roughness heights while for the sphere bed this value was around 19. This difference may be due to a slight temperature difference between the two measurement sets, or may be a result of the different bed types initiating different types of turbulence fields which are more or less susceptible to the influence of the free surface oscillation. However the evidence in this study is not sufficient to draw any conclusion of this kind, so further study is required. A series of systematic tests could examine the behaviour of oscillons (and their depth of influence) for similar flows with (i) a fixed bed type with different water temperatures, and (ii) a fixed temperature but different bed types.

Other characteristics of the oscillon behaviour warrant further research, for example the governing factors of the oscillon decay rate, and the degree to which these turbulence generated oscillons conform to traditional oscillon theory. For example in granular media and parametrically excited still water surfaces, oscillons of the same phase show a tendency to repel, while opposite signed oscillons tend to attract each other to form coupled pairs or dipoles (Hunt, 2008; Umbanhowar, et al., 1996). The data presented in this

thesis suggest that oscillon pairs may exist in this context, but does not definitively capture any attraction or repulsion between oscillons.

The potential link between the oscillon behaviour of the free surface disturbances and the initiation of bursting phenomena (spawning turbulent structures) at the bed should be fully investigated. More rigorous measurement of the near-bed properties would be advantageous, perhaps with a horizontal PIV light sheet immediately above the bed. Work could be done to decompose the flow field in order to isolate the behaviour of the free surface oscillons within the measurement plane from that of the coherent flow structures advecting downstream, and determine their effect on the sub-surface behaviour, particularly the near bed ejections.

While this study has examined the effect of bulk hydraulic conditions on the free surface pattern, the effects of surface tension and viscosity are assumed to be constant because the change in these properties is expected to be small for the temperature range examined. Nevertheless, the effects may not be negligible in some applications (for example where large temperature variations are expected), and so should be systematically examined. The effect of surface tension could be more easily examined by adding a surfactant to the water (such as ethanol) to alter the surface tension while not affecting the viscosity. The simple harmonic motion model would suggest that such a change would have a negligible effect on the free surface behaviour. Water temperature could be varied over a wider range in order to examine the effect of viscosity. Increased viscosity may suppress the oscillon behaviour, reducing the depth of influence factor, and altering the oscillation frequency.

The other quantity which warrants further investigation is the bed roughness. While this work examined the effect of two rough bed types and many of the derived expressions appear to be independent of bed type (Equations 5-7, 5-8, 5-10, 5-23, 5-33), a more systematic investigation should be performed to establish the true effects of static bed roughness type on the free surface behaviour. This would take the form of a range of experimental flow conditions over a wide range of uniform bed types. These beds would benefit from being grouped into two categories: natural gravel (to represent a realistic bed type); and spherical bed elements (to represent an idealised rough boundary). In both cases a wide range of particle sizes and particle size distributions should be examined. With the effect of static bed roughness fully characterised, work could move to the investigation of non-uniform bed structure, and of mobile bed material, and the possible inference of bed load transport from the free surface roughness pattern.

Finally, the acoustic system shows great potential for development. A linear array of receivers would allow spatial information about the free surface to be recorded, while a 2-dimensional array of receivers would allow for measurement of fluctuations within a grid of points on the free surface, facilitating spatial analysis in both streamwise and lateral directions. The development of this technology into a marketable device would allow for non-contact assessment of hydraulic conditions in environments whose constraints prevent the use of traditional invasive technologies.

6.5 **Final word**

This study has shown that turbulent free surface roughness measurably affects an incident acoustic field, and is governed by the bulk flow conditions. Perhaps more importantly however, this study has shown that the dynamic nature of the free surface of shallow turbulent flow may be explained unambiguously by simple harmonic motion. This behaviour is reminiscent of the wave-particle duality of light: the water surface features are undeniably waves, and yet they oscillate with a virtual mass, exhibiting particle-like behaviour. The free surface is clearly a continuum, but one which is defined by the presence and behaviour of individual, but not independent, features. The duality of turbulence was remarked upon by Frisch (1995), who described ‘Leonardian’ structures amidst a ‘Kolmogorovian’ field. Such a duality was best alluded to in the context of the free surface by the late David Bohm (1980) who said:

> “The best image of process is perhaps that of the flowing stream, whose substance is never the same. On this stream, one may see an ever-changing pattern of vortices, ripples, waves, splashes, etc., which evidently have no independent existence as such. Rather, they are abstracted from the flowing movement, arising and vanishing in the total process of the flow”

Reference List

Adrian, R. J., Meinhart, C. D. & Tomkins, C. D., 2000. Vortex organization in the outer region of the turbulent boundary layer. *J. Fluid. Mech.,* Volume 422, pp. 1-54.

Airy, G., 1841. Tides and waves. In: Hugh. James. Rose., ed. *Encyclopaedia Metropolitana, Mixed Sciences* 3.

Arcement, G. J. & Schneider, V. R., 2013. Guide for Selecting Manning's Roughness Coefficients for Natural Channels and Flood Plains. *USGS Water-Supply Paper 2339.*

Attenborough, K. & Taherzadeh, S., 1995. Propagation from a point source over a rough finite impedance boundary. *J. Acoust. Soc. Am.,* September, 98(3), pp. 1717-1722.

Attenborough, K. & Taherzadeh, S., 1995. Propagation from a point source over a rough finite impedance boundary. *J. Acoust. Soc. Am,,* Volume 98, pp. 1717-1722.

B&K, 2013. *Four-channel Microphone Conditioning Amplifier - Type 2690-A-0S4.* [Online]
Available at:
http://www.bksv.com/Products/transducers/conditioning/microphone/2690A0S4.aspx
[Accessed 12 July 2013].

Babakaiff, C. S. & Hickin, E. J., 1996. Coherent Flow Structures in Squamish River Estuary, British Columbia, Canada. In: *Coherent Flow Structures in Open Channels.* New York: John Wiley.

Barr, D. I. H., 1963. Tables for the Hydraulic Design of Pipes, Sewers and Channels. Hydraulic Research Station, Wallingford, UK.

Bass, F. G. & Fuks, I. M., 1979. *Wave Scattering from Statistically Rough Surfaces, International series in Natural Philosophy.* Elsevier.

Bastiaans, R. J. M., 2000. *Cross-correlation PIV : theory, implementation and accuracy,* Eindhoven: Technische Universiteit Eindhoven.

Bechle, A. J. & Wu, C. H., 2011. Virtual wave gauges based upon stereo imaging for measuring surface wave characteristics. *Coastal Engineering,* 58(4), pp. 305-316.

Benetazzo, A., Fedele, F., Gallego, G., Shih, P.-C., Yezzi, A., 2012. Offshore stereo measurements of gravity waves. *Coastal engineering,* Volume 64, pp. 127-138.

Bianchini, S., Lage, A., Siu, T., Shinbrot, T., Altshuler, E., 2013. Upstream contamination by floating particles. *Proc. R. Soc. A,* Volume 469, pp. 1471-2946.

Bloom, L. D., Wang, J. & Potter, K. D., 2013. Damage progression and defect sensitivity: An experimental study of representative wrinkles in tension. *Composites Part B: Engineering,* 45(1), pp. 449-458.

Bogard, D. G. & Tiederman, W. G., 1986. Burst detection with single-point velocity measurements. *J. Fluid Mech.,* Volume 449, pp. 225-254.

Bohm, D., 1980. *Wholeness and the implicate order.* London: Routledge.

Boulanger, P., Attenborough, K., Qin, Q. & Linton, C. M., 2005. Reflection of sound from random distributions of semi-cylinders on a hard plane: models and data. *J. Phys. D.,* Volume 38, pp. 3480-3490.

Boulanger, P., Attenborough, K., Taherzadeh, S., Waters-Fuller, T., Li, K., 1998. Ground effect over hard rough surfaces. *J. Acoust. Soc. Am.,* Volume 104, pp. 1474-1482.

Brocchini, M. & Peregrine, D. H., 2001. The dynamics of strong turbulence at free surfaces. Part 1. Description. *J. Fluid Mech.,* Volume 449, pp. 225-254.

Brown, G. L. & Thomas, S. W., 1977. Large structure in a turbulent boundary layer. *Phys. Fluids,* Volume 20, pp. s243-s252.

Brumley, B. H. & Jirka, G. H., 1987. Near-surface turbulence in a grid-stirred tank. *J. Fluid Mech.,* Volume 183, pp. 235-263.

BS5167-1, 1997. *Measurement of fluid flow by means of pressure differential devices - part 1: Orifice plates, nozzles and venturi tubes inserted in circular cross-section conduits running full.* London: British Standards Institute.

Buffin-Bélanger, T. & Roy, A. G., 1998. Effects of a pebble cluster on the turbulent structure of a depth-limited flow in a gravel bed river. *Geomorphology,* Volume 25, pp. 249-267.

Buffin-Bélanger, T., Roy, A. G. & Kirkbride, A. D., 2000. On large-scale flow structures in a gravel-bed river. *Geomorphology,* Volume 32, pp. 417-435.

Buffin-Bélanger, T., Roy, A. G. & Levasseur, M., 2001. Dynamics of shedding motions in response to large-scale flow structures in turbulent gravel-bed rivers. *Rev. Sci. Eau,* 14(3), pp. 381-407.

Chambers, J. P. & Sabatier, J. M., 2002. Recent advances in utilizing acoustics to study surface roughness in agricultural surfaces. *Applied Acoustics,* Volume 63, pp. 795-812.

Chapman, R. P. & Harris, J. H., 1962. Surface Backscattering Strengths Measured with Explosive Sound Sources. *The Journal of the Acoustical Society of America,* 34(10), pp. 1592-1597.

Cheung, T. K. & Street, R. L., 1988. The turbulent layer in the water at an air-water interface. *J. Fluid Mech.,* Volume 194, pp. 133-151.

Chow, V. T., 1959. *Open-channel hydraulics.* International student edition. New York: McGraw-Hill Book Company, Inc..

Chukharev, A. M., Barabash, V. A., Zubov, A. G. & Pavlenko, O. I., 2007. Turbulent structure of the subsurface layer of the sea according to the data of the Sigma-1 measuring complex. *Physical Oceanography,* 17(2), pp. 75-87.

Churchill Controls, 2003. *Wave monitor technical manual.* [Online] Available at: http://www.churchill-controls.co.uk/downloads/file/wave-monitor-technical-manual.html?id=30. [Accessed 12 July 2013].

Clay Mathematics Institute, 2013. *Clay Mathematics Institute - The Millenium Prize Problems - Navier Stokes Equation.* [Online] Available at: http://www.claymath.org/millennium/Navier-Stokes_Equations/ [Accessed 26 June 2013].

Colebrook, C. F., 1939. Turbulent flow in pipes, with particular reference to the transition region between the smooth and the rough pipe laws. *J. Instn. Civ. Engrs.,* Volume 11, pp. 133-156.

Cooper, J. R. & Tait, S. J., 2008. The spatial organisation of time-averaged streamwise velocity and its correlation with the surface topography of water-worked gravel beds. *Acta Geophysica,* 56(3), pp. 614-642.

Cooper, J. R., Tait, S. J. & Horoshenkov, K. V., 2006. Determining hydraulic resistance in gravel-bed rivers from the dynamics of their water surfaces. *Earth Surf. Process. Landforms,* August.

Craig, P. D. & Banner, M. L., 1994. Modeling wave-enhanced turbulence in the ocean surface layer. *Journal of Physical Oceanography,* Volume 24, pp. 2546-2559.

Cui, J., Patel, V. C. & Lin, C.-L., 2003. Large-eddy simulation of turbulent flow in a channel with rib roughness. *International Journal of Heat and Fluid Flow,* Volume 24, pp. 372-388.

Dahl, P. H., 1999. On bistatic sea surface scattering: Field measurements and modelling. *J. Acoust. Soc. Am.,* 105(4), pp. 2155-2169.

Dantec Dynamics, 2002. *FlowManager software and Introduction to PIV Instrumentation,* Skovlunde: Dantec Dynamics.

Dantec Dynamics, 2013. *Q-400 DIC - Digital image correlation system - measurement of shape, displacement and strain.* [Online] Available at: http://www.dantecdynamics.com/Default.aspx?ID=855 [Accessed 4 July 2013].

Delafon, P., 1973. *Method and devices for measurement of position.* France, Patent No. 73 29663.

Dinehart, R. L., 1999. Correlative velocity fluctuations over a gravel river bed. *Water Resources Research,* 35(2), pp. 569-582.

Dunin, S. Z. & Maximov, G. A., 1990. Scattering of scalar fields on statistically rough surfaces. *Doklady Akademii Nauk SSSR,* 314(4), pp. 841-845.

Eggers, J. & Riecke, H., 1999. Continuum description of vibrated sand. *Phys. Rev. E,* 59(4), pp. 4476-4483.

Falco, R. E., 1977. Coherent motions in the outer region of turbulent boundary layers. *Phys. Fluids,* Volume 20, pp. s124-s132.

Ferguson, R. I., 2007. Flow resistance equations for gravel bed and boulder-bed streams. *Water Res. Res.,* 43(5).

Ferguson, R. I., Kirkbride, A. D. & Roy, A. G., 1996. Markov Analysis of Velocity Fluctuations in Gravel-bed Rivers. In: *Coherent Flow Structures in Open Channels.* New York. John Wiley.

Frank, A., 2012. *Quantum Weirdness And Being A Little Bit Pregnant: (Part 3).* [Online] Available at:

http://www.npr.org/blogs/13.7/2012/05/22/153277834/quantum-weirdness-and-being-a-little-bit-pregnant-part-3. [Accessed 6 October 2013].

Frisch, U., 1995. *Turbulence.* Cambridge: Cambridge University Press.

Fujita, I., Furutani, Y. & Okanishi, T., 2011. Advection features of water surface profile in turbulent open-channel flow with hemisphere roughness elements. *Visualisation of Mechanical Processes,* 1(3).

Gavrilov, A. L., Dunin, S. Z. & Maximov, G. A., 1992. Scattering of scalar fields by rigid and compliant rough surfaces: angular distribution of the intensity". *Soviet Physics - Acoustics,* 38(5), pp. 470-476.

Glawdel, T., Almutairi, Z., Wang, S. & Ren, C., 2009. Photobleaching absorbed Rhodamine B to improve temperature measurements in PDMS microchannels. *Lab Chip,* Volume 9, pp. 171-174.

Goring, D. G., Nikora, V. I. & McEwan, I. K., 1999. Analysis of the texture of gravel-bed using 2-d structure functions. *Proc. IAHR Symp. River, Coastal and Estuarine Morphodynamics,* Volume 1, pp. 75-84.

Grass, A. J., 1971. Structural features of turbulent flow over smooth and rough boundaries. *J. Fluid. Mech.,* Volume 50, pp. 233-255.

Grass, A. J., Stuart, R. J. & Mansour-Tehrani, M., 1991. Vortical structures and coherent motion in turbulent-flow over smooth and rough boundaries. *Phil. Trans. Roy. Soc. London Ser. A,* 336(1640), pp. 35-65.

Guo, X. & Shen, L., 2010. Interaction of a deformable free surface with statistically steady homogeneous turbulence. *J. Fluid Mech.,* Volume 658, pp. 33-62.

HachFlow, 2013. *FLO-DAR / FL900 System.* [Online] Available at: http://www.hachflow.com/portable/Flo-dar-fl900.cfm [Accessed 4 July 2013].

Hardy, R. J., Best, J. L., Lane, S. N. & Carbonneau, P. E., 2009. Coherent flow structures in a depth-limited flow over a gravel surface: The role of near-bed turbulence and influence of Reynolds number. *Journal of geophysical research,* Volume 114.

Hardy, R. J., Lane, S. N., Ferguson, R. I. & Parsons, D. R., 2007. Emergence of coherent flow structures over a gravel surface: a numerical experiment. *Water Resources Research,* Volume 43.

Hazuku, T., Takamasa, T. & Okamoto, K., 2003. Simultaneous measuring system for free surface and liquid velocity distributions using PIV and LFD. *Experimental thermal and fluid science,* Volume 27, pp. 677-684.

Hegewisch, K. C. & Tomsovic, S., 2012. Random matrix theory for underwater sound propagation. *Europhysics Letters,* 97(3).

Hoff, B. J., Westerweel, J., Schneider, T. M. & Echhardt, B., 2006. Finite lifetime of turbulence in shear flows. *Nature,* Volume 443, pp. 59-62.

Horoshenkov, K. V., Nichols, A., Tait, S. J. & Maximov, G. A., 2013. The pattern of surface waves in a shallow free surface flow. *Journal of Geophysical Research: Earth Surface,* 118(3), pp. 1864-1876.

Horoshenkov, K., Yin, Y., Schellart, A., Ashley, R., Blanksby, J., 2004. The acoustic attenuation and hydraulic roughness in a large section sewer pipe with periodical obstacles. *Journal of Water Science and Technology,* 50(11), pp. 97-104.

Hunt, C. R., 2008. *The emergence of oscillons in granular media.* [Online] Available at: http://guava.physics.uiuc.edu/~nigel/courses/569/Essays_Fall2008/files/hunt.pdf. [Accessed 10 October 2013].

Hunter, D. J., 2010. *Volumetric Flow Prediction using Multiple Plane Particle Image Velocimetry - PhD Thesis,* Warwick: The University of Warwick.

IETG, 2013. *Flowhawk.* [Online] Available at: http://www.ietg.co.uk/products/flowhawk/. [Accessed 4 July 2013].

Jackson, R. G., 1976. Sedimentological and fluid-dynamic implications of turbulent bursting phenomenon in geophysical flows. *J. Fluid Mech.,* 77(3), pp. 531-560.

Johnson, D. H. & Dudgeon, D. E., 1993. *Array signal processing.* 1st ed. Upper Saddle River, NJ: PTR Prentice Hall.

Kirkbride, A. D. & Ferguson, R., 1995. Turbulent flow structure in a gravel-bed river: Markov chain analysis of the fluctuating velocity profile. *Earth Surface Processes and Landforms,* 20(8), pp. 721-733.

Kline, S. J., Reynolds, W. C., Schraub, F. A. & Runstadler, P. W., 1967. The structure of turbulent boundary layers. *J. Fluid Mech.,* Volume 30, pp. 741-773.

Komori, S., Murakami, Y. & Ueda, H., 1989. The relationship between surface renewal and bursting motions in an open channel flow. *J. Fluid Mech.,* Volume 203, pp. 103-123.

Komori, S., Ueda, H., Ogino, F. & Mizushina, T., 1982. Turbulence structure and transport mechanism at the free surface in an open channel flow. *International Journal of Heat and Mass Transfer,* 25(4), pp. 513-521.

Kostaschuk, R. A. & Church, M. A., 1993. Macroturbulence generated by dunes: Fraser river, Canada. *Sedimentary Geology,* 85(1-4), pp. 25-37.

Krogstad, P. A., Antonia, R. A. & Browne, W. B., 1992. Comparison between rough- and smooth-wall turbulent boundary layers. *J. Fluid Mech.,* Volume 245, pp. 599-617.

Kumar, S., Gupta, R. & Banerjee, S., 1998. An experimental investigation into the characteristics of free-surface turbulence in channel flow. *Phys. Fluids,* February, 10(2), pp. 437-456.

Lagergren, P., 2012. *Ultrasonic fuel level monitoring device.* United States of America, Patent No. 7287425.

Lamarre, H. & Roy, A. G., 2005. Reach scale variability of turbulent flow characteristics in a gravel-bed river. *Geomorphology,* 68(1-2), pp. 95-113.

Landau, L. D. & Lifshitz, E. M., 2011. *Fluid Mechanics.* 2 ed. Oxford: Reed Education and Professional Publishing Ltd..

Lawless, M. & Robert, A., 2001a. Scales of boundary resistance in coarse-grained channels: turbulent velocity profiles and implications. *Geomorphology,* Volume 39, pp. 221-238.

Lawless, M. & Robert, A., 2001b. Three-dimensional flow structure around small-scale bedforms in a simulated gravel-bed environment. *Earth Surf. Process. Landforms,* Volume 25, pp. 507-522.

Legleiter, C. J., Phelps, T. L. & Wohl, E. E., 2007. Geostatistical analysis of the effects of stage and roughness on reach-scale spatial patterns of velocity and turbulence intensity. *Geomorphology,* Volume 83, pp. 322-345.

Liu, P. C., 2013. Contemplating Ocean Wave Measurements. *International Journal of Geosciences,* Volume 4, pp. 229-233.

Liu, Z., Adrian, R. J. & Hanratty, T. J., 2001. Large-scale mode of turbulent channel flow: transport and structure. *J. Fluid Mech.,* Volume 448, pp. 53-80.

Lorenz, R., Kraal, E., Eddlemon, E., Cheney, J., Greeley, R., 2005. Sea-surface wave growth under extraterrestrial atmospheres: Preliminary wind tunnel experiments with application to Mars and Titan. *Icarus,* 175(2), pp. 556-560.

Luchik, T. S. & Tiederman, W. G., 1987. Timescale and structure of ejections and bursts in turbulent channel flows. *J. Fluid Mech.,* Volume 174, pp. 529-552.

Lu, S. S. & Willmarth, W. W., 1973. Measurements of the structure of the Reynolds stress in a turbulent boundary layer. *J. Fluid Mech.,* Volume 60, pp. 481-511.

Martínez-Suástegui, L., 2012. *Overview on stereoscopic particle image velocimetry, advanced methods for practical applications in fluid mechanics.* [Online] Available at: http://www.intechopen.com/books/advanced-methods-for-practical-applications-in-fluidmechanics/overview-on-stereoscopic-particle-image-velocimetry. [Accessed 14 July 2013].

McLean, S. R. & Nikora, V. I., 2006. Characteristics of turbulent unidirectional flow over rough beds: Double-averaging perspective with particular focus on sand dunes and gravel beds. *Water Resources Research,* Volume 42, p. W10409.

Müller, A. & Gyr, A., 1986. On the vortex formation in the mixing layer behind dunes. *J. Hydraul. Res.,* Volume 24, pp. 359-375.

Muste, M., Schöne, J. & Creutin, J.-D., 2005. Measurement of free-surface flow velocity using controlled surface waves. *Flow measurement and instrumentation,* Volume 16, pp. 47-55.

Nakagawa, H. & Nezu, I., 1981. Structure of space–time correlations of bursting phenomena in an open-channel flow. *J. Fluid Mech.,* Volume 104, pp. 1-43.

Nazarenko, S., Lukaschuk, S., McLelland, S. & Denissenko, P., 2010. Statistics of surface gravity wave turbulence in the space and time domains. *J. Fluid Mech.,* Volume 642, pp. 395-420.

Nelder, J. A. & Mead, R., 1965. A simplex method for function minimization. *Computer Journal,* Volume 7, pp. 308-313.

Nezu, I. & Nakagawa, H., 1993. *Turbulence in Open-Channel Flows.* Rotterdam, Netherlands: Balkema.

Nichols, A., 2008. *Control of Flow Induced Cavity Resonance (Masters Dissertation),* Durham University: Durham University.

Nichols, A., Attenborough, K. & Taherzadeh, S., 2011. Deduction of static surface roughness from complex excess attenuation. *J. Acoust. Soc. Am.,* 129(3), pp. EL89-93.

Nichols, A., Tait, S., Horoshenkov, K. & Shepherd, S., 2013. A non-invasive airborne wave monitor. *Flow Measurement and Instrumentation,* Volume 34, pp. 118-126.

Nikora, V. & Goring, D., 2000. Eddy convection velocity and Taylor's hypothesis of 'frozen' turbulence in a rough-bed open-channel flow. *J. Hydrosci. Hydraul. Eng. ,* Volume 18, pp. 75-91.

Nikora, V. I., Goring, D. G. & Biggs, B. J. F., 1998. On gravel-bed roughness characterisation. *Water Resources Res.,* 34(2), pp. 517-527.

Nikora, V. I., Goring, D., McEwan, I. & Griffiths, G., 2001. Spatially averaged open channel flow over rough bed. *J. Hydr. Eng.,* 127(2), pp. 123-133.

Nikuradse, J., 1932. Gesetzmassigeit der turbulenten stromung in glatten rohren. *Forsch. Arb. Ing.-Wes,* Volume 356.

Nimmo-Smith, W. A. M., Thorpe, S. A. & Graham, A., 1999. Surface effects of bottom-generated turbulence in a shallow tidal sea. *Nature,* 400(6741), pp. 251-254.

Nocke, C., 2000. In-situ acoustic impedance measurement using a free-field transfer function method. *Applied Acoustics,* Volume 59, pp. 253-264.

Oh, S.-H., Mizutani, N. & Suh, K.-D., 2008. Laboratory observation of coherent structures beneath microscale and large-scale breaking waves under wind action. *Experimental Thermal and Fluid Science,* Volume 32, pp. 1232-1247.

Okamoto, K., Philip, O. G. & Hassan, Y. A., 1995. Simultaneous measurement of free-surface and velocity using PIV. *Journal of the Visualization Society of Japan,* Volume 15, pp. 261-264.

Paciorek, C., 2003. *Nonstationary Gaussian Processes for Regression and Spatial Modelling, PhD Thesis,* Pittsburgh: Carnegie Mellon University.

Peakall, J. & Warburton, J., 1996. Surface tension in small hydraulic river models - the significance of the Weber number. *Journal of Hydrology (NZ),* 35(2), pp. 199-212.

Pearson, J. M., Guymer, I., Karambas, T. V. & Spyropoulou, A., 2010. Solute dispersion in the nearshore due to oblique waves. *Proceedings of the HYDRALAB III Joint User Meeting.*

Peggs, G. N. & Yacoot, A., 2002. A review of recent work in sub-nanometre displacement measurement using optical and X-ray interferometry. *Phil. Trans. R. Soc. Lond. A,* Volume 360, pp. 953-968.

Philip, O., Hassan, Y. & Okamoto, K., 1996. Fluid flow and fluid free surface interaction using particle image velocimetry. *International conference on nuclear engineering,* 1(Part A).

Plascoat, 2013. *Activated Polyolefin Technology.* [Online] Available at: http://www.plascoat.com/gb%20content/Coating%20products/Presentation%20-%20Talisman%20Roadshow%20web.pdf. [Accessed 12 July 2013].

Plé, O., Tourabi, A. & Abuaisha, M. S., 2013. 3-Dimensional Digital Image Correlation for Strains Determination in Clayey Soil. *Applied Mechanics and Materials,* Volume 353-356, pp. 463-466.

Posdziech, O. & Grundmann, R., 2007. A systematic approach to the numerical calculation of fundamental quantities of the two-dimensional flow over a circular cylinder. *Fluids Struct.,* 23(3), pp. 479-499.

Puleo, J. A., McKenna, T. E., Holland, K. T. & Calantoni, J., 2012. Quantifying riverine surface currents from time sequences of thermal infrared imagery. *Water resources research,* Volume 48.

Qin, Q., Lukaschuk, S. & Attenborough, K., 2008. Laboratory studies of near-grazing impulsive sound propagating over rough water. *J. Acoust. Soc. Am.,* August.124(2).

Rashidi, M., Hetsroni, G. & Bannerjee, S., 1992. Wave-turbulence interaction in free surface channel flows. *Physics Fluids,* Volume A4, pp. 2727-2738.

Redding, R., 1983. *Measurement of distance using ultrasound.* United Kingdom, Patent No. GB2121174A.

Robert, A., 1990. Boundary roughness in coarse-grained channels. *Prog. Phys. Geogr.,* Volume 14, pp. 42-70.

Rosgen, D. L., 1994. A classification of natural rivers. *Catena,* Volume 22, pp. 169-199.

Rothman, D. H., 1998. Oscillons, spiral waves, and stripes in a model of vibrated sand. *Phys. Rev. E,* 57(2), pp. 1239-1242.

Roussinova, V., Biswas, N. & Balachandar, R., 2010. Revisiting turbulence in smooth uniform open channel flow. *Journal of Hydraulic Research,* 46(2), pp. 36-48.

Roy, A. G., Biron, P. M., Buffin-Bélanger, T. & Levasseur, M., 1999. Combined visual and quantitative techniques in the study of natural turbulent flows. *J. Water Resource Res.,* 35(3), pp. 871-877.

Roy, A. G., Buffin-Bélanger, T. & Deland, S., 1996. Scales of turbulent coherent flow structures in a gravel bed river. In: P. J. Ashworth, S. J. Bennet, J. L. Best & S. J. McLelland, eds. *Coherent Flow Structure in Open Channels.* John Wiley, pp. 147-164.

Roy, A. G., Buffin-Bélanger, T., Lamarre, H. & Kirkbride, A. D., 2004. Size, shape and dynamics of large-scale turbulent flow structures in a gravel-bed river. *J. Fluid Mech.,* Volume 500, pp. 1-27.

Sakamoto, H. & Haniu, H., 1990. A study on vortex shedding from spheres in uniform flow. J*ournal of Fluids Engineering,* Volume 112, pp. 386-392.

Sangfelt, E., Ivansson, S. & Karasalo, I., 2013. Under-ice shallow-water sound propagation and communication in the Baltic Sea. *Proceedings of Meetings on Acoustics,* Volume 19.

Sanjou, M., Nezu, I. & Toda, A., 2010. PIV studies on turbulence structure in air/water interface with wind-induced water waves. *9th International Conference on Hydrodynamics,* pp. 338-342.

Savelsberg, R. & van de Water, W., 2008. Turbulence of a free surface. *Physical review letters,* 100(3).

Savelsberg, R. & van de Water, W., 2009. Experiments on free-surface turbulence. *J. Fluid Mech.,* Volume 619, pp. 95-125.

Shah, D. A. & Antonia, R. A., 1989. Scaling of the 'bursting' period in turbulent boundary layer and duct flows. *Phy. Fluids A,* 1(2), pp. 318-325.

Shah, M. K., Agelinchaab, M. & Tachie, M. F., 2008. Influence of PIV interrogation area on turbulent statistics up to 4th order moments in smooth and rough wall turbulent flows. *Experimental Thermal and Fluid Science,* Volume 32, pp. 725-747.

Shats, M., Xia, H. & Punzmann, H., 2012. Parametrically excited water surface ripples as ensembles of oscillons. *Phys. Rev. Lett.,* Volume 108.

Shvidchenko, A. B. & Pender, G., 2001. Macroturbulent structure of open-channel flow over gravel beds. *Water Resour. Res.,* March, 37(3), pp. 709-719.

Siegel, S., McLaughlin, T. E. & Morrow, J. A., 2001. *PIV Measurements on a Delta Wing with Periodic Blowing and Suction.* Anaheim, CA, American Institute of Aeronautics & Astronautics.

Smolentsev, S. & Miraghaie, R., 2005. Study of a free surface in open channel water flow in the regime from ”weak” to ”strong” turbulence. *Int. J. Multiphase Flow,* Volume 31, pp. 921-939.

Snyder, W. H. & Lumley, J. L., 1971. Some measurements of particle velocity autocorrelation functions in a turbulent flow. *J. Fluid Mech.,* 48(1), pp. 41-71.

Spandöck , F., 1934. Experimental investigation of the acoustic properties of materials through the Kurzton method. *Ann. d. Phys.,* 412(3), pp. 328-344.

Stoesser, T., Braun, C., Garcia-Villalba, M. & Rodi, W., 2008. Turbulence Structures in Flow over Two-Dimensional Dunes. *Journal of Hydraulic Engineering,* 134(1), pp. 42-55.

Stoesser, T. & Rodi, W., 2006. Large Eddy Simulation of Open-Channel Flow Over Spheres. *High Performance Computing in Science and Engineering,* pp. 321-330.

Tamburrino, A. & Gulliver, J. S., 2007. Free-surface visualization of streamwise vortices in a channel flow. *Water Resour. Res.,* Volume 43.

Taylor, G. I., 1938. The spectrum of turbulence. *Proc. R. Soc. London A*, 164: 476.

Tektronix, 2013. *AFG3000C Arbitrary / Function Generator.* [Online] Available at: http://www.tek.com/signal-generator/afg3000-function-generator [Accessed 12 July 2013].

Tinkler, H. J., 1997. Critical flow in rockbed streams with estimated values for Manning's n. *Geomorphology,* 20(1-2), pp. 147-164.

Tolstoy, I., 1982. Coherent sound scatter from a rough interface between arbitrary fluids with particular reference to roughness element shapes and corrugated surfaces. *J. Acoust. Soc. Am.,* Volume 72, pp. 960-972.

Tsubaki, R. & Fujita, I., 2005. Stereoscopic measurement of a fluctuating free surface with discontinuities. *Meas. Sci. Technol.,* Volume 16, p. 1894–1902.

Umbanhowar, P. B., Melo, F. & Swinney, H. L., 1996. Localized excitations in a vertically vibrated granular layer. *Nature,* Volume 382, pp. 793-796.

Ursell, F., 1949. On the heaving motion of a circular cylinder on the surface of a fluid. *Q. J. Mechanics Appl. Math.,* 2(2), pp. 218-231.

Vlaskamp, J. H. A., 2011. *An Experimental and Numerical Investigation into the Vertical Dependence of Taylor-Columns Generated by a Rotating Disc,* Warwick: The University of Warwick.

Wang, Y., Mingotaud, C. & Patterson, L., 1991. Noncontact monitoring of liquid surface level with a precision of 10 micrometers: A simple ultrasound device. *Re. Sci. Instr.,* 62(6), pp. 1640-1641.

Ward, S. N., 2003. *Classical Tsunami Theory - a la Ward.* [Online]
Available at: http://www.es.ucsc.edu/~ward/papers/Basic.pdf
[Accessed 4 July 2003].

Xie, Z., Lin, B. & Falconer, R. A., 2013. Large-eddy simulation of the turbulent structure in compound open-channel flows. *Advances in Water Resources,* Volume 53, pp. 66-75.

Xing, J., Davies, A. M. & Jones, J. E., 2012. Influence of sea surface wind wave turbulence upon wind-induced circulation, tide-surge interaction and bed stress. *Ocean dynamics,* 62(7), pp. 1017-1042.

Yalin, M. S., 1992. *River Mechanics.* Tarrytown, N. Y.: Pergamon.

Zaman, K. B. M. Q. & Hussain, A. K. M. F., 1981. Taylor hypothesis and large-scale coherent structures. *J. Fluid Mech.,* Volume 112, pp. 379-396.